ESD-TR-68-24
EXTRA COPY

ESD-TR-68-24

ESD ACCESSION LIST
ESTI Call No. ~~62780~~ 62781
Copy No. 1 of 1 cys.

A LARGE RADIO-RADAR TELESCOPE

CAMROC DESIGN CONCEPTS

D/C

Volume II
of Two Volumes

15 January 1967

The Cambridge Radio Observatory Committee

HARVARD UNIVERSITY
MASSACHUSETTS INSTITUTE OF TECHNOLOGY
MIT LINCOLN LABORATORY
SMITHSONIAN ASTROPHYSICAL OBSERVATORY

AD0676633

This document has been approved for public release and sale; its distribution is unlimited.

A LARGE FULLY STEERABLE RADIO-RADAR TELESCOPE

DESIGN CONCEPTS

15 January 1967

VOLUME II
of Two Volumes

CAMROC studies are supported by the
National Science Foundation (grant GP-5832)
and the participating institutions.

THE CAMBRIDGE RADIO OBSERVATORY COMMITTEE

CAMROC Report 1967-1

Accepted for the Air Force
Franklin C. Hudson
Chief, Lincoln Laboratory Office

UNCLASSIFIED

Security Classification

DOCUMENT CONTROL DATA – R&D

(Security classification of title, body of abstract and indexing annotation must be entered when the overall report is classified)

1. ORIGINATING ACTIVITY *(Corporate author)*

Lincoln Laboratory, M.I.T., for the Cambridge Radio Observatory Committee, Cambridge, Massachusetts

2a. REPORT SECURITY CLASSIFICATION

Unclassified

2b. GROUP

None

3. REPORT TITLE

A Large Radio-Radar Telescope – CAMROC Design Concepts, Volume II*

4. DESCRIPTIVE NOTES *(Type of report and inclusive dates)*

Progress Report

5. AUTHOR(S) *(Last name, first name, initial)*

Committee Members of Harvard University, M.I.T., M.I.T. Lincoln Laboratory, and Smithsonian Astrophysical Observatory

6. REPORT DATE	7a. TOTAL NO. OF PAGES	7b. NO. OF REFS
15 January 1967	336	46

8a. CONTRACT OR GRANT NO.	9a. ORIGINATOR'S REPORT NUMBER(S)
NSF Grant No. 5832 and in part under AF 19(628)-5167 b. PROJECT NO.	CAMROC Report 1967-1, Vol. II
c.	9b. OTHER REPORT NO(S) *(Any other numbers that may be assigned this report)* ESD-TR-68-24
d.	

10. AVAILABILITY/LIMITATION NOTICES

This document has been approved for public release and sale; its distribution is unlimited.

11. SUPPLEMENTARY NOTES	12. SPONSORING MILITARY ACTIVITY
*See ESD-TR-68-23 for Volume I.	National Science Foundation, Washington, D.C. with partial support from Air Force Systems Command, USAF

13. ABSTRACT

This document summarizes the engineering design studies relating to a large, fully steerable radio telescope. Engineering and economic considerations are detailed which led to the use of a radome to protect a 400-foot diameter, .5-cm, fully steerable parabolic antenna. The electromagnetic performance of the metal space-frame radome is discussed in detail, and the design of five different parabolic reflector configurations is described.

14. KEY WORDS

radio telescope
large steerable antenna
precision structures
deflection compensation
radio astronomy instrumentation
radomes (metal space-frame)
electromagnetic scattering
radio telescope sky noise considerations
computer programmed structural analysis
rain effects on radomes

UNCLASSIFIED

Security Classification

TABLE OF CONTENTS

VOLUME II

ANNEXES

RADOME (Electromagnetic)

1. Loss Calculation on Metal Space-Frame Radomes
2. Effect of Rain on Radome Performance

ENVIRONMENTAL CONSIDERATIONS

3. Climatic Extremes for a Large Radome Within 2 Hours of Boston, Massachusetts
4. Surface Wind-Speed Extremes in the United States

RADOME (Structural)

5. Geometric and Structural Considerations for Large Radomes
6. Estimate of Optimum Beam Dimensions for CAMROC 550-Ft-Diameter Space Frame When Exposed to 130-mph Wind
7. CAMROC Model Program
8. Theoretical Investigation on Buckling of Reticulated Radomes
9. Estimate of Critical Pressures for Model Buckling Tests
10. Experimental Study of Instability in Elements of Shallow Space Frames
11. Formulation of the Governing Equations for the Buckling of a Planar Frame

ANTENNA (Surface Considerations)

12. Surface Panel Geometry for Hammerhead Antenna Concept
13. Report to the Cambridge Radio Observatory Committee

SUPPLEMENT

Large-Diameter Rigid Radomes

VOLUME I

Section		Page
	CAMROC PUBLICATIONS	v
	PREFACE	vii
	SUMMARY	ix
1	BACKGROUND OF THE CAMROC STUDY	1-1
	1.1 Introduction	1-1
	1.2 The Choice of a Large Steerable Paraboloid	1-1
	1.3 Philosophy Underlying the CAMROC Study Program	1-3
	1.4 Performance Criteria	1-4
2	RADOME CHARACTERISTICS	2-1
	2.1 Introduction and Background	2-1
	2.2 Radome Studies	2-5
	2.3 Effect of a Radome upon Antenna Economics	2-8
	2.4 Effect of a Radome on System Performance	2-9
3	DESIGN REQUIREMENTS FOR EXPOSED AND PROTECTED ANTENNAS	3-1
	3.1 General	3-1
	3.2 Effect of Size	3-1
	3.3 Design Considerations	3-2
	3.4 Comparison of Wind and Gravity Loads on Antenna Structures	3-3

VOLUME I

(continued)

Section		Page
4	SEARCH FOR A SUITABLE ANTENNA CONFIGURATION	4-1
	4.1 Early Configuration Studies	4-1
	4.2 Conclusions of Early Configuration Studies	4-2
5	CONCEPTUAL STUDIES FOR STEERABLE PARABOLIC ANTENNAS	5-1
	5.1 Conclusions of the Conceptual Studies	5-1
	5.2 Applicability of Other Studies	5-6
6	COST ESTIMATES FOR ANTENNAS AND RADOMES	6-1
7	ELECTROMAGNETIC PROPERTIES OF SPACE-FRAME RADOMES	7-1
	7.1 The Electromagnetic Properties of Large Radomes (Metal Space Frames)	7-1
	7.2 Operational Experience with the Haystack Radome in Astronomical Observations	7-27
8	STRUCTURAL DESIGN FOR LARGE SPACE-FRAME RADOMES	8-1
	8.1 Summary	8-1
	8.2 Radome Specifications	8-1
	8.3 Environment	8-2
	8.4 Space-Frame Geometry	8-7
	8.5 Structural Analysis	8-13
	8.6 Erection Procedure	8-40
	8.7 Radome Cost	8-40
	8.8 Future Effort	8-44
	8.9 References	8-46
9	OBSERVATORY INSTRUMENTATION AND FACILITIES	9-1

APPENDICES

A	Engineering Summary of a Study to Evaluate the Effects of a Radome Environment on the Performance and Cost of a Large-Diameter Radio Telescope
B	Conceptual Studies for a 400-Ft-Diameter CORT Antenna
C	Conceptual Study of a 400-Ft-Diameter Fully Compensated Cassegrain Antenna
D	CAMROC Hammerhead Antenna Concept
E	Report on a Conceptual Study of a Large Cassegrain Antenna
F	Parametric Study of a 400-Ft-Diameter Antenna Based on CSIRO Parkes Configuration
G	Engineering Summary of a Study for a 400-Ft-Diameter Radome-Housed Radio Telescope
H	Scientific Program for a Large, Steerable Paraboloid

ANNEX 1

LOSS CALCULATION ON METAL SPACE-FRAME RADOMES

CAMROC WORKING MEMORANDUM

Prepared by

John Ruze

MIT Lincoln Laboratory

LOSS CALCULATION ON METAL SPACE-FRAME RADOMES

John Ruze

Lincoln Laboratory
Massachusetts Institute of Technology

1. INTRODUCTION

The purpose of this note is to present a method of determining the loss due to a metal space frame. Fundamentally, the method does not differ from that introduced by Kennedy (1958) and extended by Kay (1965). After certain simplifying assumptions, these methods consist of subtracting the forward-scattered field of each individual member from the unobstructed aperture axial field. It is hoped that the procedure suggested in this note will prove convenient to electrical and structural designers.

It must be realized that a rigorous formulation of the radome space frame as an electromagnetic scattering problem represents a tremendously difficult endeavor. Even such simplified problems as the transmission through a square grid have only approximate solutions, and these only in the long- or short-wavelength limit. If a rigorous formulation were available, suitable for use with modern computing machines, one would question its engineering usefulness since it would require, as one of its inputs, accurate knowledge of the scattering coefficients of various structural shapes and at all aspect angles.

It has, therefore, been customary to make certain simplifying assumptions to make the problem amenable to calculation. Principal among these is that the elements scatter as independent, infinite cylinders placed in front of an aperture with uniform phase. This implies the neglect of end effects, circulating currents at member junctions, mutual scattering, and near field effects. In addition, simplifying the calculations to average various effects implies that such an average has meaning and the number of such elements is large.

To evaluate the success of this suggested procedure, recourse must be made to experimental verifications on actual radome geometries. Unfortunately, there is a dearth of precise radome-loss measurements over a range of frequencies. We hope, the procedure, if applied to a number of structurally acceptable designs, would yield those preferable from an electromagnetic standpoint.

2. THEORETICAL DISCUSSION

2.1 FLAT-SHEET RADOME

We first consider the spherical radome as a flat sheet and determine the fraction of the aperture area blocked (Figure 1) as

$$\eta = \frac{2\sqrt{3}\, w L}{(L+2r)^2} + \frac{2\pi r^2}{\sqrt{3}\,(L+2r)^2} = \eta_m + \eta_n \quad . \tag{1}$$

The first term is the member blockage and the second the contribution of the hubs. The latter is generally 10 to 30 percent of the member blockage. The above formula is derived on the basis of equilateral triangles. For a random geometry the individual member lengths vary. It can be shown that for a variation of ± 10 percent in length the error made by using the mean length in equation (1) is 2 percent (too small).

At very high frequency (optical limit) the reduction in axial field is then simply

$$\frac{e}{e_0} = 1 - \eta_m - \eta_n \quad . \tag{2}$$

At lower frequencies the blockage must be modified by a factor that accounts for the relative scattering efficiency of the members. This factor (Kennedy, 1958; Kay, 1965), called the induced current or field ratio, is simply the ratio of the forward-scattered field of the member to the forward-radiated field of an incident plane wave of the same width. It is a complex number that depends on the member cross section, their shape, and on their orientation, θ, relative to the polarization vector. In the optical limit it approaches -1. Equation (2) then becomes

$$\frac{e}{e_0} = 1 + \eta_m \left[ICR_{\perp} \cos^2\theta + ICR_{\parallel} \sin^2\theta \right] - \eta_n \quad , \tag{3}$$

where we have not modified the smaller hub contribution, and where we have resolved the polarization vector along and perpendicular to the member axis.

If the members have a random or equiangular arrangement, then their summation in equation (3) yields

$$\frac{e}{e_0} = 1 + \eta_m \, \overline{ICR} - \eta_n \quad , \tag{4}$$

where $\overline{ICR}$ is the average induced-current ratio for the two orthogonal polarizations.

The loss in axial power is then

$$\frac{p}{p_0} = \left| 1 + \eta_m \, \overline{ICR} - \eta_n \right|^2 \approx 1 + 2\,\eta_m \, \mathcal{R}_e \, \overline{ICR} - 2\,\eta_n \quad , \tag{5}$$

where the approximation is valid as the blockage is hopefully small (see Appendix). Now by the "shadow theorem" (Burke and Twersky, 1964), the real part of the forward-scattered field is proportional to the total scattering cross section or

$$\mathcal{R}_e \, \overline{ICR} = - \frac{\overline{\sigma_{sc}}}{2w} = - g(w) \quad , \tag{6}$$

where $2w$ is the optical cross section and $\overline{\sigma_{sc}}$ the average total scattering cross section. We have alternately for the loss of axial power

$$\frac{p}{p_0} = 1 - 2\,\eta_n - 2\,\eta_m \, y(w) \quad . \tag{7}$$

The advantage in using the total scattering cross section instead of the more correct complex induced-current ratio is that many references calculate the former. Figure 2 plots the total scattering cross sections for round cylinders. Figure 3 gives the average total cross section for rectangular cylinders (van Bladel, 1964; Kay and Paterson, 1965; Mei and van Bladel, 1963; Morse, 1964; King and Wu, 1959; Mentzer, 1955).

The flat radome loss is then calculated by equation (7) with the use of equation (1) and Figure 3. This loss is independent of the aperture illumination taper.

2.2 SPHERICAL RADOMES

In a spherical radome the aspect of the members change with aperture position. It is, therefore, necessary to include this change in a modified scattering cross section or ICR and to weigh this changing contribution with the aperture illumination taper. The aspect of the members is bounded by two limiting cases; namely, 1) those members directed along great-circle paths through the beam axis, and 2) those members orthogonal to these great circles (Figure 4).

For the great-circle members the scattering is reduced by the cosine of the angle of incidence as these members are foreshortened by the radome curvature. For the orthogonal members the scattering is increased because of the greater projection of deep members. In addition, the apparent concentration of the orthogonal members increases as the cosine of the incident angle. We would therefore expect the scattering of the orthogonal system of rectangular members to vary in the optical limit (high frequency) as

$$\frac{1}{\cos\theta}\left[\cos\theta + \frac{d}{w}\sin\theta\right] \quad . \tag{8}$$

In the low-frequency limit, the rotation of the member is immaterial as the total scattering cross section here depends only on the perimeter in wavelength. Generally, we can represent the scattering of the orthogonal members as (Figure 5)

$$\frac{1}{\cos\theta}\left[\cos\theta + \frac{d}{w}\sin\theta\right]^{n(\lambda)} \quad . \tag{9}$$

The function $n(\lambda)$ varies from unity at the optical limit to zero at low frequencies. This function was determined, for rectangular members, from Kay and Paterson (1965) and Mei and Van Bladel (1963) and is plotted in Figure 6. It was found that when $n(\lambda)$ was plotted as a function of the perimeter in wavelengths that it was essentially independent of the d/w ratio. We note from Figure 6 that when the perimeter is less than half a wavelength the total scattering cross section is independent of element rotation; whereas when the perimeter is over 10 wavelengths the scattering cross section is essentially the projected optical cross section. For round members there are no rotational effects and n may be taken as zero.

As we must weigh these effects by the illumination taper and normalize by the same, we have for the loss of axial gain

$$\frac{P}{P_0} = 1 - 2\eta_n - 2\eta_m g(w) \frac{\int_0^1 f(r)\cos\theta\, r\,dr + \int_0^1 \frac{\left[\cos\theta + \frac{d}{w}\sin\theta\right]^{n(\lambda)} f(r)\, r\,dr}{\cos\theta}}{2\int_0^1 f(r)\, r\,dr} \quad , \tag{10}$$

where we have summed or integrated over circular rings and assumed that the extremes of member aspect behavior can be approximated by their mean.

3. APPLICATION

The result of our analysis is then given by equation (10) or Figure 7. Here

A. The hub blockage is calculated from equation (1) and is not modified by the curvature factor as the hubs are thin compared to their diameter. As they are uniformly distributed their effect is independent of the aperture taper.

B. The member blockage is also calculated by equation (7). However, it must be modified by the $\overline{ICR}$ or relative average total scattering cross section, g(w) (Figure 3), and by a radome curvature factor.

C. The curvature factor depends naturally on the ratio of the radome-to-antenna diameter, on the aperture taper, and on the member depth-to-width ratio. The dependence is expressed in the bracketed term of Figure 7. For given parameters it can be evaluated and is given in Figures 8, 9, and 10. For $n(\lambda) = 0$ the curvature factor is essentially unity.

An example best illustrates the procedure. A proposed space frame has the following characteristics:

Radome diameter	500 ft
Antenna diameter	400 ft
Frequency	2700 Mc
Average member length (L)	37.5 (35 to 40 ft var.)
Member width (w)	2.5 inches
Member depth (d)	20 inches
Hub diameter (2r)	42 inches
Member perimeter (p)	45 ft

from equation (1) optical blockage

$$\eta = 1.02\ \frac{2\sqrt{3}\,(2.5)\,(450)}{(492)^2} + \frac{2\pi}{\sqrt{3}}\left(\frac{42}{492}\right)^2$$

(Note: 1.02 inserted due to member length variation)

$$\eta = \eta_m + \eta_n = 0.0164 + 0.0264$$

at 2700 Mc (λ = 4.5 inches, p/λ = 10 inches, and η = 0.75 inch) from Figure 6 as $w/\lambda = 2.5/4.5 = 0.555$ inch; and d/w = 8 inches. We have equation (10)

$$p/p_0 = 1 - 2(0.0264) - 2(0.0164)\,(2.3)\,(1.9)$$

or

$$p/p_0 = 1 - 0.0528 - 0.1850 = 0.7622 \ (-1.16 \text{ db}) \quad .$$

4. EXPERIMENTAL CONFIRMATION

To establish the validity of the above procedure recourse must be made to experimental measurements on actual radome structures. Unfortunately, there is a dearth of precise measurements over a sufficiently wide frequency range and with diverse element shapes.

Figure 11 shows the correlation between the calculated and the experimentally measured data on the ESSCO model M-160 metal space frame. The measured data were obtained by periodically rotating a half-radome scale model in front of the parabolic antenna. The vertical bars indicate the signal variability while the radome section was in front of the aperture. Even with no rotation there is a signal variability of about 0.02 db.

5. SHAPED MEMBERS

The present report presents data for loss calculations of radomes consisting of round or rectangular members. At times suggestions have been made to reduce the space-frame loss by streamlining the members. This suggestion, no doubt, has its origin in the success obtained in reducing the radar cross section or backscattering coefficient of various missile shapes. Unfortunately, we are dealing in the space-frame problem with the total and not the backscattering cross section.

It can be readily shown, at least in the high- and low-frequency limits, that any member shaping or streamlining should <u>not</u> offer any advantage.

In the high-frequency limit, the scattering cross section is the optical cross section or merely twice the projected area

$$\overline{\sigma_{sc}} = 2w \quad .$$

Therefore, for a flat radome the streamlining will have no effect. For a spherical radome the streamlining will be deleterious because of the curvature factor of deep members.

In the low-frequency limit, the total average scattering cross section is given by

$$\bar{\sigma}_{sc} = \frac{\pi^2}{2k[\ell n\, p/\lambda]^2} \quad , \tag{11}$$

where $k = 2\pi/\lambda$ and p = cross-section perimeter.

As for a fixed member, width streamlining will increase the perimeter and as the perimeter-to-wavelength ratio is less than unity, the streamlining will increase the scattering cross section and hence the space-frame loss.

6. ACKNOWLEDGMENTS

I am indebted to Mr. Albert Cohen and Mr. Adam Smolski of the Electronic Space Structure Corporation for providing the experimental data of Figure 11 and, also, to Mr. Joseph Morriello for the numerical integration of equation (10).

7. REFERENCES

KENNEDY, P. D.,

1958. An analysis of the electrical characteristics of structurally supported radomes. Ohio State University, Report No. 722-8 on Contract AF 80(602)-1620, November.

KAY, A. F.

1965. Electrical design of metal space frame radomes. IEEE Transactions on Antennas and Propagation, Vol. AP-13, No. 2, pp. 188-202, March.

BURKE, J. E., AND TWERSKY, V.

1964. On scattering of waves by an elliptic cylinder and by a semielliptic protuberance on a ground plane. JOSA, Vol. 54, No. 6, pp. 732-744, June.

VAN BLADEL, J.

1964. Electromagnetic Fields. McGraw-Hill Book Company, New York, p. 375, June.

KAY, A. F., AND PATERSON, D.

1965. Design of metal space frame radomes. RADC-TDR-64-334, ASTIA AD-610037.

MEI, K. K., AND VAN BLADEL, J.

1963. Scattering by perfectly conducting rectangular cylinders. IEEE Transactions on Antennas and Propagation, Vol. AP-11, No. 2, pp. 185-192, March.

MORSE, B. J.

1964. Diffraction by polygonal cylinders. Journal of Mathematical Physics, Vol. 5, No. 2, pp. 199-214, February.

KING, R. W. P., AND WU, T. T.

1959. The Scattering and Diffraction of Waves. Harvard University Press, Cambridge, Massachusetts.

MENTZER, J. R.

1955. Scattering and Diffraction of Radio Waves. Pergamon Press, New York, p. 56.

APPENDIX

The approximation made in equation (5) requires justification. To present the problem we note:

$$p/p_0 = \left|1 + \eta\overline{ICR}\right|^2 = 1 + 2\eta\left|ICR\right|\cos\theta + \eta^2\left|ICR\right|^2 \quad ; \qquad (A\text{-}1)$$

in the optical limit the magnitude $\left|\overline{ICR}\right| \rightarrow 1$ and its phase θ approaches 180°

$$p/p_0 = 1 - 2\eta + \eta^2 \approx 1 - 2\eta \quad , \qquad (A\text{-}2)$$

and the approximation is valid. However, in the low-frequency limit, the phase angle θ approaches 90° and the approximation is not evident.

To investigate the behavior in the low-frequency limit, we insert the low-frequency asymptotic form into equation (A-1). As in the low-frequency limit, the induced-current ratio or relative total-scattering cross section does not depend on the member shape, we can use the values derived by Burke and Twersky (1964) for elliptic cylinders. Using the dominant terms of their equation 41, we have:

$$\overline{ICR} = -\frac{D}{kw}\left(1 - j\frac{2L}{\pi}\right) , \qquad (A-3)$$

where

$2w$ is the optical cross section

$$D = \frac{\pi^2}{\pi^2 + 4L^2}$$

$$f = d/w$$

$$L = \ell \text{ or } \gamma x (1+f)/2$$

d and w are the ellipse major and minor axis

$$\gamma = 1.781 \ldots$$

$$x = \pi w/\lambda ,$$

and (A-1) becomes

$$p/p_0 = 1 - \frac{2\eta}{kw} D + \left(\frac{\eta}{kw}\right)^2 D .$$

We make a 10 percent error in our loss estimate by using only the first two terms if

$$\frac{\eta}{kw} = 10\left(\frac{\eta}{kw}\right)^2$$

$$kw = 5\eta = 5.2\sqrt{3}\ w/L \quad ,$$

or

$$\lambda = \frac{\pi}{5\sqrt{3}}\ L = 0.36\ L \quad .$$

In other words, if the wavelength is smaller than about a third of the member length, the approximation made by using the total scattering cross section instead of the more correct forward-scattered field is less than 10 percent in the calculated space-frame loss. When the wavelength is greater than this value, the calculations are dubious in any case as then the wavelength is comparable to the space-frame cell size.

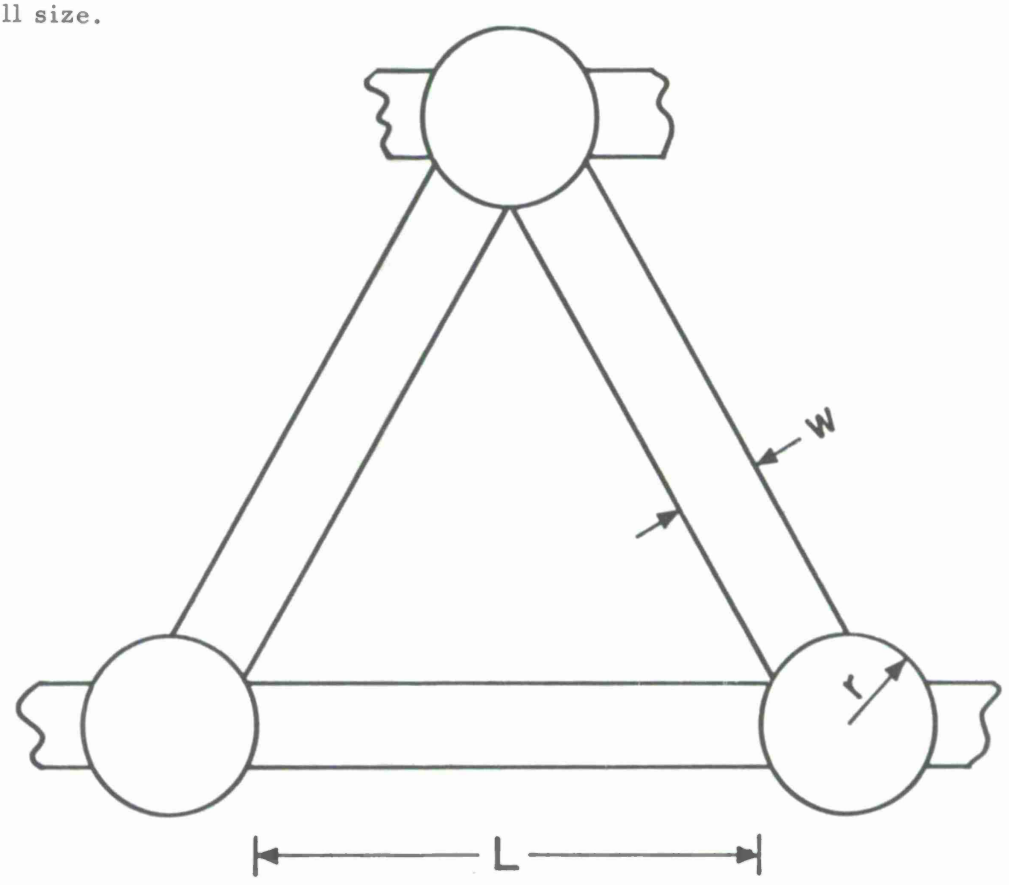

Figure 1. The aperture area blocked.

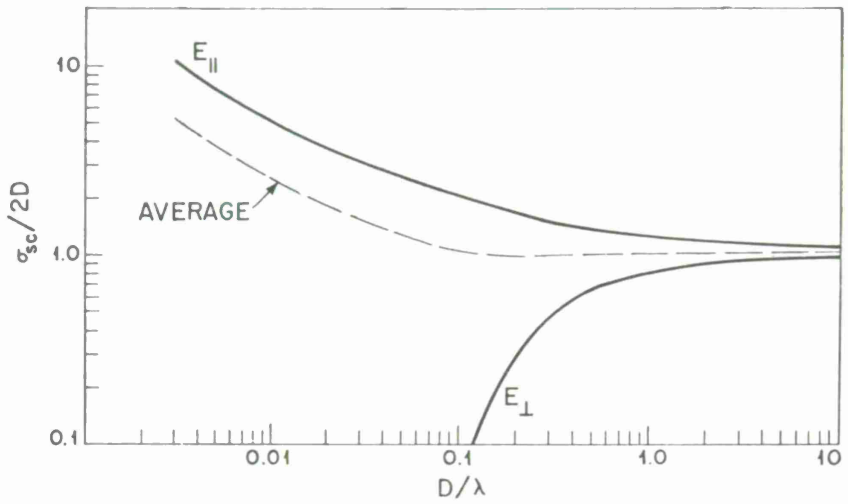

Figure 2. Total scattering cross-section round metal cylinders.

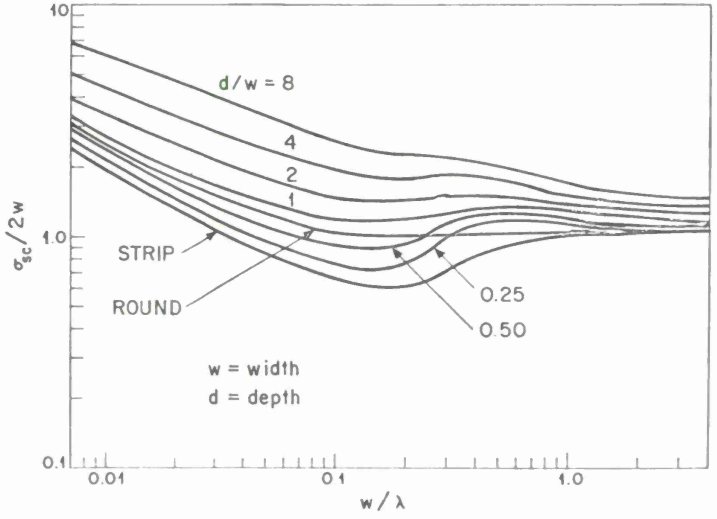

Figure 3. Total average scattering cross-section rectangular cylinders.

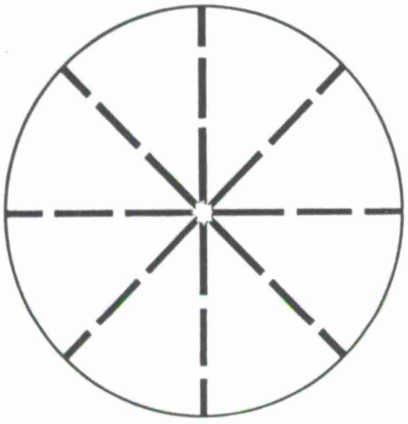

GREAT CIRCLE MEMBERS

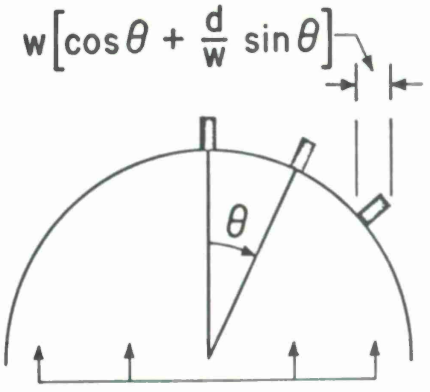

PLANE WAVE

ORTHOGONAL MEMBERS

Figure 4. Limiting disposition of members.

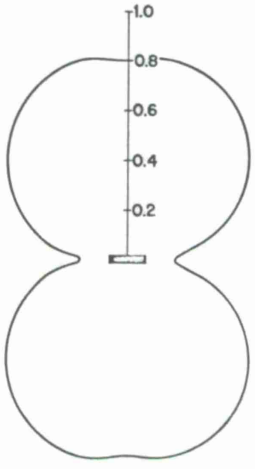

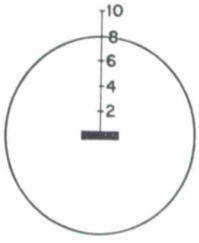

WAVELENGTH << PERIMETER
n = 1

WAVELENGTH >> PERIMETER
n = 0

Figure 5. Relative total scattering cross section generally $\frac{\bar{\sigma}}{2w} = g(w)\left[\cos\theta + \frac{d}{w}\sin\theta\right]^{n(\lambda)}$.

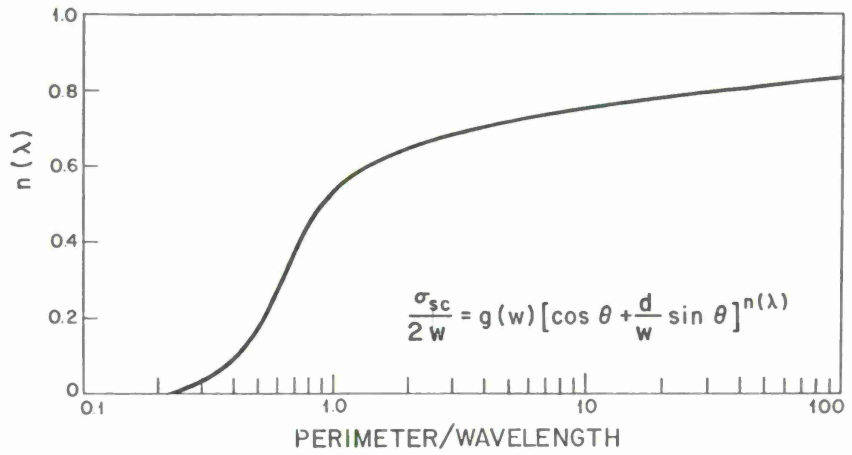

Figure 6. n(λ) plotted as a function of the perimeter in wavelengths.

$$\frac{P}{P_o} = 1 - 2\eta_h - 2\eta_m g(w)\left[\frac{\int_o^1 f(r)\cos\theta\, r\,dr + \int_o^1 \frac{\left[\cos\theta + \frac{d}{w}\sin\theta\right]^{n(\lambda)}}{\cos\theta} f(r)\, r\,dr}{2\int_o^1 f(r)\, r\,dr}\right]$$

CURVATURE FACTOR

RELATIVE SCATTERING CROSS SECTION

MEMBER FRACTIONAL BLOCKAGE

HUB FRACTIONAL BLOCKAGE

Figure 7. General loss formula.

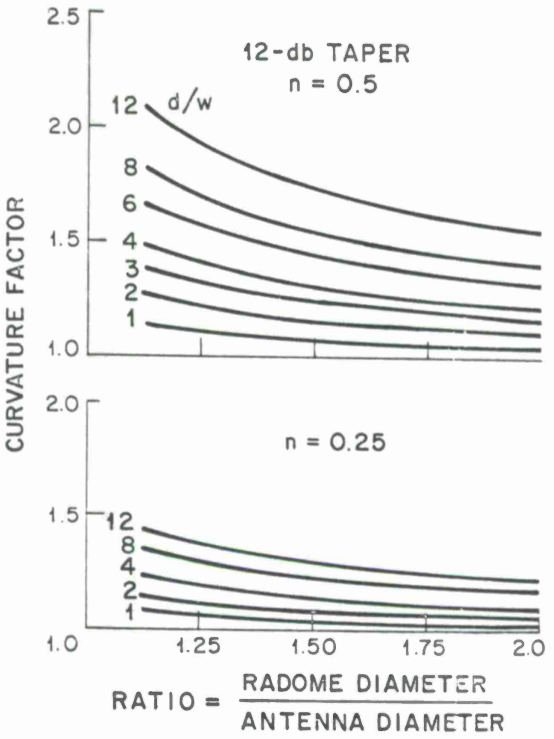

Figure 8. The curvature factor as a function of the ratio of radome to antenna diameter.

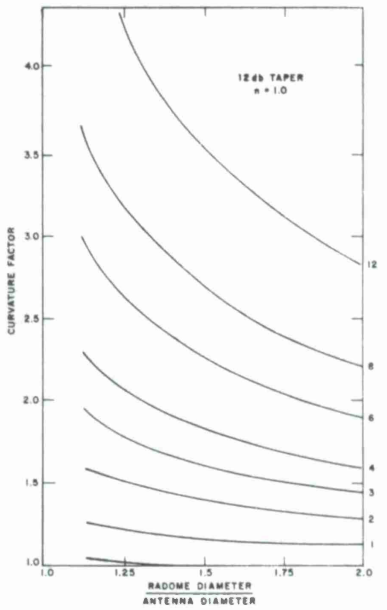

Figure 9. The curvature factor as a function of the ratio of radome to antenna diameter.

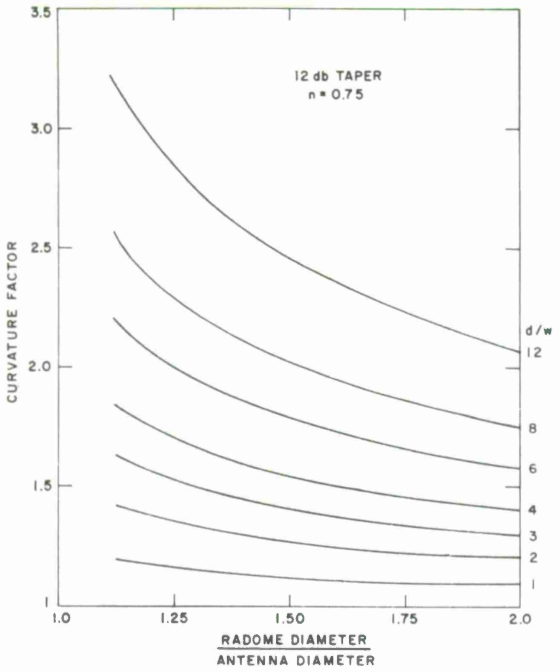

Figure 10. The curvature factor as a function of the ratio of radome to antenna diameter.

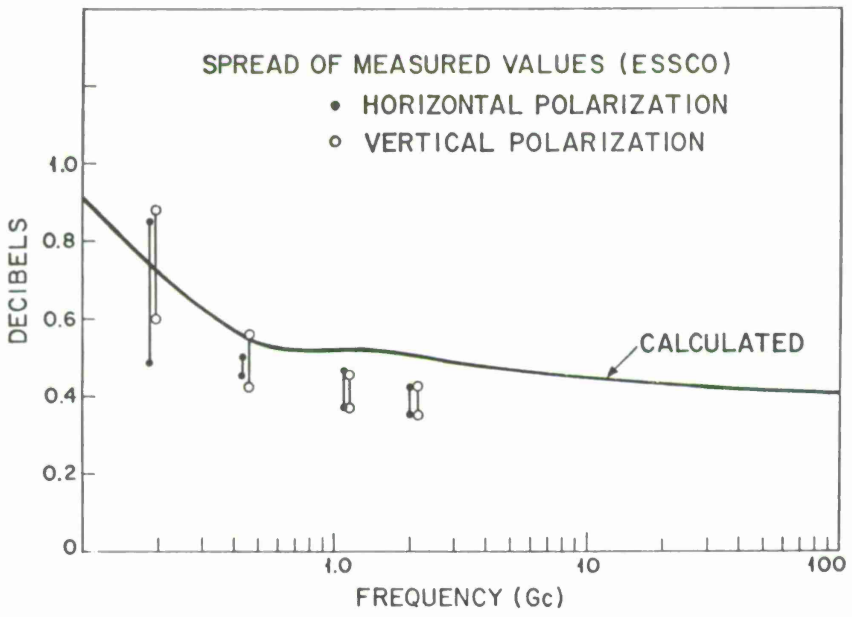

Figure 11. Space-frame loss (M-160) (80-ft antenna in 160-ft radome).

ANNEX 2

EFFECT OF RAIN ON RADOME PERFORMANCE

CAMROC WORKING MEMORANDUM

16 November 1966

Prepared by

John Ruze

MIT Lincoln Laboratory

EFFECT OF RAIN ON RADOME PERFORMANCE

Introduction

Over a year ago severe deleterious effects of rain on the 210-foot Andover inflated radome were reported by Giger (1). These effects are in agreement with calculations on water film thickness based on a formula originally derived by Gibble assuming uniform channel flow.

Recently considerably reduced losses were reported by Cohen and Smolski (2) on a 55-foot metal space-frame radome simulating the rain by means of garden sprinklers. These losses were below those calculated from the Gibble formula for this size radome. Furthermore, visual observations indicated that the water flow on the radome surface was not a uniform film but was largely due to streams and rivulets. In addition, Cohen and Smolski reported that even these lower losses could be made neglibible by treatment of the radome surface by a nonwetting agent.

The disagreement with the Gibble formula and the complex appearance of the water run-off suggested a more expert approach to this problem. Professor C. C. Mei of the M. I. T. Civil Engineering Department was therefore engaged on a consulting contract. Basically, Professor Mei modified the Gibble formulation by considering the turbulent nature of the water flow. (Report available on request.)

Professor Mei's formulation checks the rain-simulation tests of Cohen and Smolski but does not check the Andover results. For very large radomes (550-foot diameter) and high rain rates the Mei and the Gibble formulations predict the same average water-film thickness.

---

(1) Giger, A. J. "4Gc. Transmission Degradation Due to Rain at the Andover, Maine Satellite Station," BSTJ, Sept. 1965, p. 1528.

(2) Cohen, A., and Smolski, A, "Effect of Rain on Satellite Communications Earth Terminal Rigid Radomes," Microwave Journal, Sept. 1966, p. 111.

It is the purpose of this report to gather together the various effects of rain on antennas with radome enclosure with special regard to the CAMROC program (400' Diameter Antenna and 550' Radome).

1) Rain and Wind Frequency

Figure No. 1 shows the percentage of time that rainfall exceeds a given rate and wind a given number of miles per hour. The data are representative 200 feet above a level coastal plane. Individual locations are expected to vary widely from these values.

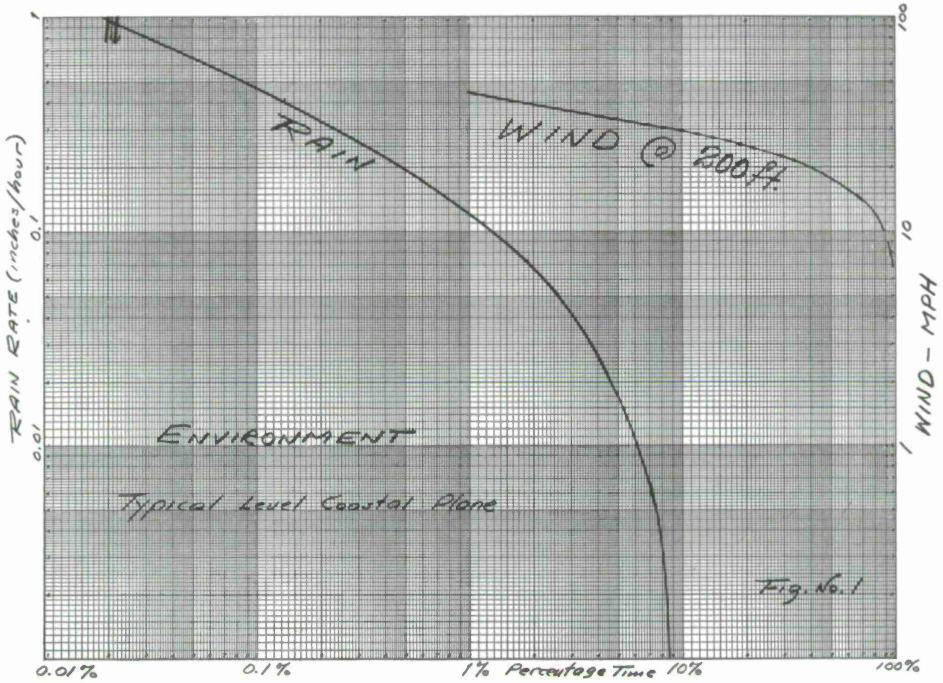

Figure 1.

It is to be noted that heavy rain occurs only 0.1% of the time, moderate rain 1%, and over 90% of the time it does not rain at all.

In contrast, at a height of 200 feet a 30-mph wind is exceeded 10% of the time and only 10% of the time is the wind less than 10 mph.

The implication of these data to an antenna system requiring precise pointing is evident.

2) Signal Attenuation in the Rain Field

The signal attenuation in a rain field is also of interest. This rain field exists in front of the antenna, typically 5 to 20 kilometers, and is quite variable. A comprehensive study by Medhurst (3) of the experimental data indicates that the measured values are several factors above the theoretical predictions. Figure No. 2 shows the expected values from his paper. In a typical installation the data may scatter an order of magnitude above and below this curve. This large variation is due primarily to lack of knowledge of the extent of the rain field, the drop size, and the rain rate.

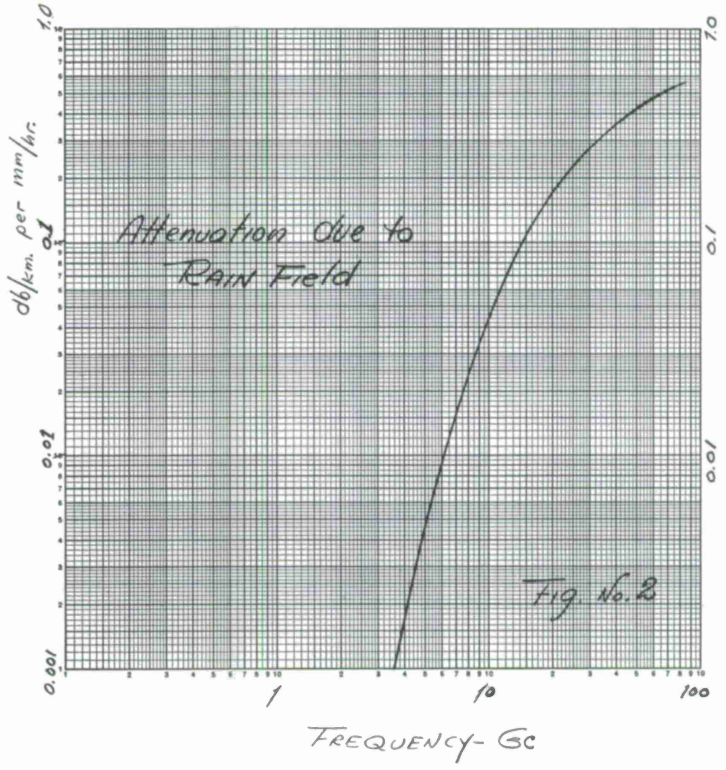

Figure 2.

Nevertheless, the curve indicates that for precise radio astronomical measurements the rain field is a serious factor above 4-cm and becomes negligible below 10-cm wavelength. This rapid dependence is, of course, due to the fourth power law of Rayleigh scattering.

(3) Medhurst, R. G., "Rainfall Attenuation of Centimeter Waves," IEEE Trans. Ant. and Prop., July 1965, pp. 550-564.

3) Rain Flow on a Radome Surface

The water flow on a radome surface must be a very complex phenomenon, involving both uniform water film flow and irregular water streaks and rivulets. The water film flow is probably comparatively slow, whereas the streaks may approach the velocity of free-falling raindrops (typically 800 cm/sec for 1.5-mm diameter drops).

Unfortunately, from the prediction point of view, the nature of this flow strongly affects the electromagnetic transmission of the radome. This is evident when we consider that the scattered energy of a water film depends on the square of the film thickness in wavelengths and for streaks directly on the number and/or on the cube of their diameter in wavelengths.

Fortunately, this strong dependence on film thickness or streak diameter means we can do something about it. Treating the surface to enhance water run-off (increasing flow velocity) implies that we are decreasing the film thickness and/or the streak diameter.

Furthermore, the high dielectric constant of water implies that the portion of the radome flow that is in steaks or rivulets should be markedly polarization sensitive. A thin water cylinder at microwave frequencies scatters over a thousand times more strongly when the electric vector is parallel to the cylinder axis. It should therefore be possible to estimate the fraction of the water that is in streams and that in uniform films.

4) Film-Thickness Formula

As mentioned, two formulas have been derived for the film thickness on the radome; the

Gibble $\quad t = 2.83\,[QR]^{1/3}$ mils

Mei $\quad t = 0.584\,[QR]^{7/12}$ mils ,

where R is the radome radius in feet,

Q is the rain rate in inches per hour.

These formulas are plotted in Figures No. 3 and 4 for radome sizes of current interest. It should be noted that the two formulas agree for large radomes and high rain rates. Otherwise the Mei formula indicates a thinner film and a different functional dependence.

5) Transmission-Loss and Noise-Increase Predictions

Assuming a uniform water-film thickness the transmission loss and the absorbed (ohmic) energy can be calculated. From the absorbed energy the temperature increase of the enclosed aerial can be computed by assuming the water temperature to be 290° K. These data are seen in Figures No. 5 and 6 (for larger values, ref. 4).

6) Experimental Measurement

Measurements have been made on the Andover, Maine, 210-foot inflated radome (1) using star sources. The results of these measurements are shown in Figures No. 7 and No. 8* with theoretical calculations based on both the formulas of Gibble and Mei.

It should be noted that the predictions based on the Gibble formula agree closely not only for the expected transmission loss and increased noise temperature but also in the general slope of these curves. From the nature of the experiment no better agreement can be expected. The Mei formulation does not agree either in magnitude or slope for the two quantities measured.

---

(4) B. C. Blevis, "Losses Due to Radomes and Antenna Reflecting Surfaces," PGAP Jan. 1965.

*In Figure No. 8, the theoretical curve considers only ohmic loss due to water film and does not include additional noise temperature due to scattered energy from the water film.

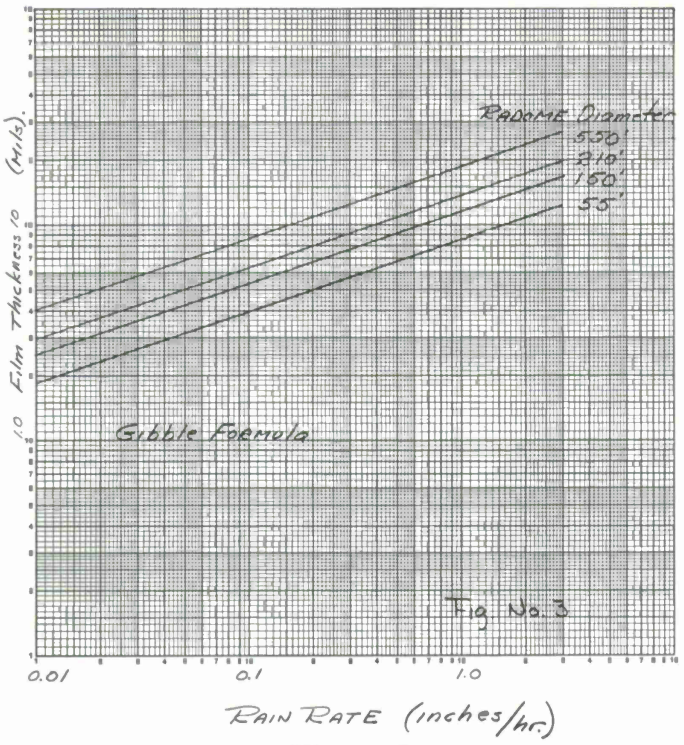

Figure 3.

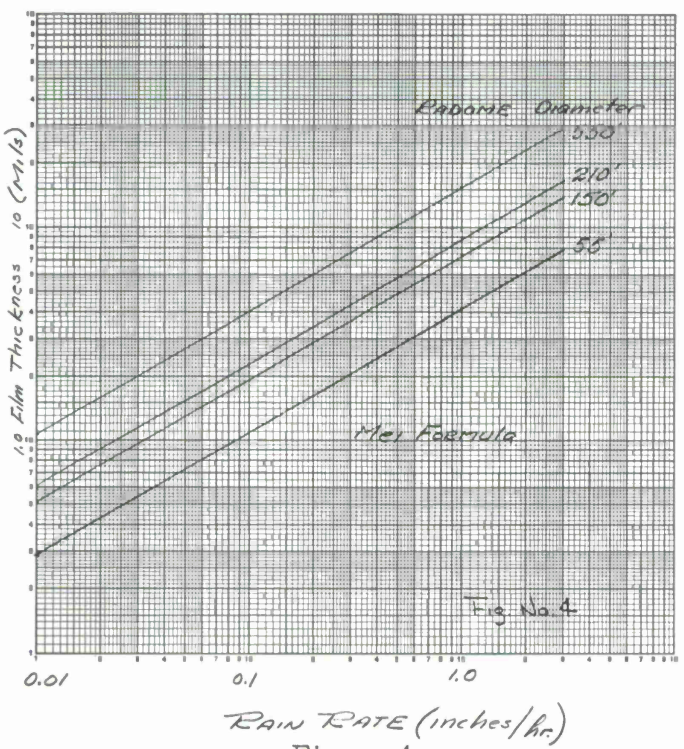

Figure 4.

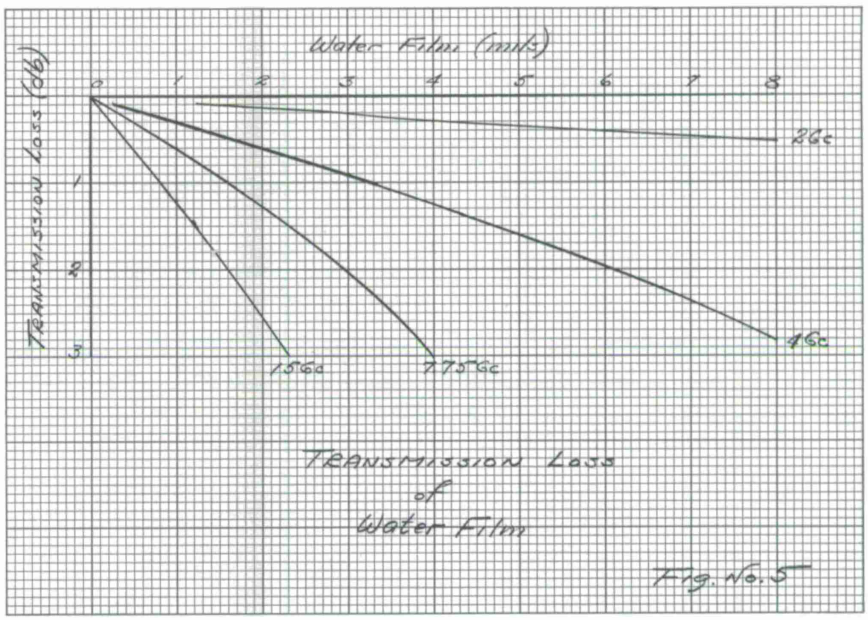

Figure 5.

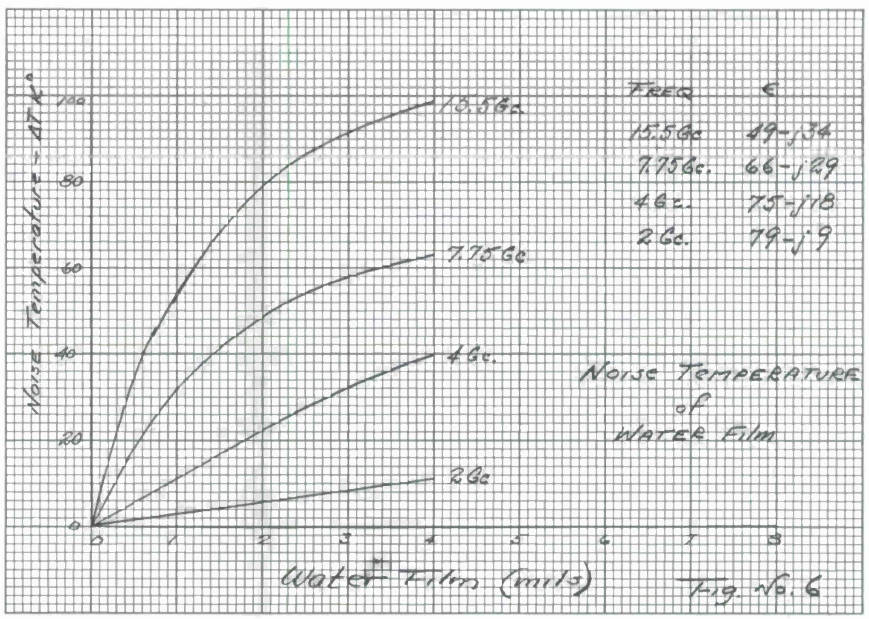

Figure 6.

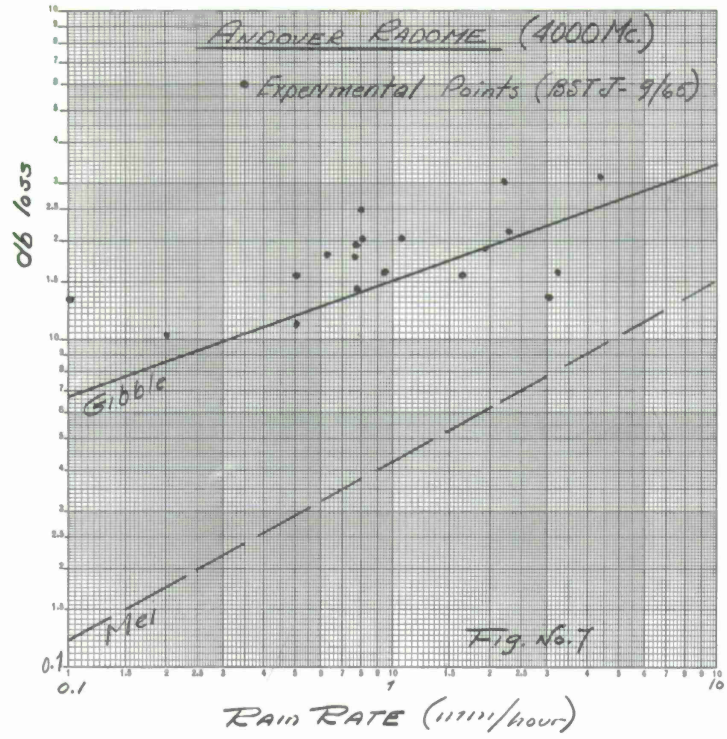

Figure 7.

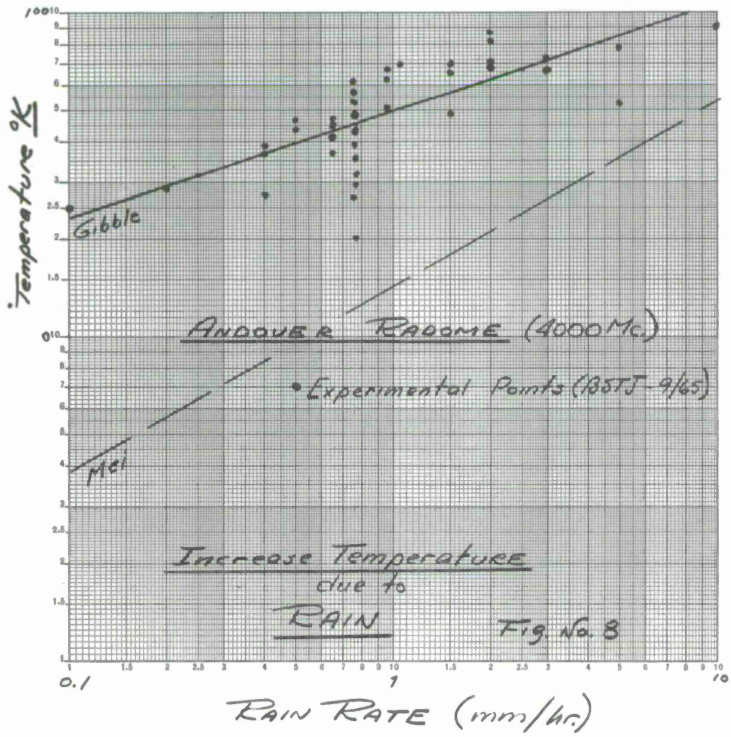

Figure 8.

In addition to the Andover data, transmission-loss measurements were made on a 55-foot metal space-frame radome with treated and untreated Fiberglas panels. The untreated radome data are shown in Figure No. 9 with the predictions based on the Gibble and Mei formulation. In this case the Mei formula agrees much more closely with the experimental data. It is also of interest to note that if the flow were completely due to water cylinders whose diameter is constant but if their number increased with rain rate, we would have a unity slope.

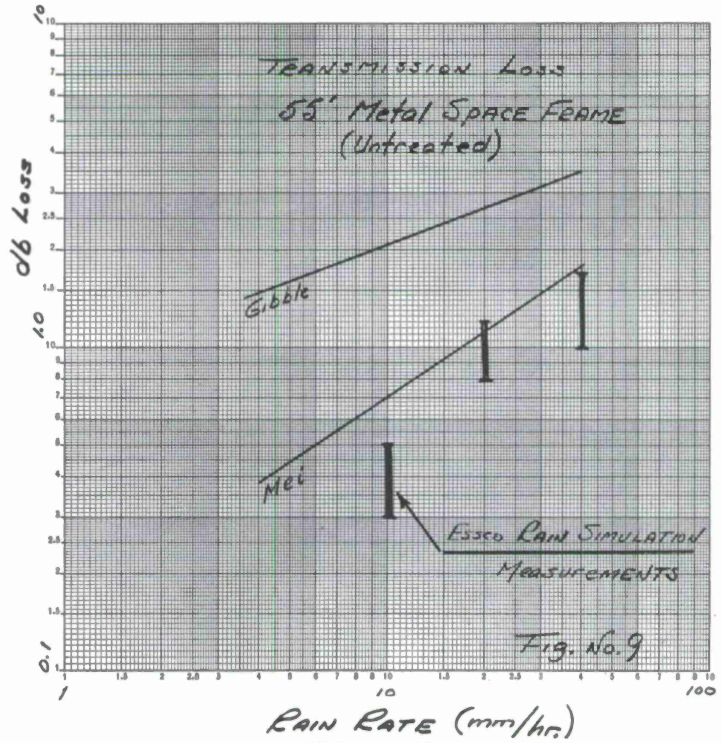

Figure 9.

7) Conclusions

a) The Gibble formula predicts closely the Andover transmission loss and increased noise temperature. The Mei formula does not.

b) The Mei formulation checks the ESSCO rain-simulation data. The Gibble formula does not.

c) Panel-surface treatment (silicone, teflon, etc.), as demonstrated by ESSCO, significantly decreases the radome rain effect.

d) At the present time it is not possible to predict the water-film thickness or streak diameter on a 550-foot treated or untreated radome.

8) Recommendations

a) That the ESSCO rain-simulation measurements be extended to both polarizations to determine, if possible, the proportion of water in film and stream.

b) That the ESSCO rain-simulation measurements be extended to higher rain rates to determine the behavior of these curves and their possible use for larger radomes and smaller rain rates.

c) That the HAYSTACK radome be implemented for rain-simulation studies. There is some difficulty here owing to the radome height.

d) That the speed of rain run-off, film or stream, be examined on large flat panels of different material and different coatings. This could be instrumented using colored water and photographic techniques or other means.

e) That means of getting rid of the water be more thoroughly investigated. Basically, what we wish to prevent is slow-moving and therefore thick uniform films. What we want, electromagnetically, are high-velocity (small-diameter) jets. These can be approximated by:

1) Surface treatment of the membranes to get rapid run-off.

2) Guides or gutters at the metal space-frame members to collect it into thicker higher velocity flow.

3) Collection of a number of these flows into spouts that would throw the liquid into high-velocity, free-fall streams off the radome.

This type of water-flow control is not out of order for as large a structure as a 550-foot radome, as it collects one hundred times the water as a 55-foot structure and is about six acres in extent.

ANNEX 3

CLIMATIC EXTREMES FOR A LARGE RADOME WITHIN 2 HOURS OF BOSTON, MASSACHUSETTS

CAMROC WORKING MEMORANDUM

Prepared by

Norman Sissenwine and Irving I. Gringorten

Aerospace Instrumentation Laboratory
Air Force Cambridge Research Laboratories

CLIMATIC EXTREMES FOR A LARGE RADOME WITHIN 2 HOURS OF BOSTON, MASSACHUSETTS

Interim Notes on Atmospheric Properties INAP No. 70

Norman Sissenwine and Irving I. Gringorten

Aerospace Instrumentation Laboratory
Air Force Cambridge Research Laboratories

1. INTRODUCTION

The Cambridge Radio Observatory Committee (CAMROC) is contemplating the establishment of a radio telescope within easy commuting distance (2 hours by surface travel) of the sponsoring organizations, which are Harvard University, Massachusetts Institute of Technology, MIT Lincoln Laboratory, and the Smithsonian Astrophysical Observatory. The telescope antenna currently under consideration is so large that it would require a radome of more than 500 ft in diameter to protect it from the elements. It has been determined that this facility should be located in an inland New England valley in order to avoid extremes of weather and difficulties in transportation found in hilly locations, and also to be out of range of the strong radio interference found in the Boston area. Extremes of wind, and perhaps several other meteorological stresses, require critical consideration in a structure of this size, since the mass of the radome must be kept to a minimum in order not to attenuate radio waves appreciably.

If a detailed examination of climatic history during preliminary design were to reveal that the greatest extreme of a meteorological stress ever observed, assuming a long period of record, could be withstood without excessive cost, it appears logical to design for this extreme plus some practical safety factor. However, should a stress or combination of stresses become critical, a more sophisticated examination of the probability of extremes is required. Also, a calculated-risk philosophy must be established that is related to the life expected of the facility. Preliminary thinking is that the facility should be built for a useful life of 25 years. Should a meteorological stress prove critical, calculated risks of 0.1 to 1.0 percent probability should be considered.

The Design Climatology Branch of AFCRL has been responsible for developing techniques and models for specifying extremes and durations of meteorological conditions in connection with the design of military equipment for many years. (Responsibility for DOD MIL STD 210A, "Climatic Extremes for Military Equipment," has recently been assigned to this branch, and revision is being considered.) Application of these techniques to practical problems invariably helps extend research efforts toward providing more meaningful results. Therefore, when Dr. Fred L. Whipple of the Smithsonian Astrophysical Observatory and Mr. Herbert G. Weiss of MIT Lincoln Laboratory called upon us for advice, we responded with seven independent notes concerning extremes of temperature, rain, snow, hail, icing, wind, and gusts. Only the latter two are interrelated. These notes are intended to serve in the development of preliminary design criteria. Refinements may be possible for some of the meteorological stresses, if they prove critical in preliminary design, once a specific location (or locations) is under consideration.

2. RAINFALL

Total rainfall and intensity of rain in valleys and other flat terrain within 50 to 100 miles of Boston will not vary sufficiently to require detailed specification by location. The intensity of rain is probably the most important consideration in designing structures. Although statistics are not available on accompanying wind, intense short-duration rain, perhaps lasting only several minutes, is frequently associated with thunderstorms. Winds of 30 mph gusting to 50 mph would not be unreal to assume in design studies concerned with such downpours. Extremes of intense rains that last several hours may be associated with hurricanes, in which case winds are in the 75- to 100-mph category. Short-duration gusts will be 50 percent higher. Rainfall intensities for a range of probabilities for a family of durations are provided in Table 1. (See Jennings, 1955, 1961, 1963.)

Table 1. Rate of rainfall (inches/hr) averaged over duration specified

	Duration			
	5 minutes	1 hour	6 hours	24 hours
Actual max (65 years)	6.72	2.10	0.91	0.35
Probability of exceeding max				
50% in any year	3.70	1.15	0.38	0.14
60% in 25 years	6.55	2.10	0.63	0.24
20% in 25 years	7.90	2.70	0.80	0.28
1% in 25 years	12.00	3.09	1.13	0.40

3. TEMPERATURE EXTREMES

To make estimates of extreme hot and cold hours within approximately 60 miles of Boston, we picked some 11 stations for which the USWB provides 30-year records, as follows:

New Haven, Connecticut
Bridgeport, Connecticut
Hartford, Connecticut
Portland, Maine
Blue Hills, Massachusetts
Pittsfield, Massachusetts
Worcester, Massachusetts
Concord, New Hampshire
Block Island, Rhode Island
Providence, Rhode Island
Burlington, Vermont.

We studied the records for January, which is generally the coldest month, and July, which is generally the hottest month.

3.1 COLD

The January average of the 11 stations gives for a "typical" station the temperature mean 25.4° F, compared with the Boston Logan Airport mean of 29.1° F. Unfortunately, the records do not give the standard deviation of the temperature. From the Handbook of Geophysics this is estimated at 11° F in January. It is further assumed that the hourly temperatures, in toto, have a normal Gaussian distribution, which is often a poor assumption. But it gives reasonable estimates of percentiles as follows:

10 percent 11° F, compared with Logan 15° F,
5 percent 7° F, compared with Logan 11° F,
1 percent 0° F, compared with Logan 3° F.

The records that are readily at hand do not give the highest and lowest temperatures in each year or the distribution of these extremes. Consequently, it is not possible to make direct estimates of the risk factors. Recently at AFCRL we developed a model of the duration and frequencies of anomalous values of meteorological elements, which has worked demonstrably well. It assumes a simple Markov process with a constant hour-to-hour correlation of normalized variates. An assumed value of 0.95 for this correlation is optimum when it is not known otherwise. Given mean 25.4° F and standard deviation 11° F, the model yields for the lowest temperature in 32 days (January 1 through February 1, inclusive):

50 percent probability -4° F
2 percent probability -15° F.

In a 25-year period the model yields for the lowest:

50 percent probability -15° F
2 percent probability -23° F.

In a 100-year period the model yields:

50 percent probability -19° F (Court, 1953a, gives -20 to -30° F)
2 percent probability -26° F.

For the 11 stations the actual observed minima in 30 years (any month) are given by the Weather Bureau, ranging from +3° F to -39° F, with an average of -19° F. The value of -39° F was observed at Portland, Maine, where the mean

January temperature is 21.8° F. All told, the model underestimates the extremes of cold, suggesting that a special effort to collect the data of extreme cold is necessary.

Using Washington, D.C., as a "typical" southern location, we find the mean January temperature is 37° F, with a standard deviation of 10° F, from which the model estimates the 25-year lowest with a 2 percent probability at -6° F (instead of -23° F).

3.2 HOT

The July average at the 11 New England stations gives as a "typical" station mean 70.6° F, compared with Logan airport's 72.2° F. From the Handbook a typical standard deviation is 8° F. The model gives the following estimates for the "typical" station:

10 percent 81° F, approximately the same for Boston,
5 percent 84° F, approximately the same for Boston,
1 percent 89° F, approximately the same for Boston.

Highest of the month

50 percent probability	92° F
2 percent probability	101° F
1 percent probability	102° F.

Highest in 25 years

50 percent probability	100° F
2 percent probability	107° F.

Highest in 100 years

50 percent probability	103° F (Court, 1953a, gives expected 102° F)
2 percent probability	109° F

Actually observed at the 11 stations in a 30-year period, any time of the year, were 97, 101, 100, 100, 101, 94, 94, 100, 91, 97, and 101° F, respectively. Boston's record temperature in the 30 years is 100° F. At Washington, D.C., where the mean July temperature is 78° F, with a standard deviation of 7° F, the model gives the 2 percentile in 25 years as 110° F.

4. SNOWFALL EXTREMES

Using Boston as typical of any station in a 60-mile radius, with respect to heavy snowfall, we have collected the following data:

Heaviest of the year:	average,	9.91 inches in 24 hours
	standard deviation,	3.54 inches in 24 hours.

The distribution in the 35 years of record fits the double exponential distribution very well, which makes the following estimates possible:

In 25 years the expected maximum is	18.9 inches in 24 hours
2 percent probable maximum	28.0 inches in 24 hours
1 percent probable maximum	30.0 inches in 24 hours.

For the 11 stations mentioned in the section on temperature, the greatest 24-hour snowfalls on record (30 years) are:

15.0, 14.3, 17.2, 21.0, 27.2, 14.5, 24.0, 19.0, 16.9, 18.3, and 14.5 inches, averaging 18.4 inches.

Boston's record is 19.4 inches for the 30 years.

5. HAIL[1]

There is a small frequency of hailstorms for a given location. It varies from about 1.1 times per year near the coast to about 1.2 times per year 50 to 100 miles inland. Statistics are not available in a form where frequency of hail by size can be related to probability at any location. The most pertinent data available are included in an AFCRL survey of New England hailstorm occurrences, obtained through cooperative reporting by residents of the area.

Over a 5-year period, 472 reports of hail were received. Most of these were well within 100 miles of Boston and so can be considered as representative of eastern Massachusetts. The most frequent size of the largest stones reported for each storm is 1/4 inch. Sizes as large as 3/4 inch were mentioned in one-quarter of the reports. Frequency of very large sizes in these 5 years were:

[1] For additional information, see United States Department of Agriculture (1941) and Chimela (1960).

Size	Frequency	Cumulative Probability
1.00 inch	11	4.45 percent
1.25 inches	4	2.12 percent
1.50 inches	5	1.27 percent
3.00 inches	1	0

Assuming that this distribution of very large hailstones is typical of that in a representative sample of hailstorms that might be encountered at any one station in eastern Massachusetts over many years, the probability that a storm at a given point in the area will include hail equal to or greater than 1.0, 1.25, and 1.50 is the same as the cumulative probability shown in the table above. Since the average incidence of a hailstorm at that station is about 1.1 times a year, assuming a Poisson distribution, the annual risk of receiving hailstones of different sizes can be obtained. The risk with various design criteria to a structure designed with a 25-year life expectancy can be approximated from $P = 1(1-p)^n$, where p is the annual risk and n the expected life. Computed values are:

Design Criteria	Annual Risk	25-Year Risk
1.00 inch	4.8 percent	71 percent
1.25 inches	2.3 percent	44 percent
1.50 inches	1.4 percent	30 percent

It appears that a hailstone design criteria of at least 1.5 inches diameter will still provide only a 70 percent probability of no damage, far from the 1 percent calculated risk considered during discussions of damage from strong wind. However, since there is good likelihood that the citizenry reporting the 472 storms from which these data were obtained exaggerated sizes in each storm, especially when they were large, a design criteria of 1.25 to 1.50 inches will probably be acceptable.

6. RIME AND GLAZE ICING

As in the case of many other meteorological parameters important in the design of structures, there is little data in a uniform format on rime and glaze (or clear) ice from which studies could be developed to provide design criteria applicable to stated calculated risks. This difficulty was encountered several years agao by Austin and Hensel (1956, 1957) when they attempted to develop

design criteria for freezing precipitation and wet snow along the eastern North American coast line in connection with radomes for aircraft warning systems. They developed expressions that can be applied to standard meteorological data to derive thicknesses of clear ice and wet snow that would accumulate on the windward side of the structure with high collection efficiencies. Rime ice was not considered a design problem for the smaller radomes being developed at that time since wind, concurrent with freezing drizzle, which forms rime ice, was thought to be sufficiently strong to divert the small drops from impacting the structure. Since there is some likelihood that rime ice can accumulate on a radome as large as 500 ft in diameter,it will not be ruled out herein.

In general there appear to be two problems related to rime and glaze: (1) the structure should be strong enough to support the total amount of ice that is likely to accumulate on it, (2) if deicing methods are to be employed, the maximum rate at which ice will accumulate is required.

The total amount of ice that could accumulate on a structure will depend upon the structure's geometry and size, as well as on the rate of precipitation and wind speed. Unfortunately, available information on ice accumulation does not permit the isolation of these factors. The most complete summary of glaze appears to be that provided by Bennett (1959). A most pertinent presentation in this summary is a set of maps for the United States that provides the results of a 9-year study by the Association of American Railroads. The extreme radial thickness of glaze on utility wires for Massachusetts provided by these maps was between 1.75 and 1.99 inches and was noted near the coast and also in the Connecticut River Valley area. During the 9 years, about 20 glaze storms were observed over coastal areas and nearly twice this number over central Massachusetts. Austin and Hensel (1956) provide an example that indicates that during a period of heavy glaze formation, the rate of accumulation on a vertical surface, in a horizontal wind of 40 mph when rain is falling at a nominal rate of 0.06 inch per hour, is 0.13 inch per hour. Applying this 2 to 1 ratio to the 2 inches of radial icing reported upon by the railroads, we can expect a nearly 1-inch accumulation on a surface such as the top of a large radome. Austin and Hensel (1956) also give some frequency distributions of rainfall rates and durations during near freezing, which indicate that 1 inch of ice on a horizontal surface is conceivable, although this seems extreme, and it is questionable whether other critical conditions would last the period of precipitation. From these data they also estimated that the precipitation rate will seldom exceed 0.1 inch per hour during near-freezing temperatures.

Another extensive survey on ice appears to have been performed by one of the most well-known climatologists of this area, the recently departed C. F. Brooks, Director of the Blue Hills Observatory. The importance of altitude is forcefully brought out in this work. His findings are summarized in a book on wind power (Brooks, 1948), where some graphs are provided. For these latitudes Brooks estimated a maximum thickness of rime ice (35 pounds per cubic ft) of about 3 1/2 inches for stations near sea level, and 5 inches for elevations of 1000 ft, the altitude of the Worcester Airport. Presumably, these values apply to surfaces with high collection efficiency, such as trees and wires. In terms of clear ice, the comparable values would be 2. 2 inches and 3. 1 inches, not in sharp disagreement with the Bennett (1959) and Austin and Hensel (1956) findings, considering that the Brooks values are estimated maximums for all times.

In summary, it appears that for the structural problem, weights commensurate with 1 inch of clear ice (56 pounds per cubic ft) on a horizontal surface and a couple of inches on vertical surfaces should be considered in preliminary design. In connection with the deicing problem, accumulation on a horizontal surface of 0. 1 inch per hour should be considered, with values at least 25 percent higher for structures with high collection efficiency. These values could be refined by consideration of the aerodynamics and geometry of the structure and by application of the Austin and Hensel techniques to the large amount of surface wind data now available on magnetic tape when a site is selected.

7. WIND EXTREMES

The best collection of data on wind extremes in the United States was made by H. C. Thom of the USWB several years ago. Unfortunately his data are in terms of the fastest mile. We shall present his data, but will also convert them to maximum 5-minute wind speeds.

In Thom's record there were eight stations considered within the vicinity of our interest:

Boston, Massachusetts
Providence, Rhode Island
Portland, Maine
Concord, New Hampshire
Hartford, Connecticut
Nantucket, Massachusetts
New Haven, Connecticut
Burlington, Vermont

In all of these cases the station was moved from the city to the airport 15 to 30 years ago. We have from 24 to 30 years of city record and 12 to 19 years of airport record at each station. They give for the annual extreme an average of 43 mph at city stations and 52 mph at airport stations. The standard deviation of these annual extremes ranges from 4 to 12 mph. In all cases the distribution of annual extremes can be fitted with confidence to the Double Exponential Distribution. This has allowed us to make estimates of the 25-year extreme wind. The 1 percentile of the 25-year extreme varies from 82 mph at the New Haven airport to 128 mph at Logan airport (see below).

To convert the above figures from fastest mile to maximum 5-minute wind we have compared Thom's record with Court's (1953b) record on 5-minute winds, limiting the comparison to the same stations and the same years. We drew three curves that best fit the conversion: (1) the 50 percentile of the 25-year maximum fastest mile to maximum 5-minute wind, (2) the 1 percentile, and (3) the 0.1 percentile (see Figure 1).

The question has been asked: How do extreme winds in New England compare with extreme wind speeds at southern Atlantic seaboard stations? To make a qualitative comparison, we looked at Figure 4-36 in the Handbook of Geophysics (Air Force Cambridge Research Laboratories, 1965) and concluded that little or nothing would be gained by searching for lower speeds at the southern stations.

In the above estimates the winds were corrected to a height of 50 ft above the ground by assuming the relation $V \propto \ln(z/z_0)$, where z_0 is the roughness parameter accepted as $z_0 = 0.1$ ft and $z >> z_0$.

In summary, we have estimates of the maximum 5-minute winds in 25 years, averaged for the three coastal stations (Boston, Nantucket, and Portland) and for the five inland stations as follows:

Height Above Ground	Ratio	Coastal			Inland		
		50 Percent	1 Percent	0.1 Percent	50 Percent	1 Percent	0.1 Percent
50 ft	1.00	72	112	130	55	82	96
100 ft	1.11	80	124	144	61	91	107
250 ft	1.26	91	141	164	69	103	121
500 ft	1.37	99	153	178	75	112	132

The actually observed greatest of all 5-minute wind speeds at the 8 stations, both in the city and at the airport, was 95 mph at the Providence city station during the 1938 hurricane. The instrument was up 250 ft above the ground.

8. WIND GUSTS

A ripple on the water surface will cause a cork to bob furiously, but will have no noticeable effect on a rowboat. Waves in Boston Harbor may make the occupants of a rowboat feel quite uncomfortable but will not trouble passengers of an ocean-going vessel. In fact, the same family of waves hitting the side of the boat will be more nauseating than when hitting it lengthwise. The larger the dimension of the floating object in the direction of wave propagation, the longer the wave required to cause vertical displacement.

The above intuitively understood principle is completely analogous to the problem of relating the structure of the horizontal wind, primarily gusts, to the maximum force on a building in any wind situation. This maximum force, due to a single gust, could blow over a structure. Another important wind structural problem is that of vortex sheddings. It is most important for towers, chimneys, cables, etc. If the frequency of shedding, dependent upon the wind speed and the geometry of the structure, corresponds to the natural period of oscillation due to elasticity of the structure, the resonance could serve as a forcing factor and bring about destruction. It is conceivable that gust frequency could add to this problem. This is a matter beoynd the scope of this paper. Because of the large diameter of the sphere being considered, this factor may be of only small importance to CAMROC.

With regard to the gust force, the wind design criteria must be specified in a form applicable to the size of the structure. Sherlock (1947) has determined that a gust must be approximately 8 times the length of the structure's down dimension, or longer, to be effective. For example, for a 100-ft-square building one should work with the statistics of 800-ft gusts, or wind data averaged over the period of time required for 800 ft of air to pass, the gust duration. In a 50 mph (73 fps) wind, gusts of 10.6 seconds would be applicable; in 100 mph, the gust need last only 5 to 6 seconds.

Available wind data that form the basis of climatic statistics are not directly applicable. In this country, around World War II, winds were obtained by rotating cup anemometers. These electrically triggered a pen to mark a time-driven chart when each mile of air passed. The greatest number of pen jogs in a 5-minute period, multiplied by 12, provides the fastest 5 minutes' average speed for the day, the duration of the chart. This was the standard entry in the climatic record of winds until shortly after World War II.

Today's basic wind entry, wind extremes that have been recorded for years, is the fastest mile, which is obtained from the shortest time between two consecutive pen marks. Duration may vary from minutes to 1/2 a minute or less, making results of statistical summaries hard to evaluate. Gusts of short duration, which might be applicable to structures of smaller dimension, are not generally recorded since the instrumentation does not have a fast-enough response. When obtained with special instrumentation, these can best be understood when related to a wind averaged over a specific period of time, such as the now-obsolete 5-minute period. In the United States at a few locations there are records from Dines (pito-static pressure tube) anemometers, which respond very well to gusts of 5 seconds or less, depending upon the authority believed. In Great Britain the Dines anemometer is a standard. In that country basic wind data are the mean hourly wind speed, obtained by "eye averaging" the wide range of pen strokes during 1 hour of travel of 1 1/2 cm of the chart, and the maximum gust during each hour. Statistical models, such as the Gumbel double exponential for extremes, can be applied to both hourly and gust data for calculated-risk thinking. However, since winds need to become strong only for a matter of minutes in order to destroy a large structure and seconds for small structures, the British have also had difficulty obtaining wind data applicable to structures. Interpolation between 5 and 360 seconds, when the function is exponential, is difficult. Also, a sudden

thunderstorm-type wind might hardly show up in the hourly average. One interesting fact, from a most pertinent recent British summary of wind speeds applicable to structural design (Shellard, 1965), is that the gust speed likely to be exceeded only once in 50 years is 50 percent higher than the 1-hour wind speed of the same probability on the windy west coast, but closer to 70 percent higher on the more sheltered inland. Inland Massachusetts will probably have a gust regime similar to the east coast of England. Pertinent to the problem of utilizing the 5-minute winds of the United States, Shellard (1965) does provide a frequency distribution of the gusts during 404 10-minute cases when the wind averaged more than 20 mph. It reveals that the maximum 5-second gusts had a 1 percent probability of being above 70 percent stronger than the 10-minute winds over open country, supporting findings that are summarized in Figure 1. Gust factors will probably be higher over cities.

The 5-minute wind speed is a statistical entry that can be utilized in structural design in accordance with methods of Sherlock (1947) if the 5-minute wind speed can be related to speeds averaged over shorter durations of time. This cannot be readily accomplished with fastest mile data because of the changing duration of the measurement. Court (1953b) made an extensive analysis of laboriously edited 5-minute wind data for the United States. His basic data sample consisted of 37 years (1912-48) of maximum annual 5-minute wind speeds for 25 stations, at which the instrumentation remained fairly constant in exposure, height, and type. Boston was not included, because it did not qualify in this way. The nearest location, Block Island, Rhode Island, had an average annual maximum of 58.4 mph, with a standard deviation of 7.5 mph, third highest in the sample.

Court recognized that it was usually the gusts, and not the 5-minute buildups of wind, that do the damage. He had no quantitative information on the size or duration of gusts applicable to structures. To make his findings more meaningful, he compared cup and Dines anemometer data, published for Washington, D.C., in two separate studies. He found that the gust factor (amount by which the 5-minute speeds should be multiplied) when winds exceed 30 mph is 1.5. This value has been substantiated as a good rough value for an envelope of few-second gusts in moderate wind speeds by many others. However, the data is probably fairly coarse, especially with regard to the exact duration of the gusts. There are many individual cases of lower and higher gust factors. There are questions of variation

with strength of 5-minute wind speed, height above ground, terrain, etc. Lettau and Haugen (1960) summarize much of the applicable data, some of it obtained during micro-meteorological research. Integrating these data requires considerable subjective treatment because of the many dependent conditions, often not known, that appear to lead to conflicts in the findings.

A set of data from the Mount Washington observatory records was employed for this CAMROC study, since special concern with gust structure of strong winds is required when a structure is being designed to last 25 years within low (1 to 0.1 percent) risk. As shown in Section 7, design winds will approach 100 mph, far in excess of speeds in the usual data sample from which gust factors are available. Even a few percent changes in a gust factor could have large effect on the gust force, considering that it varies with the square of the velocity, when a gust factor is applied to 100-mph speeds.

The gust sample selected for special analysis included eighteen 5-minute periods, which averaged 108 mph. The maximum gust duration, about 3 seconds for each of these 18, ranged from 16 to 38 mph, averaging 23.9 mph with a standard deviation of 7.9 mph. This yields a probable maximum 3-second gust, when 5-minute winds average 108 mph, of 132 mph, a 1 percent probable gust of 150 mph. This is a gust factor of 1.4. (These gusts were determined from the time of passage of 0.1 miles of air on a specially designed rotor anemometer. In a steady wind of 120 mph, this will take exactly 3 seconds.)

Also needed are gust factors for gusts of other durations. Fortunately, Durst (1960) reported upon standard deviations of gusts with durations of 5, 10, 20, 30, 60, and 600 seconds (during samples of 1-hour periods) for wind speeds in eight 10-mph groupings up to 80 mph. Manipulating these data, we found that these standard deviations vary inversely with the logarithm of the gust duration, a straight line on semilog graph paper. This relationship has been applied to the 1-percent probable gust of the eighteen 5-minute speeds, which average 108 mph (rounded to 110 mph) to form the basis of Figure 1. It is the curve on the far left. Also on this figure is the relationship obtained by Sherlock (1947) for 30-mph winds. These are average gust factors during a 70-minute period, and the 1-percent probable gust curve, not available, would be shifted considerably to the right. It closely approximates the semilog relationship, but does not fit it exactly. To give better resolution to the picture, a set of maximum gusts of 5, 10, 30, and 60 seconds was

available (Mackey, 1965) for Typhoon Mary when it crossed near Hong Kong in June 1960. This set approximates the semilog relationship and serves as the basis for the 60-mph curve, although no probabilities were available. Also shown are the strongest wind of record (Pagluica, Mann, and Marvin, 1934), 188 mph, and another very strong wind, 136 mph, both for Mount Washington. The gust factors for both these points are somewhat higher than we might get by extrapolating the family of curves to higher speeds, but are within the general range of scatter of data of this type. Both are probably within 0.1 of extrapolated gust-factor values. Another point on the graph, that for an 80-mph wind over Tiree, England, in February 1961, taken from a photo of the original strip recorder paper, appears to fit fairly well the curve for 85 mph, which gives us an interpolation between the data from Typhoon Mary and that of 1-percent probable gust from the Mount Washington sample. It appears that this figure is one possible approach to a rational application of gust factors and can usefully be applied to the 5-minute design wind determined from Section 7 above.

Heights above the ground are not well defined in these gust-factor studies. Sherlock's (1947) curve in Figure 1 applies to data obtained between 50 and 175 ft, a fairly wide range of heights. The Mount Washington data were obtained 38 ft above the ground. The height of the Tiree anemometer is believed to be standard for England, 33 ft. That of the Hong Kong anemometer is not known but is quite likely to be the same as that for England.

For large gusts, those of 1-minute duration, Lettau and Haugen (1960) present data obtained by German investigations that indicate that the gust factor remains constant up to 300 feet. It appears reasonable to assume that this relationship also holds to higher altitudes. Gust factors for few-second gusts during 5-minute speeds of 20 knots or greater and the ratio of 5-minute speeds at height to 10-ft speeds, obtained by Sherlock (1953), follow.

	Height				
Ratio	10	20	50	100	300
V/V_{10}, 5 minute	1.00	1.05	1.14	1.21	1.32
Gust factor at height	1.7	1.6	1.5	1.5	1.4

The Sherlock findings reveal that the few-second gust does not increase as rapidly with height as the 5-minute winds. Higher wind velocities at high levels are accompanied by lower gust factors, a form of compensation. Short-period gustiness associated with surface roughness tends to damp out with height, as the slower moving boundary layer air gradually merges with the faster geostrophic flow that is in equilibrium with pressure forces, at about 2000-ft altitude.

From Figure 1 and the relationship between height and velocity for 5-minute wind speeds, provided in Section 7, we can study this problem. For example, if the 5-minute design wind chosen were 85 mph at 50 ft, the 5-second gust factor will be 1.45, yielding a gust of 123 mph. At 300 ft the 5-minute wind will be 110 mph, but the 5-second gust factor would be reduced to 1.35, yielding a gust of 1.38 mph. This value is slightly larger than might be obtained by extrapolating the Sherlock findings and can probably be considered as conservative.

9. REFERENCES

AIR FORCE CAMBRIDGE RESEARCH LABORATORIES

1965. Handbook of Geophysics and Space Environment. McGraw Hill Book Co., New York.

AUSTIN, J. M., AND HENSEL, S. L.

1956. Analysis of freezing precipitation along the eastern American coast line. MIT Lincoln Lab., TR-112, March 23.

1957. Analysis of wet snow precipitation along the eastern American coast. MIT Lincoln Lab. TR-144, January 25.

BENNETT, I.

1959. Glaze, its meteorology, climatology, geographic distribution and economic effects. Army Natick Labs., TR EP-105, March.

BROOKS, C. F.

1948. Construction of maximum ice and maximum wind for the United States, Southern Canada and South Coast of Alaska. Summarized in Power and Wind, P. C. Putnam, D. van Nostrand Co., Inc., New York.

CHIMELA, A. C.

1960. Hail occurrence in New England: some relationships to radar echo patterns. Proc. 8th Weather Radar Conf., Amer. Meteorol. Soc., Boston.

COURT, A.

1953a. Temperature extremes in the United States. Geograph. Rev., Vol. 43, pp. 39-49.

1953b. Wind extremes as design factors. Journ. Franklin Inst., Vol. 256, pp. 39-56.

DURST, G. S.

1960. Wind profiles over short periods of time. Met. Mag. Vol. 89, No. 1056 pp. 181-186, July.

JENNINGS, A. H.

1955. Rainfall intensity-duration-frequency curves. Tech. Paper No. 25, USWB, December.

1961. Rainfall frequency atlas of the United States. Tech. Paper No. 40, USWB, May.

1963. Maximum recorded United States point rainfall. Tech. Paper No. 2, USWB, Revised.

LETTAU, H.H., and HAUGEN, D. A.

1960. Handbook of Geophysics. Macmillan Co., New York, pp. 5-9.

MACKEY, S.

1963. Discussion in wind effects on buildings and structures. Her Majesty's Stationary Office, London, pp. 422-423.

PAGLUICA, S., MANN, D. W., AND MARVIN, C. F.

1934. The great wind of April 11-12, 1934 on Mount Washington, N. H. and its measurement. MWR, Vol. 62, pp. 186-195, Vol. 5, WB, June.

SHELLARD, H. C.

1965. The estimation of design wind profiles. Vol. 1, Wind Effects on Buildings and Structures, Her Majesty's Stationary Office, London, pp. 29-51.

UNITED STATES DEPARTMENT OF AGRICULTURE

1941. Climate and Man. United States Department of Agriculture, Government Printing Office, p. 730.

SHERLOCK, R. H.

1947. Gust factors in the design of buildings. INT Assn. for Bridge and Structural Engineering, Vol. 8, p. 207.

1953. Variation of wind velocity and gusts with height. Paper 2553, Trans. Amer. Soc. Civil Engr., Vol. 118A, p. 463.

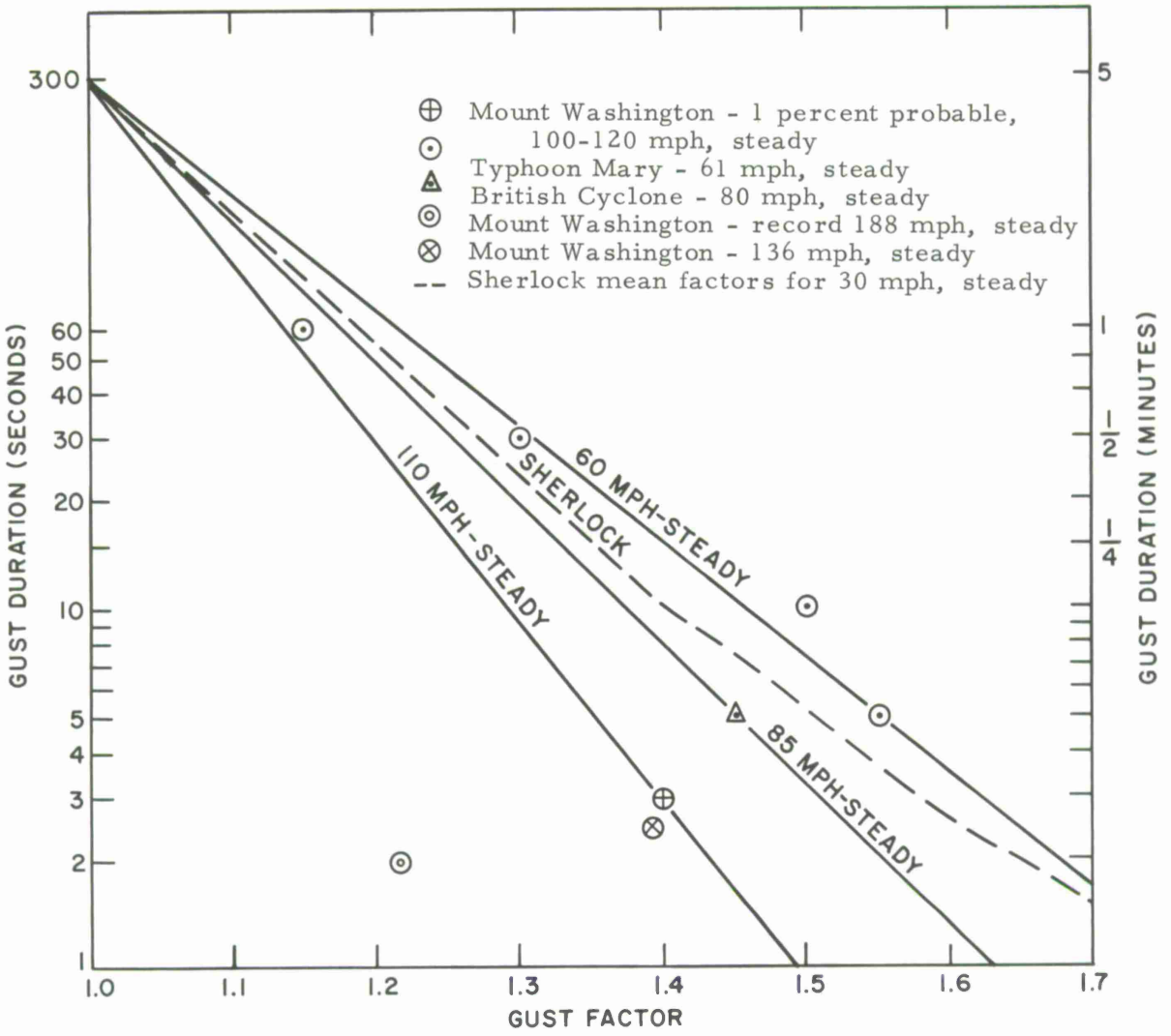

Figure 1. Estimated 1 percent probable gust factor for 5-minute steady wind.

ANNEX 4

SURFACE WIND-SPEED EXTREMES IN THE UNITED STATES

CAMROC WORKING MEMORANDUM

Prepared by

Norman Sissenwine and Irving I. Gringorten

Aerospace Instrumentation Laboratory
Air Force Cambridge Research Laboratories

INTRODUCTION

The problems are:

a. To give estimates, by isopleths on a map of the United States, of the wind speeds that will be equalled or exceeded with a 50% risk in a 50-year period, or a 1% risk in a 25-year period. The first (50% in 50 years) will be a map corresponding to Figure 3 of Thom (1959). The second (1% in 25 years) is considered to be a practical figure with respect to a structure such as a radome that is built for an intended useful life of 25 years. It will be located in open country (away from radio interference) and not on top of a mountain or hill.

b. To estimate the frequency with which the wind speed, at a height of 500 ft above the ground, will exceed 20 mph.

METHOD AND RESULT

A. Work on problem a. had been done by Thom (1959), which could be considered sufficient for the purpose of comparing the critical speed at one station with that of another. But there are a few objections. First, Thom's speeds are in terms of the "fastest mile." A fastest mile of 60 mph is a 1-min wind; at 120 mph it is a 1/2-min wind, and so on. For the effect of the wind on a structure, it is believed that the wind of a given force acting for a specific interval of time is the pertinent statistic. Thom's original record of annual extremes of wind, therefore, was reexamined and processed to yield extreme wind speeds in terms of "5-min" wind speeds, that is, a speed that is the average of the speed in a 5-min interval.

Thom's original record had both city and airport stations. Only the airport stations were selected for this study since they represent wind conditions in open fields more closely than do city stations. There were 129 such stations spread throughout the contiguous U. S. The years of record varied from 5 to 29 years. Disregarding the length of the record, the mean ($\overline{V}$) and standard deviation (Sv) of the fastest mile were obtained at each of the stations. The annual extreme wind is assumed to have a double exponential distribution (Gumbel, Lieblein, Court, and Gringorten), and an estimate ($\hat{V}$) of wind speed satisfies the relation

$$\frac{\hat{V} - \overline{V}}{S_v} = y_s \quad , \tag{1}$$

where Y_s is a standardized variate, with mean zero, variance 1. 0, and double exponentially distributed.

For the 50 percentile of the 5-year maximum, $y_s = 2.90.$

For the 1 percentile of the 25-year maximum, $y_s = 5.67.$

Thus, the extreme fastest mile (50% in 50 years, or 1% in 25 years) was estimated at each of the 129 stations.

The next step required a comparison of values of fastest mile with maximum annual 5-min wind. For some 25 stations Court (1953) gave the max 5-min wind in some 37 years. Fortunately, Thom's record included the fastest mile for each of the same 25 stations in the same 37 years. Using Equation (1) on both the Court and Thom data, it was possible to obtain pairs of estimates of the desired extremes. Figure 1 shows the estimate of the 50 percentile of the 50-year maximum, fastest mile plotted against 5-min wind. Simple regression gives

$$\hat{V}_{5\text{-min}} = 0.826\, V_{\text{fastest}} + 2.57 \quad .$$

Figure 2 shows the estimate of the 1 percentile of the 25-year maximum, fastest mile plotted against 5-min wind. Regression gives

$$\hat{V}_{5\text{-min}} = 0.785\, V_{\text{fastest}} + 6.57 \quad .$$

In Figure 3 the isopleths give estimates of the 50 percentile of 50-year max of the 5-min wind speeds throughout the U. S. The estimated values at each of the 129 stations remain plotted in Figure 3 to allow the reader to see to what extent the isopleths have been smoothed and the field generalized.

In Figure 4, the isopleths give estimates of the 1 percentile of the 25-year max of the 5-min wind speeds.

The shape of the isopleths in Figure 3 should correspond closely to Thom's Figure 3. But there are some differences, particularly over the New England region. Thom's chart suggests that there is an axis of minimum speeds passing over Lake Champlain, the Hudson River, eastern Pennsylvania, Maryland, eastern Virginia, and central North Carolina. Our Figure 3, however, shows an axis of minimum speeds passing over Utica, New York, western Pennsylvania, and West Virginia. The isopleths were drawn as faithfully as possible to the available data. But we also think that some consideration of the Appalachian mountain chain and the tracks of hurricanes is in order. We can expect high winds between the East Coast and the eastern slope of the Appalachians and lower speeds on the west side of the Appalachians.

Figure 4, which, we think, presents a more appropriate statistic, is fairly consistent with Figure 3.

B. For the probability estimate of winds exceeding 20 mph in central Massachusetts, the information source is the Handbook of Geophysics, Figures 4-31, 4-32, 4-33, and 4-34. The following are typical combinations of mean and standard

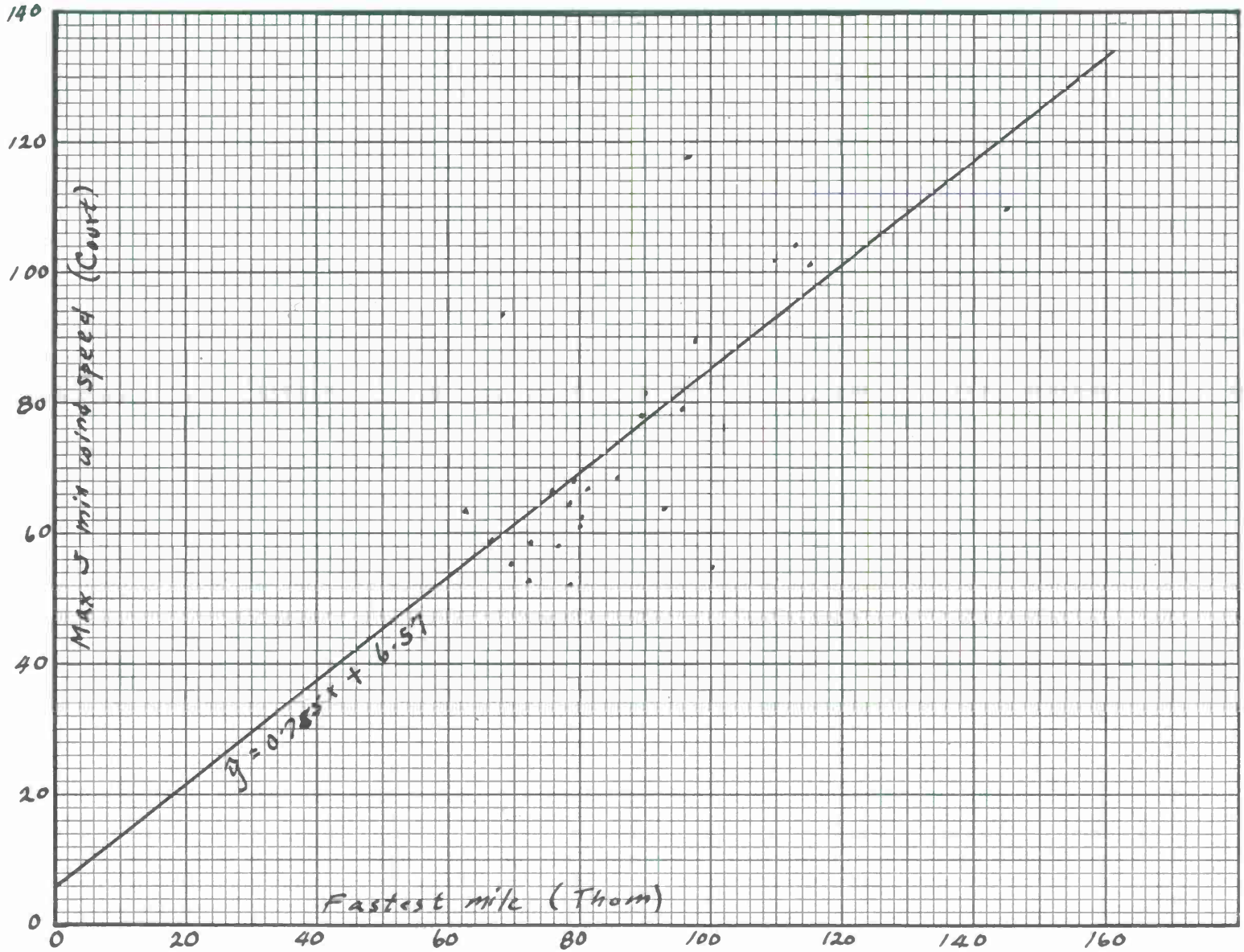

Figure 1. Comparison of 50 percentile of 50-year max 5-min wind with corresponding fastest mile.

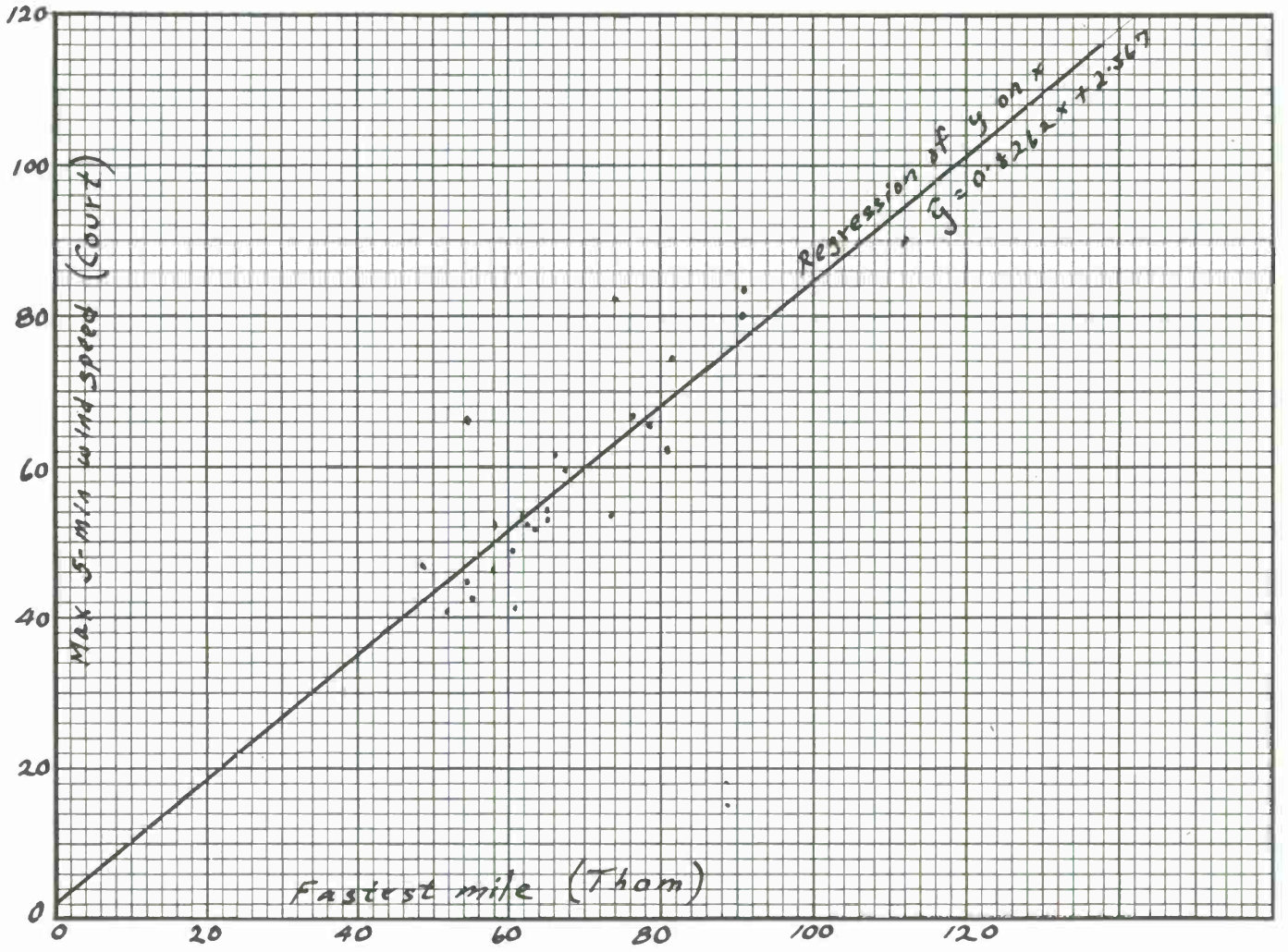

Figure 2. Comparison of 1 percentile of 25-year max 5-min wind with corresponding fastest mile.

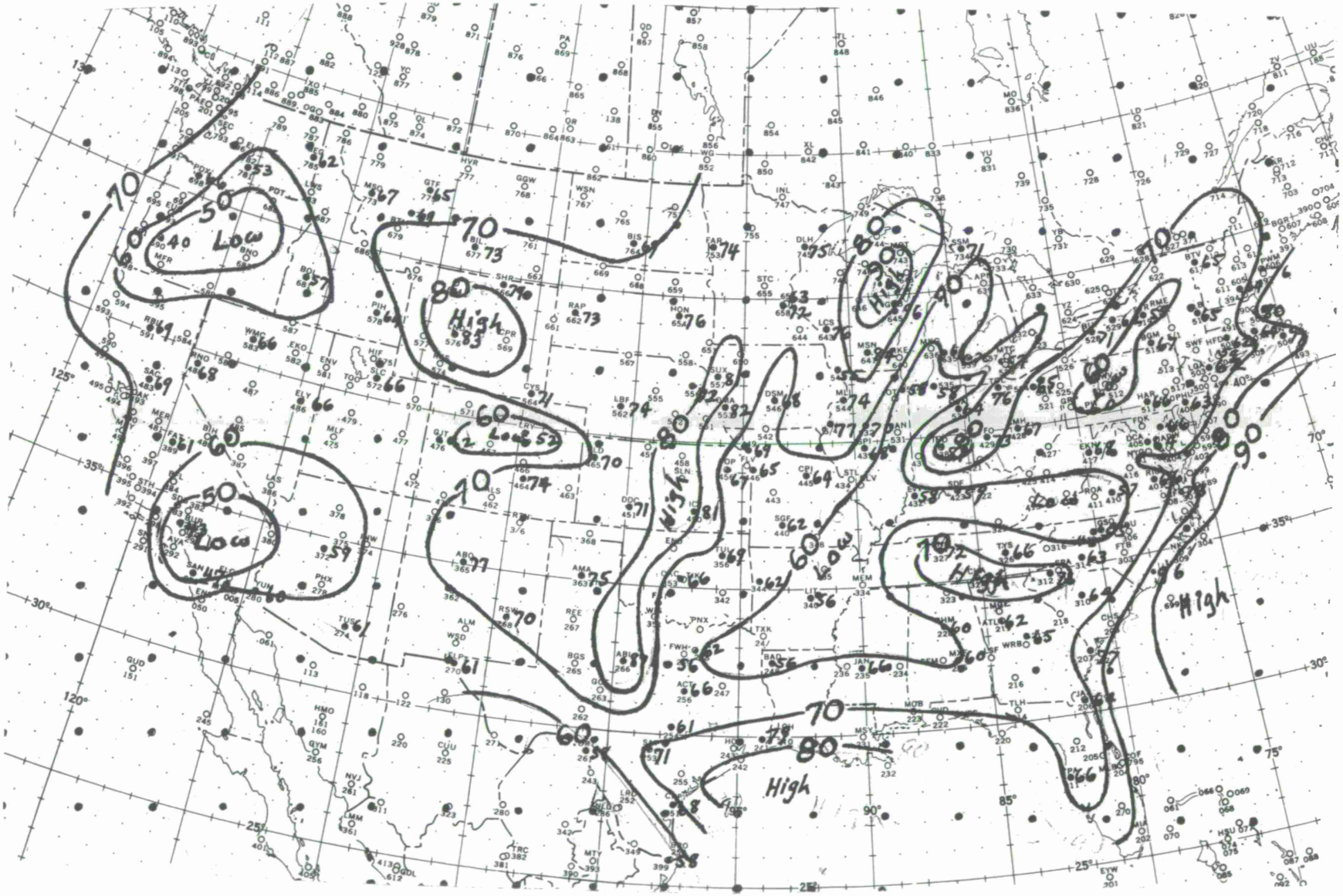

Figure 3. Isopleths of 50 percentile of 50-year max 5-min wind.

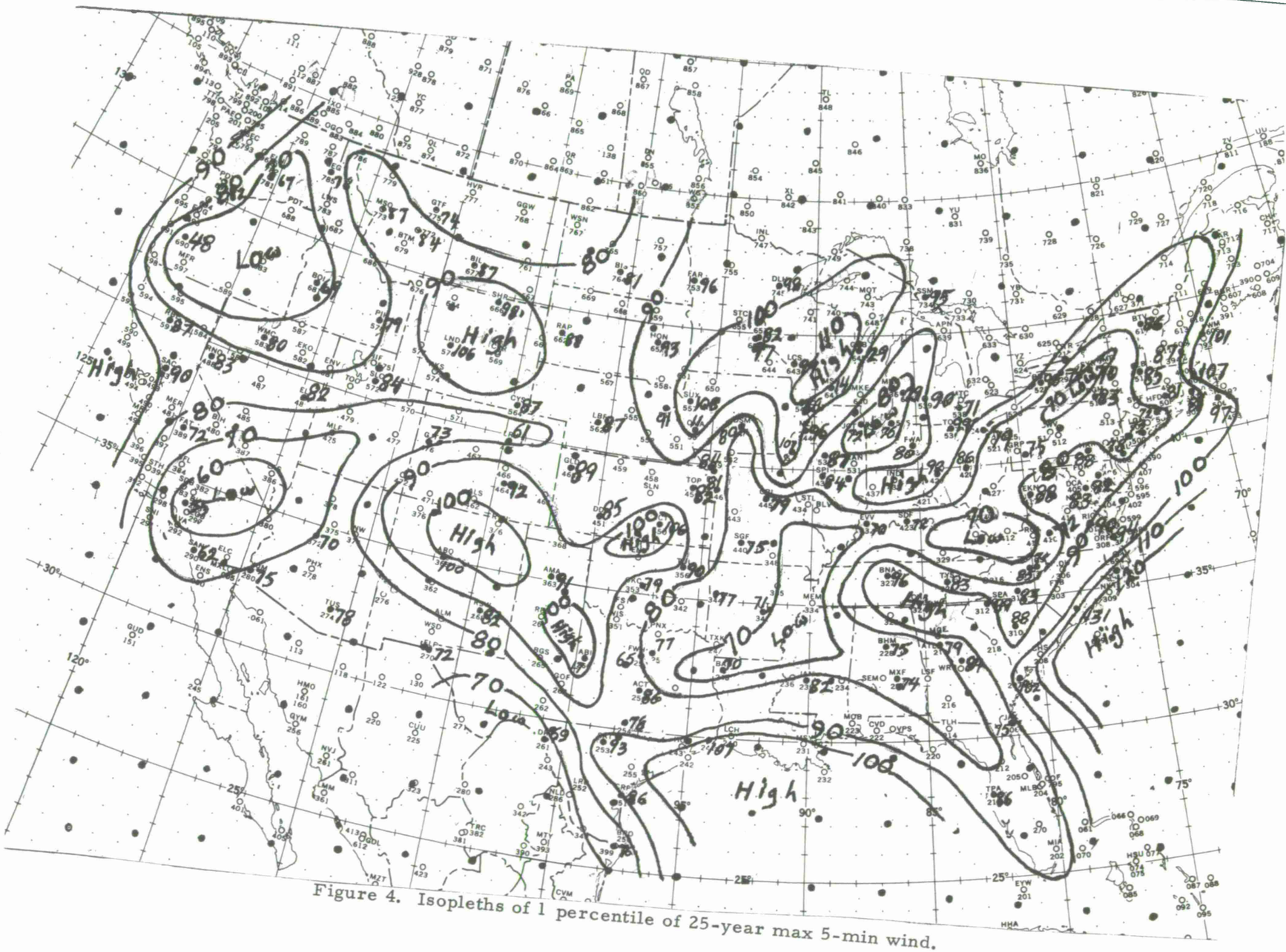

Figure 4. Isopleths of 1 percentile of 25-year max 5-min wind.

deviations at 50 ft above the ground in central Massachusetts and corrected to 500 ft by the relation:

$$\frac{V_{500}}{V_{50}} = \frac{\ell n\ 500/0.1}{\ell n\ 50/0.1} = 1.37$$

	50 ft		500 ft	
Month	Mean	s. d	Mean	s. d.
January	10	5	13.7	6.8
	11	6	15.1	8.2
April	10	5	13.7	6.8
	12	5	16.4	6.8
July	9	4	12.3	5.5
	10	5	13.7	6.8
October	10	4	13.7	5.5

As found in the preparation of the Handbook of Geophysics, the gamma distribution is a useful relation to estimate upper percentiles ($\hat{V}$) of wind speed as follows:

$$\frac{\hat{V} - \overline{V}}{s_V} = y_s \quad ,$$

where $P(y_s) = \int_{-\infty}^{y_s} f(y)\, dy$, where $f(y) = 1/2\ (y^2 \cdot e^{-y})$. Values for $P(y_s)$ are given in Section 4.5.1 of the Handbook, and lead to the following answers:

Month	Frequency of speed exceeding 20 mph	
	at 50 ft	at 500 ft
January	8%	20%
April	6%	21%
July	3%	14%
October	2%	13%

At 500 ft, the rawinsonde might give information on the wind speed by interpolation between 1000 ft (reported) and the surface wind. Such data were not at hand, and it is not possible to judge whether they would yield lower or higher estimates of the wind.

REFERENCES

Court, A., "Some New Statistical Techniques in Geophysics," Advances in Geophysics, New York, N. Y., Academic Press, 286 pp., 1952.

Court, A., "Wind Extremes as Design Factors," J. Franklin Inst., vol. 256, pp. 39-56, 1953.

Gringorten, I. I., "A Simplified Method of Estimating Values from Data Samples," J. Appl. Meteorol., vol. 2, pp. 82-89, 1963.

Gumbel, E. J., "Statistics of Extremes," Columbia University Press, New York, 375 pp., 1958.

Lieblein, J., "A New Method of Analyzing Extreme-Value Data," NACA Tech. Note 3053, Washington, D. C., 88 pp., 1954.

Thom, H. C. S., "Distribution of Extreme Winds in the United States," U. S. Weather Bureau, Washington, D. C., 23 pp., 1959.

ANNEX 5

GEOMETRIC AND STRUCTURAL CONSIDERATIONS FOR LARGE RADOMES

CAMROC WORKING MEMORANDUM

June 17, 1966

Prepared by

R. A. Muldoon

MIT Lincoln Laboratory

GEOMETRIC AND STRUCTURAL CONSIDERATIONS FOR LARGE RADOMES

By

R. A. Muldoon

I. Introduction

I plan to review very briefly the approximate methods that were used in space-frame radome analysis prior to the employment of the computer and to indicate those areas where the computer is being adapted to radome design, and also to sketch the benefits that derive from the precise analyses afforded by the computer. I shall consider only the stress analysis of the radome. Prof. James Mar and Dr. Howard Simpson will consider the problems related to the buckling of space-frame radome structures.

Rigid ground radomes are designed to protect antennas from adverse environmental conditions, e.g., wind, snow, and ice. The structural components of the radome must be sufficiently sized and properly located so that the radome maintains its mechanical integrity under the anticipated climatic loads. Yet the size and distribution must be minimized in order to prevent undue interference with the transmission of electromagnetic radiation. It is this stringent electrical requirement that differentiates a radome from all other type structures. Thus, the successful radome design must effect a judicious compromise between these conflicting mechanical and electrical requirements.

The inclusion of a radome in a communications system confers many major benefits on the antenna structure. The most important is a reduction in the stiffness and rigidity, and thus the total weight and cost of the antenna structure itself. When an antenna is exposed to the environment, increased stiffness and rigidity are essential in order that the structure survive climatic conditions that occur but once in many years, e.g., winds in excess of 100 mph. This survival criterion dominates and controls the whole antenna design; it demands sturdier and more costly structural components that are rarely utilized at their design capacity; higher power requirements are necessary to drive a heavier antenna against the prevailing low-velocity winds; moderate wind and snow storms compel a shut down of the whole system; exposure to the elements increases the frequency of maintenance and repair time with a corresponding increase in shut-down time. All these factors degrade the efficiency of the site.

Now with the tendency toward more accurate and precise dishes where surface deflections must be kept within sixteenths of an inch, then the controlled environment provided by a radome is essential. The radome by excluding the weather not only removes the major source of mechanical loading from the antenna but permits the smaller deflections resulting from the gravity and thermal loads to be controlled with

precision. Thus, the predictable deflections developed by the predictable gravity load may be compensated for by means of cables or other such devices, while the deflections due to thermal gradients may be minimized by proper heat and ventilation methods.

II. Space-Frame Radomes

1. General

Space-frame radomes in common with other radomes are spherical structures truncated along a parallel circle (see Figure 1). They are distinguished from other radome types by the presence of a continuous metal frame wove to produce triangular-type cells that are comprised of individual load-carrying beam elements. The beam elements are distributed about the surface of a sphere in accordance with some prescribed geometric pattern. Each beam begins and ends at a hub and follows a chordal line between these two hub points, which lie on the surface of the sphere. Each triangular cell is covered by a thin, plastic, membrane of acceptable dielectric property that is secured to these beam elements.

Space-frame radomes are generally subdivided into two classes — uniform and random — depending on the geometry of the frame. A uniform configuration is characterized by parallel sets of intersecting arc segments that proceed for large distances along great circles of the sphere and form the sides of the triangular cells. This regularity readily distinguishes the uniform from the random geometry, and conversely the lack of symmetry in beam orientation identifies the random geometry.

2. Development of Space-Frame Geometry

In general, the geometry of the space frame is developed by considering an icosahedron or some variation of this model (see Figure 2). An icosahedron consists of 20 identical equilateral triangles disposed as illustrated. Each vertex point falls on the surface of a sphere that circumscribes the icosahedron. Any one of the equilateral triangles can be further decomposed into another system of triangles. In Figure 2 the centroid of the triangle ABC, point G, has been raised to the surface of the sphere and chords drawn from this centroid to the apices of the equilateral triangle. All the triangles resulting from this operation are congruent. Now the triangle AEG may be further decomposed into another set of triangles. This latter set can be made either regular or random. This last process as applied to a 550-ft-diameter radome consists in developing a triangular type grid of 15-20 points, which fall on the surface of the sphere and the associated beams — chordal connections between the vertex points. Once this basic net is established, computer programs have been written and are in operation that rotate and reflect the points and beam elements in this basic unit to give the complete space-frame geometry. Thus, if AEG is reflected about the line AG, then the unit AGF results. Rotating the quadrilateral AEFG 120° counterclockwise about G gives

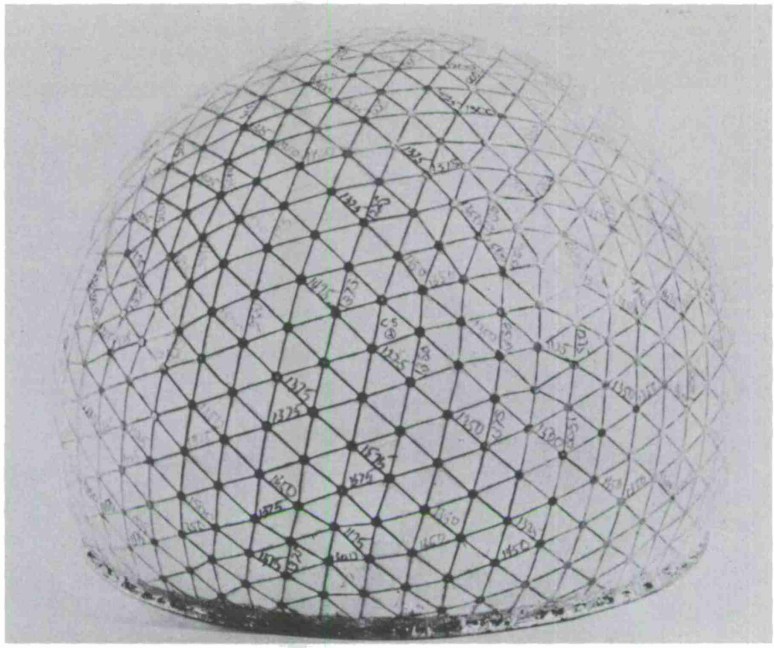

Uniform Geometry Space Frame Radome

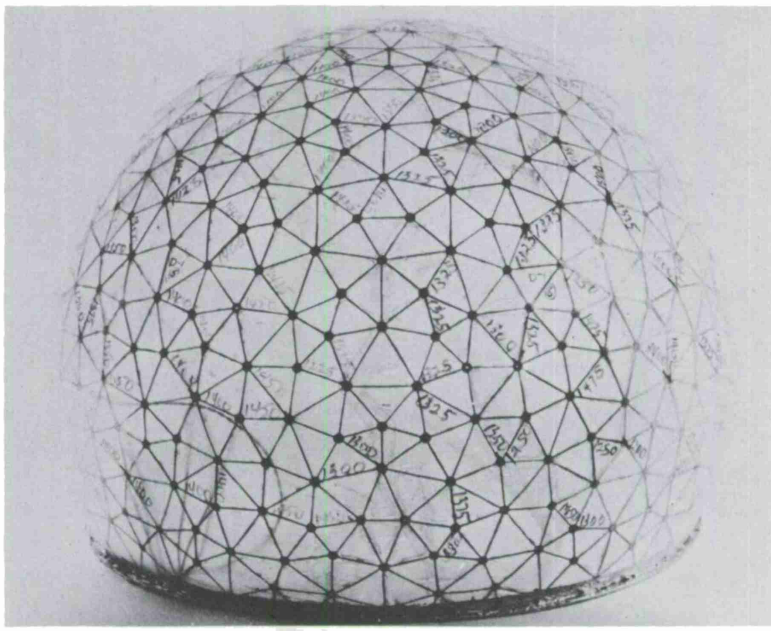

Random Geometry Space Frame Radome

Figure 1. Typical 27.5-inch-diameter uniform and random-geometry space-frame radome models used in shock-tube testing.

GEBD; a rotation 240° counterclockwise gives GDFC. A rotation of ABC 72° clockwise about B gives BCC′. If five more rotations are performed, the hub points and beams for a complete spherical radome result.

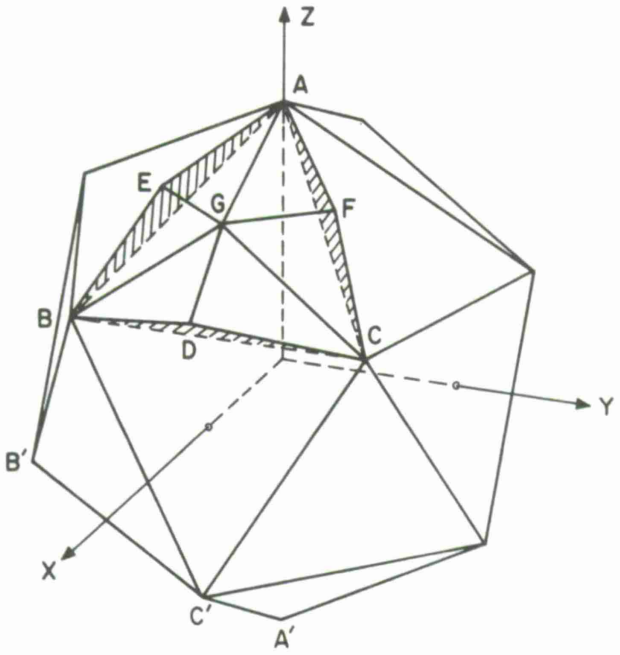

Figure 2. Breakdown of icosahedron used in development of TTR random space-frame radome geometry.

In the past only the basic unit AEG, which defined the number and lengths of beams framing into each hub type, were required for the structural analysis. Now the complete stress analysis of the entire frame made possible by the computer requires that the location of every beam and hub in the frame be known exactly. Computer programs that perform as described above yield this information.

III. Radome Loads

Experience at radome installations has confirmed the expectation that wind storms consitute the most severe loading imposed on the radome structure by the environment. It has been demonstrated that snow and ice do not seriously challenge the mechanical integrity of the radome. The maximum wind velocity that must be protected against is usually obtained from the available meteorological data compiled at the installation nearest to the site.

The distribution of pressures engendered about the surface of the radome by the wind load (see Figure 3) is dependent on the radome base angle, the configuration of the tower upon which the radome rests, the size and proximity of adjacent buildings, and the prominent features of the surrounding terrain. The distribution of pressures is

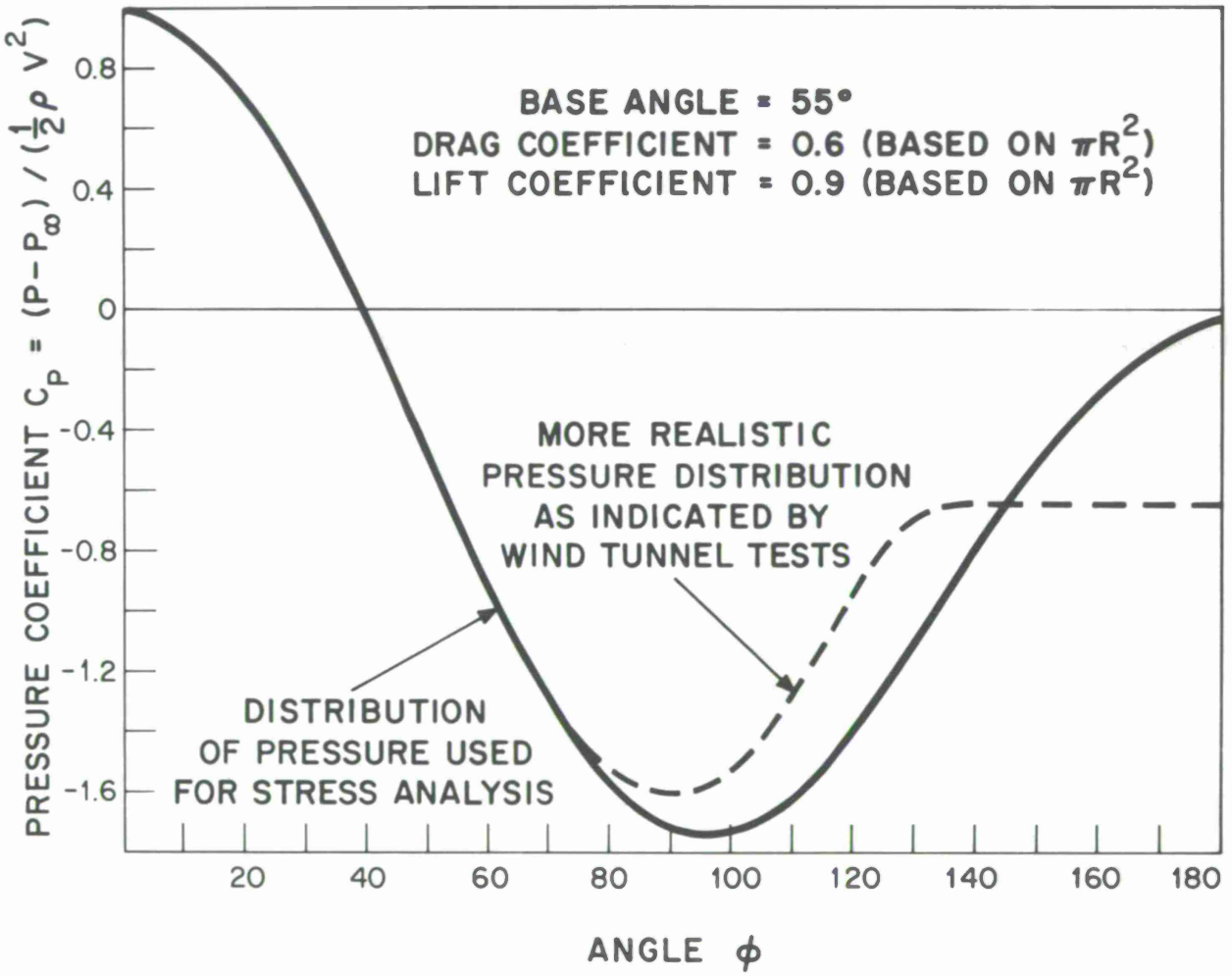
BASE ANGLE = 55°
DRAG COEFFICIENT = 0.6 (BASED ON πR²)
LIFT COEFFICIENT = 0.9 (BASED ON πR²)
MORE REALISTIC
PRESSURE DISTRIBUTION
AS INDICATED BY
WIND TUNNEL TESTS
DISTRIBUTION
OF PRESSURE USED
FOR STRESS ANALYSIS
PRESSURE COEFFICIENT $C_p = (P-P_\infty) / (\frac{1}{2}\rho V^2)$
0.8
0.4
0
-0.4
-0.8
-1.2
-1.6
20
40
60
80
100
120
140
160
180
ANGLE ϕ

Figure 3.

usually determined by wind-tunnel tests. The resulting data are then approximated by a three-term Fourier series where the arbitrary constants are adjusted to yield the measured lift and drag coefficients and also to preserve the dynamic pressure at the stagnation point.

The use of the computer will permit a more accurate representation of the pressure distribution either by extending the number of terms in the Fourier series or by using the actual pressure result measured at each section of the radome model during testing.

For very large-diameter radomes of the kind contemplated for the CAMROC system, the escalation in wind velocity with height and the resulting change in pressure distribution must be accounted for and included in the analysis.

IV. Structural Analysis

1. Modes of Failure

The loading imposed on the radome by the wind can fail the structure either by overstressing one of the major components or by promoting a condition of unstable equilibrium. Two distinct types of instability can result: The first is called general instability and is characterized by a buckling collapse of several adjacent panel groups. The second involves a column-buckling failure of one of the beam members in the space frame.

2. Figure of Merit

The electromagnetic and mechanical performances of the radome are related through the optical blockage of the space frame — the shadow cast by the frame on the plane of the antenna. Thus, the width, depth, length, number, and distribution of beams in the space frame establish the mechanical sufficiency of the structure. These same parameters impede the electromagnetic transmission of the radome, which is indexed by the optical shadow of the frame in the antenna plane. Then that space frame that successfully resists the wind load and develops the minimum amount of blockage is judged the most efficient.

In the past, the optical blockage was calculated by means of approximate formulas or even in some cases determined by illuminating a scale-model frame, recording the shadow photographically, and measuring the result.

A computer program is now in operation that calculates the optical shadow from the beam dimensions and frame geometry.

3. Past Methods of Stress Analysis

Previously, the stress analysis of the radome structure consisted in calculating the membrane stresses developed by the three-term Fourier representation of the wind pressures in an ideal, homogeneous, spherical shell. The maximum membrane

stresses were then expressed in terms of axial loads in the beam members by considering the condition of equilibrium between a planar arrangement of the minimum number of beams that frame into a hub and the maximum membrane stresses (see Figure 4).

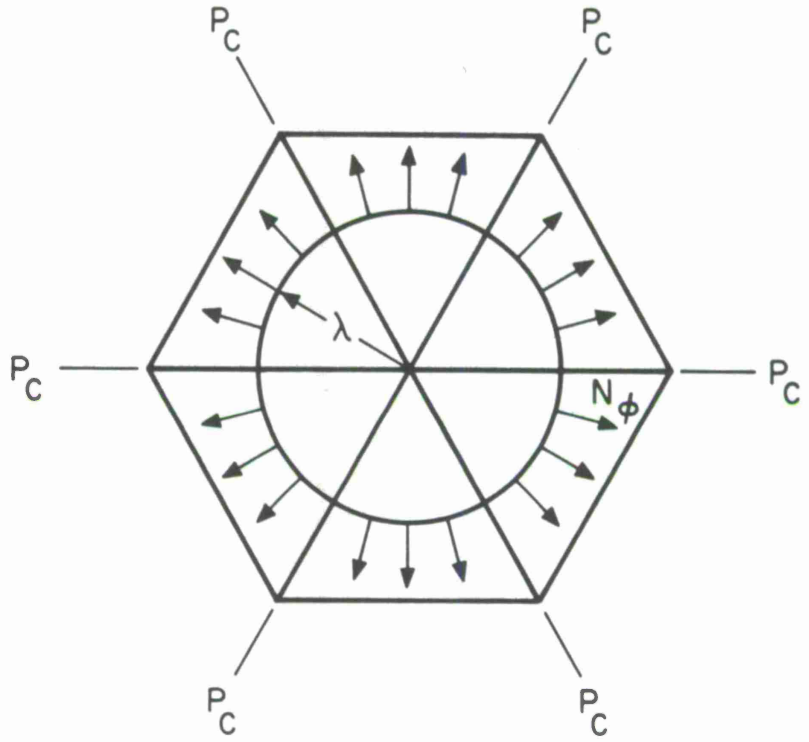

Figure 4. Relation between membrane stresses and compressive axial loads in space frame.

The local transverse loads carried by each beam member in the frame are next estimated (see Figure 5), and together with the axial load they form the total loading on the beam member. The local transverse loads associated with each beam are calculated by assuming that one third of the pressure load imposed on each triangular panel is carried by each beam member that constitutes the triangular frame. The distribution of the transverse load along the beam length is determined by dividing each triangle into three equal areas and multiplying the area by the local pressure. Because each beam member serves two triangular panel elements, then the contributions from both adjoining panels are summed. With the axial and transverse loads determined, a beam-column analysis is performed for a fixed-ended beam to ascertain the maximum stresses in the frame member (see Figure 6). This procedure was repeated for all the triangular cells that occur in the basic geometric unit, and the beam dimensions that are everywhere equal are based on the maximum beam stress.

The above method incorporates many conservative approximations that in turn result in beam sizes that are conservative. As a consequence, the radome cost is increased and its electromagnetic performance is downgraded.

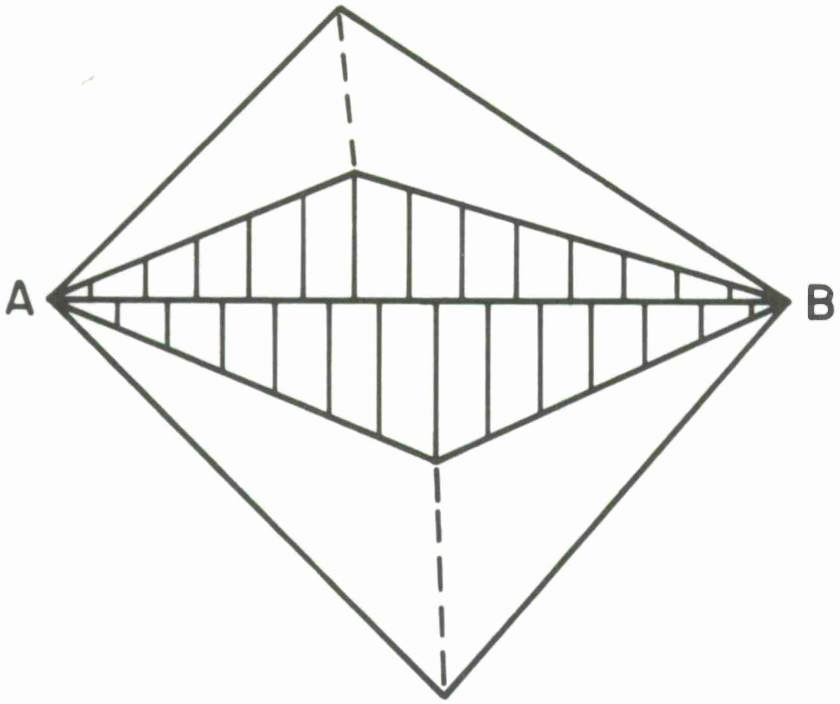

Figure 5. Area of local transverse loading imposed on beam by adjacent panels.

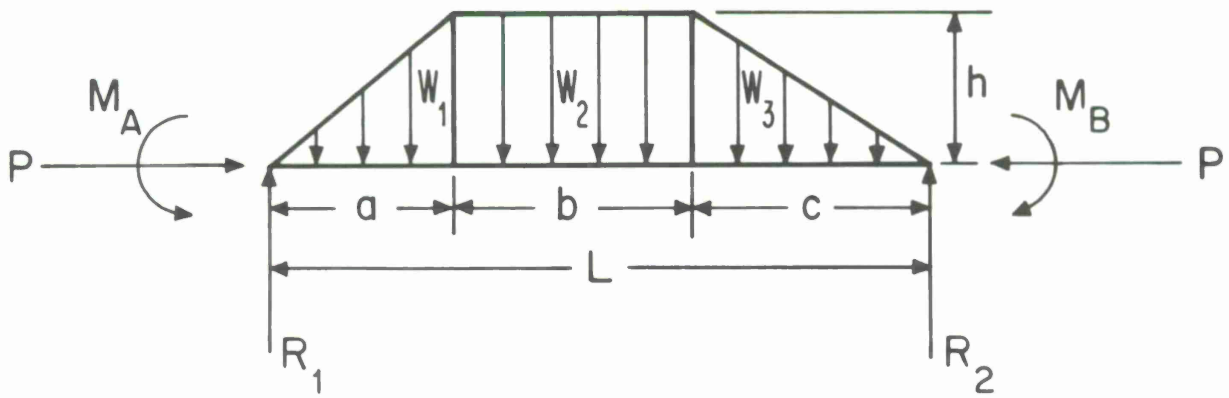

Figure 6. General loading diagram for beam-column action.

4. Computer Methods for Future Design Analysis

With the advent of computer programs capable of analyzing highly redundant space-frame structures, the means for calculating the exact stress in any beam member are available.

Then the contemplated sequence of computer operations for the stress design of space-frame radomes is

1) For the complete space frame, generate all the hub points and identify the two hub combinations that define each beam.

2) Develop the overpressure due to the wind at each point on the radome surface.

3) Input this information along with some estimate of the cross-sectional dimensions of the beam and determine the stress for every beam in the space frame.

4) Calculate the optical blockage due to this space frame.

5) Examine the beam stresses and alter the cross-sectional dimensions of the individual members — increasing the dimensions where high stresses occur and reducing the dimensions where low stresses occur and then reading this new information into step 3.

The latter steps are to be repeated until a space-frame structure of minimum optical blockage and all of whose members are loaded up to the working stress by the design wind results.

5. Anticipated Improvements in Radome Design Due to Computer Applications

It is estimated that the application of computer-design techniques by allowing a more realistic modeling of the radome exposed to wind loads and thus eliminating the large safety factors will permit the following improvements in the design of the radome space frame:

1) The dimension of each beam member in the frame will be altered such that it will be stressed to its capacity by the design wind load, thus minimizing the cost and optical blockage of the structure.

2) The maximum working stress can be advanced to the elastic limit.

3) In some cases the maximum working stress might be able to be advanced beyond the elastic limit and into the plastic range.

4) The use of longer beam lengths where the effective l/r ratio is reduced by means of guy wires, as suggested in a recent A & W report, can be adopted if feasible.

5) Lastly, a very large volume of space-frame geometries may be rapidly investigated in the search for the most efficient radome structure for the CAMROC application.

ANNEX 6

ESTIMATE OF OPTIMUM BEAM DIMENSIONS FOR CAMROC 550-FT-DIAMETER SPACE FRAME WHEN EXPOSED TO 130-MPH WIND

CAMROC WORKING MEMORANDUM

Prepared by

R. A. Muldoon

MIT Lincoln Laboratory

Errata

The average length of beam in a space-frame radome was estimated in this report by relating the arc length of one of the sides of a spherical icosahedral triangle to the number of beams that lie on that side. A better approximation of the average beam length is obtained by equating the area of a sphere to the total sum of the triangular areas that constitute the frame. This improved method yields a total beam length that is 1.18 times greater than the results obtained in this report.

It is recommended that all optical-blockage and weight results plotted herein be multiplied by the factor of 1.18 to obtain a more realistic appraisal of the anticipated space-frame performance.

ESTIMATE OF OPTIMUM BEAM DIMENSIONS FOR CAMROC 550-FT-DIAMETER SPACE FRAME WHEN EXPOSED TO 130-MPH WIND

Summary

A 550-ft-diameter space-frame radome whose height is 7/10 of the equatorial diameter has been proposed as a protective enclosure for the CAMROC radio telescope. It is tentatively assumed that the radome structure must withstand 130-mph winds.

The choice of an optimum-length beam member must take into account the total frame weight, cost, ease of fabrication and erection, the problems associated with membrane manufacture and assembly, as well as the increasing membrane depth associated with an increasing beam span. These problems, which are not treated in this study, will define a maximum acceptable beam length. Under these conditions the choice of an optimum length for a beam member will depend on the optical blockage, which is the shadow cast by the beams in the plane of the antenna. This shadow degrades the electromagnetic performance of the protected antenna. Thus, the beam dimensions that yield a minimum optical blockage within the permitted maximum length are considered optimum. This study is a first attempt to relate the beam dimensions to the optical blockage for a range of space-frame parameters.

The preliminary calculations of this report consider the beam members of the space frame only from the standpoint of beam-column behavior. The effect of general instability on the size of the beam members, which can have a considerable effect, is currently under intensive investigation.

The analysis in this study was carried out by expressing the axial and transverse loads in a typical member as a function of the beam length. A pin-end support condition was assumed for the typical member. It is recognized that both of these assumptions are only rough, first approximations to the physical situation. These assumptions are justified only for preliminary estimates to meet the need for a quick look at the beam parameters of a 550-ft-diameter radome.

Two cases are considered in the calculations. The first case was based on a condition of maximum stress. For this case, it was assumed that only radial deformation was allowed with deformation in the plane of the membranes being prevented by the membranes themselves. The second case did not limit the beam to radial deformation but also included column buckling in the plane of the membrane. The size of the beams calculated from these two cases were then used to estimate the optical blockage of the frame as a function of the beam dimensions.

The calculations were based on a cross-sectional configuration for the beam consisting of two identical steel channel sections with 4.0-inch flanges (see Figure 7).

Channel thicknesses of 1.0, 1.50, and 2.0 inches each in combination with channel widths of 2.0, 4.0, 6.0, and 8.0 inches were considered. The beam depth was varied according to the maximum stress requirements. Material yield stresses of 40,000, 60,000, and 80,000 psi were investigated.

1. INTRODUCTION

In sharp contrast to the antenna, many of the major structural features of a radome are fixed and permanent. Thus, electromagnetic requirements demand point symmetry and the radome design must be spherical. The size of the enclosed antenna coupled with economy fixes the diameter and the height of the radome. If the antenna is large, the skin must still be thin, and shell, sandwich, and inflated radomes are eliminated in favor of space-frame structures. Because the wind loads produce significant bending moment, which must be sustained with a minimum of framing material, triangular grids are necessary. Thus, only the triangular grid geometry, beam-member size, hubs, and membranes remain to be designed.

Currently, the CAMROC facility envisions a radio-telescope antenna whose plan diameter is 400 ft and which is protected from the environment by enclosure within a 550-ft-diameter space-frame radome. The radome height is 7/10 of the spherical diameter. It is tentatively assumed that the radome must survive under 130-mph winds.

There is an infinite variety of frame geometries – both uniform and random – that can be developed to enclose and protect the antenna. Each geometry type can be further distinguished by the range of beam lengths and total number of beams utilized in the construction of the frame. For a given geometry and cross-sectional configuration, the width and depth of the individual beam can be determined from the requirement that the frame be structurally sufficient under the design wind load.

When the geometry, number, and dimensions – length, width, and depth – of the frame members are established, then the optical blockage – the shadow cast by the

beams in the plane of the antenna – is calculated. The optical blockage serves to index the electromagnetic efficiency of the radome. Thus, it is anticipated that the frame that yields the smallest optical blockage will permit the most efficient performance of the enclosed antenna.

An investigation of the effect of the frame geometry and beam dimensions on blockage will be made here. Particular attention will be devoted to obtaining an optimum length beam for the space frame.

2. OBJECT

For a space-frame radome exposed to wind loading, this memo will attempt to determine:

1. The relation between the number and length of beams for a given geometry.
2. The relation between the length and cross-sectional dimensions of a beam necessary in order to maintain the structural sufficiency of the radome under wind loading.
3. The relation between the optical blockage, frame geometry, and beam dimensions.

And finally,

4. To determine from these relations and for a 550-ft-diameter space-frame radome exposed to a 130-mph wind, the most efficient beam size for a given cross-sectional configuration.

3. RADOME FAILURE MODES

Wind loading can fail a space-frame radome structure through:

1. Overstressing one of the major components.
2. Column buckling of a beam member.
3. Promoting a condition of general buckling instability of the space frame.

This investigation will not be concerned with a general buckling collapse of the radome structure. The relation between the external load and frame parameters that promotes a general buckling failure is at present poorly understood and is currently the subject of active analytic and experimental investigations under CAMROC sponsorship.

4. ANALYSIS

The distribution of pressures engendered on the radome by the wind load is resisted by the space frame. Structurally, the radome skin serves to transfer the local pressures to the adjacent frame members and exerts some undetermined influence in preventing column buckling in the plane of the membrane. The individual beam must sustain the axial loading developed throughout the frame and the transverse loading transmitted

by the adjacent panels. The maximum stresses induced in any member of the frame may be calculated by treating the individual beam as a beam-column exposed to the axial and transverse loads developed by the wind.

1. Forces and Moments Due to Wind Load

a) Axial Load

The axial load acting on the individual beam member is estimated by considering an idealized planar section of the space frame composed of six equilateral triangles meeting at a common hub as depicted in Figure 1. Now the maximum compressive membrane stress $N_{\phi max}$, which acts in a spherical structure exposed to a wind load, is assumed to act along a circular element of the space-frame section, which is centered at the common hub. Then, from static equilibrium considerations along the circumference

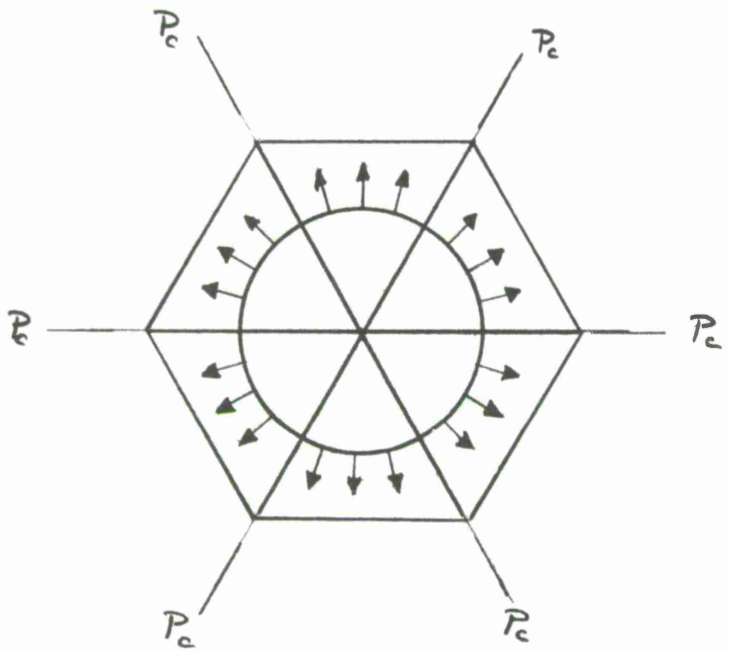

Figure 1. Relation between membrane stresses and compressive axial loads in space frame.

$$\int_s N_{\phi max}\, ds = 6\, P_c \quad . \tag{1}$$

Now,

$$N_{\phi max} = \frac{q R}{2} \quad , \tag{2}$$

$$q = \frac{1}{2}\, \rho\, V^2 \quad , \tag{3}$$

where P_c is the compressive axial load, R the radome radius, q the dynamic pressure, ρ the air density, and V the wind velocity.

Considering the triangular and circular areas defined by γ and ℓ in Figure 2, where one-third of the area of each triangle is apportioned to each hub in the triangle gives

$$\pi\, r^2 = 6\, (\frac{A}{3}) \quad , \tag{4}$$

where

$$A = \frac{\ell^2}{2} \sin 60° \quad . \tag{5}$$

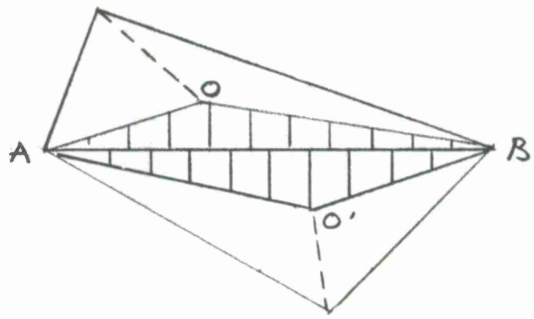

Figure 2. Area of local transverse loading imposed on beam by adjacent panels.

Using equations (2) to (5) and equation (1) reduces to

$$P_c = 0.275\, q\, R\, \ell \quad . \tag{6}$$

Thus, the axial load acting in a radome space-frame member is seen to be linearly dependent on the dynamic pressure q, radome radius R, and beam length ℓ.

b) Transverse Load

The transverse loads that act on each beam member derive from the local loads carried by the two panels that are adjacent to every beam in the frame save some of the base beams.

It is assumed that each triangular panel sustains a local load equal to the panel area multiplied by its local overpressure and that one-third of this local panel load is transferred to each of the beam edge members that constitutes the triangular panel frame. The load that is transferred to the beam member is directed perpendicular to the beam (along the radome radius).

The distribution of the load along the beam length is dependent on the location of the panel centroid in relation to the beam length; thus, the load increases linearly from zero at the beam end to a maximum at the projection of the panel centroid on the beam axis. Thereafter, it decreases linearly to zero at the opposite end of the beam. For simplicity, it will be assumed that for both adjacent panels, the projections of the centroids coincide with the midpoint of the beam. The scheme is depicted in Figure 3.

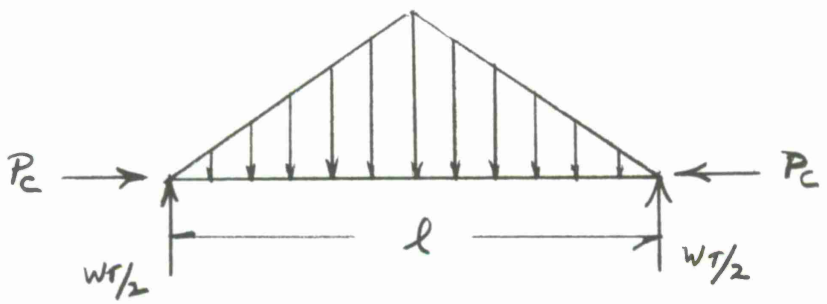

Figure 3. Loading imposed on frame member by wind.

Thus, the total load W_T supported by a beam member is

$$W_T = 2\, q(A/3) \tag{7}$$

and the area A of the triangular panel is

$$A = \ell^2/2 \sin 60^\circ \quad . \tag{8}$$

Then

$$W_T = 0.2886\, q\, \ell^2 \quad . \tag{9}$$

For the assumed triangular load distribution where the maximum intensity w of the load is reached at the midpoint of the beam,

$$w = \frac{2 W_T}{\ell} \quad , \tag{10}$$

or

$$w = 0.5772\, q\, \ell \quad . \tag{11}$$

c) Beam-Column Action

With the axial and transverse loads acting on a space-frame membrane established, the resulting moment distribution in the beam and finally the maximum stress can be determined. The loading scheme developed on the beam member as a result of the interaction of the wind with the spherical radome is illustrated in Figure 3.

For this loading condition the elastic deflection of the beam is

$$EI \frac{d^2 y}{dx^2} = M(x) - P_c Y \quad , \tag{12}$$

where E is the elastic modulus, I the area moment of inertia of beam, y the deflection along transverse axis, x the distance along beam, P_c the compressive axial load, M(x) the moment induced by transverse loading, and

$$M(x) = \frac{W_T}{2} \left[1 - \frac{4}{3} \left(\frac{x}{\ell} \right)^2 \right] \quad . \tag{13}$$

Substituting equation (13) into equation (12) and solving for the moment distribution yields

$$M = \frac{4 W_T}{k^2 \ell^2} \left[\frac{1}{k \cos \frac{k\ell}{2}} \sin kx - x \right] \quad . \tag{14}$$

The maximum moment occurs at $x = \ell/2$ and is

$$M_{max} = \frac{4 W_T}{k^2 \ell^2} \left[\frac{1}{k} \tan \frac{k\ell}{2} - \frac{\ell}{2} \right] \quad , \tag{15}$$

where

$$k = \sqrt{P_c / EI} \quad .$$

2. Maximum Stress

The maximum stress S_{max} developed in the space-frame beam member by the axial and transverse loads caused by the interaction of the wind with the spherical radome is

$$S_{max} = \frac{P_c}{A} + \frac{M_{max} C}{I} \quad , \tag{16}$$

where A is the cross-sectional area of beam and C is the distance from neutral axis to outermost fiber.

3. Column Buckling

The critical buckling load P_{cr} for a column is given as

$$P_{cr} = \frac{\pi^2 E I}{(k_1 \ell)^2} \quad , \tag{17}$$

where E is the elastic modulus, I the area moment of inertia about the buckle axis, ℓ the length of column, and k_1 the constant depending on the manner of end restraint for the column.

The minimum buckling load for a column of fixed dimensions occurs in the pin-ended support case where $k_1 = 1$.

In order that the radome beam member be sufficient against column buckling by itself — without the introduction of guy wires or invoking panel restraint — it is required that

$$P_{cr} > P_c \quad ,$$

or

$$\frac{P_{cr}}{P_c} > 1 \quad , \tag{18}$$

where P_c is the axial compressive load developed in the beam member by the wind load on the radome (see equation (6)).

4. Length and Number of Beams in Uniform Frame Geometry

In general, the geometry of the radome space frame — the length, number, disposition, and orientation of the beam members in the frame — is developed by considering the icosahedron or some variation of this model. An icosahedron consists of 20 identical equilateral triangles disposed as illustrated in Figure 4. Each vertex point

falls on the surface of a sphere, which can be made to circumscribe the icosahedron. When the legs of the equilateral triangles are raised to the surface of the circumscribing sphere, they are transformed into arc lengths. The result is shown in Figure 5.

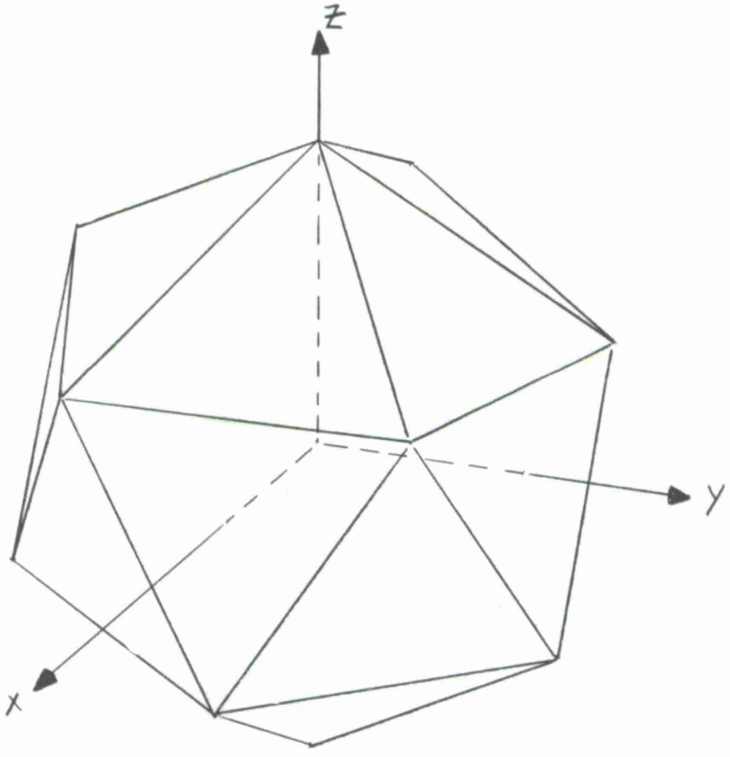

Figure 4. Icosahedron used in development of radome geometry.

In order to develop an approximate relation between the length and number of beams required for a radome space frame, one planar equilateral triangle whose sides are made equal to the arc length (see Figure 6) is considered. This unit is then decomposed into planar triangles by performing equal subdivisions of each triangular leg. Relations are then established between the length and the number of beams for the triangular unit. The 20 triangular units that constitute the complete sphere are then summed while carefully excluding duplicate contributions to the total at the contiguous edges. By imposing equal subdivisions on the three legs of the triangular unit, all the beam members are made equal and the resulting geometry is uniform.

The development of the relation between the length and number of beams for the triangular unit is illustrated in Figure 6. The equations are given below.

The length of any side L_s in the planar equilateral triangular unit is

$$L_s = R\phi \quad , \tag{19}$$

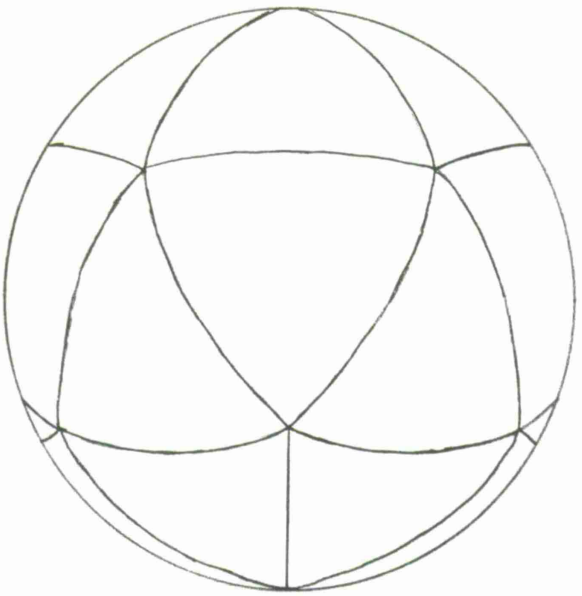

Figure 5. Icosahedron expanded to circumsphere used in the development of space-frame radome geometry.

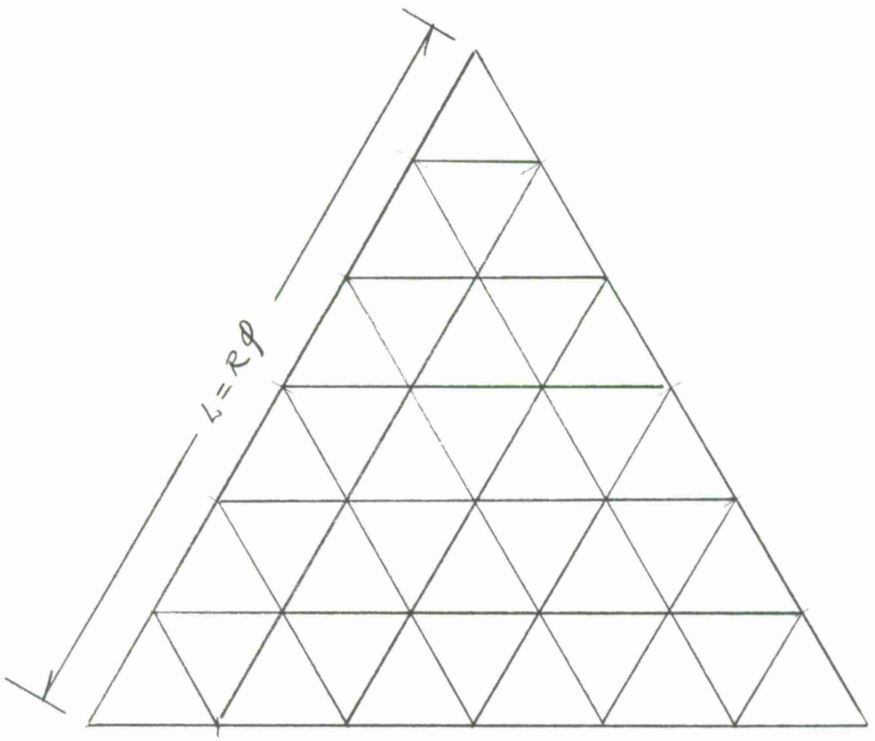

n = number of equal lengths into which icosahedral sides are subdivided.

$N_V = \sum_{1}^{n+1} N$ number of vertices

$N_E = 3 \sum_{1}^{n} N$ number of edges

$N_T = n^2$ number of triangles

Figure 6. Planar icosahedral unit used in estimating elements of space frame.

where R is the radome radius, and ϕ is the angular separation between any two adjacent vertex points on the icosahedron – 63.435°.

If each leg of the equilateral unit is subdivided into n number of beams of ℓ length, then it is seen from Figure 6 that the unit has N_V vertices, N_E edges, and N_T triangles, where

$$\ell = \frac{R\phi}{n} \quad , \tag{20}$$

$$N_V = \sum_{1}^{n+1} N \quad , \tag{21}$$

$$N_E = 3 \sum_{1}^{n} N \quad , \tag{22}$$

$$N_T = n^2 \quad . \tag{23}$$

The number of edges in a complete radome is obtained by summing the results from the triangular unit in accordance with the relative disposition of the triangular units while eliminating duplication between contiguous edges of the triangles. It is noted that the radome can be subdivided into top and bottom pentagonal caps consisting of five triangular units, and a center belt consisting of 10 triangular units. From equation (22) and Figure 6 the number of beams in the separate radome sections are

$$\text{Top cap} = 5 \, \triangle_s - 5 \text{ common sides} \quad ,$$

$$\text{Top cap} = 5 \left(3 \sum_{1}^{n} N - n \right) \quad . \tag{24}$$

Similarly for the bottom cap,

$$\text{Bottom cap} = 5 \left(3 \sum_{1}^{n} N - n \right) \quad . \tag{25}$$

While for the middle belt

$$\text{Middle belt} = 10 \, \triangle_s - 15 \text{ common sides,}$$

$$\text{Middle belt} = 10 \left(3 \sum_{1}^{n} N \right) - 15 \, n \quad . \tag{26}$$

Summing the results of equations (24), (25), and (26) to get the number of beams N_{ER} in a complete radome gives

$$N_{ER} = 30 \left(2 \sum_{1}^{n} N - n \right) \quad , \tag{27}$$

or

$$N_{ER} = 30\, n^2 \quad , \tag{28}$$

where N_{ER} is the number of beams in a complete radome and

$$n = \frac{R\phi}{\ell} \quad .$$

The total length of beams in a complete radome $\sum L$ is calculated by multiplying the total number of beams by the length of the individual beam or

$$\sum L = N_{ER}\, \ell \quad . \tag{29}$$

Substituting equations (20) and (28) into the above gives

$$\sum L = 30\, (R\phi n) \tag{30}$$

or

$$\sum L = 30\, (R\phi)^2 / \ell \quad . \tag{31}$$

For an actual radome structure that, of course, is less than one diameter high, equation (30) or (31) must be multiplied by the ratio of height to diameter.

5. Frame Weight

The weight of the radome frame exclusive of hubs and membranes is

$$W_R = \rho A \left(\sum L\right) \quad , \tag{32}$$

where ρ is the density of beam-member material, A is the cross-sectional area of beam members, and $\left(\sum L\right)$ is the total length of beams in a complete radome.

Equation (32) gives the weight for a radome that is a complete sphere. For an actual radome, this result should be multiplied by the ratio of height to diameter for the radome design.

6. Optical Blockage

The optical blockage is a measure of the percent of the radiating antenna plane that is obstructed owing to the shadow cast by the beams and hubs of the radome-space frame. The optical blockage serves to index the electromagnetic performance of the radome. That is, in general, a small value of the optical blockage allows a greater efficiency in the operating performance of the antenna. Because the optical blockage indexes the electromagnetic behavior and is expressed in terms of the frame geometry

and beam dimensions, it serves as a figure of merit in evaluating the relative efficiency of different space frames.

The equations that express the optical blockage for a space frame in terms of the coordinates of each individual beam and hub in the frame have been developed. Using these equations in conjunction with the 7090 computer, extensive results were obtained for the random Haystack geometry over a wide range of solid, rectangular, cross-sectional beam dimensions.

Omitting the hub contribution, which was negligible in comparison to the beam shadow, an empirical equation was fitted to these results. The equation is

$$\%B = \frac{87.85}{4\pi}\left(\frac{\sum L}{R^2}\right)\left[\frac{\sin\theta}{1+\cos\theta}\,h + b\right] \quad , \tag{33}$$

where

%B is the percent of the antenna plane shadowed by the beams,
$\sum L$ is the total length of beams in complete spherical radome,
R is the radome radius,
h is the beam depth,
b is the beam width,

$$\sin\theta = R_P/R \quad ,$$

and R_P is the plan radius of the antenna.

Because θ must always be less than 90°, the coefficient of h in equation (33) will always be less than 1. Then it follows that increasing the beam width will always produce a greater increase in blockage than a corresponding increase in the beam depth. Thus, for maximum efficiency in space-frame design, a minimum beam width must be developed for the space frame.

Also, it is noted from equation (33) that as the antenna plan diameter decreases in relation to the radome radius, the effect of the beam depth on blockage is further minimized.

Lastly, it is seen from equations (31) and (33) that a scaling up of the antenna and radome radii while maintaining the dimensions of the individual beam member constant will have no effect on the blockage.

Although the blockage equation pertains to a random-frame geometry and the calculations performed in this study relate to a uniform geometry, it is felt that because of the large number of beam members involved the effect will not be significant.

7. Member Properties

In order to apply the equations that have been presented to the preliminary development of an efficient space-frame radome structure for the CAMROC facility, a material

and cross-sectional configuration for the individual beam member must be selected. In order to maximize the buckling and stress capacity of the frame, steel has been chosen for the beam material. To permit a high area moment of inertia consistent with a reasonable total frame weight, a channel section shown in Figure 7 has been selected. The separate channel elements could be laced together by means of diagonal struts. However, for the sake of simplicity, the effect of the struts has been conservatively omitted.

For this cross section, the member properties are:

The area A is

$$A = 2bT + 4(D - T)T \quad . \tag{34}$$

The area moment of inertia about the x axis I_x is

$$I_x = \frac{b}{12}\left[h^3 - (h - 2T)^3\right] + \frac{T}{6}\left[(h - 2T)^3 - (h - 2D)^3\right] \quad . \tag{35}$$

The area moment of inertia about the y axis I_y is

$$I_y = \frac{Db^3}{6} - \frac{(D - T)(b - 2T)^3}{6} \quad , \tag{36}$$

where b is the beam width, h is the beam depth, T is the channel thickness, and D is the flange depth.

The flange depth is held constant at D = 4.0 inches, and for steel, $E = 30 \times 10^6$ psi, $\rho = 0.285$ lb/in^3.

5. RESULTS AND DISCUSSION

By applying the equations that have been presented, an effort is made to determine the most efficient beam dimensions for the CAMROC 550-ft-diameter space-frame radome when exposed to a 130-mph wind. The beam dimensions — length, width, and depth — the cross-sectional configuration, and channel thickness are considered constant throughout the complete frame, and differing space frames corresponding to variations in these parameters are investigated and the relative efficiencies of these frames evaluated. The cross-sectional configuration is as shown in Figure 7. To maximize the stress and column-buckling capacity of the beam members, it is assumed that the beams are fabricated from steel and various yield stress capacities are investigated.

Beam lengths that vary from 10 to 70 ft in increments of 10 ft are considered, while for each length, beam widths of 2.0, 4.0, 6.0, and 8.0 inches are investigated by calculating the minimum depth consistent with the assumed yield stress required to resist the maximum stress. Yield stresses of 40,000, 60,000, and 80,000 psi are investigated. This procedure is repeated for channel thicknesses of 1.0, 1.5, and 2.0 inches. The optical blockage and total space-frame weight is next calculated for

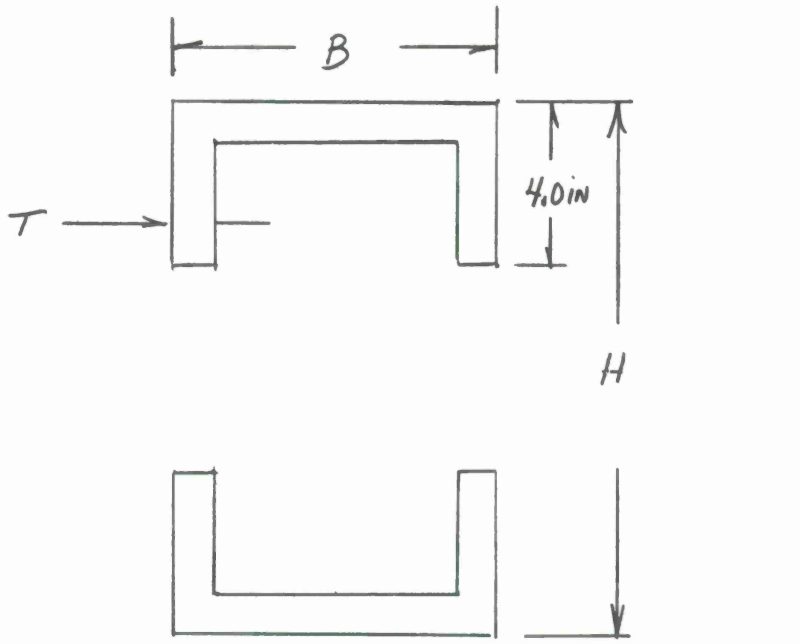

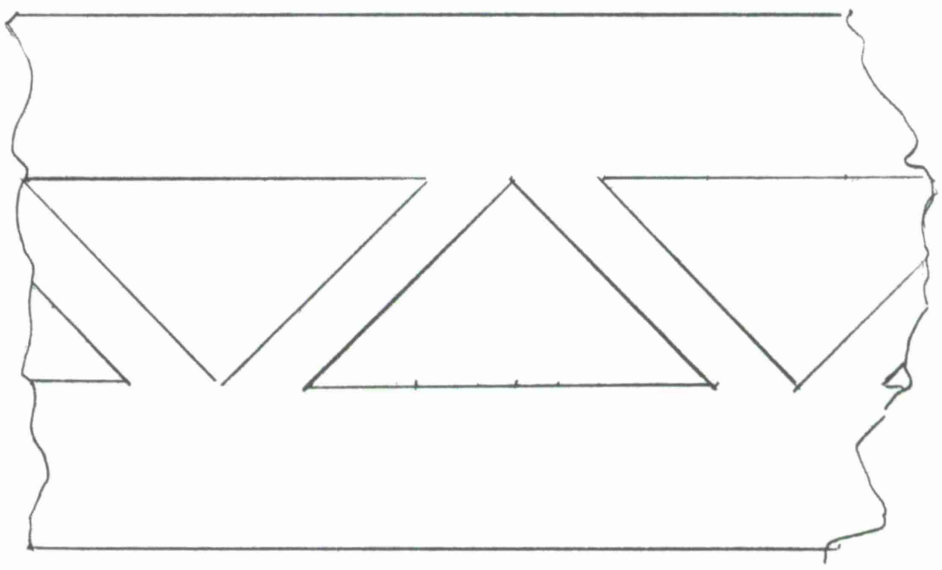

Figure 7. Type beam member for use in 550-ft-diameter space-frame radome.

this range of beam sizes. The most efficient beam dimensions are then those that give a minimum optical blockage. Because the weight of the space frame is one of the most influential factors in determining the cost of the total radome structure, a range of optical blockage-beam dimensions is considered in terms of the space-frame weight.

The procedure outlined above is performed for two distinct cases. In the first case, only the maximum stress is allowed to limit the beam dimensions. It is assumed that column buckling can be restrained with no important increase in optical blockage through use of a system of wires interconnected to the beams as suggested by Ammann & Whitney or by attaching the panel membranes in some fashion that enjoins the membrane stress in preventing excessive beam deflections. In the second case, the beam widths are restricted to those values that guarantee a buckling capacity about the weak axis in excess of the wind-induced axial load, and the minimum permissible beam depth is then calculated to accord with the assumed yield stress.

1. General

The parameters of the space frame, the loading components induced in the individual beam by the interaction of the radome with the wind load, and also those beam parameters that are independent of beam depth are illustrated in Figures 8 to 13. These features possess some generality and are applicable throughout the study.

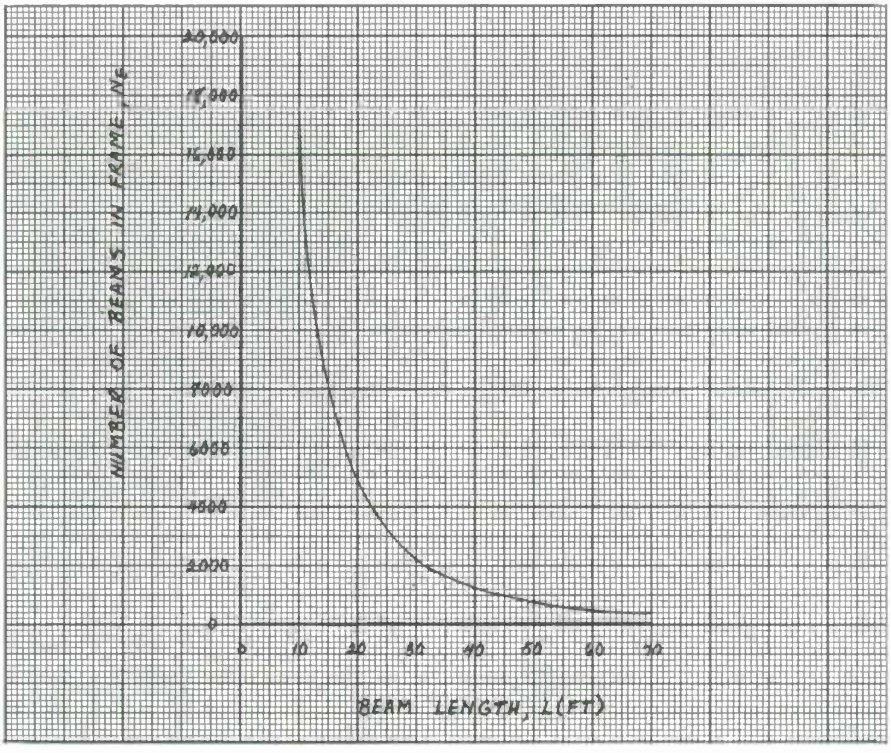

Figure 8. Number of beam elements in 550-foot-diameter space-frame radome designed to resist 130-mph wind versus length of individual beam.

Figure 8 indicates the number of beams as a function of the beam length for the 550-ft-diameter CAMROC radome whose total height is 7/10 of the diameter. This result is derived from equations (28) and (20).

The axial and transverse loads imposed on the individual beam element in the space frame by the interaction of the 550-ft-diameter radome with a 130-mph wind are plotted in Figure 9 as a function of the beam length. These results are calculated from equations (6) and (9), respectively. From this plot once the beam length is established for the structure, the beam loads are immediately available for the determination of the cross-sectional dimensions of the beam member.

The area and area moment of inertia about the y axis are calculated from equations (34) and (36) and are plotted in Figure 10 versus the beam width for the three channel thicknesses investigated in this report.

In Figures 11, 12, and 13 the ratio of the critical column load about the y axis for a pin-ended beam to the imposed axial load is calculated from equations (17) and (6) and shown as a function of the beam length for beam widths of 2.0, 4.0, 6.0, and 8.0 inches and the three channel thicknesses, T = 1.0, 1.5, and 2.0 inches. Above the dashed line, $P_{cr} > P_c$, the beam member develops a sufficient buckling capacity to resist the axial load, while below, the member must be assisted in some fashion — such as introducing interconnecting guy wires or invoking panel restraint. For the range of beam widths investigated, these figures delineate at $P_{cr} = P_c$ the maximum length beam that is stable without external assistance.

2. Optimum Beam Dimensions in Space-Frame Independent of Column Buckling

a) Beam Dimension

The results in this section assume that external restraints are readily introduced to increase the column-buckling capacity and that this is accomplished without an appreciable increase in the optical blockage of the space frame. Thus, for a range of beam lengths extending from 10 ft to 70 ft in increments of 10 ft, a range of beam widths extending from 2.0 inches to 8.0 inches in increments of 2.0 inches; a range of channel thicknesses 1.0, 1.5, and 2.0 inches, and a range of yield stresses 40,000, 60,000 and 80,000 psi, the minimum beam depth consistent with the yield stress is calculated. The resulting optical blockage and frame weight for the calculated beam dimensions are then determined.

In Figures 14 to 22 the minimum beam depth is calculated by permitting the maximum stress to reach the yield stress. Equations (16), (15), (9), (34), and (35) are utilized for this purpose. Figures 14, 15, and 16 plot this information for a channel thickness of T = 1.0 inch and yield stresses of 40,000, 60,000, and 80,000 psi, respectively. Figures 17, 18, and 19 consider the same range of yield stresses for a channel thickness of T = 1.5, while Figures 20, 21, and 22 maintain the same range of yield stresses for a channel thickness of T = 2.0 inches.

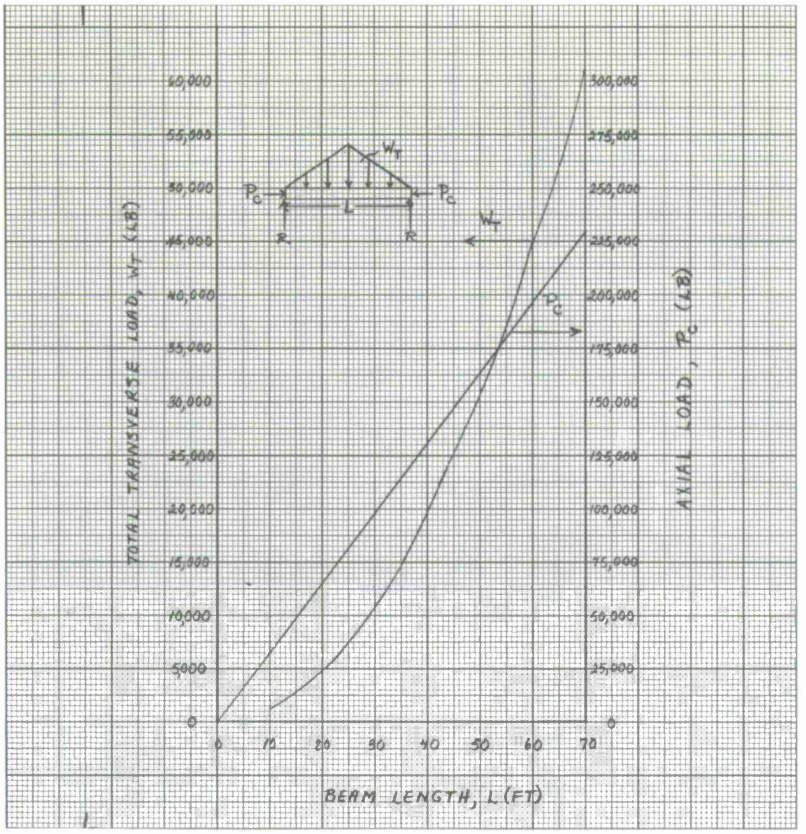

Figure 9. Total transverse and axial loads developed by 130-mph wind versus length of individual beam in 550-ft-diameter space-frame radome.

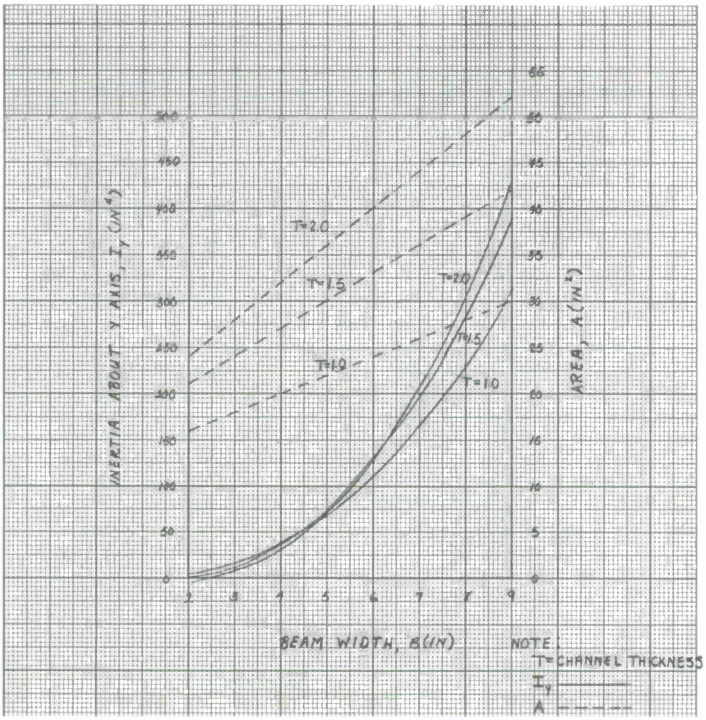

Figure 10. Area and area moment of inertia about weak axis versus beam width for 550-ft-diameter space-frame radome designed to resist 130-mph wind.

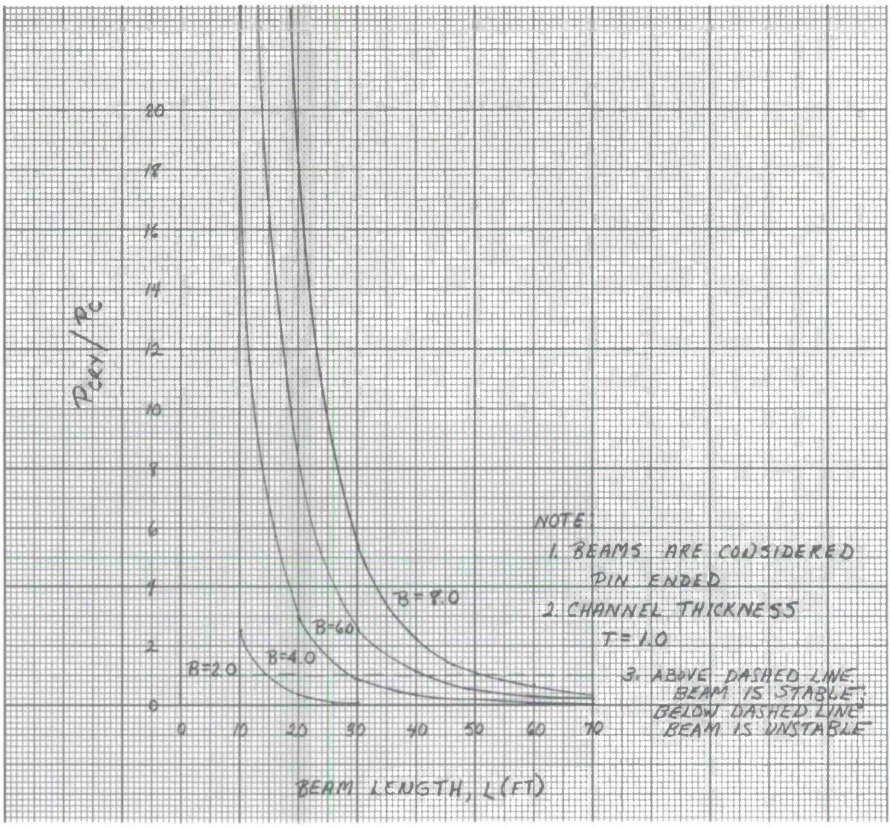

Figure 11. Ratio of critical euler load about weak axis to axial load versus beam length in 550-ft-radome designed to resist 130-mph wind.

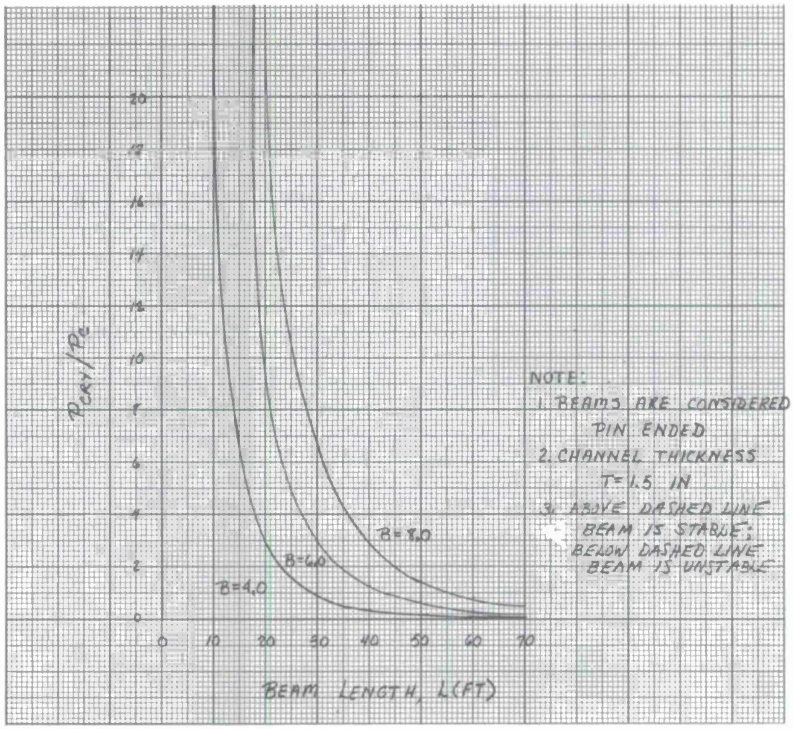

Figure 12. Ratio of critical euler load about weak axis to axial load versus beam length in 550-ft-radome designed to resist 130-mph wind.

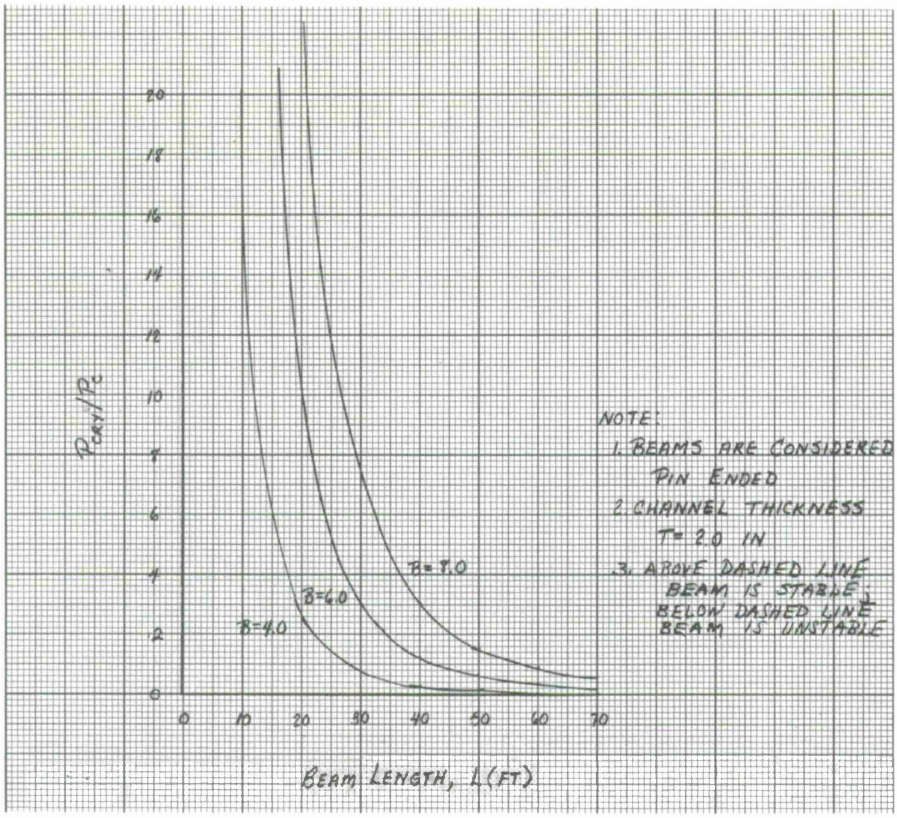

Figure 13. Ratio of critical euler load about weak axis to axial load versus beam length in 550-ft-radome designed to resist 130-mph wind.

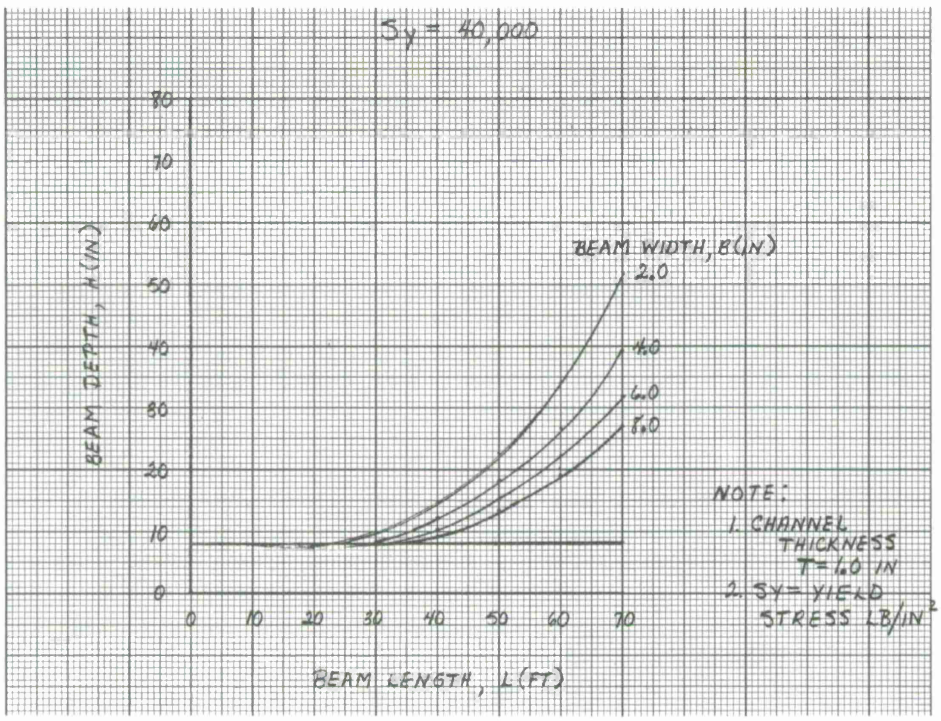

Figure 14. Depth of beam in 550-ft-diameter radome required to resist 130-mph wind load at constant yield stress versus beam length.

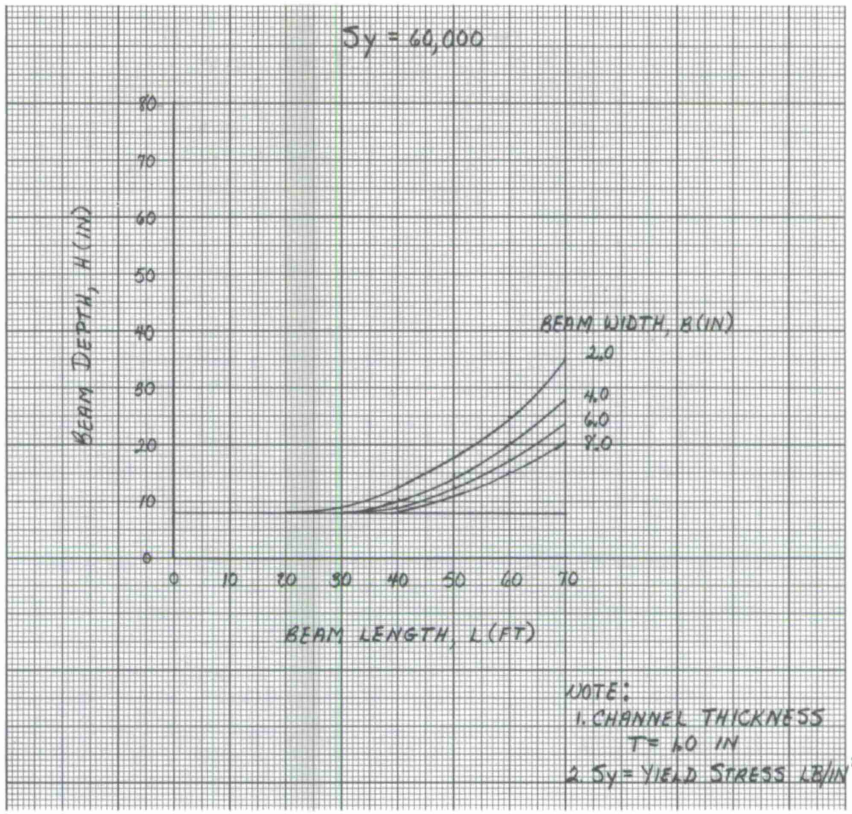

Figure 15. Depth of beam in 550-ft-diameter radome required to resist 130-mph wind load at constant yield stress versus beam length.

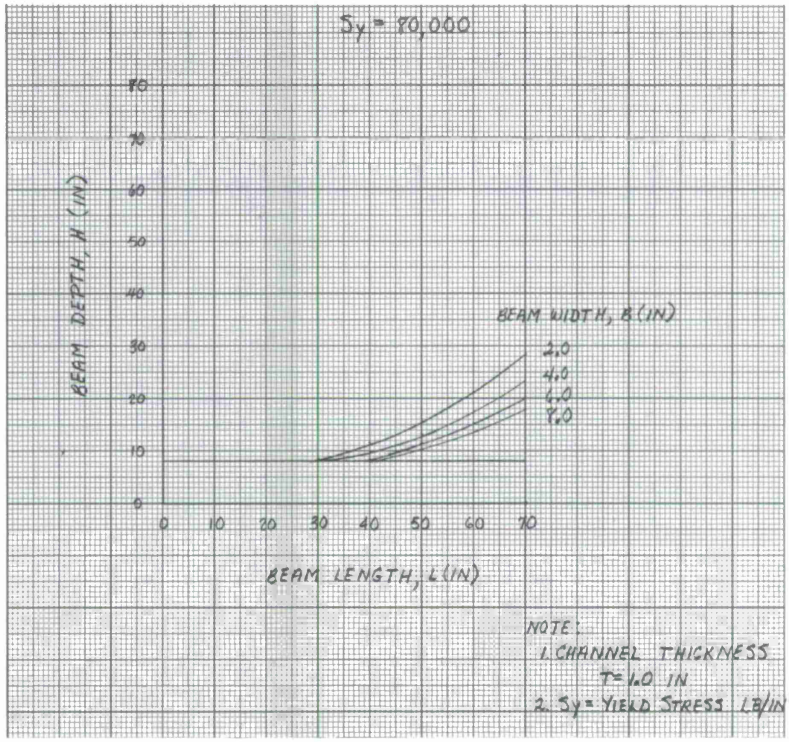

Figure 16. Depth of beam in 550-ft-diameter radome required to resist 130-mph wind load at constant yield stress versus beam length.

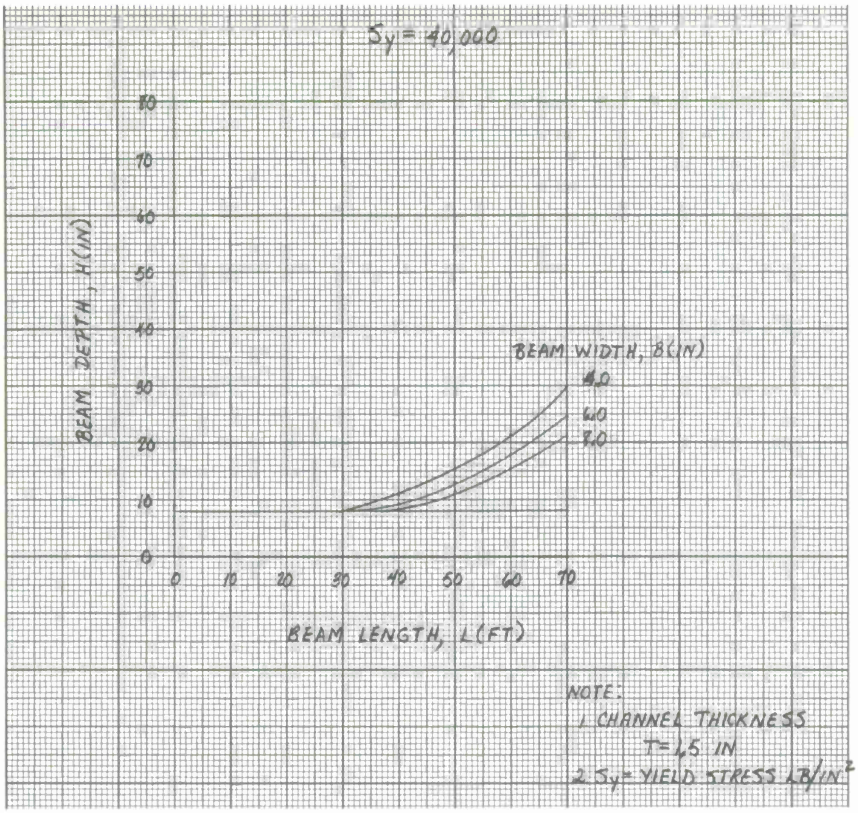

Figure 17. Depth of beam in 550-ft-diameter radome required to resist 130-mph wind load at constant yield stress versus beam length.

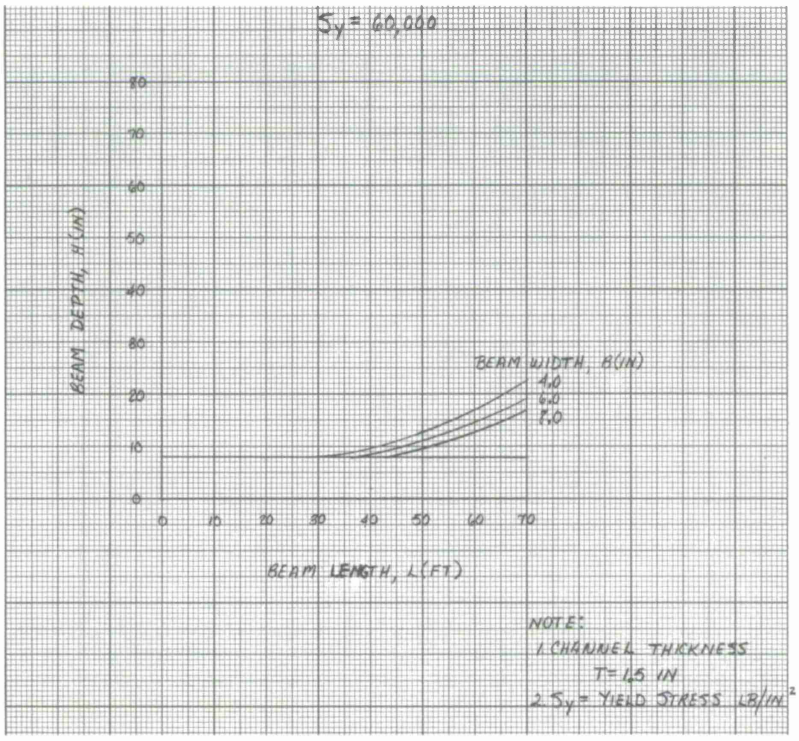

Figure 18. Depth of beam in 550-ft-diameter radome required to resist 130-mph wind load at constant yield stress versus beam length.

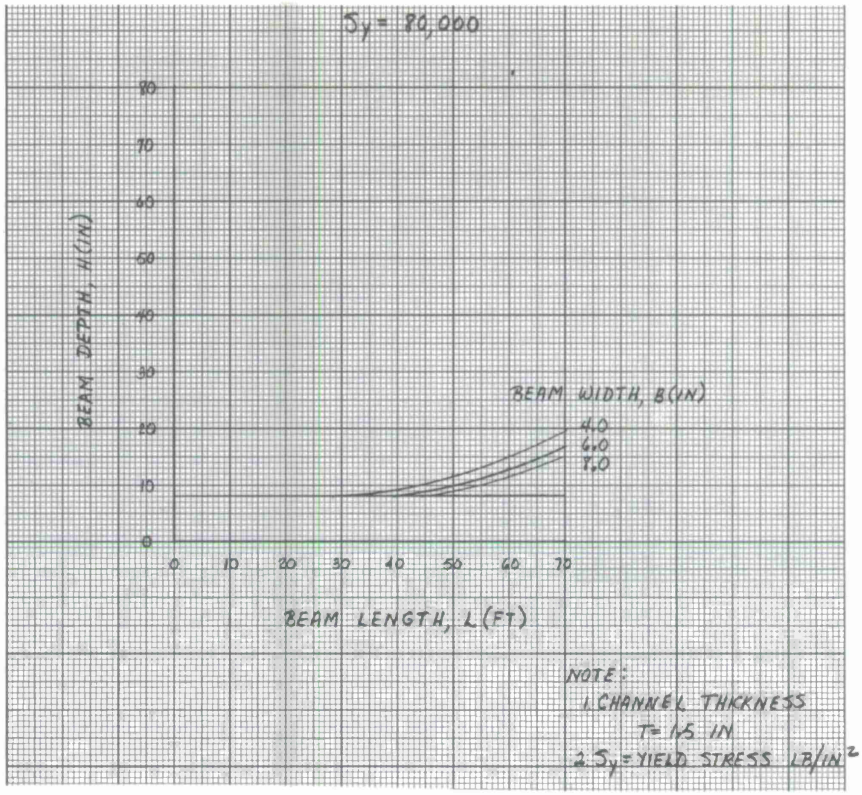

Figure 19. Depth of beam in 550-ft-diameter radome required to resist 130-mph wind load at constant yield stress versus beam length.

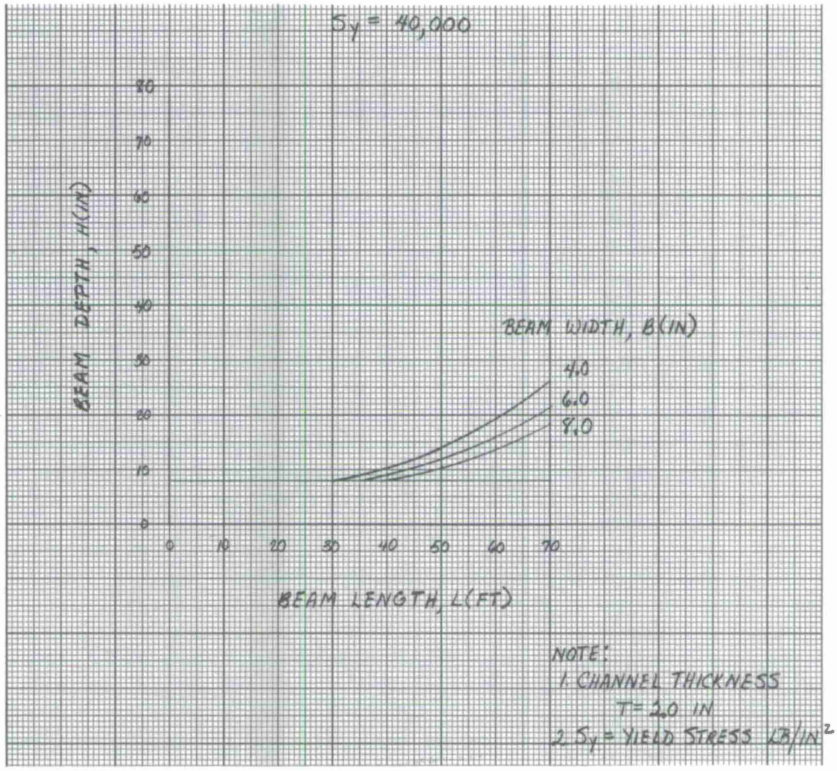

Figure 20. Depth of beam in 550-ft-diameter radome required to resist 130-mph wind load at constant yield stress versus beam length.

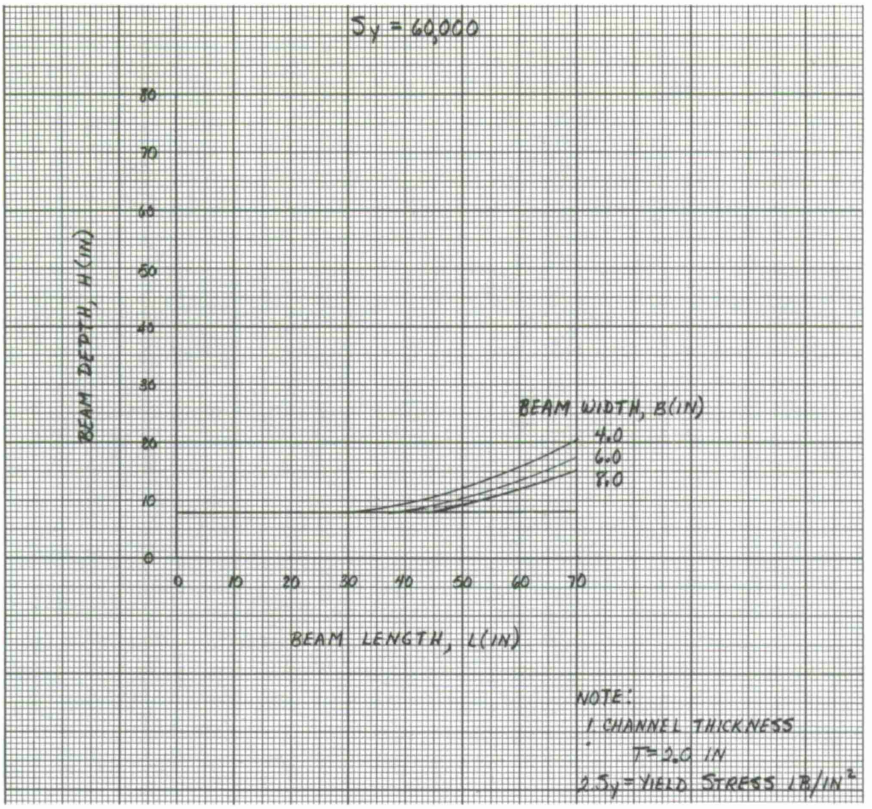

Figure 21. Depth of beam in 550-ft-diameter radome required to resist 130-mph wind load at constant yield stress versus beam length.

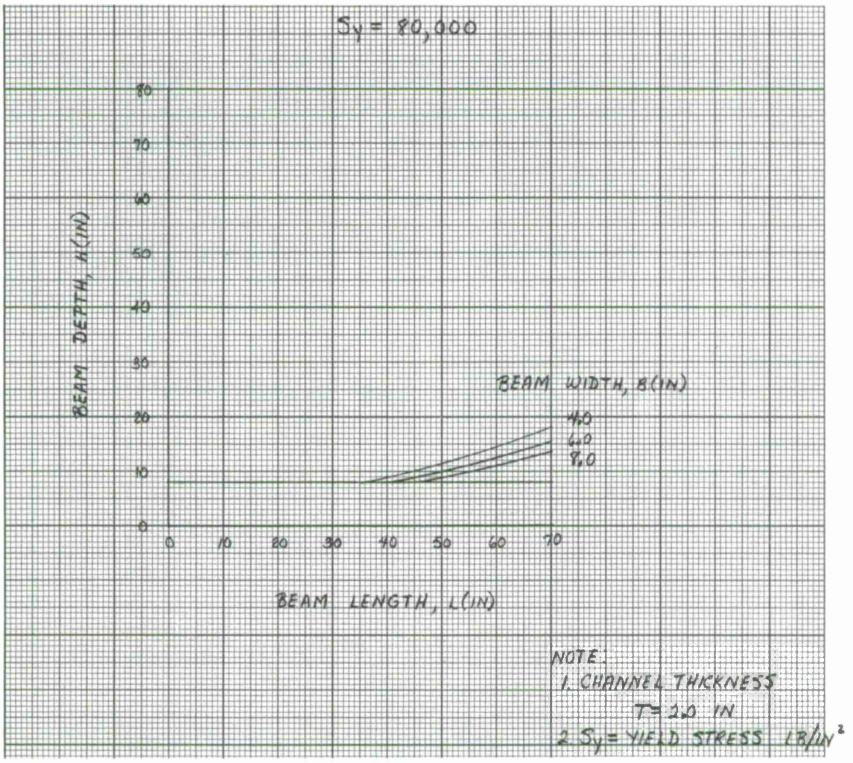

Figure 22. Depth of beam in 550-ft-diameter radome required to resist 130-mph wind load at constant yield stress versus beam length.

Examination of Figures 14 to 22 demonstrates that the required beam depth

a) increases with increasing length,
b) decreases with increasing beam width,
c) decreases with increasing yield stress,
d) decreases with increasing channel thickness.

It is noted that because the channel flanges are fixed at 4.0 inches, beam depths less than 8.0 inches are not possible. Also, channel thicknesses of 1.5 and 2.0 inches exclude beam widths of 2.0 inches.

These graphs establish a wide range of dimensions, channel thicknesses, and yield stresses for beam members that successfully resist the maximum stress developed in the 550-ft-diameter space-frame radome when subjected to a 130-mph wind.

b) Optical Blockage

In Figures 23 to 31, the optical blockage of 550-ft-diameter space-frame radomes capable of withstanding 130-mph winds is plotted as a function of the beam length for beam widths of 2.0, 4.0, 6.0, and 8.0 inches. This information is developed for the three channel thicknesses with three yield stresses for each channel thickness being considered.

The beam dimensions — length, width, and depth — were extracted from the previous plots and incorporated into equation (33) for the determination of the optical blockage. The beam depth is not explicitly given in these figures but is readily obtained by comparison with Figures 14 to 22.

Consulting equation (33) it is noted that the beam width is more influential in minimizing blockage than the beam depth. This is reflected in Figures 23 to 31 where it is seen that for a given channel thickness and yield stress the minimum optical blockage for the same length is always obtained for the minimum beam width; also, it is noted that the optical blockage decreases with increasing length, reaches a minimum, and then begins to increase. However, the difference between minima for any channel thickness-yield stress combination is less than 0.5%. As the beam width increases in 2.0-inch increments, the blockage minimum occurs at beam lengths that advance approximately in increments of 10 ft.

Increasing the yield stress and/or the channel thickness reduces the beam depth required to resist the maximum stress while the other beam dimensions remain constant. This reduction in beam depth decreases the optical blockage.

From the figures it appears that the greatest improvement in performance is obtained in increasing the yield stress from 40,000 to 60,000 psi and increasing the channel thickness from 1.0 to 1.5 inches. The increase in blockage benefits obtained from increasing the yield stress from 60,000 to 80,000 psi and/or increasing the channel thickness from 1.5 to 2.0 inches is less than obtained before.

However, if the absolute minimum in optical blockage is required, then the following beam properties are necessary:

Channel Thickness	— 2.0 inches,
Beam Width	— 4.0 inches,
Beam Depth	— 14.5 inches,
Beam Length	— 60 ft,
Optical Blockage	— 3.6%,
Yield Stress	— 80,000 psi.

c) Frame Weight

The frame weight is calculated from equations (32) and (34), and the results are plotted in Figures 32 to 34 as a function of length for the selected beam widths and channel thicknesses. The frame weight increases with the beam width and channel thickness but decreases with increasing length.

Because only the channel sections and not the lacing that binds them into a beam are considered, the frame weight is independent of the beam depth. The number of beams in the frame varies inversely as the length and is more influential in controlling the frame weight than the beam width or channel thickness.

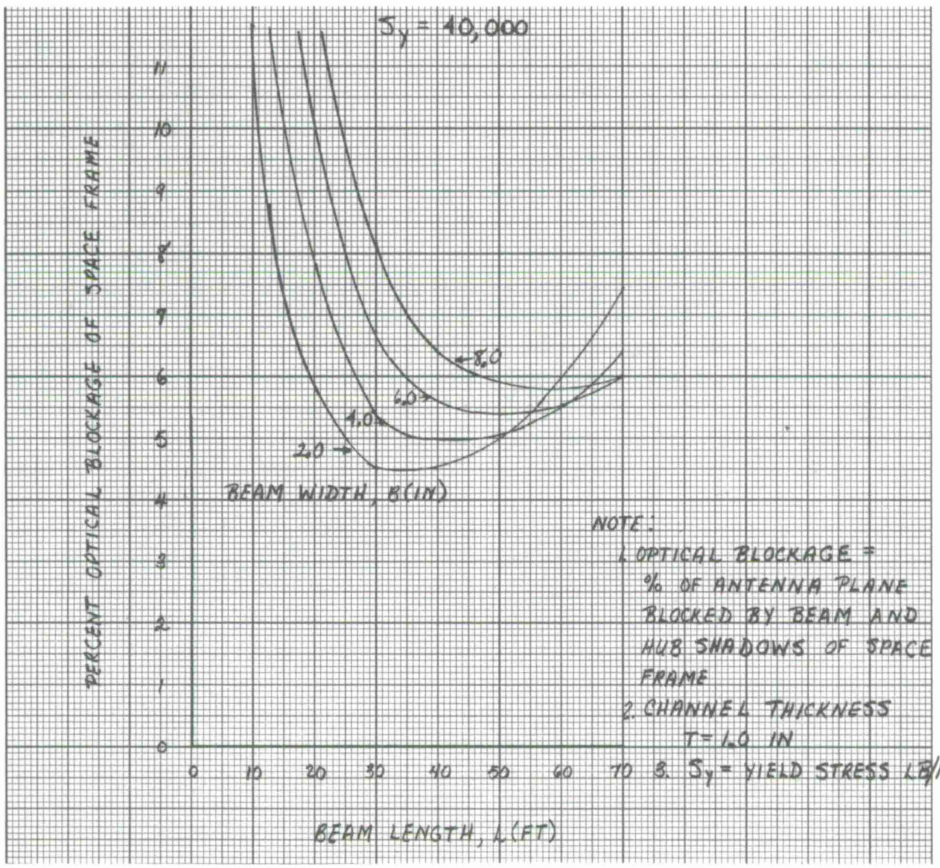

Figure 23. Optical blockage of frame versus length of individual beam in 550-ft-diameter space-frame radome designed to resist 130-mph wind.

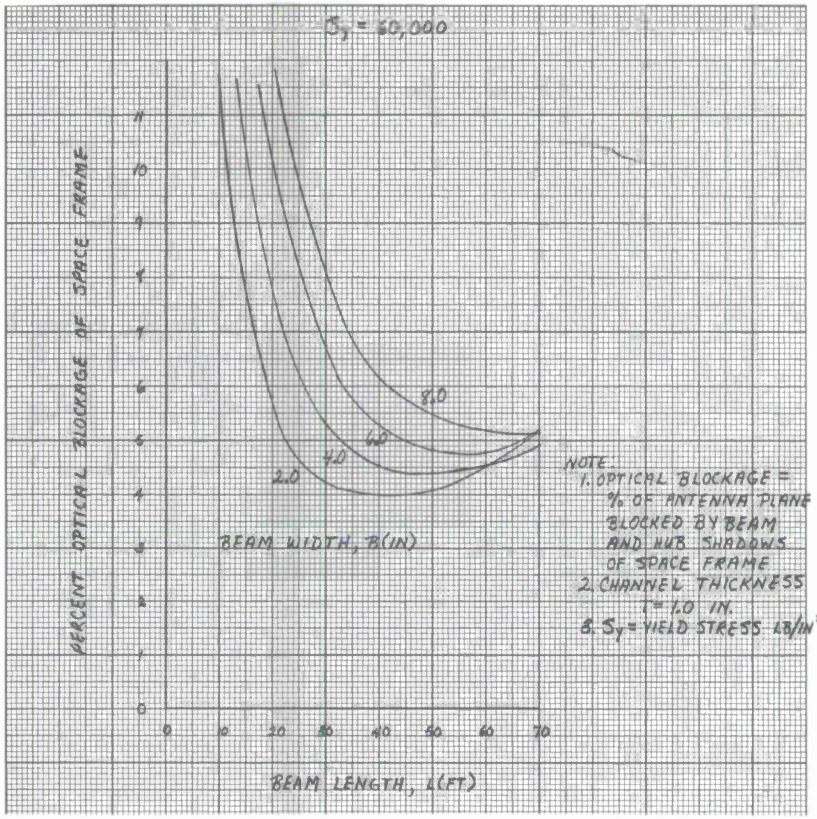

Figure 24. Optical blockage of frame versus length of individual beam in 550-ft-diameter space-frame radome designed to resist 130-mph wind.

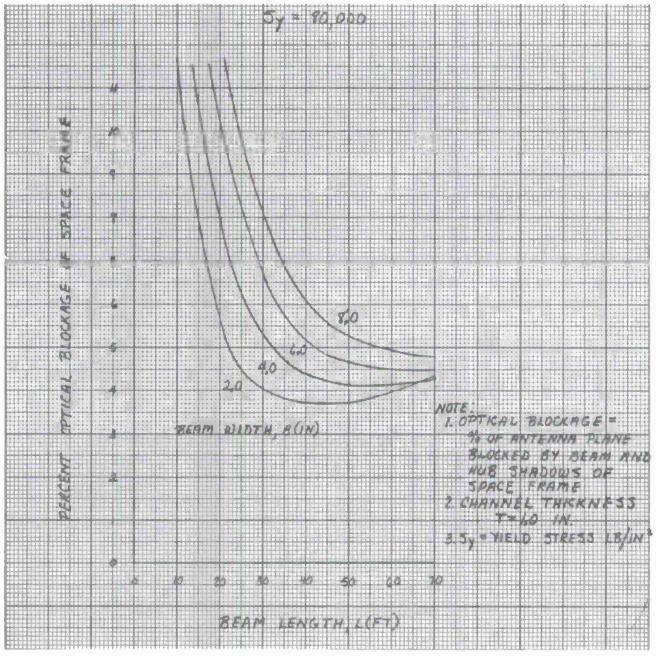

Figure 25. Optical blockage of frame versus length of individual beam in 550-ft-diameter space-frame radome designed to resist 130-mph wind.

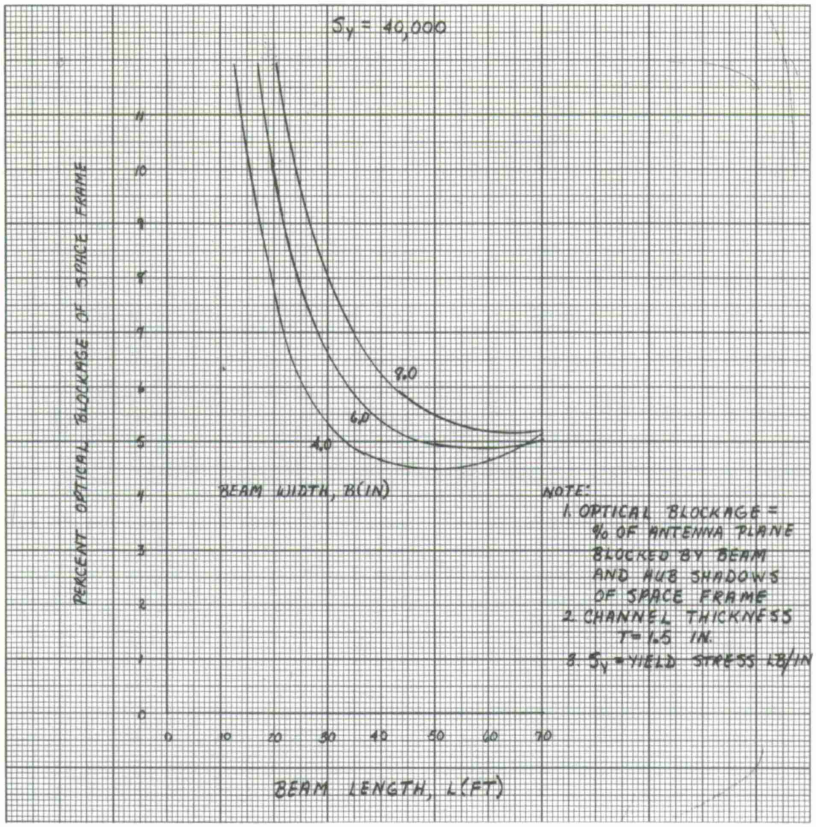

Figure 26. Optical blockage of frame versus length of individual beam in 550-ft-diameter space-frame radome designed to resist 130-mph wind.

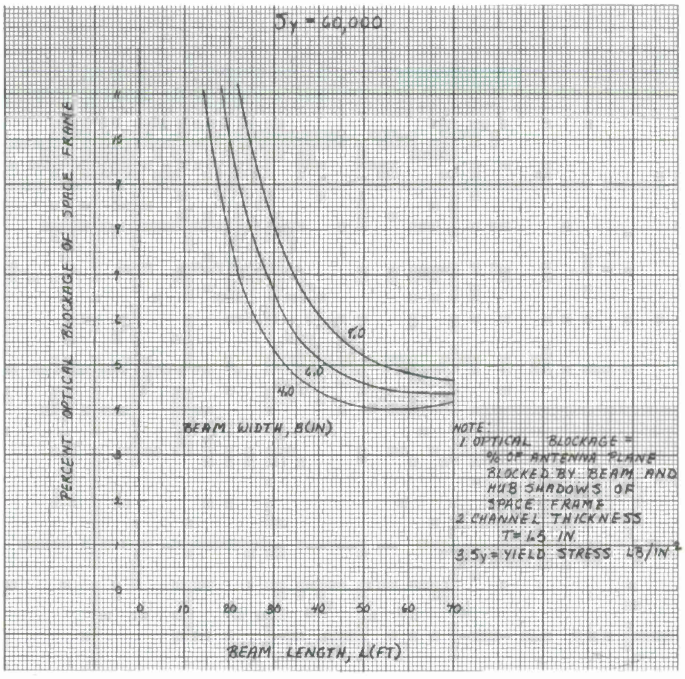

Figure 27. Optical blockage of frame versus length of individual beam in 550-ft-diameter space-frame radome designed to resist 130-mph wind.

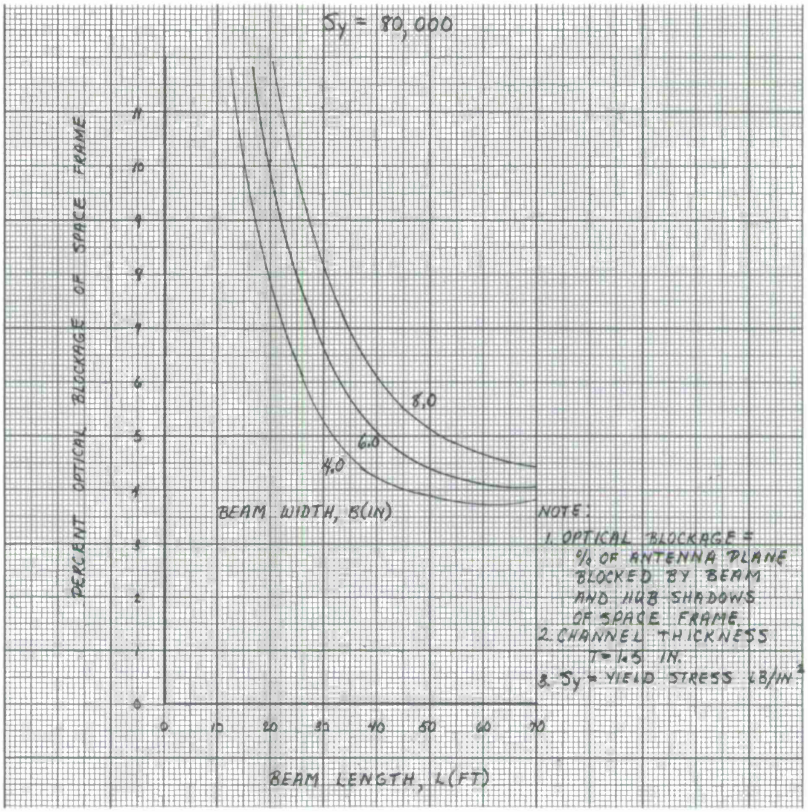

Figure 28. Optical blockage of frame versus length of individual beam in 550-ft-diameter space-frame radome designed to resist 130-mph wind.

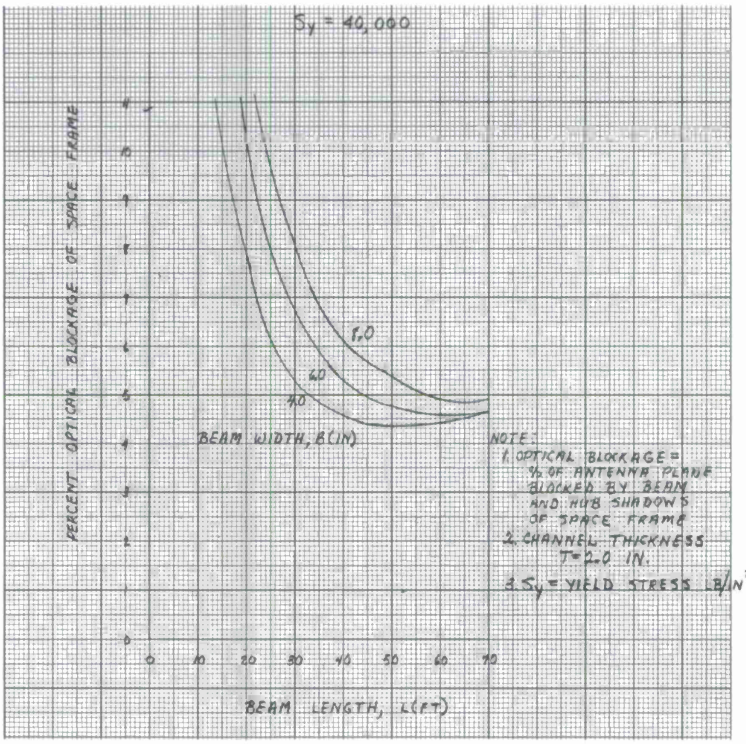

Figure 29. Optical blockage of frame versus length of individual beam in 550-ft-diameter space-frame radome designed to resist 130-mph wind.

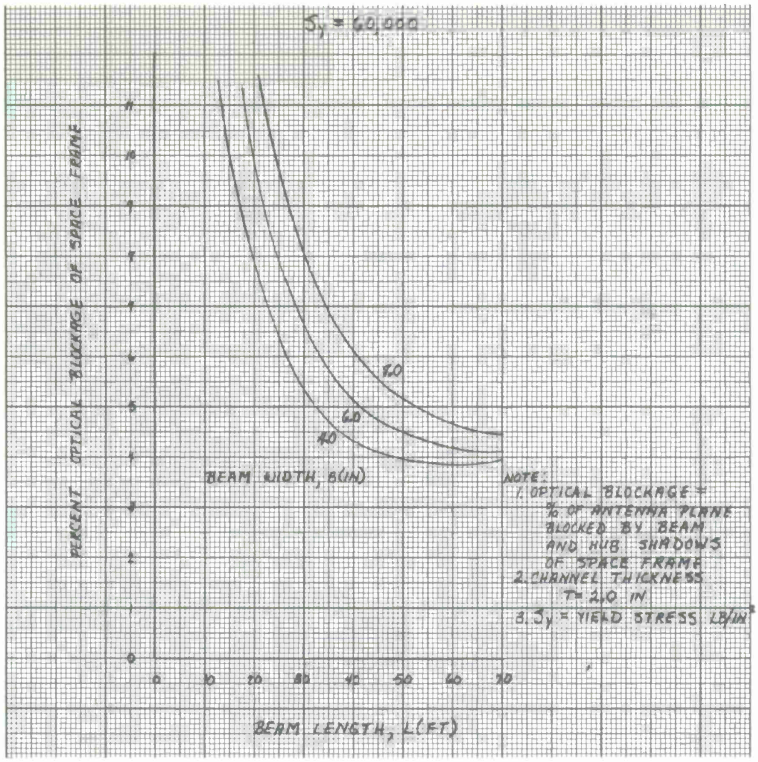

Figure 30. Optical blockage of frame versus length of individual beam in 550-ft-diameter space-frame radome designed to resist 130-mph wind.

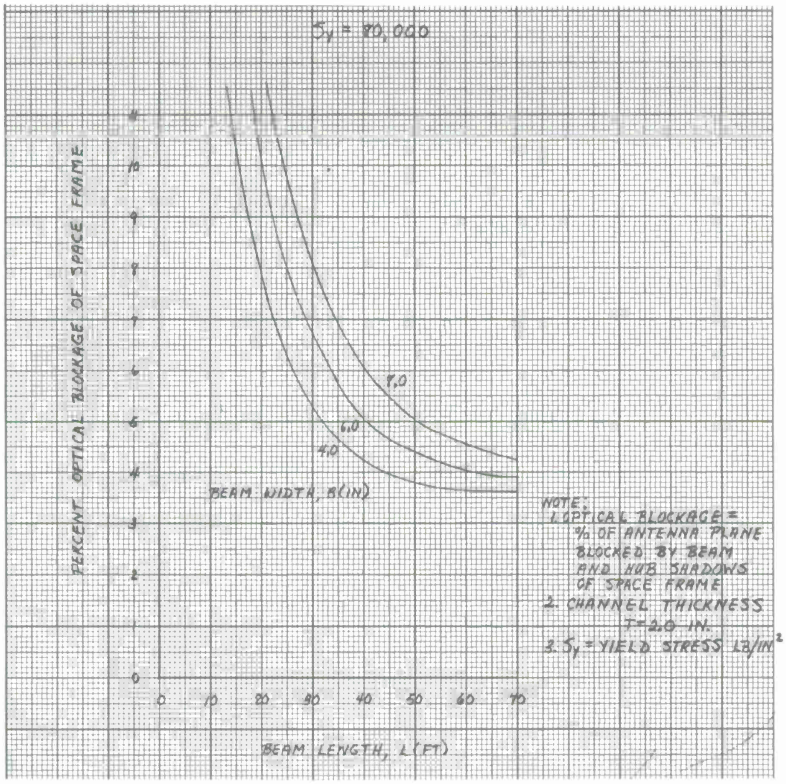

Figure 31. Optical blockage of frame versus length of individual beam in 550-ft-diameter space-frame radome designed to resist 130-mph wind.

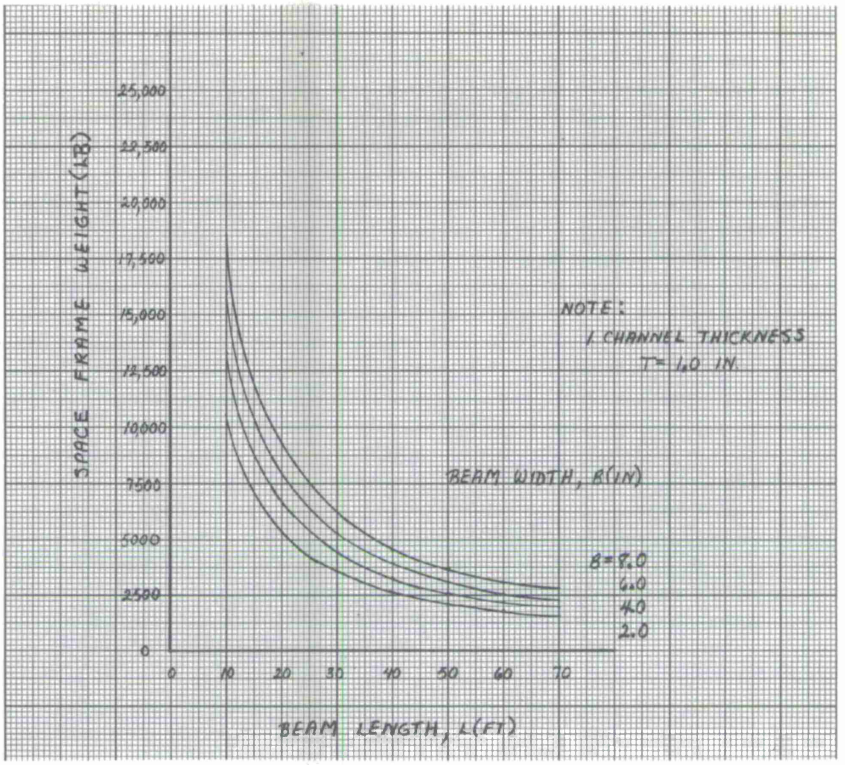

Figure 32. Weight of space frame for 550-ft-diameter radome designed to resist 130-mph wind versus length of individual beam.

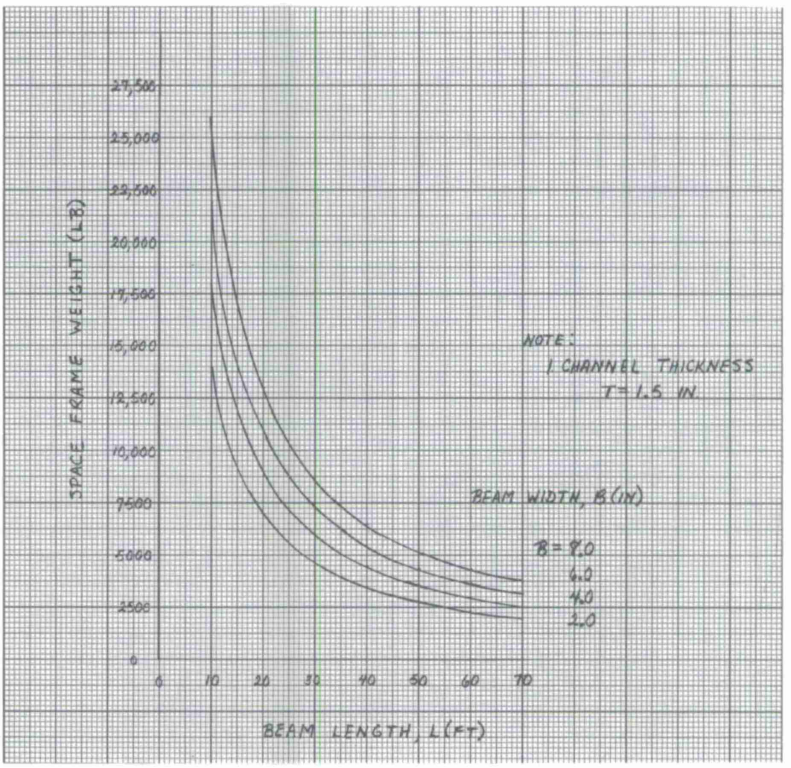

Figure 33. Weight of space frame for 550-ft-diameter radome designed to resist 130-mph wind versus length of individual beam.

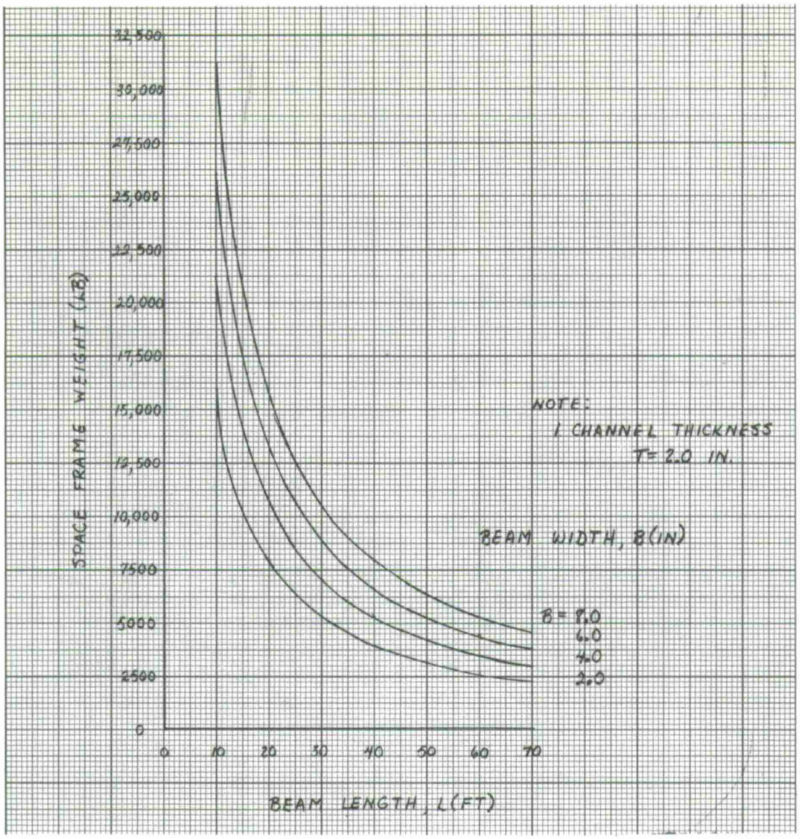

Figure 34. Weight of space frame for 550-ft-diameter radome designed to resist 130-mph wind versus length of individual beam.

d) Method of Selection of Optimum Beam Dimensions for 550-ft-Diameter Space-Frame Radome

The selection of optimum beam dimensions for use in the CAMROC 550-ft diameter space-frame radome when exposed to a 130-mph wind must depend on a judicious balance between optical blockage, frame weight, and maximum length beam. Although an absolute minimum in optical blockage is eminently desirable, the weight penalties incurred in securing the last fractional decrease in blockage must be considered. Also, the difficulties associated with fabricating membranes and erecting the radome frame with large length beam components (beam lengths in excess of 40 ft) must be taken into account

If a range of practical beam lengths is fixed along with a channel thickness and yield stress, then it is seen from Figures 23 to 31 that for a constant length, the minimum optical blockage is obtained for a minimum beam width. Under a condition of fixed length, the minimum beam width also gives a minimum weight.

If an absolute minimum optical blockage is necessary, then the minimum width beam at maximum yield stress, channel thickness, and length is required.

It is noted that the optical blockage minima tend to be relatively flat. Thus, if the beam length or frame weight is considered excessive for the minimum blockage, then some favorable adjustment can be made without unduly affecting the blockage.

In any case, Figures 23 to 34 permit the rapid selection of the most efficient space frame for the CAMROC application once a range of acceptable beam lengths and frame weights is established. The amount of restraint that will have to be provided to prevent column buckling for the selected beam can be determined from Figure 11.

3. Optical Beam Dimensions in Space Frame Consistent with Column-Buckling Requirements

a) Beam Dimensions

The dimensions of the beam element are now limited by the additional requirement that the minimum buckling capacity of the beam be at least equal to the axial load developed in the member by the 130-mph wind. This limitation is used to establish the relation between the minimum acceptable beam width for a given beam length and channel thickness. Equations (36), (17), and (6) are used for this purpose. The results are plotted in Figure 35. Under this restriction the minimum beam depth consistent with the assumed yield stress is calculated. These results are plotted in Figures 36 to 38 for the different yield stresses — 40,000, 60,000, and 80,000 psi — and the different channel thicknesses — 1.0, 1.5, and 2.0 inches.

It is seen from these figures that the increasing beam length demands an increasing beam width to prevent column buckling, and also an increasing beam depth to accommodate the larger axial and bending stresses. As the yield stress of the beam material increases, the required beam depth is lowered. As the channel thickness increases, a smaller beam width will stabilize the column for a given length by increasing the area moment of inertia about the weak axis. Also, the increase in area and area moment of inertia about the strong axis reduces the required depth.

b) Optical Blockage

In Figures 39 to 41, the optical blockage is plotted against the minimum beam width-beam length combination for the various yield stresses and channel thicknesses. For a given channel thickness, the optical blockage improves with an increasing yield stress. This result reflects the smaller beam depth for any length that is associated with the higher yield stresses. Also, as the channel thickness increases, the decrease in beam width and depth for any given length causes a corresponding decrease in the optical blockage.

From Figures 39 to 41, it is seen that within a beam length range of 20-60 ft, a minimum occurs that is relatively flat. Thus, substantially the same minimum optical blockage can be preserved for minor changes (5 to 10 ft) in the beam length.

c) Frame Weight

The weight of the space frame is plotted as a function of beam width, length, and channel thickness in Figure 42. Again, because the lacing between the separate channel sections has not been included, the frame weight is independent of the height.

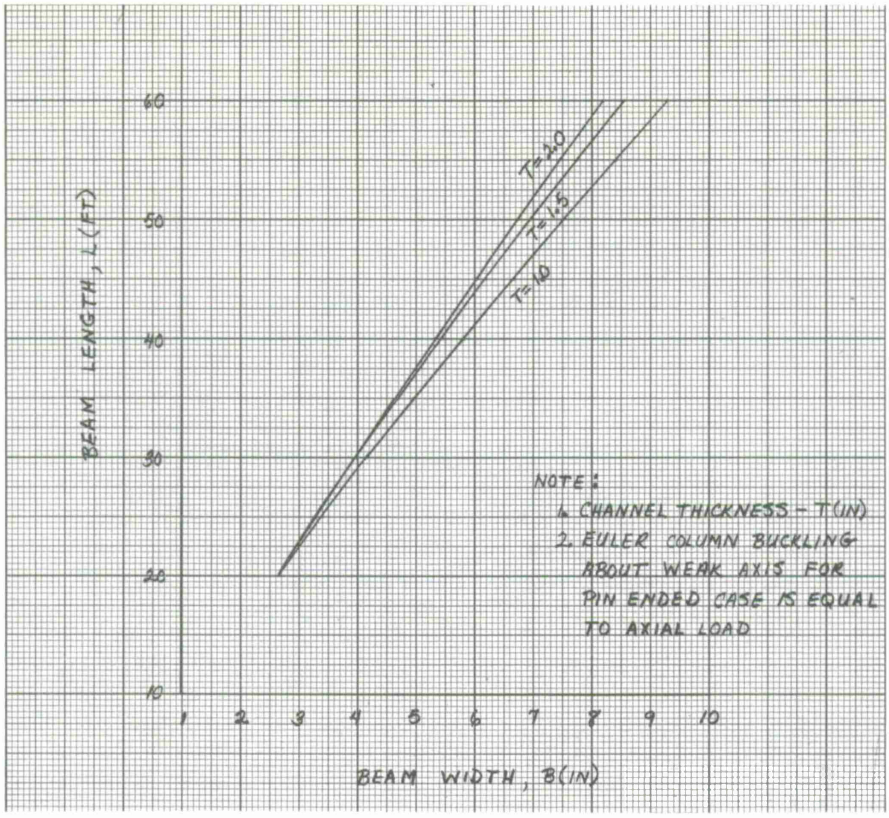

Figure 35. Minimum beam width versus beam length in 550-ft-diameter space-frame radome required to resist 130-mph wind.

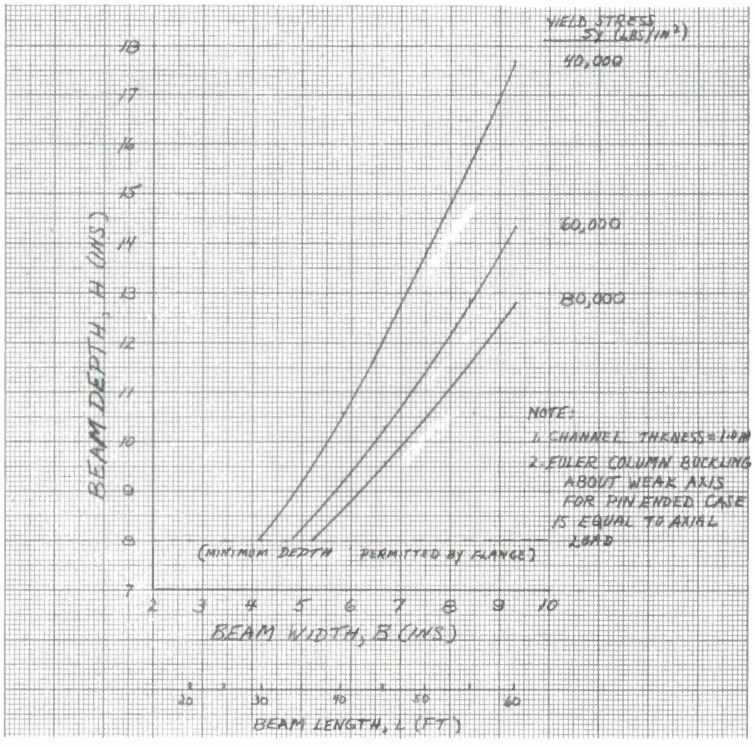

Figure 36. Minimum beam depth versus constant beam width and length for beam element in 550-ft-diameter radome required to resist 130-mph wind.

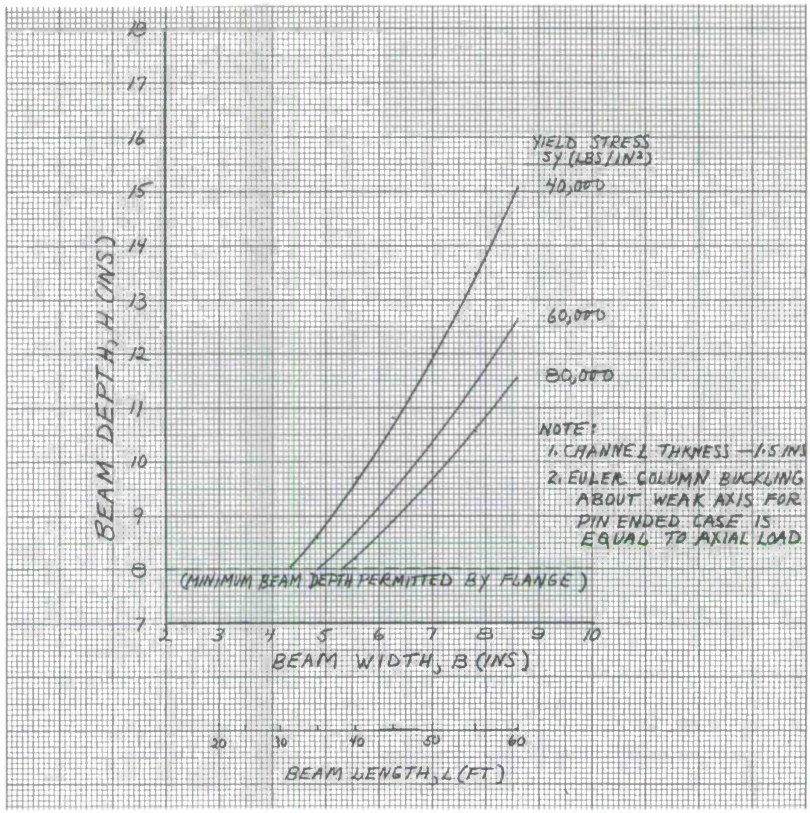

Figure 37. Minimum beam depth versus constant beam width and length for beam element in 550-ft-diameter radome required to resist 130-mph wind.

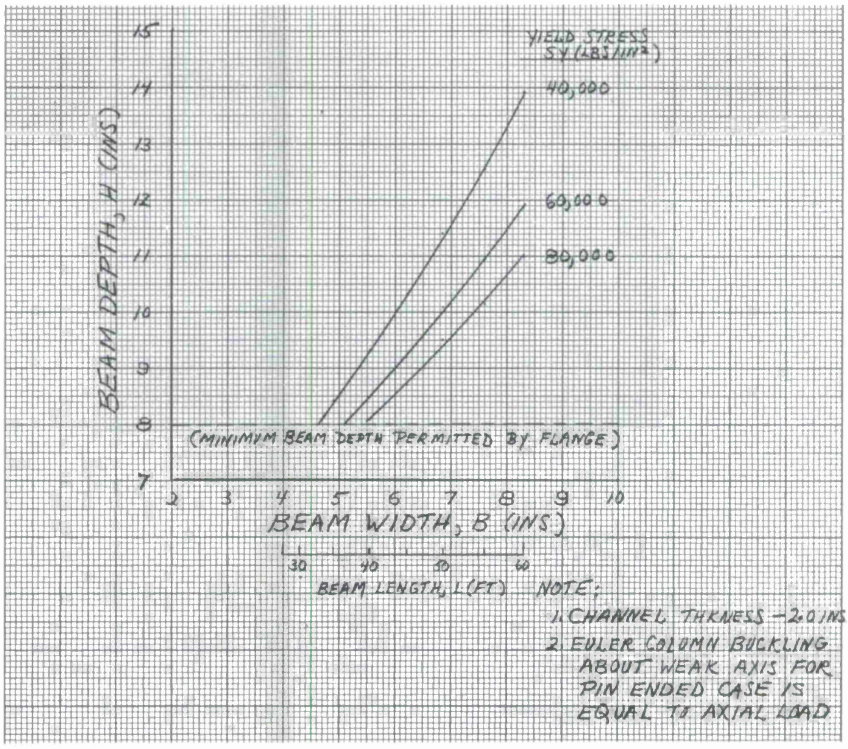

Figure 38. Minimum beam depth versus constant beam width and length of beam element in 550-ft-diameter radome required to resist 130-mph wind.

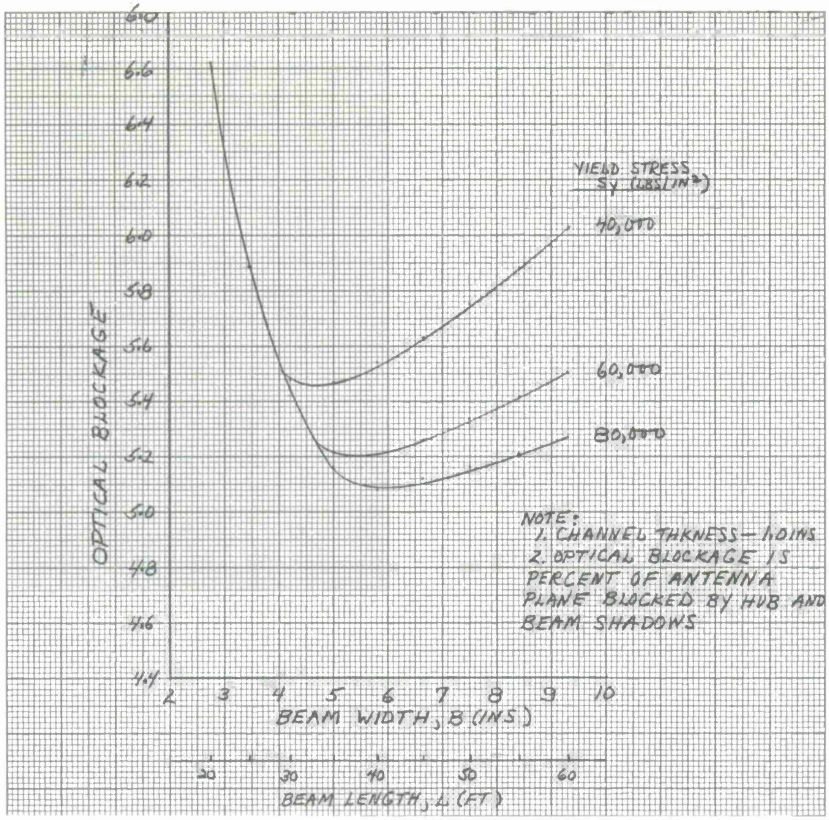

Figure 39. Optical blockage of frame versus width and length of individual beam in 550-ft-diameter space-frame radome designed to resist 130-mph wind.

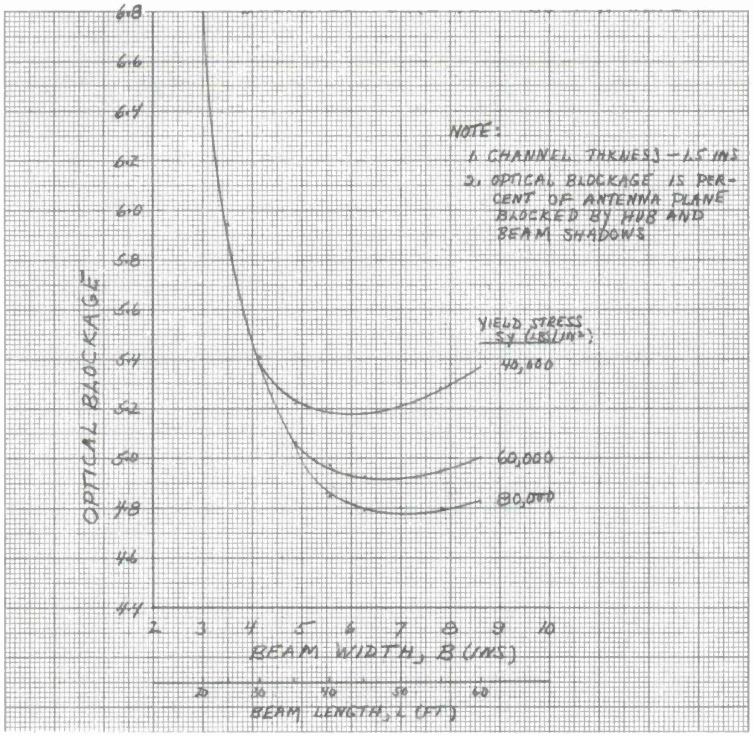

Figure 40. Optical blockage of frame versus width and length of individual beam in 550-ft-diameter space-frame radome designed to resist 130-mph wind.

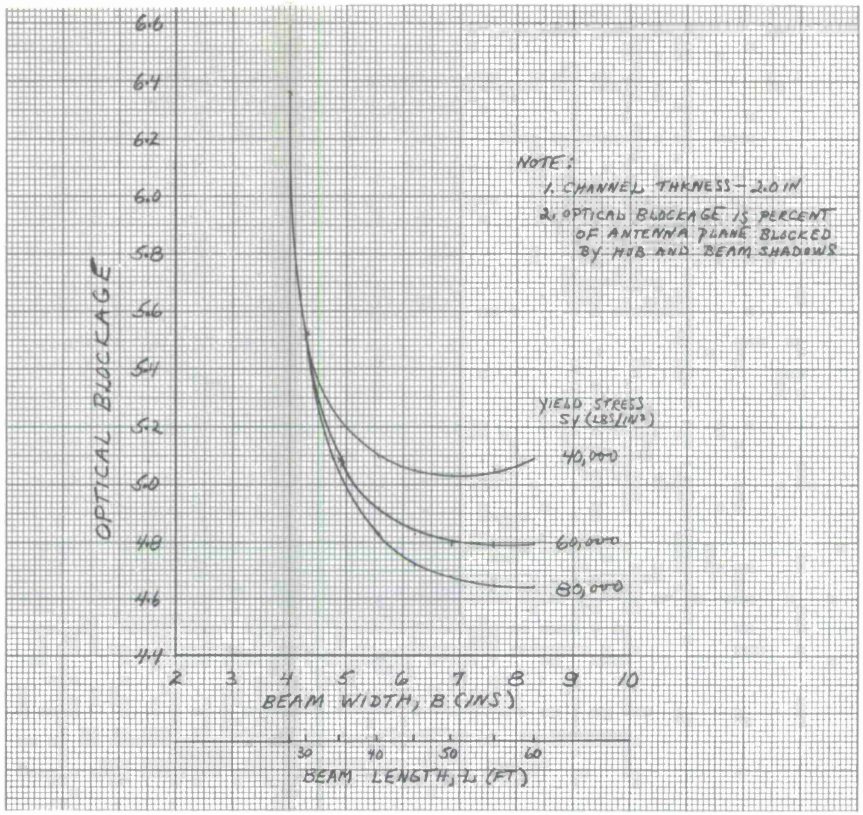

Figure 41. Optical blockage of frame versus width and length of individual beam in 550-ft-diameter space-frame radome designed to resist 130-mph wind.

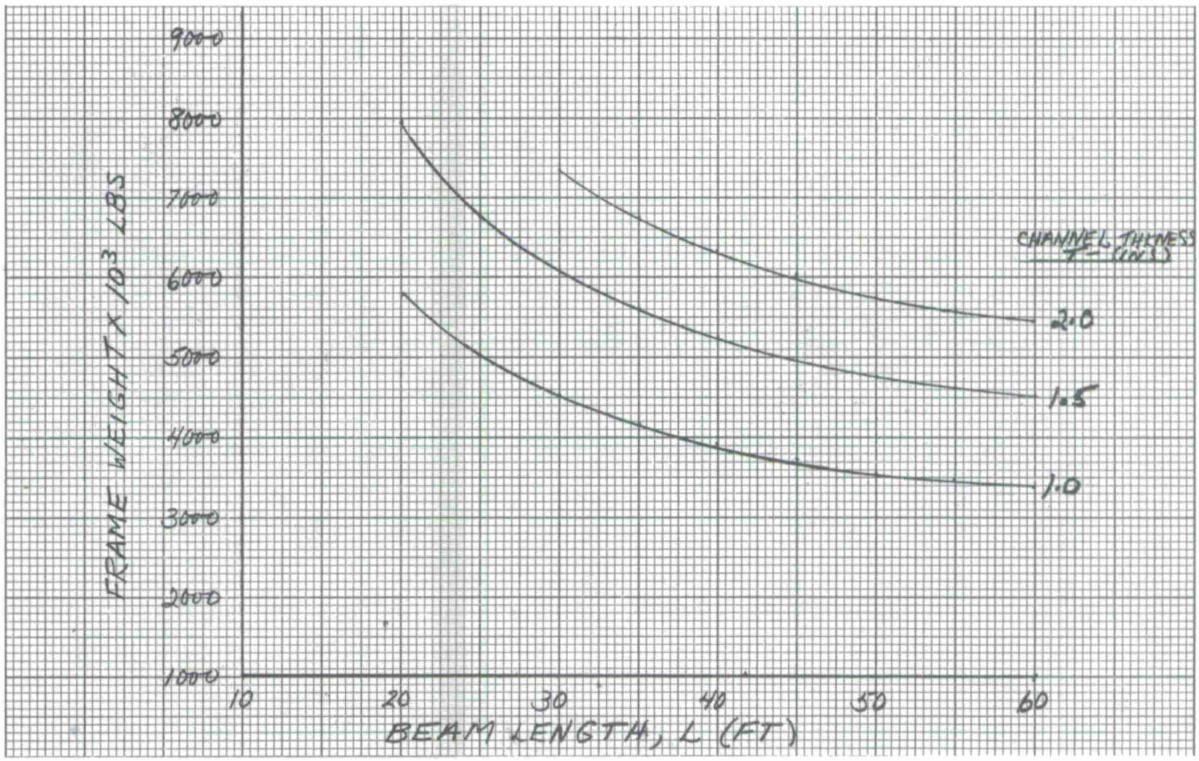

Figure 42. Weight of space frame required to resist 130-mph wind versus beam length for 550-ft-diameter radome.

The total length of beam is the most influential parameter in determining the space-frame weight. Because this parameter varies inversely with the length of the individual component, the frame weight is caused to decrease with increasing beam length.

d) Method of Selection of Optimum Beam Dimensions for 550-ft-Diameter Space-Frame Radome

The selection of optimum dimensions for the beam element in the space frame depends on establishing a compromise between frame weight, maximum length beam, and optical blockage. The maximum length beam will be restricted by the cost and capability of fabricating the membrane panels, while an acceptable frame weight will be influenced by cost and erection procedures. Once a tolerable range of these parameters is specified, then the minimum optical blockage that can be developed under these specifications can be obtained from Figures 35 to 42.

6. COMPUTER STRESS ANALYSIS OF RADOMES

A computer stress analysis of radomes entitled STAR for STress Analysis of Radomes is in the process of being developed and should be available within several months. When completed, this will permit a complete stress analysis of various candidate geometries for the CAMROC 550-ft-diameter space-frame radome using the model 360 computer.

The procedure will be as follows:

a) Develop the complete radome geometry from a small batch of input vertex points and beam members that fall on a surface element (approximately 1/90 of the complete radome surface area), which is repeated continuously over the radome surface.

b) Using the known pressure distribution about the surface of the radome and an assumed cross-section configuration of the beams, develop the axial loads acting in each beam member in the frame by means of the STAIR computer program.

c) Determine the transverse load and load distribution from the local pressure and the geometry of the two triangles adjacent to each beam in the frame.

d) With these loads perform a beam-column analysis for every member in the frame to ascertain the maximum stress and critical column-buckling load for each member.

e) Increase the cross-sectional dimensions of the beam members in the frame in those areas where the stresses are high; decrease the cross-sectional dimensions in those areas where the stresses are low. All changes will be maintained consistent with column-buckling requirements.

f) Repeat steps (b) to (e) until the procedure converges to constant cross-sectional dimensions for each beam member.

g) Calculate the optical blockage for each final geometry-beam member combination.

After a selection of different geometries has been analyzed in this fashion, several of the most promising will be extensively investigated using the more precise FRAN computer program.

The accuracy of the computer stress analysis suggests that the stress results be carefully examined to see if any substantial advantage can be accorded to the space-frame design through reducing still further the dimensions of selected beam members and thus permitting these members to be stressed into the plastic region. The relative infrequency of the design winds and the modest distortions in the frame that would result should be balanced against the anticipated advantages accruing to the antenna over its life span.

Also, some consideration should be given to revising the geometric pattern of the space frame over that portion of the radome surface area where a change in the basic length will yield improvements in the optical blockage. These length changes could be compensated for by adjusting the beam depth or by using interconnecting wires in the selected area.

7. REMARKS

Although the optical blockage calculated in this report does index the electromagnetic performance of the radome, the precise electromagnetic behavior is determined by other methods. The most promising beam-member dimensions developed in this study will be submitted for precise electromagnetic calculations.

Present indications are that the estimated design wind speed of 130 mph, which was used in the development of the Haystack radome, is on the high side. However, it is felt that the reduction in design wind speed will not significantly influence the relative merits of the different geometry-beam-member combinations reported herein. In any event the calculations are readily performed for any wind speed.

The assumption of pin-ended joints is severe and leads to conservative stress results and column-buckling loads. A more precise estimate of end fixity can be developed through a comparison of STAIR and FRAN computer runs.

At some future date, several different cross-sectional configurations will be evaluated. A box design consisting of two identical channel sections joined at the midline will probably be considered.

It is recognized that if the total frame weight is relatively unimportant, then in the limit a solid cross section is always the most efficient. The increase in area and moments of inertia effected by a solid section will permit some reduction in the cross-sectional dimensions and thus an improvement in the optical blockage.

If it is decided that the antenna will operate for longer periods over certain areas of the sky or that the data from certain portions of the sky are more significant, then this bias can be built into the radome. The radome areas of major viewing importance can probably be rendered more efficient at the expense of areas of less importance.

ACKNOWLEDGMENT

I wish to thank Mrs. Elaine Shea for her very capable assistance in developing the computer program used to generate the information contained herein and also for plotting the enclosed graphs.

ANNEX 7

CAMROC MODEL PROGRAM

CAMROC WORKING MEMORANDUM

September 1966

Prepared by

S. Dean Lewis and E. A. Witmer

Aeroelastic and Structures Research Laboratory
Department of Aeronautics and Astronautics
MIT

BACKGROUND DISCUSSION

The present effort involves the design, construction, and testing of an appropriate space-frame radome model to provide, among the objectives, buckling data to check both present and in-development prediction methods. Following preliminary study and discussions with the CAMROC Radome Structural Committee, the following (tersely listed) decisions pertaining to the subject model were reached:

1) TTR random space-frame geometry.

2) 14-ft model diameter.

3) At least 45° half-angle cone intercept on sphere.

4) Straight rectangular cross-section beams fixed rigidly to hubs.

5) 7075-T6 beam material selected for greatest ratio of yield strength to modulus of elasticity.

6) Hubs of hardened SAE 4150 steel with inner and outer disks, beveled to receive beams.

7) Two #4-40 bolts rigidly attach each beam end to a hub. Special bolts of SAE 4037 steel, 170,000 psi min. ult., 2200-lb double shear, 0.065-inch smooth cylinder, diameter tolerance 0.1075 to 0.1120.

8) Beam cross section 0.200×0.313 inch allows model to buckle with normal load of between 100 and 200 lbs per hub joint.

9) Preliminary testing with 64 hubs equally loaded.

10) Specific model being built will have 64 loaded hubs, 57 intermediate hubs, 40 terminal hubs attached rigidly to mandrel, and 440 beams.

11) Large steel mandrel is needed to support model during construction and testing, and able to be assembled in MIT Building 41.

The design for the radome model is based upon providing a small space frame that can yield experimental measurements to verify analytical techniques. The features of the full-scale radome important to buckling are accurately represented by the test configuration. Four areas of special consideration, based on previous model testing in this laboratory, are:

(a) seek an initial condition of zero stress in the model,
(b) joints should lie on the same spherical surface,
(c) seek geometric continuity of the members at the joints, and
(d) model to be large as possible to increase construction accuracy.

The first three items listed involve design of the hub (the fitting that connects the members together at joints). Of several possible construction methods available, the

best seemed to involve a pair of flat disks with the beam ends clamped in between. With beams curved to lie in the spherical surface, each would come tangentially into a hub and it would be a simple matter to fasten every beam end with two bolts in double shear. In fact, some previous model work had been done with curved beams.

However, it was decided that in spite of increased model-construction complexity and cost, the model should be built with straight beams that are representative of full-scale radome-construction techniques. While this decision slightly simplified beam construction, it has greatly increased the complexity of design and construction of the hubs.

The last item (d) above, model size, was limited by the space available in the ASRL laboratory. The model chosen represents a part of a 14-ft-diameter sphere and in fact covers the spherical surface within a cone of half angle 42.7° to the lowest row of unsupported hubs, or 52.0° to the lowest row of anchor hubs.

In selecting a beam material to study elastic buckling, it is desirable to obtain a high ratio of yield strength to modulus of elasticity. The most promising materials considered are listed as follows:

Item	Material	f_{yp}	E	f_{yp}/E
1	7178-T6, T651	78,000 psi	10.4×10^6 psi	7.5×10^{-3}
2	7075-T6, T651	69,000 psi	10.4×10^6 psi	6.6×10^{-3}
3	4340	162,000 psi	29×10^6 psi	5.6×10^{-3}
4	4150	135,000 psi	29×10^6 psi	4.6×10^{-3}

Of these materials, Item 1 is not readily available commercially. Item 2 was therefore selected. While beams could be machined from plate stock to the beam geometry, it was considered less expensive to buy a minimum order for special rolling from Alcoa (300 lbs) and have it delivered in the desired hardness. The order was placed through Edgcomb Steel of New England, Inc. The aluminum alloy has the further advantage over steel that even in the hardened condition it can still be machined easily.

Having selected aluminum alloy for the beam material, then the cross sections were determined from equivalent shell calculations. While the full-scale CAMROC radome may be designed for lower pressures, practical considerations of model construction indicate a buckling pressure close to 1 psi. Figure 6 of CAMROC Technical Memo. No. 6 dated 10 May 1966 provides a graph for beam cross-section dimensions for this model. From this graph, the most appropriate rectangular dimensions are 0.2 inch wide by 0.3 inch deep. Consideration of a typical hub-panel geometry indicates that the 1-psi design pressure loading will be equivalent to concentrated loads of about 100 lbs per hub for the subject model. Since 64 hubs are to be so loaded, a total force of over 6000 lbs will be required to cause buckling. Although there was an expressed

desire for a larger ratio of depth to width on the beams, this was not feasible for the contemplated mechanical beam-to-hub attachment if the beams were to have simple rectangular shapes without thickened ends.

Euler buckling of individual beams in this model structure, based on a rigid-end attachment at the hubs, is calculated to occur at the following loads:

Beam length	Euler buckling load
7.91 inches (shortest)	1312 lbs
13.15 inches (longest)	475 lbs

compared with a compressive nonbuckling strength of 4260 lbs for the beam material. Connection of beam to hub was provided (adequately) by two #4 bolts in double shear. This connection was computed to carry 2080 lbs, limited by beam material at the first bolt hole. The bolts were separated by 0.375 inch in order to give adequate end rigidity to delay buckling about the more flexible axis. For hub construction AISI 4150 steel, heat treated to Rockwell C 33, was selected. This material exceeds the strength requirements for bearing but will be useful in the intended construction procedure wherein the beams will be drilled in place through the hubs. Also, it is anticipated that beams could be replaced after a model has been buckled, and the hubs reused.

Before ordering beam and hub materials, sample hub-beam models of both longest and shortest beams were tested under compressive loading. While it is not difficult to calculate the strength of such a joint, it was uncertain what end fixity would be obtained. These models were mounted in the testing machine with the hubs rigidly fixed and the beam material initially under no bending load. If the buckling load for rigid-ended beams is taken as

$$L_B = \frac{4\pi^2 E h^2 A}{12\,\ell^2} = 4\pi^2\,\frac{EI}{\ell^2} \quad ,$$

where E is Young's modulus of elasticity, h the beam width, A the beam cross-sectional area, and ℓ the beam length to outer bolts, then one may compare the measured to the theoretical buckling load as

$$\epsilon = \frac{L_B \text{ measured}}{L_B \text{ calculated}} \quad .$$

For the short beam, measured buckling loads were 1290 and 1305 lbs, while for the long beam, measured buckling loads were 470 and 435 lbs. The last-mentioned load was disregarded, owing to an initial beam curvature incurred during manufacture. Values of ϵ were then as follows:

Beam	ϵ
Long beam	0.992
Short beam	0.988

Aside from achieving a close approximation to the theoretical buckling load, it was also observed that no end failure occurred, even when the beam center had laterally displaced by about 1/2 inch. Therefore, it was concluded that the hub-to-beam connection design is adequate.

Lincoln Laboratory supplied position data in both rectangular and angular coordinates for all the hubs of interest on a 14-ft-diameter sphere for the TTR random-geometry configuration. With these and other data, it was possible to select the exact geometry of the model, including the locations of the 64 hubs (uniformly distributed about the north pole) that are to be loaded, 57 intermediate hubs, and 40 hubs to be anchored rigidly to the mandrel. In addition, detail design information was extracted and an order was placed on July 22, 1966, with the F. W. Dixon Company to manufacture a complete set of the required hubs together with necessary spares. In all, 196 hubs were ordered, of 14 different kinds. Each is made in two parts, an upper and a lower hub disk. These hubs contain beveled surfaces to meet the individual beams at the correct angle, with an angular tolerance limit of $\pm$ 4 min in order to minimize initial bending in the beams.

It was decided that construction of the model would require a mandrel to support all hubs accurately and rigidly in position. The beams will then be drilled, reamed, and bolted in place. Finally, when the model radome has been completed, it will be released from the mandrel except for the 40 anchor hubs around the base. The mandrel will also be useful as a reference for the measurement of hub deflection under load and for auxiliary use during the loading procedure. This mandrel thus becomes a very important part of the test arrangement. The central part of the mandrel design is a spherical dished head of 76-inch radius. This is a standard item commonly used in boiler construction. It provides a surface that is located 8 inches inside the radome surface. Around the perimeter of the dished head is a flat machined surface that will support the anchor hubs. The mandrel is large and heavy and had to be designed for disassembly into elements small enough to be entered through the loading doors at Building 41, MIT. It will weigh approximately 6000 lbs. This mandrel was ordered from Hodge Boiler Works on August 12, 1966.

A large template, guided by the machined outer surfaces of the mandrel and working in an angular coordinate system (latitude and longitude), will be used to locate the hub supports on the mandrel and also to adjust the hubs into place during the manufacture of the radome structure. This template has not as yet been designed. It probably will be built in the ASRL machine shop.

The support system (steel weldments) for the anchor hubs has been designed and the material is on order. This will also be built in the ASRL machine shop if feasible.

The hub supports for the 64 loading and 57 intermediate hubs have been designed and the parts have been ordered. These items are required to hold the hubs rigidly during manufacture and to provide limits to prevent excessive damage to the model when it buckles. They also are intended to be used to reestablish the radome surface during model repair or if other model beams are to be tested.

In order to lift the mandrel into its position and onto its leg supports, lifting pads are being attached to the ceiling in the laboratory. Three lifting stations around the perimeter will carry 2-ton chain hoists. A central lifting station will assist during assembly of the mandrel.

PRESENT STATUS

1) Special #4-40 bolts were ordered 6-1-66 and were delivered 8-26-66.
2) Aluminum 7075-T6 beam material which was ordered 6-14-66 for August delivery was delivered on 9-27-66.
3) Hubs ordered 7-22-66 for delivery on 9-16-66, but most probable date is now 10-15-66.
4) Steel mandrel ordered 8-12-66 and promised latter part of October.
5) Material for hub supports ordered and expected before end of September.
6) Template yet to be designed.
7) Loading rig yet to be designed.
8) One lifting pad attached to ceiling; others to be completed by end of September.

ANNEX 8

THEORETICAL INVESTIGATION ON BUCKLING OF RETICULATED RADOMES

CAMROC WORKING MEMORANDUM

Prepared by

Howard Simpson

SIMPSON GUMPERTZ & HEGER, INC.

1. INTRODUCTION

1.1 General

The investigation reported herein constitutes the first phase of an analytical study of the buckling behavior of reticulated radomes and of their load-deformation characteristics. The scope of this phase is as follows:

a) Derivation of the governing nonlinear algebraic equations expressing the end forces acting on a bar in terms of its end displacements, and formulation of the problem for solution by a modified existing computer program for linear analysis of structures.

b) Selection of an available large-capacity linear analysis program, and formulation of the required modifications in the selected program.

The derivation of the governing nonlinear equations* and the method of solution of these equations are discussed in Section 2; the selection of the computer program and the required modifications are discussed in Section 3. The proposed extension of this effort is described in the last section.

1.2 Historical Background

Nonlinearity in the behavior of space-frame structures under static loads is due either to nonlinearity in the material or to the change in the geometry of the structure caused by its own deformation. The latter, referred to as geometric nonlinearity, is especially significant for shell-like structures such as space-frame domes.

Although a number of large reticulated domes have been built in the past few years, the methods of analysis for such structures still consist, in general, of establishing an analogous homogeneous shell that can be analyzed by the use of the existing solutions for continua. This method is considered adequate for linear analysis and for design purposes if general stability of the dome can be guaranteed. Wright [1]† and Buchert [2] have applied this analogy to the determination of the buckling load of reticulated structures; however, it is unlikely that the method has sufficient accuracy for the economical design of large structures.

The snap-through buckling of ideally hinged reticulated domes has been studied by Besseling [3], Aguilar [4], and Carpenter et al. [5]. In reference [5] the solution to the problem is obtained by first solving the linear problem. Next, the bar forces are corrected so that equilibrium is satisfied in the deformed state. This correction causes a further deformation that in turn causes a second correction to bar forces. Repetition of this operation will yield the solution to the nonlinear problem if it converges.

*The details for the derivation of these equations are presented in a supplementary report prepared for CAMROC, but are not included here.

†Numbers in brackets refer to entries in the list of References.

For framed structures undergoing small displacements and rotations, the elastic instability load has been determined by numerous investigators employing various techniques. A recent survey of these techniques is presented in reference [6]. Chu [7] and Absi [8] derived the nonlinear equations for elastic buckling of frames under conditions of small displacements and rotations and discussed the behavioral characteristics of these equations in detail. The problem of elastic stability of plane frames using finite deflection theory has been investigated by Saafan [9], who neglected the flexural shortening of the bar. The inclusion of flexural shortening was studied for plane structures by Williams [10], who investigated the instability of a shallow toggle both mathematically and experimentally. He indicated that a very close agreement can be achieved between the load-deformation relationship established theoretically and that obtained experimentally if the flexural shortening is included in the analysis.

The problem of finite deflection of space-frame structures has been investigated by Johnson and Brotton [11]. The governing nonlinear equations are derived neglecting the flexural shortening of the bars and the effect of axial load in the bars on their flexural stiffness. The solution is obtained by first performing a linear analysis. Since the initial solution does not satisfy the applied load, a correction solution is obtained by applying the unbalanced forces and performing another linear analysis. This process is repeated until the unbalances are sufficiently small.

The level of investigations performed is insufficient for an adequate study of the buckling behavior of reticulated radomes and their load-deformation characteristics. The available theories are not general enough for this purpose. For the most part, they are developed for plane structures or involve approximations that cannot easily be justified for large reticulated radomes. Another point of interest is that the volume of numerical results accompanying these investigations is very small. Consequently, many of the questions that could have been answered by analyses of coarse mathematical models are yet to be investigated. The insufficiency of numerical investigations may be related to the lack of sufficiently rapid methods of solution for nonlinear equations.

2. DERIVATION OF GOVERNING EQUATIONS

2.1 Introduction

The governing nonlinear equations for finite deformation of a linearly elastic bar are derived in terms of its end displacements and end rotations. In this derivation the bar is assumed to be composed of linearly elastic material under a condition of small strains. The deformation of the bar is assumed to obey the Bernoulli-Navier approximation of the simple-beam theory.

In the following sections of this chapter the governing nonlinear equations are discussed; a method of solution, which may be considered an extension of Newton's method for finding roots of polynomials, is presented; and the application of this method to the solution of the governing equations is described.

2.2 Formulation of Nonlinear Equations

The approximations involved in the derivation of the nonlinear equations that govern the deformation of an elastic bar are as follows:

1) The bar is composed of linearly elastic material.

2) The bar is prismatic and homogeneous.

3) The deformation of the material is in a state of small strains.

4) The Bernoulli-Navier approximation for the deformation of a simple beam holds. (This includes the neglecting of the shear deformations.)

5) The torsional buckling of the bar and the local buckling of its components do not occur; furthermore, the bar is free to warp.

The nonlinearity is introduced by the finite end displacements of the bar and by the inclusion of the effect of the axial load in the bar on its stiffness.

The finite displacements of the bar are assumed to produce moderate, but not very large, rotations. This limitation on the rotation of the bars is equivalent to the approximation involved in neglecting the square of the rotations of the bar when compared to unity. For determination of prebuckling deformation configurations of the structure, this approximation seems quite valid. The error involved will probably demonstrate itself when post-buckling configuration is being investigated. Even then a stressed configuration with an intrinsic coordinate system may be adopted.

The effect of the axial load in bars on their stiffnesses and flexural shortening produces a very complicated form of nonlinearity.

The following equations present the stress resultants at an end of a bar in terms of the displacements and rotations of both ends of the bar (see Figure 1 for notation*):

$$F_1 = -\frac{AE}{L}\left[u_r - u_1 + \frac{1}{2L}(v_r - v_1)^2 + \frac{1}{2L}(w_r - w_1)^2 + \frac{L}{8}\left(\theta_{z1}^2 + \theta_{zr}^2 + 2\theta_{z1}\theta_{zr}\frac{\omega_z}{\phi_z}\right.\right.$$

$$\left.\left. + \theta_{y1}^2 + \theta_{yr}^2 + 2\theta_{y1}\theta_{yr}\frac{\omega_y}{\phi_y}\right) + \frac{L}{16}\,\xi_z(\theta_{z1} + \theta_{zr})^2 + \frac{L}{16}\,\xi_y(\theta_{y1} + \theta_{yr})^2\right] , \tag{1.1}$$

*The usual symbols A, E, G, I, and J designate, respectively, cross-sectional area, Young's modulus, shear modulus, and moments of inertia for flexure and for torsion.

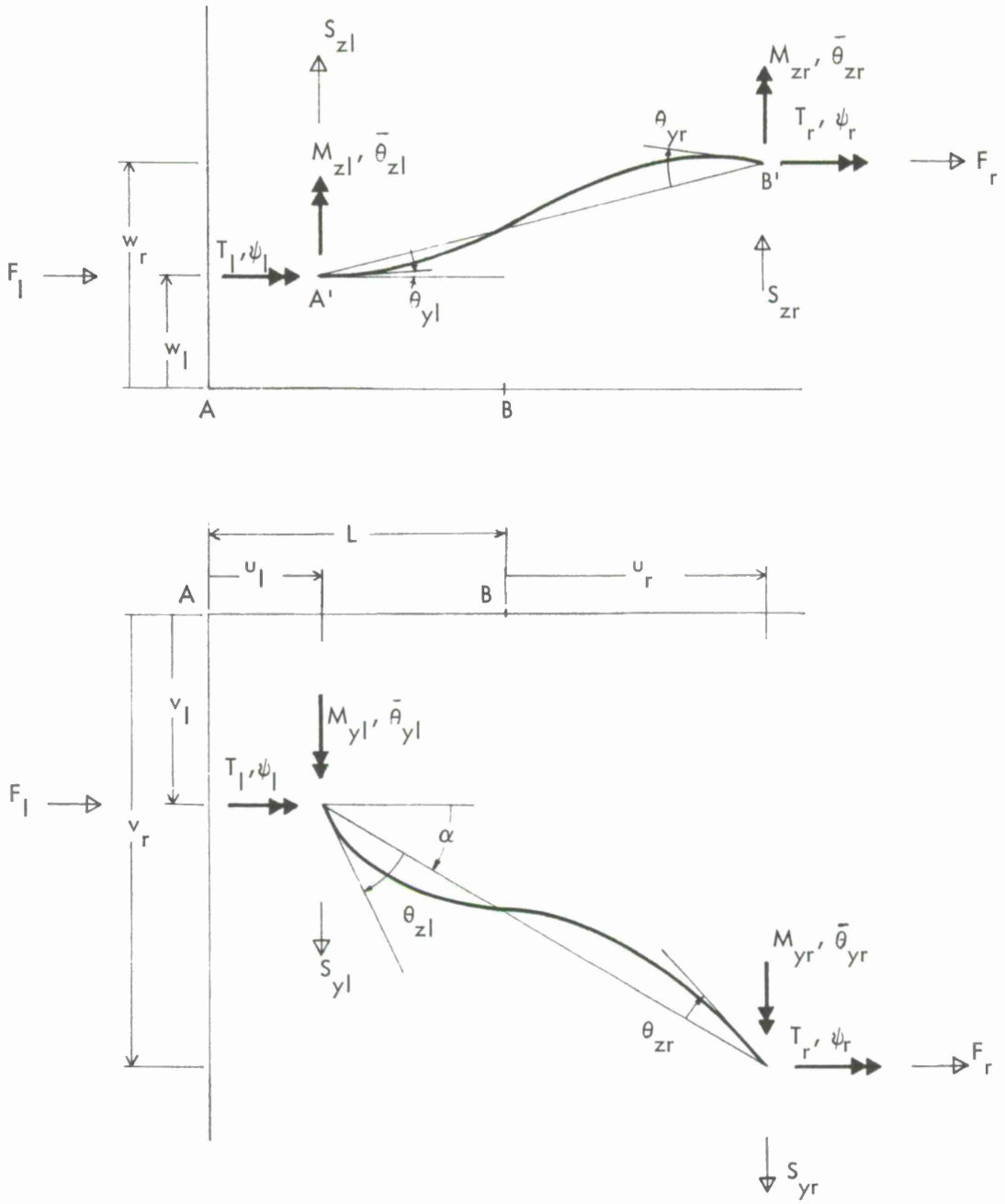

Figure 1. Notation.

$$S_{yl} = \frac{2E I_z}{L^2} \phi_z(\theta_{zl} + \theta_{zr}) + F_L \frac{v_r - v_l}{L} \quad , \tag{1.2}$$

$$S_{zl} = -\frac{2E I_y}{L^2} \phi_y(\theta_{yl} + \theta_{yr}) + F_L \frac{w_r - w_l}{L} \quad , \tag{1.3}$$

$$T_l = \frac{GJ}{L}(\psi_l - \psi_r) \quad , \tag{1.4}$$

$$M_{yl} = \frac{E I_y}{L}\left[\theta_{yl}(\phi_y + \omega_y) + \theta_{yr}(\phi_y - \omega_y)\right] \quad , \tag{1.5}$$

$$M_{zl} = \frac{E I_z}{L}\left[\theta_{zl}(\phi_z + \omega_z) + \theta_{zr}(\phi_z - \omega_z)\right] \quad , \tag{1.6}$$

where

$$\theta_{zl} = \overline{\theta}_{zl} - \frac{v_r - v_l}{L} \quad ,$$

$$\theta_{yl} = \overline{\theta}_{yl} + \frac{w_r - w_l}{L} \quad ,$$

$$\omega_z = \frac{\beta_z L}{2} \cot\frac{\beta_z L}{2} \qquad \text{for axial compression} \quad ,$$

$$= \frac{\beta_z L}{2} \coth\frac{\beta_z L}{2} \qquad \text{for axial tension} \quad ,$$

$$\phi_z = \frac{\beta_z^2 L^2/4}{1 - \omega} \qquad \text{for axial compression} \quad ,$$

$$= \frac{\beta_z^2 L^2/4}{\omega - 1} \qquad \text{for axial tension} \quad ,$$

$$\xi_z = -\frac{\omega_z}{\phi_z} - \frac{\phi_z}{\omega_z}\left(1 + \frac{3\omega_z - \phi_z}{L^2\beta_z^2/4}\right) \qquad \text{for axial compression} \quad ,$$

$$= -\frac{\omega_z}{\phi_z} - \frac{\phi_z}{\omega_z}\left(1 + \frac{\phi_z - 3\omega_z}{L^2\beta_z^2/4}\right) \qquad \text{for axial tension} \quad ,$$

$$\beta_z^2 = \frac{F_1}{E I_z} \qquad \text{for axial compression} \quad ,$$

$$= - \frac{F_1}{E I_z} \qquad \text{for axial tension} \quad .$$

Similarly, other variables may be defined.

The variations of the coefficients ω, ϕ, and ξ with the axial force in the bar are presented in Figure 2. It is important to note that the compression in an unbraced bar cannot be more than four times its Euler buckling load corresponding to simply supported ends. This limit is its buckling load when its ends are fully fixed.

If in the above equations appropriate simplifications are made, they reduce exactly to the equations derived by Chu [7] for the determination of buckling loads of truss members, by Williams [10] for the determination of the behavior of rigid jointed plane frameworks, and by Wah [12] on the buckling of gridworks.

2. 3 Method of Solution

The method of solution of the nonlinear equations consists of approximating them by a sequence of linear equations that can easily be solved numerically. The method consists first of assuming a solution for the nonlinear equations. The linearization is achieved by expanding the nonlinear terms appearing in the governing equations in Taylor series in a neighborhood of the assumed solution and retaining only the linear terms.

The technique involved is demonstrated for the solution of the following system of two simultaneous nonlinear equations:

$$F(x, y) = P_1$$

$$G(x, y) = P_2 \quad , \qquad (2)$$

where x and y are in the independent variables. Assume a solution, say $x = x_0$ and $y = y_0$. If

$$\Delta P_1 = P_1 - F(x_0, y_0)$$

and

$$\Delta P_2 = P_2 - G(x_0, y_0) \qquad (3)$$

do not identically vanish, then a correction to x_0 and y_0 can be obtained by noting that in some neighborhood of point (x_0, y_0)

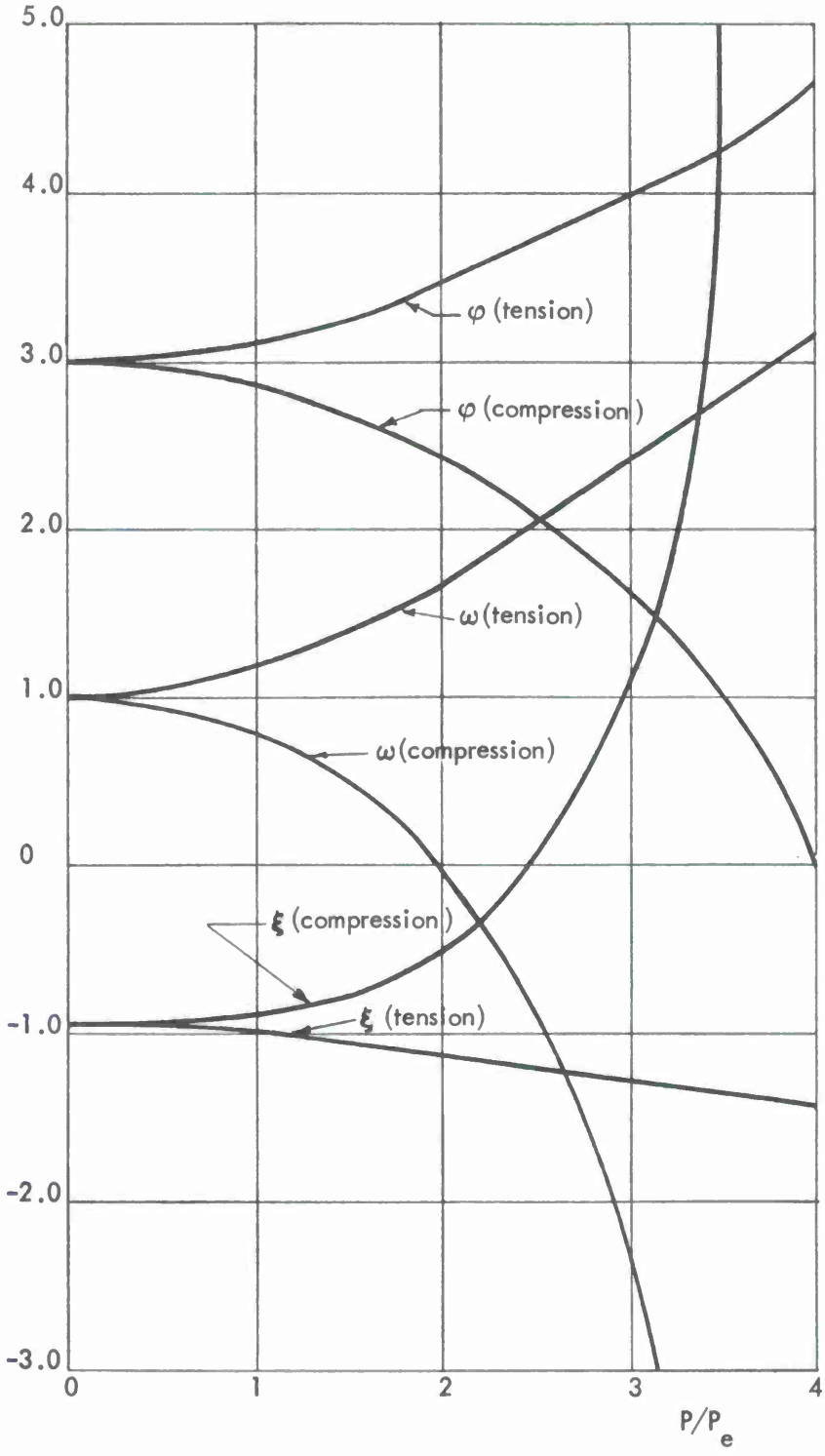

Figure 2. Coefficient ω, ϕ, and ξ vs. axial force in the bar.

$$F(x, y) = F(x_0, y_0) + (x - x_0)F_x(x_0, y_0) + (y - y_0)F_y(x_0, y_0) + \cdots$$

$$G(x, y) = G(x_0, y_0) + (x - x_0)G_x(x_0, y_0) + (y - y_0)G_y(x_0, y_0) + \cdots \quad , \qquad (4)$$

where subscripted functions are partial derivatives with respect to the subscript variables. If system (4) is substituted back into system (2), the following is obtained:

$$(x - x_0)F_x(x_0, y_0) + (y - y_0)F_y(x_0, y_0) + \cdots = \Delta P_1$$

$$(x - x_0)G_x(x_0, y_0) + (y - y_0)G_y(x_0, y_0) + \cdots = \Delta P_1 \quad . \qquad (5)$$

An approximate solution of this nonlinear problem can be found by assuming that $x - x_0$ and $y - y_0$ are small and hence dropping all the higher order terms (quadratic and beyond). The linearized problem can then be solved; the new solution, say x_1 and y_1, can replace x_0 and y_0; and the process can be repeated if desired. This process in most cases converges very rapidly to the desired solution of the nonlinear problem.

Physically speaking, the values of x_0 and y_0 correspond to an assumed deformation configuration. If the set of assumed values is not a solution to the problem, then the unbalanced forces ΔP_1 and ΔP_2 have to be eliminated by an appropriate correction solution, say $x - x_0$ and $y - y_0$. The correction solution is approximately determined from the linearized equations (5). The corrected solution, the sum of the assumed solution and the correction solution, may again be considered as a new assumed solution and correction to this solution can in turn be obtained.

In obtaining the load-deformation relationship, incremental loads can be successively imposed on the structure. Regardless of the previous history, a sufficient number of iterations can bring the numerical solution as close as desired to the "exact solution." Therefore, it is not essential to obtain an accurate solution at each load increment. Since accurate convergence is not required for progressing forward, the load-deformation relationship can be established rapidly by applying only a single correction to the solution of the previous increment and then obtaining the higher corrections to the problem at only a few points on the load-deformation diagram.

The method of solution of Eqs. (1) consists, therefore, of the following:

1) Assume a deformation configuration for all the joints in the piece of structure being analyzed. The assumed configuration may be that obtained for the previous load increment.

2) Compute the end displacements and rotations for each bar.

3) Compute the forces at the ends of each bar. For a given joint, the end forces computed on the basis of the assumed configuration will in general not be in equilibrium with the external loads applied at that joint. Compute the system of unbalanced forces at all joints. If these forces are more than a prescribed limit, the computation proceeds by progressing to step (4); otherwise, the solution is in fact an approximate solution of the problem.

4) The linearized system described later in this chapter is solved, subjected to these unbalanced forces at the joints.

5) The assumed deformation is modified by the calculated corrections and the process can be repeated by considering the modified deformations as assumed values.

A significant feature of this method when it is applied to the solution of nonlinear problems in structural mechanics is possible symmetry of the linearized system. The governing equations of equilibrium of an elastic mechanical system can be written by setting the first variation of the total potential energy equal to zero. In terms of a generalized coordinate system, say x_i, this corresponds to the following relationship:

$$\frac{\partial U}{\partial x_i} = P_i \quad , \tag{6}$$

where

U = the strain energy of the structure,

x_i = the components of the generalized coordinates,

P_i = the components of the generalized force.

In applying the method described herein to the solution of these nonlinear equations, a corresponding linearized system is obtained as follows:

$$\sum_{j=1}^{N} \Delta x_j \frac{\partial^2 U}{\partial x_i \partial x_j} = \Delta P_i \quad . \tag{7}$$

It is obvious that the coefficient matrix $[\partial^2 U/\partial x_i \partial x_j]$ is, in fact, symmetric.

2.4 Linearized Equations

The governing nonlinear equations expressing the end forces of a bar in terms of its end displacements, Eqs. (1), can be linearized by the method discussed in Section 2.3. The linearized stiffness matrix of the structure can then be established from a suitable assemblage of the linearized stiffness matrices of the component members.

In this section the linearized stiffness matrix of a single bar is presented. The details of the derivation of this matrix are given in a supplementary report prepared for CAMROC, but are not included here.

The force-displacement relationships for a single bar express the 12 force components acting at both ends of the member in terms of its 12 end displacement components. In linear analysis, it is expedient to group the expressions relating to either end. Then,

$$\begin{Bmatrix} P_L \\ P_R \end{Bmatrix} = \begin{bmatrix} K_{LL} & K_{LR} \\ K_{RL} & K_{RR} \end{bmatrix} \begin{Bmatrix} D_L \\ D_R \end{Bmatrix} \quad , \tag{8}$$

where P_L is the force vector at the left end and D_L is the displacement vector at that end. It can easily be shown from the equations of equilibrium of the bar that

$$K_{LR} = K_{LL} E^T \quad ,$$

$$K_{LR} = E K_{LL} \quad ,$$

$$K_{RR} = E K_{LL} E^T \quad , \tag{9}$$

where E is the end force transformation matrix defined by the following expression:

$$P_R - E P_L = 0 \quad . \tag{10}$$

To obtain the linearized equations for a nonlinear system, the above relationship must be somewhat modified since the matrix E will also depend upon the deformation of the structure. In fact, Eqs. (10) can be written as follows:

$$P_R - E_1 P_L - E_2 (D_L - D_R) = 0 \quad , \tag{11}$$

where

$$E_1 = - \begin{bmatrix} & 1 & & & & \\ & 0 & 1 & & & \\ & 0 & 0 & 1 & & \\ & 0 & 0 & 0 & 1 & \\ (-w_r^0 - w_l^0) & 0 & L & 0 & 1 & \\ (v_r^0 - v_l^0) & -L & 0 & 0 & 0 & 1 \end{bmatrix} \quad ,$$

the superscript 0 refers to the assumed values, and

$$E_2 = \begin{bmatrix} 0 & & & & & \\ 0 & 0 & & & \mathbf{0} & \\ 0 & 0 & 0 & & & \\ 0 & 0 & 0 & 0 & & \\ 0 & 0 & -F_1^0 & 0 & 0 & \\ 0 & F_1^0 & 0 & 0 & 0 & 0 \end{bmatrix} .$$

Hence, it can be shown that

$$K_{LR} = K_{LL}\, E_1^T + E_2^T \quad ,$$

$$K_{RL} = E_1\, K_{LL} + E_2 \quad ,$$

$$K_{RR} = E_1\, K_{LL}\, E_1^T + E_1\, E_2^T - E_2 \quad .$$

The matrix K_{LL}, which is derived by an appropriate linearization of system (1), is presented in Appendix 1 of this report.

2.5 Discussion

The distributivity of the load was not considered in the mathematical derivation. However, its only effect will be on the value of the end moments corresponding to a deformation configuration and consequently on the resulting unbalanced joint forces. The computer program will incorporate the effect of load distributivity.

3. SOFTWARE DEVELOPMENT

3.1 Introduction

To minimize the magnitude of the required programming effort, it is desirable to base the software necessary for the solution of the linearized system on an existing space-frame analysis program of adequate capacity. The program selected must be well documented and of a nature such that the necessary modifications and extensions can be economically accomplished. Since computer time is an important factor in the proposed application, the program should be very efficient in information handling.

3.2 Selection of Existing Analysis Program

Because of the fundamental difference in the method of formulation, analysis programs based on the flexibility method were rejected a priori. A detailed survey was made of the programs discussed below, all of which, with the exception of GISMO, employ the deflection method of formulation.

1) FRAN is a large-capacity program for the analysis of space-frame structures. The solution is obtained by reducing the stiffness matrix to a triangular matrix; this is an efficient method with relatively small round-off errors. This program, however, is slow and is not completely documented.

2) GISMO consists essentially of mathematical operators for manipulating matrices. It is designed to be used in connection with auxiliary routines to provide its input. For purposes of generality, it ignores the fact that many terms in stiffness matrices for large assemblages are identically zero. As a result, it executes tape search and matrix manipulation for a single row at a time, which causes it to be excessively slow.

3) MAST (an extension of STAIR) is a large-capacity computer program for the solution of assemblages of axially loaded bars and of plate elements carrying in-plane stress resultants. An outstanding feature of this program is that its procedure for partitioning the stiffness matrix for solution is externally read. This requires a manual input preparation that increases its susceptibility to human error, but renders a more efficient method of solution. The conversion of this program to include the analysis of continuous framed structures would involve considerable effort, especially with respect to bookkeeping difficulties.

4) STIFFEIG is a moderately small computer program for static analysis and free vibration analysis of framed structures. Since it works entirely in core, its use is restricted to very small structures.

5) STEIGR is a large-capacity version of STIFFEIG. However, it differs from STIFFEIG in its solution of the static deflection problem, because it obtains the complete inverse of the stiffness matrix for static solutions. This makes STEIGR unnecessarily slow for the proposed application.

6) STRESS is a programming system for the solution of a variety of structural engineering problems, including space frames. A significant feature of this program is its adaptability to modification and expansion. The capacity limitations that exist in modifying and expanding this program are much relaxed by a dynamic memory allocation procedure that provides flexibility in information handling. (This flexibility, however, causes difficulties in gaining access to a bit of information.) As a result of the dynamic memory allocation, the core storage available for the solution process is increased.

7) SIGMA is a program for static and free vibration analysis of structures composed of beams, pinned bars, and "membrane" panels. A unique feature of this program is its generality and its acceptance of infinitely rigid bars and nonsymmetric cross sections. It is written, however, for the ELEA computer system, which is not readily available. Furthermore, this program is not at the present time sufficiently well documented.

The computer program STRESS was finally selected on the basis of its speed, ease of modification, efficiency in information handling, and availability of sufficient documentation.

3. 3 Modifications of STRESS

The required modifications of STRESS to make it capable of solving the nonlinear problems of buckling of reticulated radomes by a sequence of linear approximations is discussed in this section.

STRESS is composed of a number of small subroutines. On the basis of the level of modification required, these subroutines fall into three distinct categories. The first category consists of those that must be deleted; the second category contains those remaining unchanged or with minor modifications; the subroutines that involve major modification or require complete rewriting constitute the third category. The following is a list of the subroutines contained in each category.

Category 1 - Subroutines to be deleted.

a) Subroutines used to restore and save the initial input data for later reuse:

RESTOR
SAVE

b) Subroutines used in the introduction of member releases:

MRELES
FIXM
CARRY
PERMUT
UNPCK
LSTOR

c) Subroutines related to the prescribed member distortions and joint displacements:

MDISTN
JDISPL

d) Subroutine for combining the results of different loading conditions:

COMBLD

Category 2 - Subroutines involving minor or no modifications.

a) Subroutines used for checking input, initialization, etc. :

ITEST
ICNT
CLEAR

b) Subroutines used in connection with the dynamic memory allocator:

START
DEFINE
ALOCAT
RELEAS
REORG
SSLAD
STER
DUMP
FILES
DUMPER
NEWADR

c) Subroutines that transform the member stiffness matrix into global coordinates and set up the lower half of the system stiffness matrix:

TRANS
ATKA
KOFDG
IOFDG
IFDT

d) Subroutines related to the modification of the system stiffness matrix and of the load vector for support joint releases:

JRELES
STEP2
STEP5
BUGER
FOMOD
ADRESS

e) The subroutine related to the solution of the system stiffness matrix:

SOLVER

f) Certain subroutines used in matrix handling and operation:

PACKW
COPY
MAMUL
MATRIP
TTHETA
MAPROD
MAPRDT

Category 3 - Subroutines involving significant modifications or complete rewriting.

a) Subroutines related to input-output phases:

PHAS1A
LISTS
MEMDAT
SIZED
JTDAT
READ
MATCH
DPRINT
SELOUT
ANSOUT
PHAS1B

b) Subroutines used for output error messages; new messages must be included and irrelevant messages must be deleted:

PRERR
PRER2

c) The subroutine that computes axes-transformation matrices (the sections dealing with plane structures must be deleted):

TRAMAT

d) Subroutines that compute member distortions, member forces, support reactions, and loads. These subroutines must be modified to compute the unbalanced joint loads, to check the magnitudes of the unbalanced forces, and to modify the loads and unbalanced forces on the structure, as necessary:

BAKSUB
DEFSUB
AVECT
STATCK
MEMBLD
LOADPC
LOADPS
CASE2
JTLOAD
LINEAR
EFVDTL
STICLD

e) Subroutines used to form member stiffness matrices and to connect various subroutines (these must be completely rewritten):

MEMBER
MEMFOD
MAIN

Note: In the process of modification, a number of subroutines may be deleted or combined to form a smaller number of subroutines. A block flow chart of the modified STRESS program is presented in Figure 3.

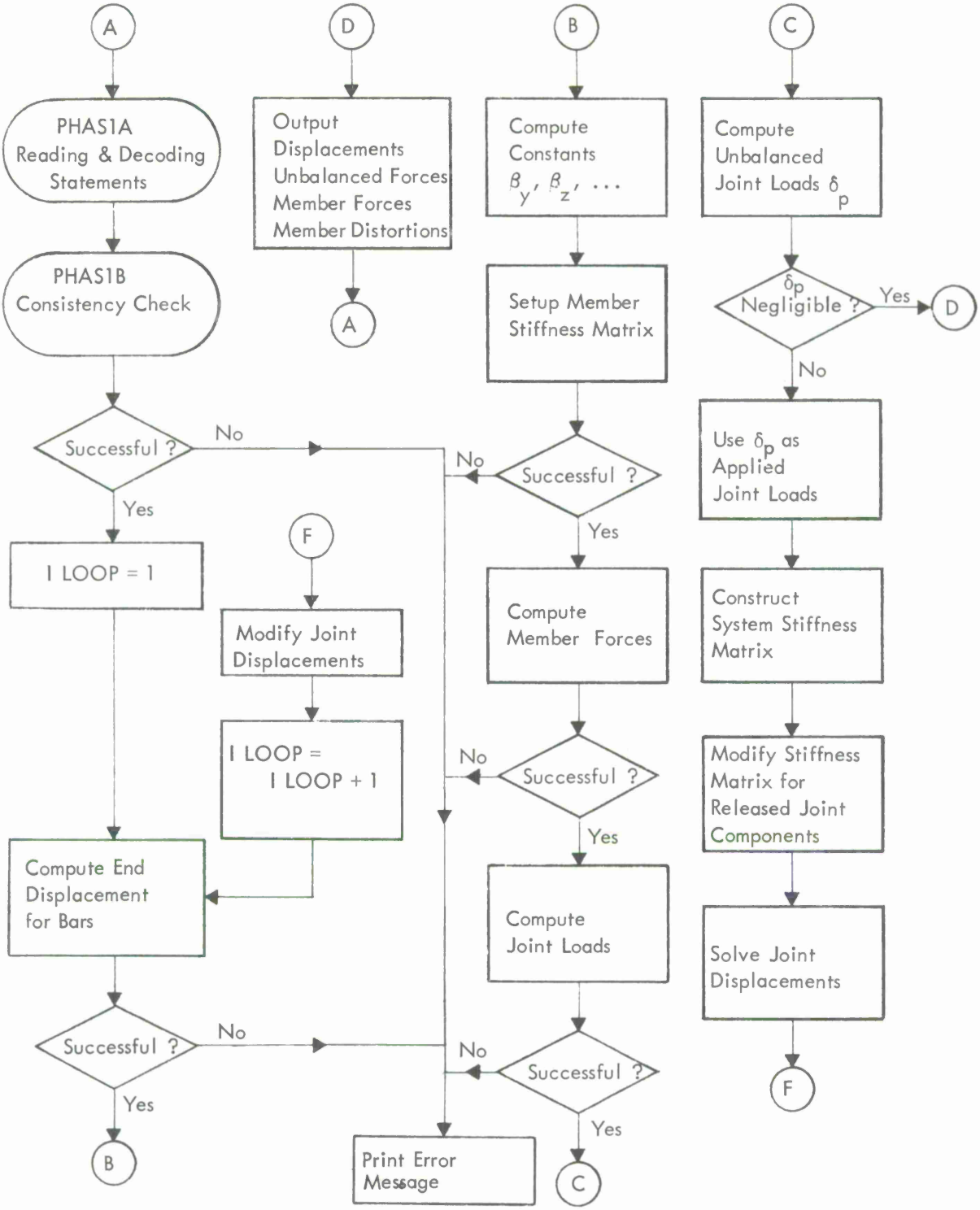

Figure 3. Execution flow chart.

3.4 Additions to STRESS

Only two entirely new subroutines must be added to STRESS. They consist of a subroutine for computing the variables ω_y, ϕ_y, ξ_y, etc., for each bar, and a subroutine to modify joint displacements for the subsequent solution.

4. CONCLUSIONS

The nonlinear equations governing the finite deformations of an elastic bar have been derived. These equations express the end forces of a bar in terms of the components of the end displacements. A method of solution, which is a generalization of the Newton method for finding roots of polynomials, has been presented. The method consists of an iterative solution of a linearized system. The linearized problem may be solved by an appropriately modified available program for linear analysis of structures.

A survey of available large-capacity computer programs for solving linear problems in structural mechanics revealed that the program STRESS is most suitable for extension for the solution of geometrically nonlinear problems.

5. RECOMMENDATIONS

The recommended future work for the continuation of the effort reported on herein can be divided into the following tasks:

TASK 1. Perform the modification and extension of the STRESS program as described in Section 3. The final computer program will be able to establish a branch of the load-deformation diagram for any given reticulated radome with elastic joints. ("Load-deformation diagram" refers to the behavior of a scalar function defining the intensity of the joint loads with respect to a properly defined deformation parameter.)

TASK 2. Test the validity and accuracy of the program and the mathematical model by establishing the load-deformation relationships for a few small structures for which exact solutions are available or can easily be obtained. Perform and test any modifications of the program that are found to be necessary from a study of the results of these applications.

TASK 3. Utilize the mathematical model by calculating the buckling loads and load-deformation relationships for the test structures and comparing them with the corresponding experimental results. The discrepancies between the experimental and theoretical results should be analyzed to determine if simplifications or other refinements should be made in the mathematical model. Additional numerical analyses will be useful in the planning of the subsequent experimental program and in the interpretation of the test results.

6. REFERENCES

1. Wright, D. T., "Membrane Forces and Buckling in Reticulated Shells," J. of Structural Division, ASCE Proceedings, Feb. 1965, pp. 173-201.

2. Buchert, K. P., "Buckling Considerations in the Design and Construction of Doubly Curved Space Structure," International Conference on Space Structures 1966, Blackwell Scientific Publications Ltd., 1966.

3. Besseling, J. F., "Stress Distribution and Jump Phenomenon in Spherical Frameworks under Pressure Loading," MIT Radome Symposium, Sept. 1958.

4. Aguilar, R. F., "Snap-Through Buckling of Framed Triangulated Domes," Submitted for Publication in the Journal of the Structural Division, Proceedings of the American Society of Civil Engineers.

5. Carpenter, W. C., Ely, J. F., and Bramer, C. R., "The Joint Instability of Latticed Structures and Generalized Load," International Conference on Space Structures 1966, Blackwell Scientific Publications Ltd., 1966.

6. Van de Woude, F., "The Elastic Instability of Frames," International Journal of Mechanical Sciences, Vol. 7, 1965, pp. 747-757.

7. Chu, Kuang-Han, "Secondary Moments, End Rotations, Inflection Points and Elastic Buckling Load of Truss Members," Publications, International Association for Bridge and Structural Engineering, Vol. 19, 1959, pp. 17-46.

8. Absi, E., "Systems Hyperstatiques Tridimensionnels et Effet des Efforts Tranchants et Normaux," Publications, International Association for Bridge and Structural Engineering, Vol. 23, 1963, pp. 27-32.

9. Saafan, S. A., Ph. D. Thesis, University of Manchester, 1962.

10. Williams, F. W., "An Approach to the Nonlinear Behavior of the Members of a Rigidly Jointed Plane Framework with Finite Deflections," Quarterly Journal of Mechanics and Applied Mathematics, Vol. 17, 1964, pp. 451-469.

11. Johnson, D., and Brotton, D. M., "A Finite Deflection Analysis for Space Structures," International Conference on Space Structures 1966, Blackwell Scientific Publications Ltd., 1966.

12. Wah, T., "The Buckling of Gridworks," J. of Mechanics and Physics of Solids, Vol. 13, 1965, pp. 1-16.

APPENDIX 1

STIFFNESS MATRIX OF A SINGLE MEMBER

In this appendix the matrix $K_{LL'}$, as defined in Section 2.4, is presented. The following variables are defined for the sake of simplicity of the final matrix:

$$k_{1,1} = \frac{AE}{L} \quad ,$$

$$k_{1,2} = \frac{AE}{L}\frac{v_r^0 - v_1^0}{L} + \frac{2\,EA}{L^3}\Phi_z\left(\bar{\theta}_{z1}^0 + \bar{\theta}_{zr}^0 - 2\frac{v_r^0 - v_1^0}{L}\right) \quad ,$$

$$k_{1,3} = \frac{AE}{L}\frac{w_r^0 - w_1^0}{L} - \frac{2\,EA}{L^3}\Phi_y\left(\bar{\theta}_{y1}^0 + \bar{\theta}_{yr}^0 + 2\frac{w_r^0 - w_1^0}{L}\right) \quad ,$$

$$k_{1,5} = \frac{AE}{L^2}\left[\bar{\theta}_{y1}^0(\Phi_y + \Omega_y) + \bar{\theta}_{yr}^0(\Phi_y - \Omega_y) + 2\frac{w_r^0 - w_1^0}{L}\Phi_y\right] \quad ,$$

$$k_{1,6} = \frac{AE}{L^2}\left[\bar{\theta}_{z1}^0(\Phi_z + \Omega_z) + \bar{\theta}_{zr}^0(\Phi_z - \Omega_z) - 2\frac{v_r^0 - v_1^0}{L}\Phi_z\right] \quad ,$$

where superscript 0 refers to the assumed values of the components of deformation, and Φ and Ω are defined as follows:

$$\Phi_z = \frac{d\phi_z}{d(\beta_z^2)} = -\frac{L^2}{8}\left(1 + \frac{\omega_z}{\phi_z} + \xi_z\right) \quad ,$$

$$\Omega_z = \frac{d\omega_z}{d(\beta_z^2)} = -\frac{L^2}{4}(1 + \xi_z/2) \quad .$$

	δu_1	δv_1	δw_1	$\delta \psi_1$	$\delta \bar{\theta}_{y1}$	$\delta \bar{\theta}_{z1}$
δF_1	$k_{1,1}$	$k_{1,2}$	$k_{1,3}$	0	$k_{1,5}$	$k_{1,6}$
δS_{y1}	$k_{1,2}$	$\frac{4EI_z}{L^3}\phi_z - \frac{F_L^0}{L}$ $+ \frac{L}{EA} k_{1,2}^2$	$\frac{L}{EA} k_{1,2}\, k_{1,3}$	0	$\frac{L}{EA} k_{1,2}\, k_{1,5}$	$\frac{L}{EA} k_{1,2}\, k_{1,6}$ $+ \frac{2EI_z}{L^2}\phi_z$
δS_{z1}	$k_{1,3}$	$\frac{L}{EA} k_{1,2}\, k_{1,3}$	$\frac{4EI_y}{L^3}\phi_y - \frac{F_L^o}{L}$ $+ \frac{L}{EA} k_{1,3}^2$	0	$\frac{L}{EA} k_{1,3}\, k_{1,5}$ $- \frac{2EI_y}{L^2}\phi_y$	$\frac{L}{EA} k_{1,3}\, k_{1,6}$
δT_1	0	0	0	$\frac{GJ}{L}$	0	0
δM_{y1}	$k_{1,5}$	$\frac{L}{EA} k_{1,2}\, k_{1,5}$	$\frac{L}{EA} k_{1,3}\, k_{1,5}$ $- \frac{2EI_y}{L^2}\phi_y$	0	$\frac{L}{EA} k_{1,5}^2$ $+ \frac{EI_y}{L}(\phi_y + \omega_y)$	$\frac{L}{EA} k_{1,5}\, k_{1,6}$
δM_{z1}	$k_{1,6}$	$\frac{L}{EA} k_{1,2}\, k_{1,6}$ $+ \frac{2EI_z}{L^2}\phi_z$	$\frac{L}{EA} k_{1,3}\, k_{1,6}$	0	$\frac{L}{EA} k_{1,5}\, k_{1,6}$	$\frac{L}{EA} k_{1,6}^2$ $+ \frac{EI_z}{L}(\phi_z + \omega_z)$

ANNEX 9

ESTIMATE OF CRITICAL PRESSURES FOR MODEL BUCKLING TESTS

CAMROC WORKING MEMORANDUM

Prepared by

R. A. Muldoon

MIT Lincoln Laboratory

I. INTRODUCTION

During the radome hardening studies conducted by Lincoln Laboratory, a 7.42-ft-diameter space-frame radome was fabricated and statically tested under a uniform external pressure by air evacuation from the interior of the model until a buckling failure developed.[1] The beam elements in the space frame were oriented according to the random geometry depicted in Figures 1 and 2. This geometry has been designated the TTR Radome. Photographs of the model before and after testing are shown in Figures 3 and 4. All the individual beam elements were fabricated from 4150 steel and featured constant rectangular cross sections of width b = 0.131 inch and depth h = 0.195 inch.

By means of the equivalent shell method[2, 3] and the appropriate frame geometry and beam parameters, an empirical buckling coefficient can be obtained. This coefficient can then be applied to establish approximate critical buckling pressures for space-frame structures of the same TTR random geometry but different beam parameters, e.g., beam width, depth, and material. In this fashion the cross-sectional dimensions of the beam members necessary to resist a desired pressure level can be estimated.

II. CALCULATION OF STATIC BUCKLING COEFFICIENT FOR TTR RANDOM GEOMETRY

By means of the equivalent-shell method, the critical buckling pressure for a space-frame radome with constant rectangular cross-section beam members can be expressed as

$$p_{cr} = \frac{K\left(\sum_n L_s\right) E\, b\, h^2}{8\, R^4} \qquad (1)$$

where p_{cr} is the critical pressure, R the radome radius, L_s the length of individual beam member in space frame, n the number of beams in complete sphere, E the elastic modulus of beam material, b the beam width, h the beam width, and K the empirical coefficient.

---

[1] MIT Lincoln Laboratory, "TTR 2-psi Hardened Radome," Division 7, Final Report vol. I, September 1961.

[2] A. F. Foerester, "Stress Distribution and Stability Criteria of Spherical Ground Radomes Subjected to Wind Loads," Proceedings of the OSU-WADC Radome Symposium, vol. I, June 1958.

[3] R. A. Muldoon, "Dynamic Buckling of Space Frame Radome Models," MIT Lincoln Laboratory, Group Report 71G-3, 15 February 1962.

$$F + V = E + 2$$
$$1700 + 852 = 2550 + 2$$

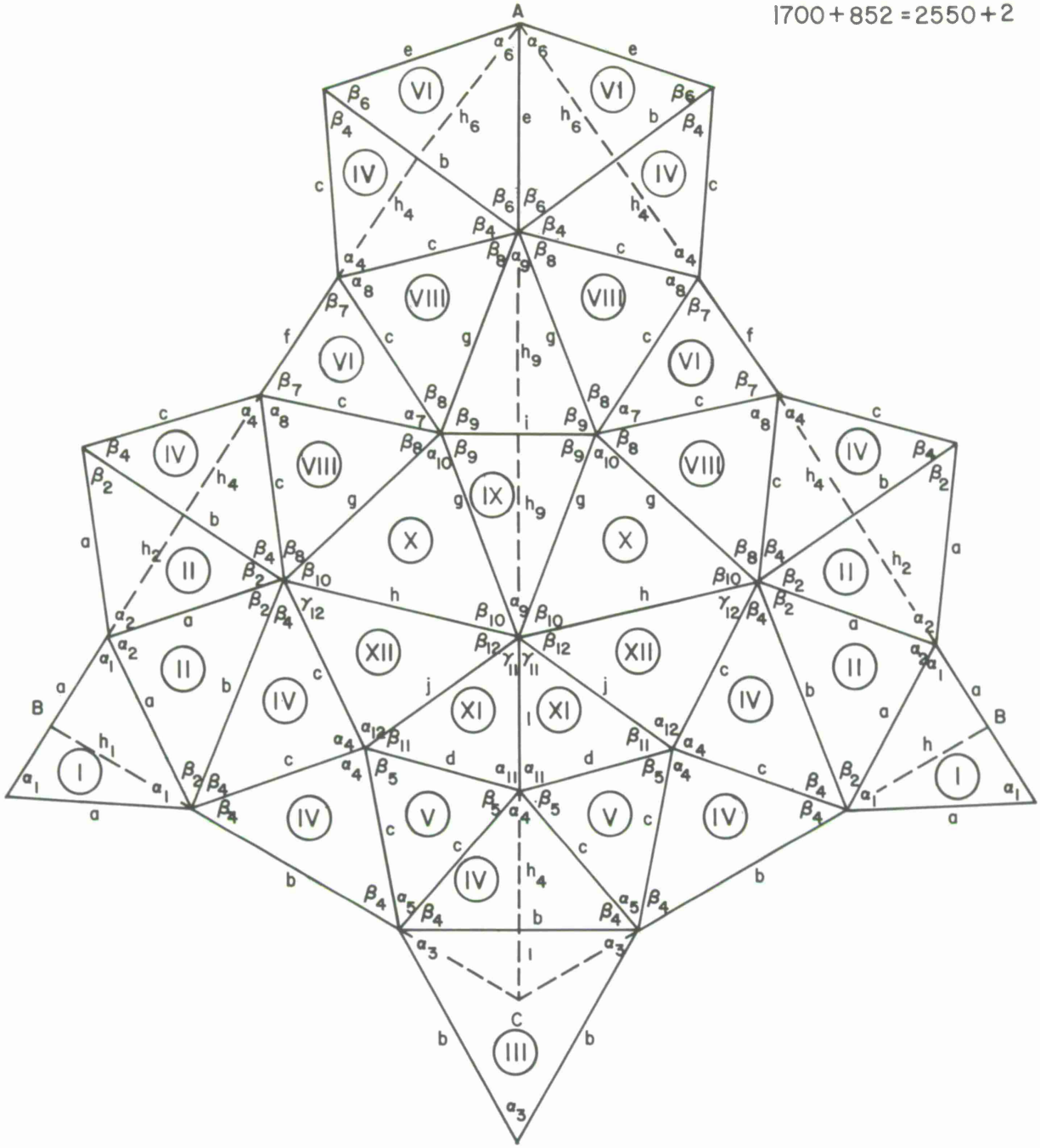

Figure 1.

Figure 2. TTR Radome (Random Geometry)

Spherical angles and sides (degrees)

ΔI	$\alpha_1 - 60.132115$	a − 7.234506
		$h_1 - 6.269428$
ΔII	$\alpha_2 - 79.911923$	a − 7.234506
	$\beta_2 - 50.269316$	b − 9.277440
		$h_2 - 5.557689$
ΔIII	$\alpha_3 - 60.217541$	b − 9.277440
		l − 2.685015
		2 − 5.358290
ΔIV	$\alpha_4 - 80.779032$	b − 9.277440
	$\beta_4 - 49.832313$	c − 7.169611
		$h_4 - 5.472761$
ΔV	$\alpha_5 - 50.226604$	c − 7.169611
	$\beta_6 - 65.059102$	d − 6.072676
		$h_5 - 6.497964$
ΔVI	$\alpha_6 - 72$	b − 9.277440
	$\beta_b - 54.259974$	e − 7.908331
		$h_6 - 6.412012$
ΔVII	$\alpha_7 - 42.497430$	c − 7.169611
	$\beta_7 - 68.902763$	f − 5.184998
		$h_7 - 6.686760$
ΔVIII	$\alpha_8 - 70.707721$	c − 7.169611
	$\beta_8 - 54.858114$	g − 8.282600
		$h_8 - 5.857710$
ΔIX	$\alpha_9 - 42.099198$	g − 8.282600
	$\beta_9 - 69.150997$	i − 5.931769
		$h_9 - 7.736829$
ΔX	$\alpha_{10} - 69.484348$	g − 8.282600
	$\beta_{10} - 55.538634$	k − 9.418005
		$h_{10} - 6.821413$

Figure 2 (continued)

Spherical angles and sides (cont.)

ΔXI	$\alpha_{11} - 74.551382$	d − 6.072676
	$\beta_{11} - 51.385486$	l − 5.837604
	$\gamma_{11} - 54.361665$	j − 7.207670
ΔXII	$\alpha_{12} - 81.997348$	c − 7.169611
	$\beta_{12} - 49.050102$	j − 7.207670
	$\gamma_{12} - 49.399994$	k − 9.418005

For the TTR random space-frame radome model tested statically

$R = 3.71$ ft $\quad E = 30 \times 16$ lb/inch^2 $\quad b = 0.131$ inch

$\left(\sum_n L_s\right) = 28,388$ inches .

Substituting these results into equation (1), the buckling coefficient is calculated as

$K = 0.248$. (2)

By means of equations (1) and (2) the critical buckling pressure may be estimated for a TTR random geometry space-frame radome with the same rectangular cross section throughout.

III. RESULTS

Using equations (1) and (2), the rectangular cross-sectional dimensions required by aluminum beam members to resist buckling at various static pressure levels are determined for the TTR random geometry and a radome radius R = 7ft. The results are plotted in Figure 5.

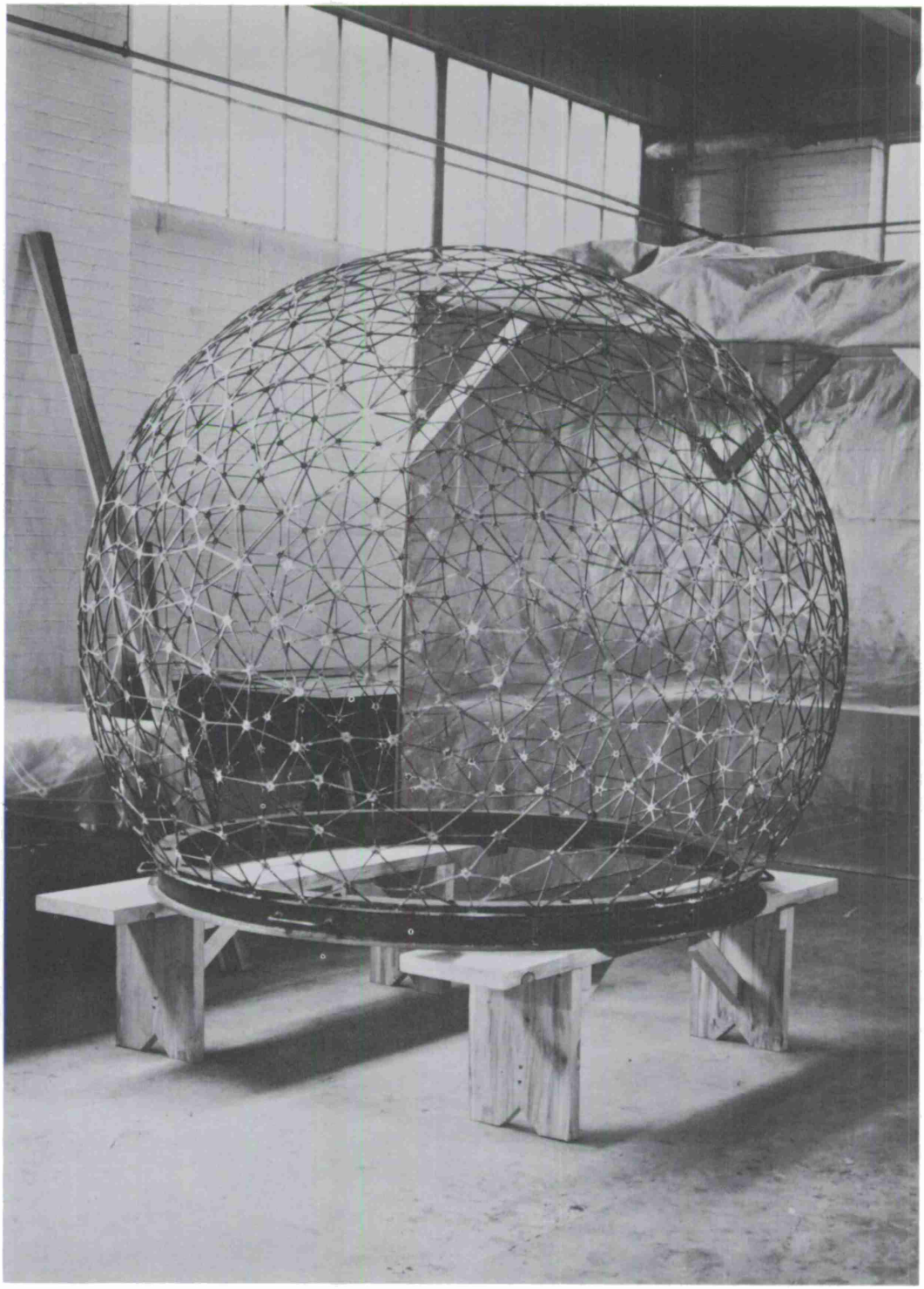

Figure 3.

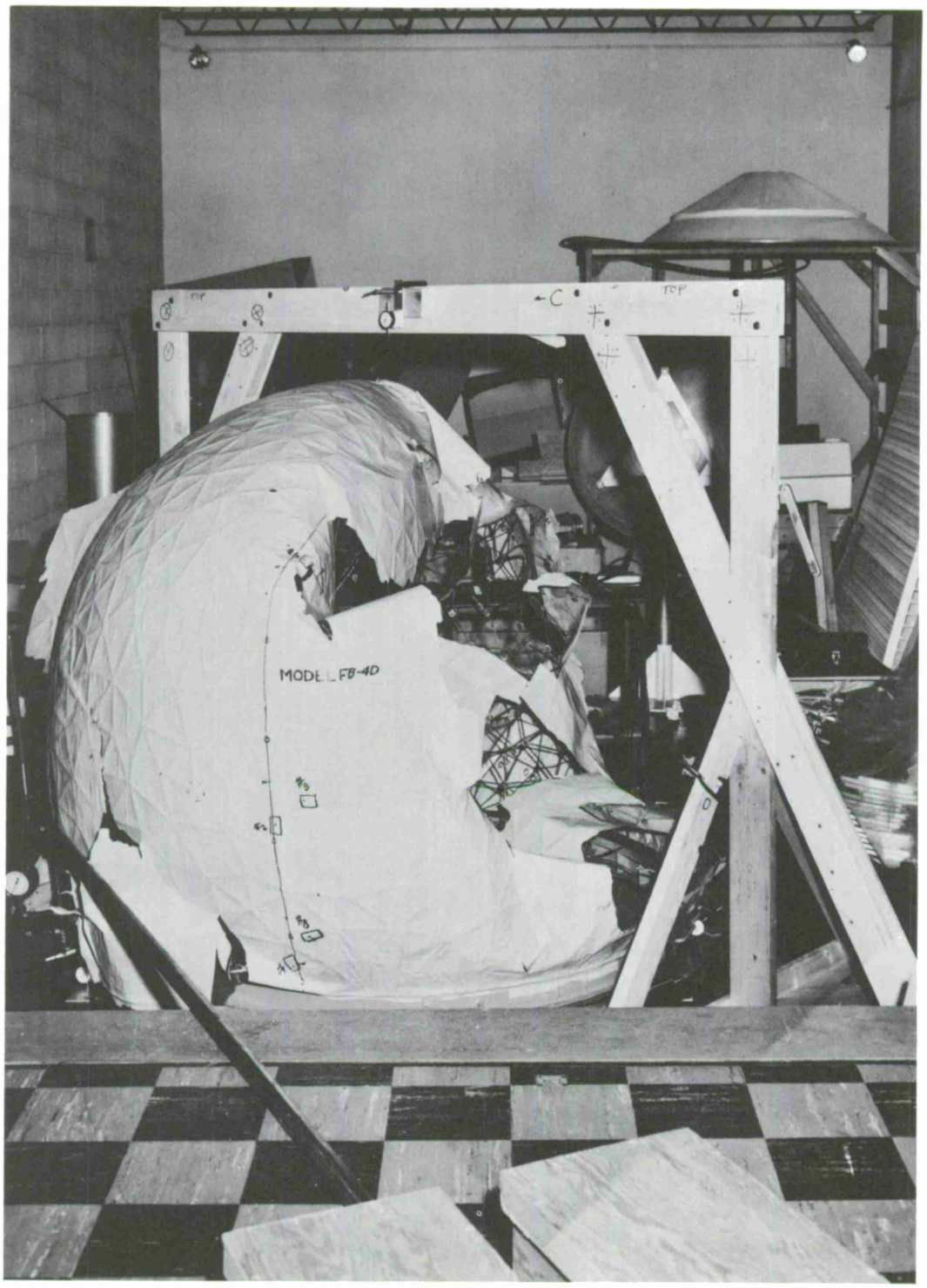

Figure 4.

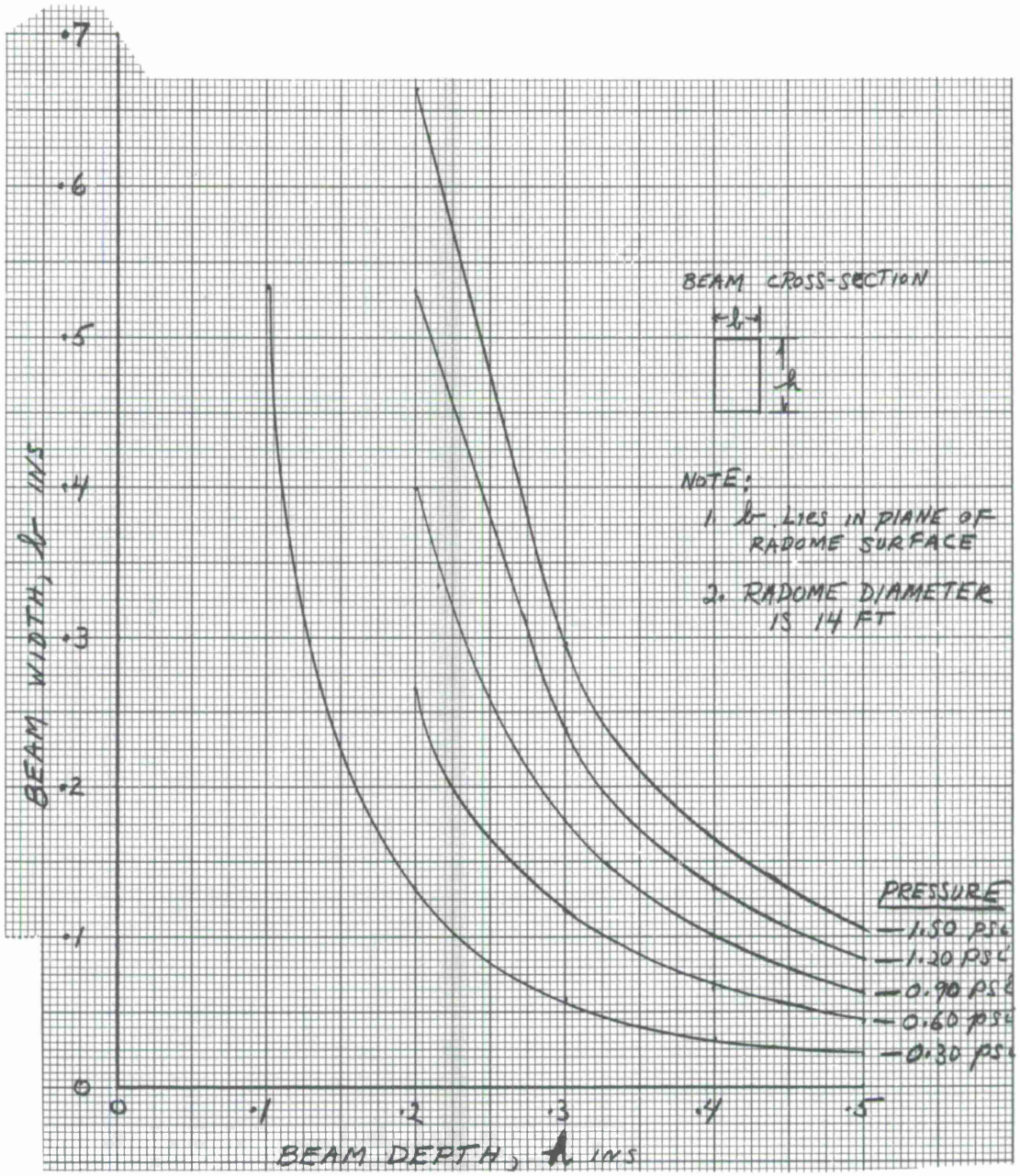

Figure 5. Beam width versus depth for rectangular cross-section aluminum beam members in TTR random geometry space frame radome models required to resist buckling at various pressure levels.

ANNEX 10

EXPERIMENTAL STUDY OF INSTABILITY IN ELEMENTS OF SHALLOW SPACE FRAMES

CAMROC WORKING MEMORANDUM

September 1966

Prepared by

P. H. Griggs

Department of Civil Engineering
Massachusetts Institute of Technology

1. INTRODUCTION

This report describes a series of experimental structural model tests performed during the period from July 1 to September 15, 1966, on a unit element of the space frame of a large radome. The purpose of the study was to obtain, in as short a time as possible, experimental data to make initial performance checks of the analytical methods of analysis that were being developed concurrently by others. Both the magnitude of the proposed radome and the complexity of its nonlinear analysis contributed to the need for an accurate model study.

Owing to the extremely short period of time allotted to the study, its scope was necessarily limited. Development of loading frame, experimental procedure, and fabrication techniques required a large proportion of the time. However, it has been possible to test two Plexiglas and two polyvinyl chloride (PVC) models, all of which had the same basic geometry shown in Figure 1. One model of each material had members 0.70" × 0.70" and failed by "snap-through" buckling while the other had members 0.70" × 0.35" and failed by local buckling of the compression members about the weak axis. Each model was tested at least twice under vertical dead load applied at the center joint; the Plexiglas models were also tested twice under applied deflection.

Owing to various factors explained in the report, the latter models F 1 D and F 2 D are considered to have given the best results. These results, together with essential data pertinent to them, may be obtained directly from the report as follows: the model is defined in Figure 1, while detailed dimensions are available from Appendix 1; the material properties are given in Table 1; Table 2 gives test statistics; and, finally, the load deflection curves applicable are shown in Figures 17 and 18.

2. MODEL FABRICATION

2.1 Selection of Materials

It was evident, both from inspection of the model's configuration and from the results of some preliminary tests, that the production of models with fully fixed joints was a critical requirement. To ensure that this would be achieved, and for other reasons, two dissimilar model materials were chosen, Plexiglas and PVC type II. The Plexiglas model was cemented together with P. S. 18, an adhesive manufactured by Rohm and Haas Company, whereas the PVC was heat welded.

Both model materials have been used many times in the past. With the correct techniques, both can be cut and machined. Each material has a low modulus of elasticity, a stress-strain curve essentially linear up to stresses approaching 2000 psi, and a great reserve of strength and toughness. Although the creep of the Plexiglas is approximately twice that of the PVC, it was not expected to be significant, since the unit stresses were below 1000 psi and the test duration was short. As is typical of plastics, the mechanical

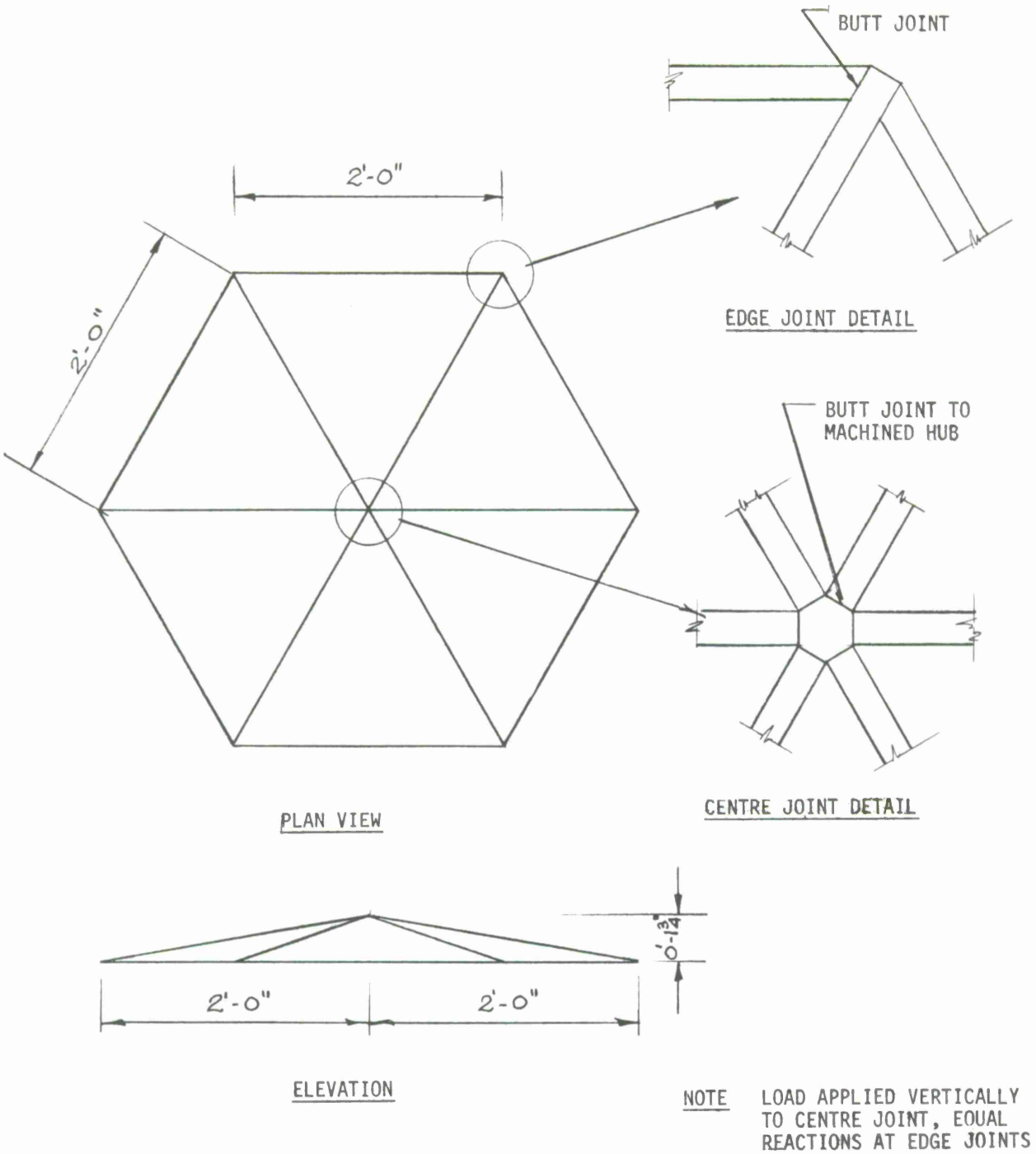

Figure 1. Geometry and joint details of model.

Table 1. Results of modulus tests.

Material	Test No.	Orientation of cross section *	Joints in member	Number of deflection readings	Modulus	Averages
Plexiglas	1		None	9	437,000	
	2		None	9	444,000	439,800
	3		None	9	437,000	
	4		None	6	451,000	
	5		None	6	440,000	440,000
	6		None	6	429,000	
	7		Two	6	448,000	
	8		cemented	6	443,000	448,000
	9		joints	6	454,000	
	10		None	6	479,000	
	11		None	6	465,000	
	12		None	6	467,000	471,800
	13		None	32	476,000	
	14		Two cemented joints	32	484,000	484,000
PVC	1		None	36	432,000	
	2		None	36	411,000	417,500
	3		None	9	405,000	
	4		None	9	422,000	
	5		Two	8	395,000	
	6		welded	8	405,000	403,700
	7		joints	8	411,000	

Note:

All data given are for 72° F and 50% relative humidity. Method of obtaining data is described in text and Figure 2.

*Square cross sections were approximately 0.70" × 0.70". Rectangular cross sections were approximately 0.35" × 0.70".

Table 2. Details of models tested and results.

Model no.	Material	Cross-section dimensions		Date tested	Ambient conditions		Loading	Duration of test	Max. load	Mode of failure	Load-deflect diagram
		width ins.	depth ins.		temp.	R. H.		mins.	sustained lbs.	*	Figure no.
F1-1	Plexiglas	0. 350	0. 700	8/9	72	50	D. L.	5	14. 9	1	13
F1-2	Plexiglas	0. 350	0. 700	8/22	72	50	D. L.	10	15. 4	1	13
F2-2	Plexiglas	0. 703	0. 703	8/10	72	50	D. L.	7	40. 1	2	14
F2-3	Plexiglas	0. 703	0. 703	8/17	72	50	D. L.	13	56. 5	3	14
F3-1	PVC	0. 354	0. 702	8/19	72	50	D. L.	7	12. 4	1	15
F3-2	PVC	0. 354	0. 702	8/22	72	50	D. L.	7	13. 0	1	15
F4-1	PVC	0. 701	0. 700	8/23	72	50	D. L.	12	45. 2	2	16
F4-2	PVC	0. 701	0. 700	8/24	72	50	D. L.	7	47. 6	4	16
F1D-1	Plexiglas	0. 350	0. 700	9/12	72	50	Applied deflection	--	14. 9	1	17
F1D-2	Plexiglas	0. 350	0. 700	9/14	72	50	Applied deflection	10	15. 4	1	17
F2D-2	Plexiglas	0. 703	0. 703	9/14	72	50	Applied deflection	11	45. 7	2	18
F2D-3	Plexiglas	0. 703	0. 703	9/14	72	50	Applied deflection	27	55. 6	5	18

*1 = local buckling of compression members about weak axis.
2 = test discontinued prior to failure.
3 = snap-through buckling followed by fracture starting at center joint.
4 = failure of center joint either simultaneously with or prior to snap-through buckling.
5 = overall buckling (constant load at increasing deflection).

properties are sensitive to both temperature and humidity changes; however, a fully controlled environment was available for the project and all tests on models and materials were performed at 72° F and 50% relative humidity.

2. 2 Jointing Methods

Although it was the first use of the P. S. 18 cement in this model laboratory, the results obtained for the Plexiglas were ideal. A thin glue line with strength in excess of the Plexiglas itself was consistently obtained — in virtually all of several dozen breakages that occurred during the work, the fracture line passed through the virgin material. The stiffness of the joints was investigated by means of a cantilever-bending specimen as shown in Figure 2. A total of 11 tests indicated the cemented beams to be stiffer by approximately 2%.

A commercially produced, heat-welded PVC model was tested in the Civil Engineering Model Laboratory earlier in 1966. The excellent results obtained prompted the laboratory to invest in a basic welding machine produced by the Kamweld Company of Massachusetts. This equipment was used to fabricate the PVC. The resulting models gave results that are considered to be slightly inferior to those of the Plexiglas models. The reason for this lies in the difficulty of producing 100% strength and penetration butt welds in square and rectangular stock with relatively inexperienced welders. The technique of producing the initial tack welds (or root sealing bead) by heating the parts and pushing them together gave incomplete fusion, which initiated the failure of model F4 (PVC square member section). The stiffness of the welds was investigated in the same manner as for the Plexiglas cement. A reduction of 4% in the cantilever-beam stiffness indicated a greater reduction at the weld itself, attributed to the presence of some small voids and, perhaps, to the effect of heating the material to beyond its transition or softening temperature.

2. 3 Dimensional Control

All model material was initially taken from 1" thick plate. First cutting to shape was done on a band saw with a blade in the order of 20' long to avoid heating the material. To eliminate the effect of residual stresses and to obtain straight members, it was found necessary to reduce the members to size by taking cuts symmetrical with respect to the center line of the finished member. Similarly, in the following operation of milling the sections down to final size, an equal number of cuts was taken from each side.

The models were assembled on a plywood jig with the joint configuration detailed in Figure 1.

After assembly, the dimensions of the models were established by second-order triangulation from a fixed base line with a Wild T-1 optical transit. The T-1 reads directly to 10 sec, and by four-fold repetition readings of both the angle required and its explement, all angles were established to within ±0. 05 sec. The base line was set out using

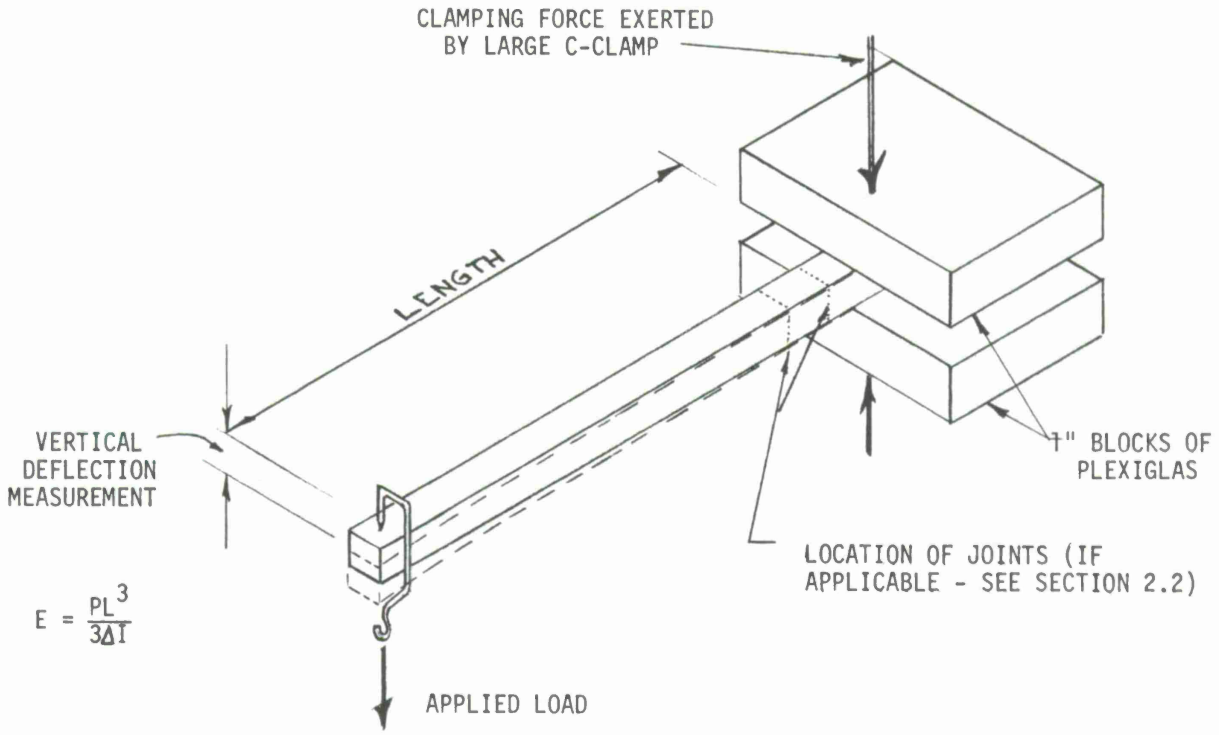

CANTILEVER BEAM MODULUS MEASUREMENT
(USED FOR STUDY)

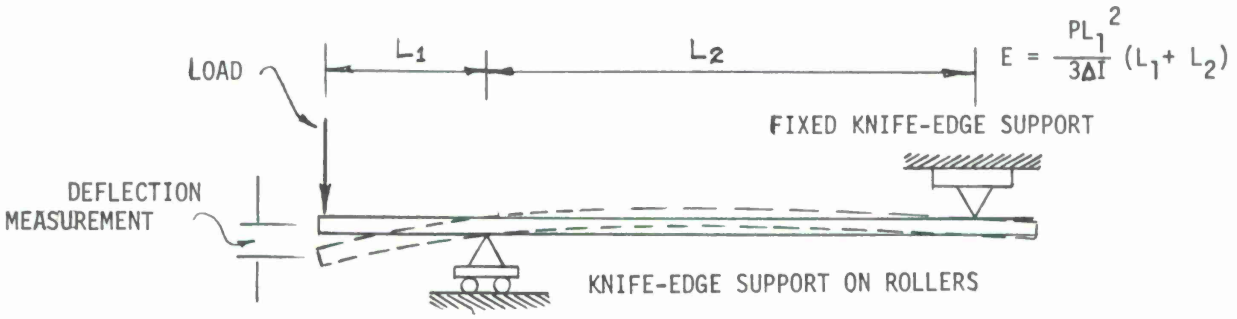

ARRANGEMENT PREFERRED FOR FUTURE MODULUS TESTS

Figure 2. Modulus tests.

a standardized surveying chain. The surveying data were reduced to angles and lengths required with the help of the Dept. of Civil Engineering Systems Laboratory IBM 1620 computer and the COGO program. The output is given in Appendix 1. Lengths are estimated to be accurate to ±0.003", which, at a model scale of 1:20, is equivalent to ±1/16" in the prototype structure.

Since the two models with rectangular member sections were expected to buckle in compression, it was thought desirable to know the degree of initial curvature as measured by the distance between the true center of the member and the line passing through its ends. These data are also shown in Appendix 1.

2.4 Modulus Tests

Modulus of elasticity tests were performed on cantilever beams of material that was either cut from the model after testing or taken at random from the members that had been prepared for fabrication. A total of 14 separate tests involving 145 deflection readings were done on Plexiglas samples, while the evident repeatability of the test allowed a reduction to 7 tests for the PVC. The detailed results, given in Table 1, show the effect of the Poisson's ratio restraint when a wide beam is clamped as a cantilever. Because of this, the average values for modulus include only square or rectangular beams stressed on their major axis; the beam shown in Figure 2 is recommended for future tests.

3. TESTING APPARATUS

3.1 Description of Loading Frame

The supporting frame, shown in Figure 3, consists of a large "box" fabricated from slotted angles. The model, which hangs inside the frame, is supported at each of the six circumferential joints. To attain equal vertical reactions at each joint, the load from three pairs of supports was collected, by means of machined aluminum beams, to give three main reactions at the frame. One of the beams is illustrated in Figure 4. The support for the beam includes a weigh pan and spring. The spring was designed to have a 10" deflection at maximum load so that any unforeseen contortions of the structure during loading would not affect the equality of the reactions. The weights served only the purpose of eliminating the initial tension in the spring. In the symmetrical cases tested thus far, the springs proved unnecessary and were discarded for some of the later tests.

3.2 Application of Load

In all models tested to date, the load has been applied vertically at the center by means of a spherical seat, visible in the photograph of Figure 5. Load was measured with an aluminum load cell (see also Figure 5) equipped with four EWR strain gauges. With one gauge in each arm of the wheatstone bridge a temperature compensated output of 51.3 microinches per inch for each pound of load was obtained, with linear response

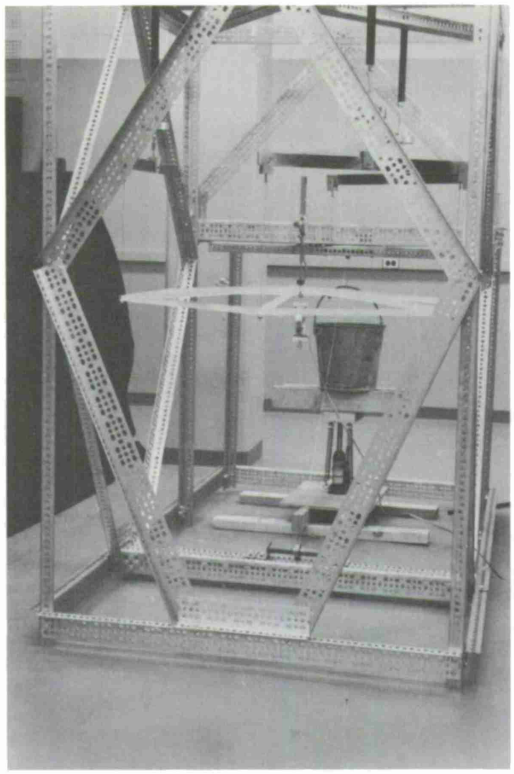

Figure 3. Overall view of loading frame.

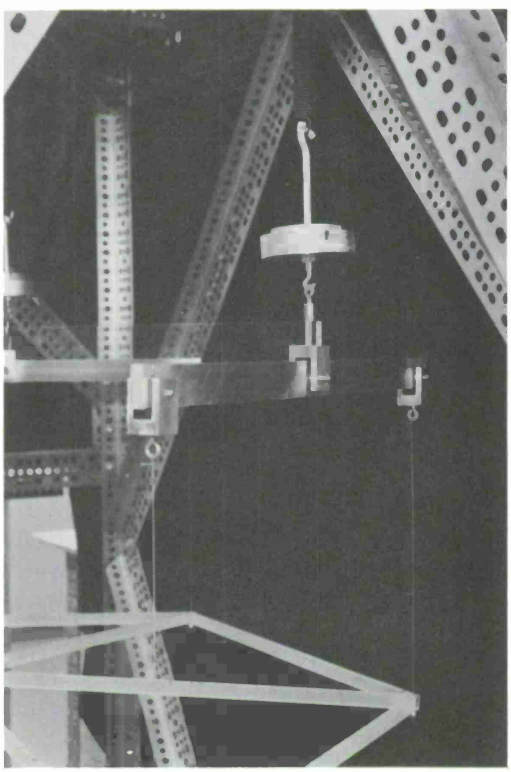

Figure 4. View of beam-support structure.

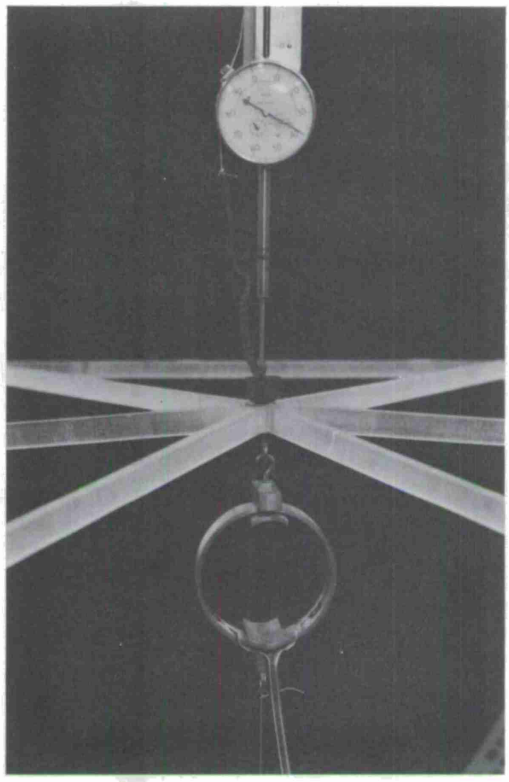

Figure 5. View of arrangement at center joint.

to 50 lbs. When computing the load on the model, a correction was made for both the weight of the load cell and the spring force of the dial gauge used.

For some tests, dead load was applied to the model by means of a wire, pulleys, and steel weights. In other tests, a deflection was applied and the load measured in an attempt to define post-buckling behavior. In the latter tests, the loading wire was wound onto a shaft that was connected to a hand crank. A chain drive with a large reduction ratio enabled the operator to set deflection to an accuracy of ±0. 001".

3. 3 Instrumentation

Due to the symmetry of the initial loading cases described in this report, the only data required were the vertical deflection of the center joint relative to the exterior ring. In later asymmetrical tests, two or more components of deflection and perhaps of rotation will be required. However, in all dead load tests described herein, the center deflection was measured relative to the center yoke of the load-collecting beams by the Plexiglas support visible in Figure 6. Because some deflection was discovered in the tension wires connecting the model to the beams, the models tested under applied deflection were equipped with a further nine vertical dial gauges, one at each of the circumferential joints and one on the supporting yoke of each load-collecting beam. The true net deflection of the center joint with respect to the edges could, therefore, be computed.

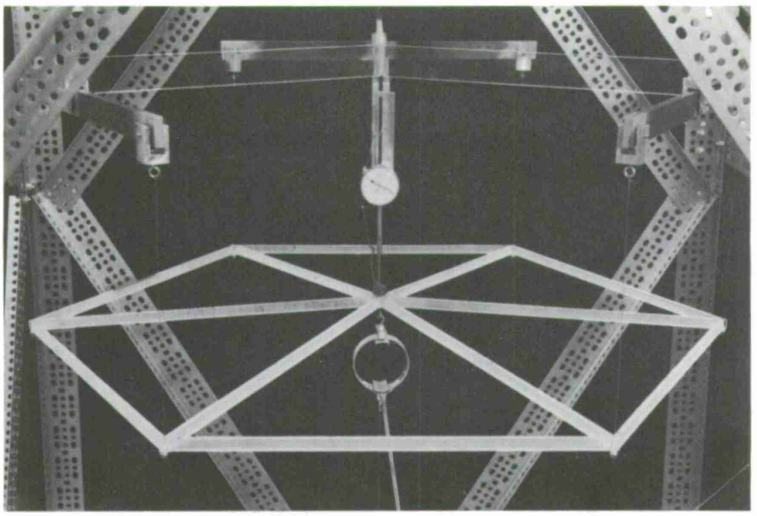

Figure 6. Model F 1 ready for testing.

4. TESTS AND RESULTS

4.1 Models with Member Section 0.70" × 0.35"

A total of six tests was performed on two models with nominal cross-sectional dimensions as given above, all with the weak axis oriented perpendicular to the plane of the model. The overall behavior was the same for all tests; the load could be increased until column buckling about their weak axis occurred in the compression (radial) members; due to the symmetry, the center joint rotated and behaved as a pinned connection, whereas the circumferential tension members supplied rotational restraint at the edge joints. The post-buckling behavior was similar to the typical Euler column case with essentially constant load under increasing deflections.

Two of the tests were performed with dead load applied to a PVC model (F3), which sustained 12.4 and 13.0 lbs before buckling at 13.8 and 13.5 lbs, respectively, to give a buckling load somewhere between 13.0 and 13.5 lbs. In this and other cases where a model was tested more than once, it was completely removed from the loading frame between tests. Photographs of model F 3 before and after buckling are shown in Figures 9 and 10. Table 2 and Figure 15, respectively, give essential data and load-deflection curves. The difference between the two load deflection curves in Figure 15 is partially attributed to support deformation between loading beams and model. The discrepancy in some of the results was noticed after the dead-loading tests (F 1 to F 4) had been completed. In subsequent applied-deflection tests (F 1 D and F 2 D), the support deformation was found to be 0.028" for the rectangular section models and 0.079" for the square section models, both figures being valid at maximum load. Thus, the results of all models

tested by dead load have a systematic error of slightly less than 10% in the deflection readings (actual deflections being smaller than those measures); however, the buckling loads are correct.

The remaining four tests of the local-buckling behavior were done on a Plexiglas model. The three photographs in Figures 6, 7, and 8 clearly illustrate the original appearance and buckled shape typical of all tests done on the model. Again, Table 2 gives essential statistics relevant to the tests, while the results are given graphically in Figures 13 and 17. Figure 13 shows the excellent repeatability generally obtained with the Plexiglas and defines the buckling load to be between 15.4 and 16.0 lbs. Figure 17 gives the results for the applied-deflection case (model F 1 D). The average buckling load was 15.2 lbs. Post-buckling behavior is clearly shown.

4.2 Models with Square Member Section 0.70" × 0.70"

Six tests were made on models that were designed to fail by overall buckling. The PVC model F 4 did not yield useful results since it suffered from the support deflection described above and failed prematurely at a weld (see section 2.2). The Plexiglas model gave excellent results. For the dead-load case (F2), two coincident load-deflection curves were obtained (see Figure 14). In the second test, a maximum load of 56.6 lbs was momentarily sustained before a short period of rapidly increasing deflection and, finally, fracture of the model as it tried to snap through. The same model was successfully repaired and tested under applied deflection (model F 2 D; results in Table 2 and Figure 18). Again, coincident load-deflection curves were obtained for two tests. The maximum load was, at 55.6 lbs, slightly lower than for the dead-load test. Figures 11 and 12 illustrate the original and buckled configuration.

5. CONCLUSION

An experimental apparatus and procedure has been developed for the study of the behavior of small-scale structural models representing a hexagonal element of a spherical framework.

A total of 12 tests has been completed on four models differing in material properties and member cross-section characteristics. In all tests, the load was applied vertically at the center joint of the model, with equal and symmetrical reactions at the other six joints. The dimensions of the individual members were chosen so that two distinct facets of behavior, local and overall buckling, could be simulated. The results from models F 1 D, and F 2 D, in particular, are considered to be of the highest accuracy attainable with structural engineering model studies of this type and scope.

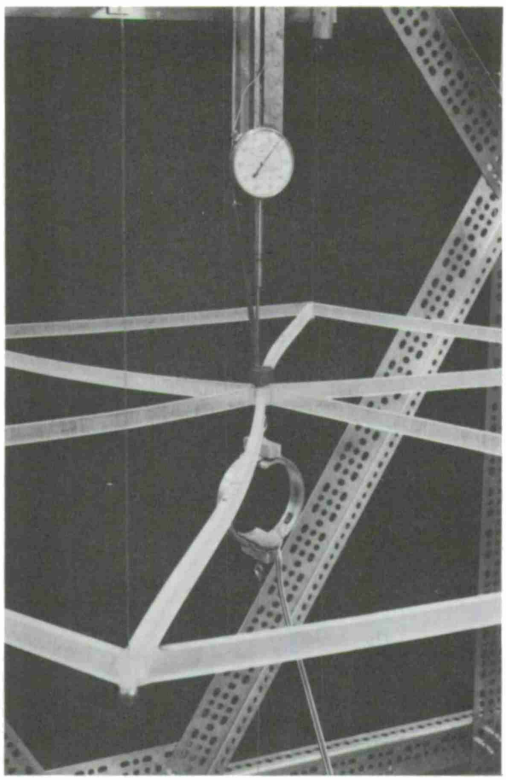

Figure 7. Model F 1 after buckling.

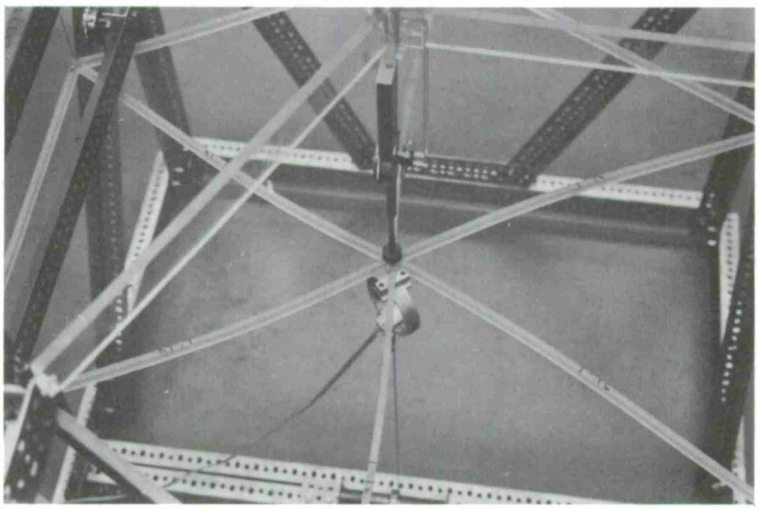

Figure 8. Model F 1 after buckling.

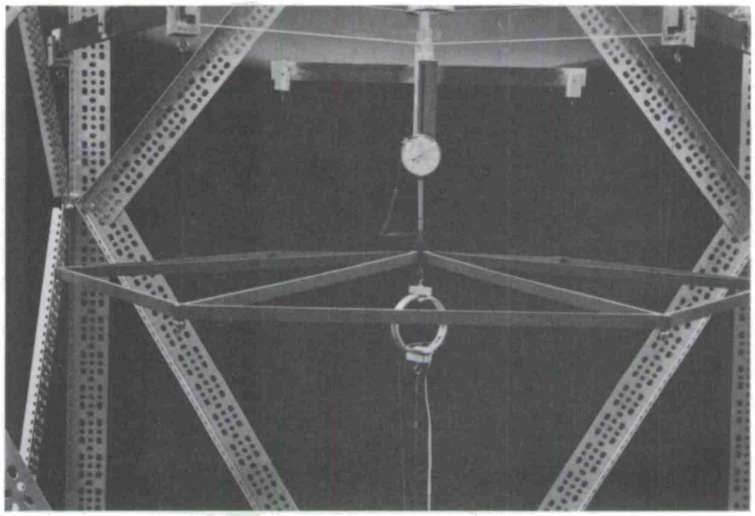

Figure 9. Model F 3 ready for test.

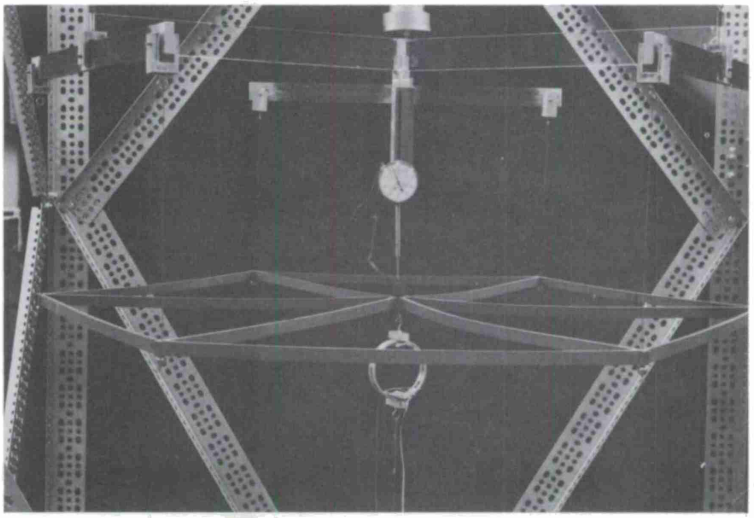

Figure 10. Model F 3 in buckled position.

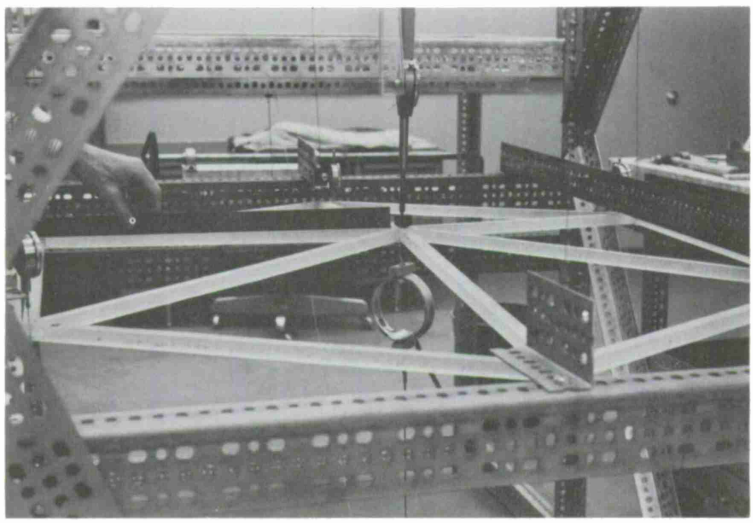

Figure 11. Model F 2 D ready for test.

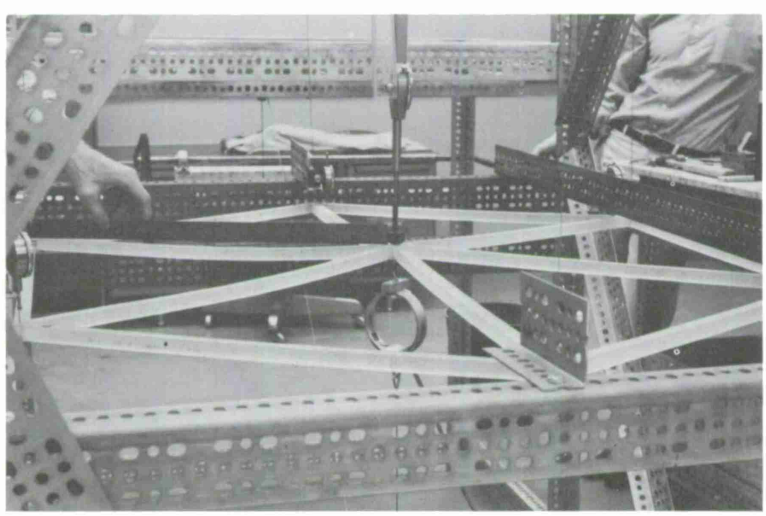

Figure 12. Model F 2 D with maximum load applied.

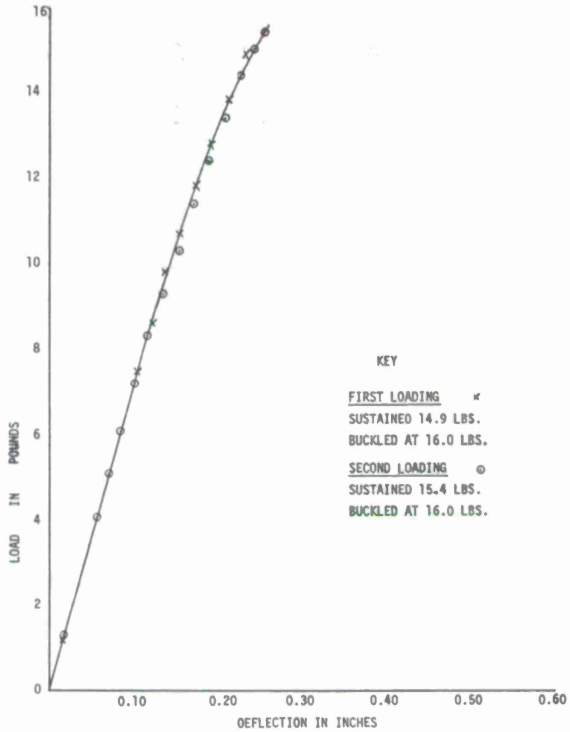

Figure 13. Load-deflection curves for model F 1.

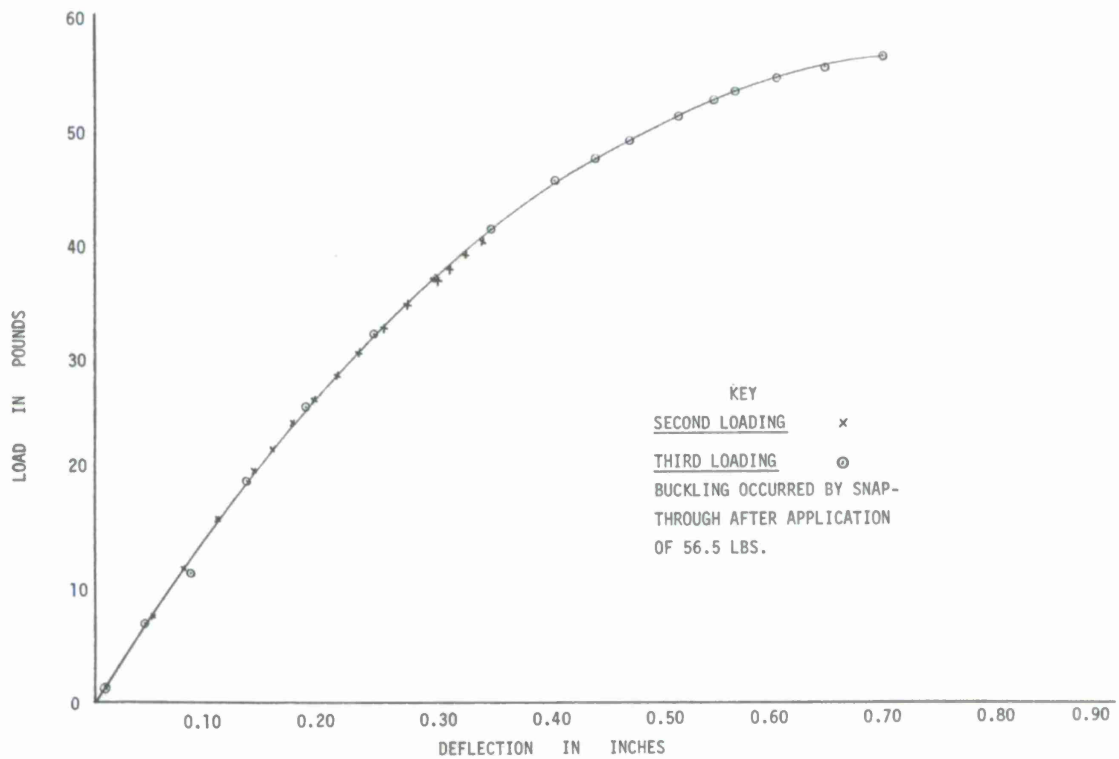

Figure 14. Load-deflection curves for model F 2.

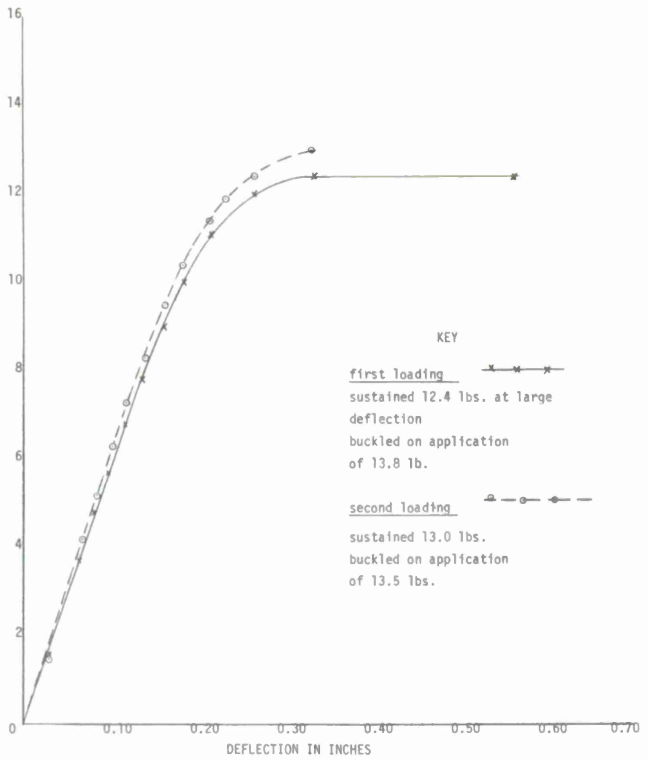

Figure 15. Load-deflection curves for model F 3.

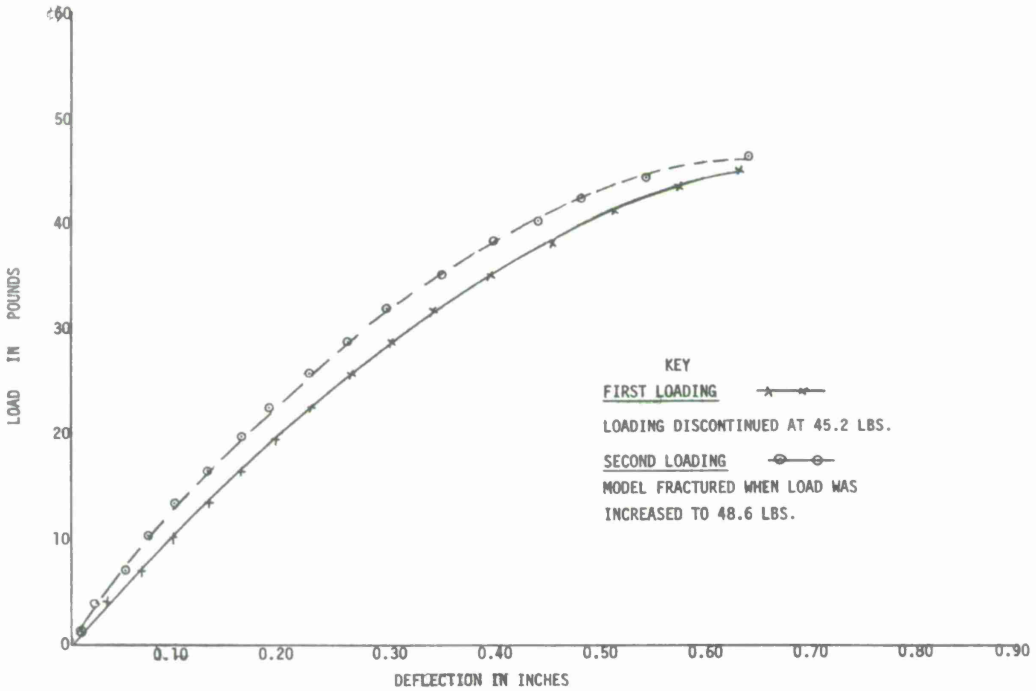

Figure 16. Load-deflection curves of model F 4.

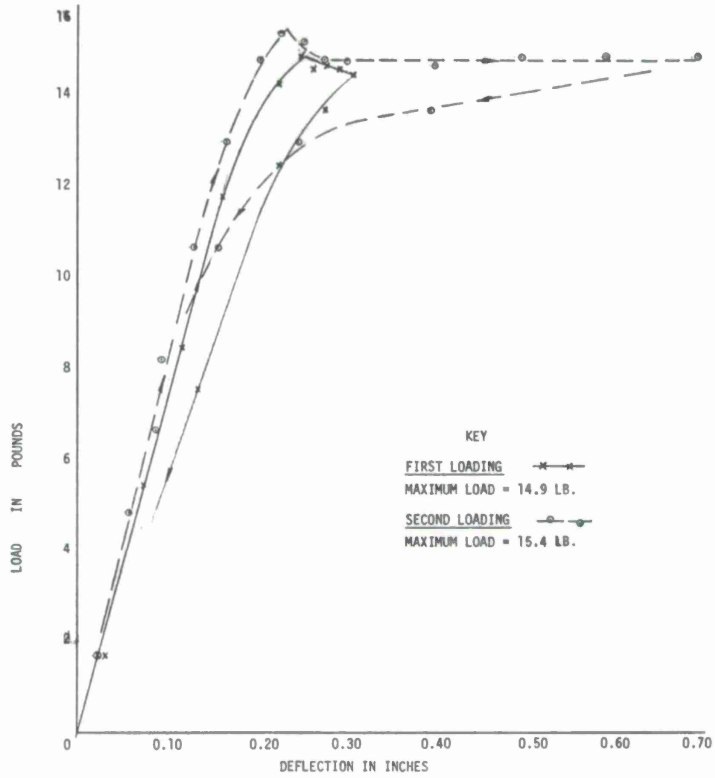

Figure 17. Load-deflection curves for model F 1 D.

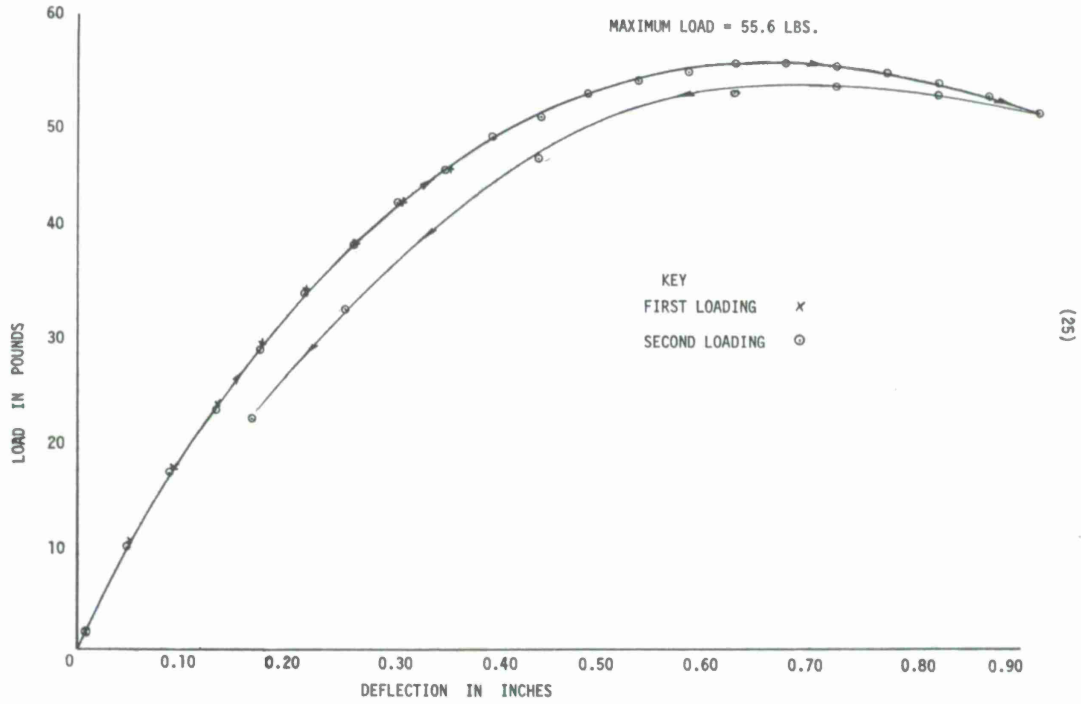

(25)

Figure 18. Load-deflection curves for model F 2 D.

To obtain more data for further checks on theoretical work, it is considered desirable to use the existing apparatus, with slight modifications, to perform the following tests:

1. Models with rectangular and square-section members loaded with vertical and horizontal loads that lie in a vertical plane containing two radial members. In this case, the symmetry retained would reduce the demands on instrumentation to that required to measure two components of translation and one or two components of rotation at the center joint, and at least one horizontal reaction at an exterior joint. Some benefit might also accrue from measuring displacements at the exterior joints.
2. Square-section models with completely asymmetrical loading.
3. Finally, it might be useful to test a model whose member properties differed widely from those used in the tests so far. For example, although it would be more expensive, it would be possible to fabricate a three-plate I-section with the same area as the rectangular sections but with a much lower torsional-to-bending stiffness ratio.

APPENDIX 1

EXPLANATION OF DIMENSIONAL DATA

The following pages give the angles at the center joint and the lengths of the radial members for each model. Angles are given in degrees, minutes, and seconds with an accuracy of better than ±5 sec, whereas lengths are given in inches with an accuracy of ±0. 003 inch.

To read the data, it is necessary to know that the circumferential joints are numbered 3 to 8 consecutively in a counter-clockwise direction, and the center joint is assigned number 9. Thus, the angle between legs 7 - 9 and 6 - 9 of model F 1 is (angle 796) 59° 42' 56", and the lengths of the legs are, respectively, 24. 017" and 24. 015".

The last page of the appendix gives a measure of the initial curvature of the radial (compression) members of models F 1 and F 3.

MODEL F 1

```
*       ID GRIGGS     70073
*                     DIMENSIONS OF MODEL FOR CAMROC RADOME PROJECT
CLEAR                 1  99
STORE                  1 1180. 0 1000. 0
                      2  1000. 0  1000. 0
*                     MODEL SECTION 0. 70 BY 0. 35
AZ/INTERSECT          3 1 114 55 09.  2 61 55 41.
          3         1096. 1988        1180. 3766
                      4 1 121 01 59.  2 68 01 50.
          4         1072. 2482        1179. 0953
                      5 1 121 12 20.  2 73 25 59.
          5         1059. 2837        1199. 2828
                      6 1 116 26 52.  2 72 21 06.
          6         1070. 2148        1220. 6988
                      7 1 111 09 43.  2 67 01 17.
          7         1094. 0970        1221. 9086
                      8 1 109 50 33.  2 62 01 27.
          8         1107. 1831        1201. 7872
                      9 1 115 46 08.  2 67 27 42.
          9         1083. 2080        1200. 5020
ANGLE                 3 9 8
          3             9                 8
         60            13         35. 335200
                      8 9 7
          8             9                 7
         59            58         12. 939600
                      7 9 6
          7             9                 6
         59            42         56. 484000
                      6 9 5
          6             9                 5
         60             9         46. 526400
                      5 9 4
          5             9                 4
         59            58         16. 158000
                      4 9 3
          4             9                 3
         59            57         12. 567600
DISTANCE              8 9
          8             9         24. 009521
                      7 9
          7             9         24. 016927
                      6 9
          6             9         24. 015286
                      5 9
          5             9         23. 955345
                      4 9
          4             9         24. 049199
                      3 9
          3             9         23. 953968
DUMP                  1  99
   10. 000000         1         1180. 0000        1000. 0000
   10. 000000         2         1000. 0000        1000. 0000
   10. 000000         3         1096. 1988        1180. 3766
```

MODEL F 2

```
*          ID GRIGGS   70073
*                      DIMENSIONS OF MODEL FOR CAMROC RADOME PROJECT
CLEAR                  1  99
STORE                   1 1180. 0 1000. 0
                       2  1000. 0  1000. 0
*                      MODEL 2) SECTION 0. 70 BY 0. 70
AZ/INTERSECT           3 1  114  38 02.  2  61  43  18.
          3          1097. 1717          1180. 6307
                       4 1  120  46 34.  2  67  47  21.
          4          1073. 2133          1179. 3065
                       5 1  121  01 36.  2  73  13  42.
          5          1060. 0840          1199. 3637
                       6 1  116  17 09.  2  72  11  16.
          6          1070. 9427          1220. 7984
                       7 1  110  57 59.  2  66  51  47.
          7          1094. 8980          1222. 0880
                       8 1  109  36 50.  2  61  52  04.
          8          1108. 0112          1202. 0134
                       9 1  115  33 09.  2  67  16  50.
          9          1084. 0397          1200. 7117
ANGLE                  3 9 8
          3              9                   8
         59             55          31. 724400
                       8 9 7
          8              9                   7
         59             57          46. 951200
                       7 9 6
          7              9                   6
         60              2           2. 5332000
                       6 9 5
          6              9                   5
         60              6          55. 324800
                       5 9 4
          5              9                   4
         59             56          59. 262000
                       4 9 3
          4              9                   3
         60              0          44. 215200
DISTANCE               8 9
          8              9          24. 006815
                       7 9
          7              9          23. 976006
                       6 9
          6              9          23. 979300
                       5 9
          5              9          23. 993596
                       4 9
          4              9          23. 987361
                       3 9
          3              9          23. 993665
DUMP                   1  99
   10. 000000          1          1180. 0000       1000. 0000
   10. 000000          2          1000. 0000       1000. 0000
   10. 000000          3          1097. 1717       1180. 6307
   10. 000000          4          1073. 2133       1179. 3065
```

```
*          ID GRIGGS   70073
*                      DIMENSIONS OF MODEL FOR CAMROC RADOME PROJECT
CLEAR                  1  99
STORE                   1 1180. 0 1000. 0
                       2  1000. 0  1000. 0
*                      PVC MODEL, DIMENSIONS 0. 70 × 0. 35
AZ/INTERSECT           3 1 114 12 30.  2 61 18 25.
          3         1098. 8233        1180. 5563
                       4 1 120 34 38.  2 67 05 31.
          4         1075. 0559        1177. 6122
                       5 1 121 15 54.  2 72 54 10.
          5         1060. 5249        1196. 7729
                       6 1 116 43 35.  2 72 18 18.
          6         1069. 8155        1218. 8266
                       7 1 111 16 50.  2 67 07 05.
          7         1093. 6102        1221. 8012
                       8 1 109 30 55.  2 61 54 57.
          8         1108. 1596        1202. 6995
                       9 1 115 36 20.  2 67 07 25.
          9         1084. 2768        1199. 7403
ANGLE                  3 9 8
           3              9                 8
          59             53         29. 655600
                       8 9 7
           8              9                 7
          60              0         17. 236800
                       7 9 6
           7              9                 6
          60              4         56. 827200
                       6 9 5
           6              9                 5
          59             58         14. 775600
                       5 9 4
           5              9                 4
          60             15         25. 192800
                       4 9 3
           4              9                 3
          59             47         36. 322800
DISTANCE               8 9
           8              9         24. 065430
                       7 9
           7              9         23. 954032
                       6 9
           6              9         23. 946107
                       5 9
           5              9         23. 936545
                       4 9
           4              9         23. 972438
                       3 9
           3              9         24. 075434
DUMP                   1  99
    10. 000000         1         1180. 0000        1000. 0000
    10. 000000         2         1000. 0000        1000. 0000
    10. 000000         3         1098. 8233        1180. 5563
    10. 000000         4         1075. 0559        1177. 6122
    10. 000000         5         1060. 5249        1196. 7729
    10. 000000         6         1069. 8155        1218. 8266
    10. 000000         7         1093. 6102        1221. 8012
    10. 000000         8         1108. 1596        1202. 6995
```

```
*          ID GRIGGS   70073
*                      DIMENSIONS OF MODEL FOR CAMROC RADOME PROJECT
CLEAR                  1  99
STORE                   1 1180.0 1000.0
                       2  1000.0  1000.0
*                       PVC MODEL 0.700 × 0.700
AZ/INTERSECT           3 1 66 30 30.  2 117 38 36.
          3          1098.3682        812.18510
                       4 1 60 26 05.  2 111 55 52.
          4          1074.7217        814.41500
                       5 1 59 51 07.  2 106 30 56.
          5          1060.8355        794.82730
                       6 1 64 19 37.  2 107 21 38.
          6          1070.9335        773.10360
                       7 1 69 34 07.  2 112 27 42.
          7          1094.6846        770.97790
                       8 1 71 07 15.  2 117 20 20.
          8          1108.3388        790.44630
                       9 1 65 17 36.  2 112 11 38.
          9          1084.5960        792.64050
ANGLE                  3 9 8
          3              9                8
        299             53         26.232000
                       8 9 7
          8              9                7
        300             15          7.6320000
                       7 9 6
          7              9                6
        300              3         43.632000
                       6 9 5
          6              9                5
        299             42         26.532000
                       5 9 4
          5              9                4
        299             39          6.3000000
                       4 9 3
          4              9                3
        300             26          9.7080000
DISTANCE               8 9
          8              9         23.843972
                       7 9
          7              9         23.896611
                       6 9
          6              9         23.840184
                       5 9
          5              9         23.860918
                       4 9
          4              9         23.908797
                       3 9
          3              9         23.909514
DUMP                   1  99
    10.000000          1         1180.0000        1000.0000
    10.000000          2         1000.0000        1000.0000
    10.000000          3         1098.3682        812.18510
    10.000000          4         1074.7217        814.41500
```

INITIAL CURVATURE OF COMPRESSION MEMBERS
FOR MODELS F 1 AND F 3

Model	Member	"Initial curvature" inches
F 1 (plexiglas)	3-9	-0. 025
	4-9	-0. 015
	5-9	+0. 045
	6-9	+0. 085
	7-9	+0. 010
	8-9	-0. 025
F 3 (PVC)	3-9	-0. 065
	4-9	-0. 025
	5-9	-0. 010
	6-9	+0. 020
	7-9	+0. 035
	8-9	-0. 015

Note

The "initial curvature" given is the ordinate of the actual center-line of the member with respect to the theoretical center-line. Measurement is made in plane of buckling.
F 1: total deviations +0. 140, -0. 065, net 0. 075 average 0. 013.
F 3: total deviations +0. 055, -0. 115, net 0. 060 average 0. 010.
The maximum deviation of 0. 085" is 1/280 of span, and the average deviation is 1/2200 of span.

ANNEX 11

FORMULATION OF THE GOVERNING EQUATIONS FOR THE BUCKLING OF A PLANAR FRAME

CAMROC WORKING MEMORANDUM

Prepared by

J. Connor

Civil Engineering Department
MIT

INTRODUCTION

In what follows, the derivation of the governing equations for the planar deformation of a planar member is outlined. The material is considered to be linear elastic and the rotation of the tangent to be sufficiently small such that the square of the rotation with respect to unity can be neglected. The notation for the end actions and displacements is summarized in Figure 1. The X_1 direction coincides with the centroidal axis.

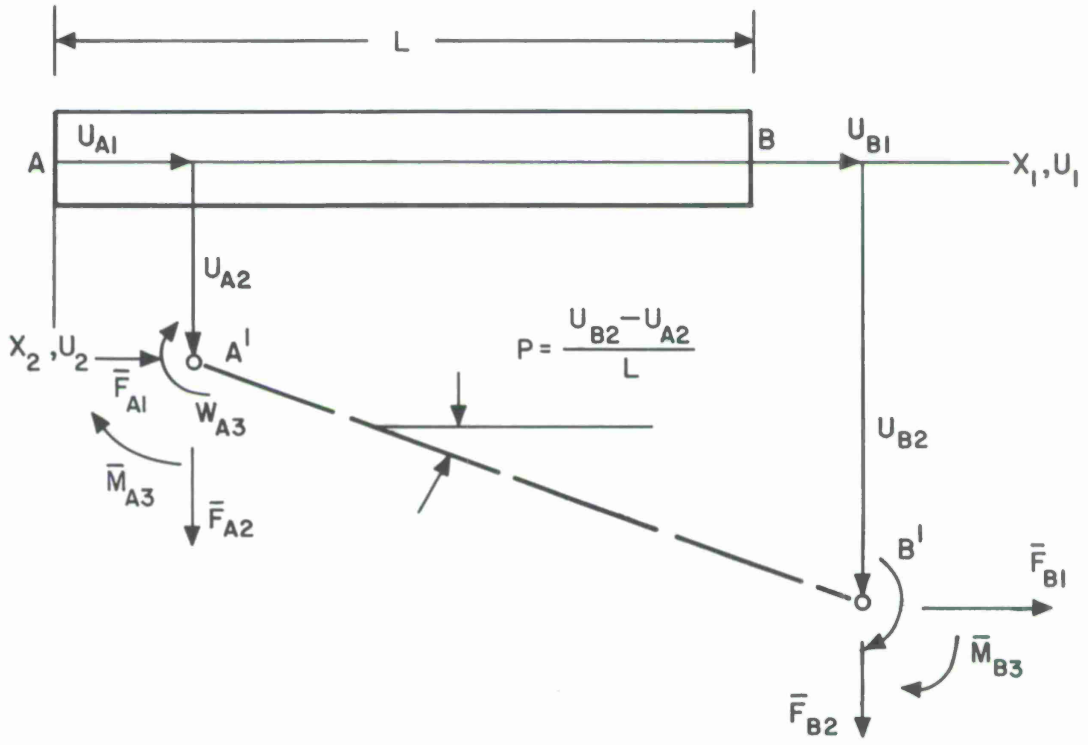

Figure 1

DIFFERENTIAL EQUATIONS AND BOUNDARY CONDITIONS

The strain-displacement relations are specialized for the case of a "small-finite" rotation and negligible transverse shear deformation:

$$
\begin{aligned}
(\varepsilon)_\zeta &= \varepsilon - \zeta K \quad , \\
\varepsilon &= U_{1,1} + \frac{1}{2}\omega^2 \quad , \\
K &= \omega, 1 \quad ,
\end{aligned}
\tag{1}
$$

where

$$
\omega = \text{rotation of the normal} = U_{2,1} \quad . \tag{2}
$$

For convenience, the subscript 3 on ω and M is dropped and the notation ( ) is used to indicate differentiation with respect to x_1. The stress resultants are related to the deformation measures by

$$
\begin{aligned}
N &= AE\varepsilon \quad , \\
M &= EIK \quad ,
\end{aligned}
\tag{3}
$$

where A is the cross-sectional area and I is the second moment of the area with respect to the x_3 axis:

$$
\begin{aligned}
A &= \int_A dx_3\, dx_3 \quad , \\
I &= \int_A x_2^2\, dA = \int \zeta^2\, dA \quad .
\end{aligned}
\tag{4}
$$

The positive sense of the internal forces is shown in Figure 2. Note that

$$
\begin{aligned}
\sin\omega &\approx \omega \quad , \\
\cos\omega &\approx 1 \quad ,
\end{aligned}
\tag{5}
$$

for $\omega^2 << 1$. The transverse shear is related to M by

$$
V = -\frac{dM}{dx_1} \quad . \tag{6}
$$

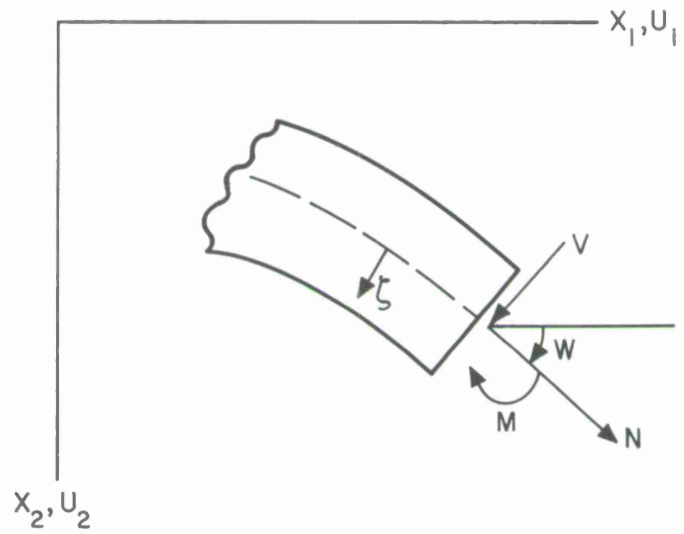

Figure 2

The principle of virtual displacements is used to establish the force-equilibrium equations and force-boundary conditions consistent with the initial geometrical approximation (i.e., $\omega^2 << 1$). The general principle is

$$dW_D = dW_E \quad , \tag{7}$$

where dW_D is the first-order work done by the internal forces (N, M) and dW_E represents the first-order work done by the external forces. For this problem, dW_D and dW_E are given by

$$dW_D = \int_0^L (N\delta\varepsilon + M\delta K)\, dx_1 \quad ,$$

$$dW_E = \overline{F}_{B1}\,\delta U_{B1} + \overline{F}_{B2}\,\delta U_{B2} + \overline{M}_B\,\delta\omega_B$$

$$+ \overline{F}_{A1}\,\delta U_{A1} + \overline{F}_{A2}\,\delta U_{A2} + \overline{M}_A\,\delta\omega_A \quad . \tag{8}$$

The first-order increments in the strain measures follow from (1):

$$\delta \varepsilon = \delta U_{1,1} + \omega \delta \omega \quad ,$$

$$\delta K = \delta \omega_1 \quad ,$$

$$\delta \omega = \delta U_{2,1} \quad . \tag{9}$$

Substituting (9) into (8) and carrying out the necessary partial integration leads to the following differential equations and boundary conditions:

$0 \leq x_1 \leq L$

$$\frac{dN}{dx_1} = 0 \quad , \tag{10}$$

$$\frac{d^2M}{dx_1^2} - \frac{d}{dx_1}(N\omega) = 0 \quad , \tag{11}$$

$x_1 = 0$

$$\overline{F}_{A1} = - N \quad ,$$

$$\overline{F}_{A2} = - N\omega_A + M_{,1} = - N\omega_A - V \quad ,$$

$$\overline{M}_A = - M \quad , \tag{12}$$

$x_1 = L$

$$\overline{F}_{B1} = + N \quad ,$$

$$\overline{F}_{B2} = N\omega_B - M_{,1} = N\omega_B + V \quad ,$$

$$\overline{M}_B = M \quad . \tag{13}$$

SOLUTION OF THE EQUATION

From (10)

$$N = \text{const} = \overline{F}_{B1} \quad . \tag{14}$$

The relative axial displacement is found from

$$\varepsilon = \frac{N}{AE} = U_{1,1} + \frac{1}{2}\,\omega^2 = U_{1,1} + \frac{1}{2}\,(U_{2,1})^2 \quad . \tag{15}$$

Integrating (15) leads to

$$U_{B1} - U_{A1} = \frac{L\overline{F}_{B1}}{AE} - \frac{1}{2}\int_0^L \omega^2\, dx_1 = \frac{L\overline{F}_{B1}}{AE} - \frac{\Delta}{2} \quad . \tag{16}$$

Equation (11) is expressed in terms of U_2 using

$$M = E\,I\,U_{2,11} \quad ,$$

$$N = \overline{F}_{B1} \quad . \tag{a}$$

The resulting equation is

$$\frac{d^4}{dx_1}(u_2) + \lambda^2 \frac{d^2}{dx_1^2}(u_2) = 0 \quad , \tag{17}$$

where

$$\lambda^2 = -\frac{\overline{F}_{B1}}{E\,I} \quad .$$

For convenience, the subscript on x_1 is dropped and the solution to equation (17) is expressed as

$$U_2 = -\frac{1}{\lambda^2}\,(C_1 \sin \lambda x + C_2 \cos \lambda x) + C_x x + C_4 \quad . \tag{18}$$

The integration constants are found from the displacement boundary conditions at $x = 0,\ L$:

$$-\frac{C_2}{\lambda^2} + C_4 = U_{A2} \quad ,$$

$$-\frac{C_1}{\lambda} + C_3 = \omega_A \quad ,$$

$$-\frac{S}{\lambda^2} C_1 - \frac{C}{\lambda^2} C_2 + C_3 L + C_4 = U_{B2} \quad ,$$

$$-\frac{C}{\lambda} C_1 + \frac{S}{\lambda} C_2 + C_3 = \omega_B \quad , \tag{19}$$

where

$$S = \sin \lambda L \qquad \text{and} \qquad C = \cos \lambda L \quad .$$

Now,

$$\phi = \lambda L = \left\{ -\frac{\overline{F}_{B1} L^2}{E I_B} \right\}^{1/2} \quad . \tag{20}$$

Note that ϕ is dimensionless. If λ is replaced by ϕ/L, then it is convenient to write

$$\overline{C}_1 = L C_1 \quad ,$$

$$\overline{C}_2 = L C_2 \quad ,$$

$$\overline{C}_4 = \frac{C_4}{L} \quad . \tag{21}$$

The "barred" constants are dimensionless. With this notation, the equations become

$$\frac{U_2}{L} = -\frac{1}{\phi^2} \left(\overline{C}_1 \sin \frac{\phi}{L} x + \overline{C}_2 \cos \frac{\phi}{L} x \right) + C_3 \frac{x}{L} + \overline{C}_4 \quad ,$$

$$\omega = -\frac{1}{\phi} \left(\overline{C}_1 \cos \phi \frac{x}{L} - \overline{C}_2 \sin \phi \frac{x}{L} \right) + C_3 \quad , \tag{22}$$

$$M = \frac{E I}{L} \left(\overline{C}_1 \sin \phi \frac{x}{L} + C_2 \cos \phi \frac{x}{L} \right) \quad , \tag{23}$$

and

$$-\frac{\overline{C}_2}{\phi^2} + \overline{C}_4 = \frac{U_{A2}}{L} \quad ,$$

$$
\begin{aligned}
&-\frac{\bar{C}_1}{\phi} + C_3 = \omega_A \quad , \\
&-\frac{S}{\phi^2}\bar{C}_1 - \frac{C}{\phi^2}\bar{C}_2 + C_3 + \bar{C}_4 = \frac{U_{B2}}{L} \quad , \\
&-\frac{C}{\phi}\bar{C}_1 + \frac{S}{\phi}\bar{C}_2 + C_3 = \omega_B \quad ,
\end{aligned} \tag{24}
$$

where

$$S = \sin\phi \qquad \text{and} \qquad C = \cos\phi \quad .$$

Solving the first two equations gives

$$
\begin{aligned}
C_3 &= \omega_A + \frac{1}{\phi}\bar{C}_1 \quad , \\
\bar{C}_4 &= \frac{U_{A2}}{L} + \frac{1}{\phi^2}\bar{C}_2 \quad .
\end{aligned} \tag{25}
$$

The remaining equations take the form

$$
\begin{aligned}
&\left\{-\frac{S}{\phi^2} + \frac{1}{\phi}\right\}\bar{C}_1 + \left\{-\frac{C}{\phi^2} + \frac{1}{\phi^2}\right\}\bar{C}_2 = \rho - \omega_A \quad , \\
&\left\{-\frac{C}{\phi} + \frac{1}{\phi}\right\}\bar{C}_1 + \left\{\frac{S}{\phi}\right\}\bar{C}_2 = \omega_B - \omega_A \quad ,
\end{aligned} \tag{a}
$$

where

$$\rho = (U_{B2} - U_{A2})/L \quad .$$

The solution of (a) is

$$\bar{C}_1 = \frac{\phi}{1-C}(\omega_B - \omega_A) - \left(\frac{S}{1-C}\right)\bar{C}_2 \quad , \tag{26}$$

$$\bar{C}_2 = -k_1\omega_A - k_2\omega_B + k_3\rho \quad , \tag{27}$$

where

$$k_1 = \frac{\phi (S - C\phi)}{2(1 - C) - S\phi} \quad ,$$

$$k_2 = \frac{\phi (\phi - S)}{2(1 - C) - S\phi} \quad ,$$

$$k_3 = k_1 + k_2 = \frac{\phi^2 (1 - C)}{2(1 - C) - S\phi} \quad . \tag{28}$$

This solution is valid for $\phi \neq 0$ and $\phi \neq 2\pi$.

EVALUATION OF THE END MOMENTS AND SHEARS

The end moments are

$$\overline{M}_B = [M]_{x = L} \quad ,$$

$$\overline{M}_A = [-M]_{x = 0} \quad .$$

Specializing (23) yields

$$\frac{L}{EI} \overline{M}_A = - \overline{C}_2 \quad ,$$

$$\frac{L}{EI} \overline{M}_B = S\overline{C}_1 + C\overline{C}_2 \quad . \tag{29}$$

If we substitute for $\overline{C}_1$ by use of (26), the expression for $\overline{M}_B$ becomes

$$\frac{L}{EI} \overline{M}_B = - \overline{C}_2 + \frac{S\phi}{1 - C} (\omega_B - \omega_A) \quad . \tag{30}$$

Finally, if we substitute for $\overline{C}_2$, the resulting relations are

$$\frac{L}{EI} \overline{M}_A = k_1 \omega_A + k_2 \omega_B - k_3 \left(\frac{U_{B2} - U_{A2}}{L} \right) \quad ,$$

$$\frac{L}{EI}\overline{M}_B = k_2\omega_A + k_1\omega_B - k_3\left(\frac{U_{B2} - U_{A2}}{L}\right) \quad . \tag{31}$$

The shears are determined using (12) and (13). This leads to (note that $k_1 + k_2 = k_3$)

$$\overline{F}_{B2} = \frac{EI}{L^2}k_3\left\{-\omega_A - \omega_B + 2\left(\frac{U_{B2} - U_{A2}}{L}\right)\right\} + \overline{F}_{B1}\rho \quad ,$$

$$\overline{F}_{A2} = \frac{EI}{L^2}k_3\left\{\omega_A + \omega_B - 2\left(\frac{U_{B2} - U_{A2}}{L}\right)\right\} - \overline{F}_{B1}\rho \quad . \tag{32}$$

Note that the term involving $\overline{F}_{B1}$ is due to the rotations ρ of the member. If the joint displacements are small (e.g., no sidesway), this term can be omitted.

DETERMINATION OF (Δ/L)

The quantity Δ/L is defined by

$$\frac{\Delta}{L} = \frac{1}{L}\int_0^L \omega^2\,dx \quad , \tag{a}$$

where ω is the rotation of the tangent to the centroidal axis. Now, from (22),

$$\omega = -\frac{1}{\phi}(\overline{C}_1\cos\lambda x - \overline{C}_2\sin\lambda x) + C_3 \quad . \tag{b}$$

Substituting for ω in (a) and evaluating the resulting integrals leads to

$$\frac{\Delta}{L} = C_3^2 + \frac{2C_3}{\phi^2}\left[-S\overline{C}_1 + (1-C)\overline{C}_2\right] + \overline{C}_1 C_2\left[-\frac{S^2}{\phi^3}\right]$$
$$+ \frac{\overline{C}_1^2}{2\phi^2}\left[1 + \frac{SC}{\phi}\right] + \frac{\overline{C}_2^2}{2\phi^2}\left[1 - \frac{SC}{\phi}\right] \quad . \tag{33}$$

If the effect of bending is neglected, $\omega \approx \rho$ and

$$\frac{\Delta}{L} \approx \rho^2 = \left(\frac{U_{B2} - U_{A2}}{L}\right)^2 \quad . \tag{34}$$

SUMMARY OF FORCE-DISPLACEMENT RELATIONS

$\underset{\sim}{\bar{F}}$ and $\underset{\sim}{u}$ are defined as

$$\underset{\sim}{\bar{F}} = \left\{F_1, F_2, M_3\right\} \quad ,$$

$$\underset{\sim}{u} = \left\{u_1, u_2, \omega_3\right\} \quad .$$

Collecting (16), (31), and (32), the complete set of end action — end displacement relations are written in matrix form as

$$\begin{Bmatrix} \underset{\sim}{\bar{F}}_B \\ \hline \underset{\sim}{\bar{F}}_A \end{Bmatrix} = \left[\begin{array}{cc:c} \underset{\sim}{k}_{BB} & \underset{\sim}{k}_{BA} & \underset{\sim}{U}_B \\ \hline \underset{\sim}{k}^T_{BA} & \underset{\sim}{k}_{AA} & U_A \end{array}\right] + \begin{Bmatrix} \underset{\sim}{F}_0 \\ \hline -\underset{\sim}{F}_0 \end{Bmatrix} \quad , \tag{35}$$

where $\underset{\sim}{k}_{BB}$ $\underset{\sim}{k}_{AA}$ are symmetrical and $\underset{\sim}{F}_0$ contains the second-order terms due to the rotation, i.e., the nonlinear geometrical terms. The expanded form of (35) is listed below:

$$\begin{Bmatrix} F_{B1} \\ F_{B2} \\ M_{B3} \\ F_{A1} \\ F_{A2} \\ M_{A3} \end{Bmatrix} = \begin{array}{c} \begin{matrix} U_{B1} & U_{B2} & \omega_{B2} & U_{A1} & U_{A2} & \omega_{A3} \end{matrix} \\ \begin{bmatrix} \frac{AE}{L} & & & -\frac{AE}{L} & & \\ & 2k_3\frac{EI_3}{L^3} & -k_3\frac{EI_3}{L^3} & & -2k_3\frac{EI_3}{L^3} & -k_3\frac{EI_3}{L^2} \\ & -k_3\frac{EI_3}{L^2} & k_1\frac{EI_3}{L} & & k_3\frac{EI_3}{L^2} & k_2\frac{EI_3}{L} \\ -\frac{AE}{L} & & & \frac{AE}{L} & & \\ & -2k_3\frac{EI_3}{L^3} & k_3\frac{EI_3}{L^2} & & 2k_3\frac{EI_3}{L^3} & k_3\frac{EI_3}{L^2} \\ & -k_3\frac{EI_3}{L^2} & k_2\frac{EI_3}{L} & & k_3\frac{EI_3}{L^2} & k_1\frac{EI_3}{L} \end{bmatrix} \end{array} \begin{Bmatrix} U_{B1} \\ U_{B2} \\ \omega_{B3} \\ U_{A1} \\ U_{A2} \\ \omega_{A3} \end{Bmatrix} + \begin{Bmatrix} \frac{AE}{2}(\Delta/L) \\ \bar{F}_{B1}\rho \\ 0 \\ -\frac{AE}{2}(\Delta/L) \\ -\bar{F}_B\rho \\ 0 \end{Bmatrix} \quad ,$$

$$\rho = \frac{1}{L}\left(U_{B2} - U_{A2}\right) \quad . \tag{36}$$

INCREMENTAL LOADING TECHNIQUE

The general end-action – end-displacement relations are given by (35), which are written as

$$\underset{\sim}{F} = \underset{\sim}{K}\,\underset{\sim}{U} + \underset{\sim}{F}_0 \quad . \tag{37}$$

Now, $\underset{\sim}{K}$ depends on the axial force, i.e., the nonlinearity in $\underset{\sim}{K}$ is due to the effect of axial force on the flexibility of the member. Fortunately, the coefficients (k_1, k_2, k_3) vary rather slowly with ϕ, the axial force parameter. The elements of $\underset{\sim}{F}$ are due to the finite chord rotation ρ and the effect of rotation (of the tangent) on the axial strain.

Now, it is assumed that the system is in equilibrium and an incremental joint load is applied. Since $\underset{\sim}{K}$ varies slowly with ϕ, the change in $\underset{\sim}{K}$ is neglected. This is reasonable if the loading increment is small. The increments in the end actions are

$$\Delta\underset{\sim}{F} \approx \underset{\sim}{K}\,\Delta\underset{\sim}{U} + \Delta\underset{\sim}{F}_0 \quad , \tag{38}$$

where $\underset{\sim}{K}$ is evaluated at the position prior to the application of the load increment; ΔF_0 remains to be evaluated:

$$\underset{\sim}{F}_0 = \begin{Bmatrix} \underset{\sim}{F}_0 \\ \text{----} \\ -\underset{\sim}{F}_0 \end{Bmatrix} \quad , \tag{a}$$

$$\underset{\sim}{F}_0 = \begin{Bmatrix} \frac{AE}{2}\left(\frac{D}{L}\right) \\ \text{------} \\ \bar{F}_{B1}\,\rho \\ \text{------} \\ 0 \end{Bmatrix} \quad .$$

Assuming $\Delta\underset{\sim}{a}$ is small,

$$\Delta \underset{\sim}{F}_0 \approx d \underset{\sim}{F}_0 = \left\{ \begin{array}{c} \frac{AE}{2} d(\Delta/L) \\ \hline \bar{F}_{B1} \, d\rho + \rho d \bar{F}_{B1} \\ \hline 0 \end{array} \right\} \quad , \tag{b}$$

where d( ) denotes the first differential, i.e., the first-order change due to increments in the end displacements. Now,

$$d\rho = \frac{1}{L} \left(\Delta U_{B2} - \Delta U_{A2} \right) \quad ,$$

$$d\bar{F}_{B1} = \frac{AE}{L} \left(\Delta U_{B1} - \Delta U_{A1} \right) + \frac{AE}{2} d(\Delta/L) \quad , \tag{c}$$

$$d\left(\frac{\underset{\sim}{\Delta}}{L}\right) = \frac{2}{L} \int_0^L \omega \, d\omega \, dx \quad . \tag{d}$$

Now,

$$d\omega = \text{const} = d\rho \quad . \tag{e}$$

This is consistent with neglecting the change in $\underset{\sim}{K}$, and corresponds to neglecting the incremental rotation due to bending. Equation (d) reduces to

$$d(\Delta/L) \approx \frac{2}{L} d\rho \int_0^L \omega \, dx \quad .$$

But,

$$\omega = \frac{dU_2}{dx}$$

It follows that

$$\frac{1}{L} \int_0^L \omega \, dx = \frac{U_{B2} - U_{A2}}{L} = \rho$$

and

$$d(\Delta/L) \approx 2\rho \, d\rho \quad . \tag{f}$$

Finally,

$$\Delta\underset{\sim}{F}_0 = \left\{ \begin{array}{c} \dfrac{AE\rho}{L}\left(\Delta U_{B2} - \Delta U_{A2}\right) \\ \hline \dfrac{AE\rho}{L}\left(\Delta U_{B1} - \Delta U_{A1}\right) + \left(\dfrac{AE\rho^2}{L} + \dfrac{\bar{F}_{B1}}{L}\right)\left(\Delta U_{B2} - \Delta U_{A2}\right) \\ \hline 0 \end{array} \right\} \quad ; \tag{39}$$

$\Delta\underset{\sim}{F}_0$ is expressed as

$$\Delta\underset{\sim}{F}_0 = \underset{\sim}{k}_G(\underset{\sim}{U}_B - \underset{\sim}{U}_A) \quad , \tag{40}$$

where

$$\underset{\sim}{k}_G = \underset{\sim}{k}_G^T = \begin{bmatrix} 0 & \dfrac{AE\rho}{L} & 0 \\ \dfrac{AE\rho}{L} & \dfrac{AE\rho^2}{L} + \dfrac{\bar{F}_{B1}}{L} & 0 \\ 0 & 0 & 0 \end{bmatrix} \tag{41}$$

Using (40)

$$\Delta\underset{\sim}{F}_0 = \underset{\sim}{K}_G \, \Delta\underset{\sim}{U} \quad , \tag{42}$$

where

$$\underset{\sim}{K}_G = \underset{\sim}{K}_G^T = \left[\begin{array}{c|c} \underset{\sim}{k}_G & -\underset{\sim}{k}_G \\ \hline -\underset{\sim}{k}_G & \underset{\sim}{k}_G \end{array}\right] \quad . \tag{43}$$

Substituting for $\Delta\underset{\sim}{F}_0$ in (38) leads to the following equations for $\Delta\underset{\sim}{F}$:

$$\Delta\underset{\sim}{F} = (\underset{\sim}{K} + \underset{\sim}{K}_G)\,\Delta\underset{\sim}{U} = \underset{\sim}{K}_I \, \Delta\underset{\sim}{U} \quad . \tag{44}$$

The expanded form of (44) is

$$\begin{Bmatrix} \Delta\bar{F}_B \\ \hline \Delta\bar{F}_A \end{Bmatrix} = \left[\begin{array}{c|c} \underset{\sim}{k}_{BB} + \underset{\sim}{k}_G & \underset{\sim}{k}_{BA} - \underset{\sim}{k}_G \\ \hline \underset{\sim}{k}^T_{BA} - \underset{\sim}{k}_G & \underset{\sim}{k}_{AA} + \underset{\sim}{k}_G \end{array}\right] \begin{Bmatrix} \Delta\underset{\sim}{U}_B \\ \hline \Delta\underset{\sim}{U}_A \end{Bmatrix} \quad . \tag{45}$$

Note that $\underset{\sim}{K}_I$ is evaluated at the position defined by $\underset{\sim}{U}$, i.e., the position before the incremental load is applied.

CORRECTION PROCEDURE

The exact end-action — end-displacement relations are given by

$$\underset{\sim}{F} = \underset{\sim}{K}\,\underset{\sim}{U} + \underset{\sim}{F}_0 \quad . \tag{a}$$

Since $\underset{\sim}{K}$ and $\underset{\sim}{F}_0$ depend on $\underset{\sim}{U}$, one must generally resort to an iterative procedure in order to obtain the solution for a specified loading. It is convenient to evaluate $\underset{\sim}{K}$ and $\underset{\sim}{F}_0$ using $\underset{\sim}{U}$ determined from the previous cycle. That is, the relations for cycle n + 1 are

$$\underset{\sim}{F}^{(n+1)} = \underset{\sim}{K}^{(n)}\,\underset{\sim}{U}^{(n+1)} + \underset{\sim}{F}_0^{(n)} \quad , \tag{46}$$

where $\underset{\sim}{K}^{(n)}$ denotes $\underset{\sim}{K}$ evaluated at $\underset{\sim}{U} = \underset{\sim}{U}^{(n)}$. The iteration is continued until successive values of the joint displacements agree to the desired accuracy.

Now, the linearized incremental approach is combined with the iterative procedure outlined above. This involves correcting the solution after a certain number of loading increments. The displacements obtained with the incremental approach are used as starting values for the iteration. Once convergence is obtained, then the process is repeated again with the incremental approach, using K_I evaluated at the corrected displacements. This procedure is illustrated below:

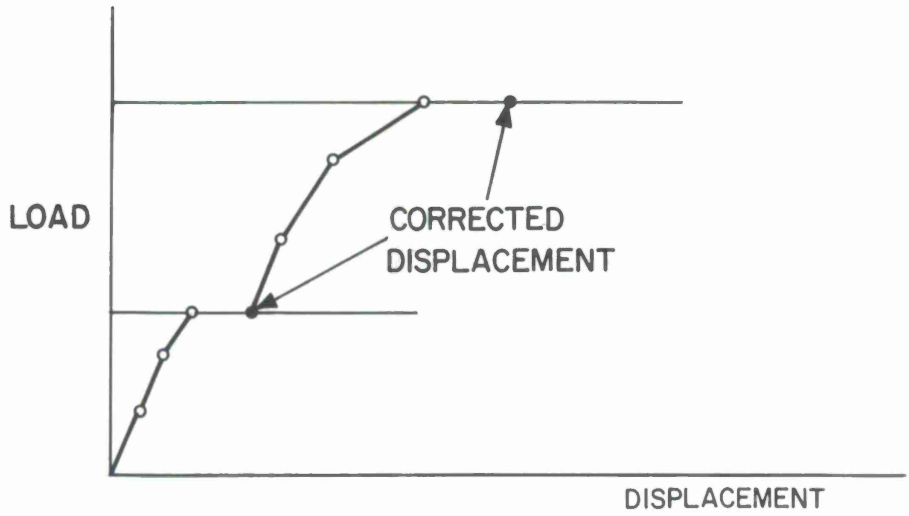
LOAD
CORRECTED
DISPLACEMENT
DISPLACEMENT

ANNEX 12

SURFACE-PANEL GEOMETRY FOR HAMMERHEAD ANTENNA CONCEPT

CAMROC WORKING MEMORANDUM

5 January 1967

Prepared by

John F. Hutzenlaub

MIT Lincoln Laboratory

SURFACE-PANEL GEOMETRY FOR HAMMERHEAD ANTENNA CONCEPT

I. INTRODUCTION

Most present paraboloidal antenna reflectors have been designed as structures having circular symmetry about the paraboloidal axis. Such structures naturally provide support points for pie-shaped surface panels. The number of different types of panels required for the complete surface is essentially a function of the radial dimensions of successive circular rows of panels.

The structural concept employed for the Hammerhead antenna reflector is rectangular in keeping with the fact that the only appreciable mechanical loading experienced is that due to gravity. If a surface supporting substructure is to be avoided in the Hammerhead concept, it would appear that square or rectangular panels should be utilized. However, in the limit of doubly curved sections of the paraboloid, a great number of different type panels would result since there would be just four panels of any given type, one in each quadrant of the paraboloid.

In an attempt to minimize the number of types of rectangular surface panels required for Hammerhead, geometries other than sections of a paraboloid are considered in this memorandum. For this purpose, a portion of the error budget for surface inaccuracies and deviations has been allotted to the resulting nonideal geometry of the surface panels. In this memoradum, the geometrical R. M. S. surface error has been assumed to be a maximum of 0. 025 inch. Thus, if the total permissible R. M. S. surface error were 0. 075 inch, the contribution from all other sources than geometry would be limited to 0. 0707-inch R. M. S.

The coordinate system used for this analysis is shown in Figure 1. The vertex of the paraboloid is at the origin and the z axis is the RF axis of the reflector. It is assumed that the reflector of interest has a nominal diameter of 400 feet and a focal length of 160 feet.

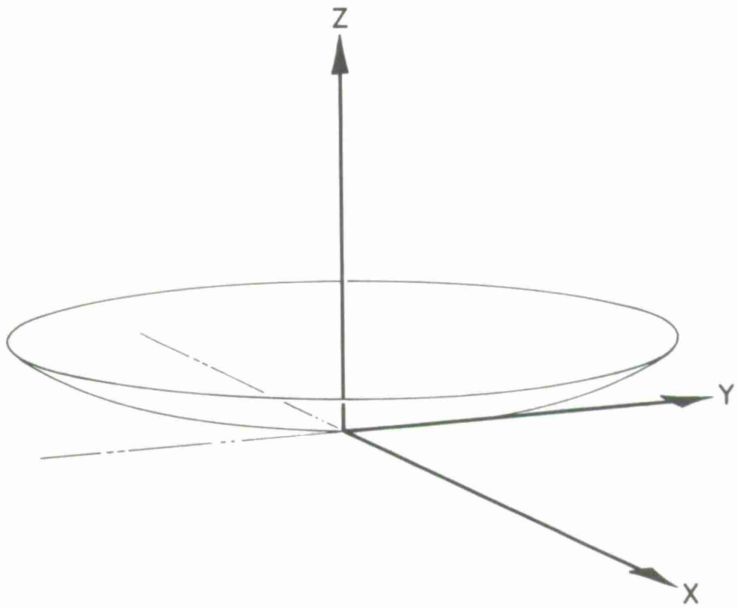

Figure 1. Coordinate system for paraboloid of revolution.

II. SURFACE-PANEL GEOMETRY

A. Flat-Plate Panels

The simplest type of panel is a flat plate. Square panels with their edges parallel to the xz and yz planes are utilized to approximate the surface of the paraboloid. For a given panel, the equation of the plane is

$$z - z_0 = mx + ny, \tag{1}$$

where z_0 = z axis intercept of the plane

m = slope of edge of panel parallel to the xz plane

n = slope of edge of panel parallel to the yz plane.

The geometry involved in fitting a typical panel is shown in Fig. 2. This represents the projection of the panel edge parallel to the xz plane on the xz plane. A similar projection on the yz plane exists for the other edge of the flat-plate panel. It should be noted that the focal length, f, of the parabola shown is the same as the focal length of the paraboloid.

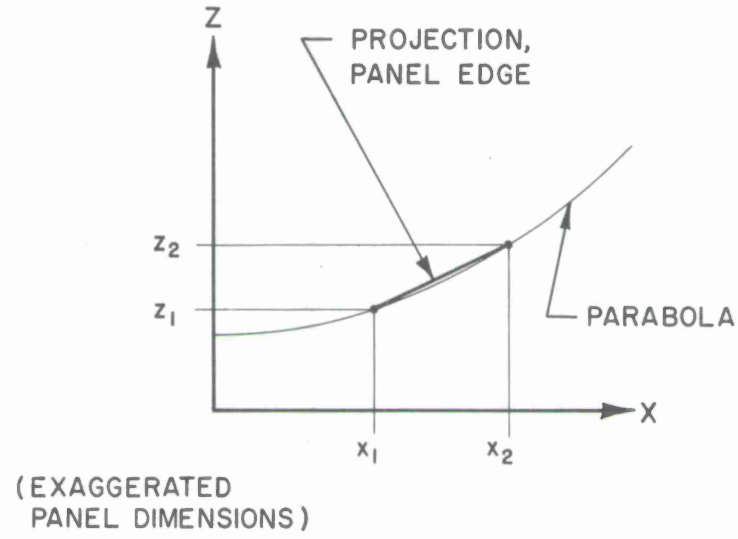

Figure 2. Geometry for flat-plate surface panel.

For given values of x_1 and z_1, which at the vertex of the paraboloid would be $x_1 = 0$ and $z_1 = 0$, one determines x_2, z_2 and m in terms of the panel-edge dimension, w, as follows:

$$x_2^2 = 4fz_2 \tag{2}$$

$$\left(x_2 - x_1\right)^2 + \left(z_2 - z_1\right)^2 = w^2 \quad . \tag{3}$$

Solving these simultaneously,

$$x_2^4 + 16f^2\left(1 - \frac{z_1}{2f}\right)x_2^2 - 32f^2\, x_1 x_2 + 16f^2\left(x_1^2 + z_1^2 - w^2\right) = 0 \quad .$$

Having determined x_2, z_2 is obtained from (2) and,

$$m = \frac{z_2 - z_1}{x_2 - x_1} \quad . \tag{4}$$

A similar calculation is performed for the panel edge parallel to the yz plane to obtain the value of n in (1). Finally, values of x, y, and z for a point in the plane are substituted in (1) to obtain the value of z_0.

The deviations of the flat-plate panel from the paraboloid can be obtained by taking the difference between the z obtained from (1) and the z for the paraboloid given by

$$z = \frac{x^2 + y^2}{4f} \quad . \tag{5}$$

The minimum R. M. S. error or best fit for the panel is obtained by a translation of the panel parallel to the z axis such that the mean of the average deviation in z is zero. For this purpose, averages of the deviations over the range of 0.25 - 1.0 square foot of the panel are adequate.

To fit panels to the complete surface of the paraboloid, one starts at the vertex for which $x_1 = y_1 = z_1 = 0$ and then uses the x_2 and y_2 for this panel as the x_1 and y_1 for the next successive row and column of panels. Thus, adjacent panels have their respective edges in the same plane with the planes of the flat plates tilted with respect to each other. From the minimum R. M.S. errors for the separate panels, a measure of the geometrical R. M. S. surface error for the paraboloid can be obtained as the square root of the mean of the square of the individual panel errors. This last calculation assumes equal weighting for all panels. If illumination taper or other effects are introduced, suitable weighting factors should be assigned to the individual panels.

In fitting a flat-plate panel to the surface of the paraboloid, the resulting R. M. S. error will depend upon the radius of curvature of the paraboloid. The smaller the radius of curvature, the larger the error for a given panel dimension, w. Thus, the deviations will be a maximum in the central portion of the reflector for a fixed w. To determine the order of magnitude of errors involved, the above relationships were used to calculate the minimum R. M. S. errors for flat-plate panels having a nominal dimension, w = 4 feet.

For a 4-foot square panel in the region of the vertex of the paraboloid the minimum R. M. S. error is 0. 030 inch. In the regions of y = 0, x = ±200 feet and y = ±200 feet, x = 0, the error is 0.026 inch. In the regions of y = ±140 feet, x = ±140 feet, the error is 0. 025 inch.

If the maximum allotted geometrical R. M. S. surface error of 0. 025 inch is to be met, it would appear advisable to reduce the individual panel errors to this value in the intensely illuminated central portion of the reflector. The resulting panel dimension for this error is approximately 3. 65 feet. Since the area of the paraboloid is approximately 137, 000 square feet, more than ten thousand (10, 000) 3. 65-foot square flat-plate panels would be required to meet the allotted geometrical surface error. This number is considered excessive from installation and rigging standpoints. Panels other than rectangular flat plates were therefore investigated for possible application in the Hammerhead antenna concept.

B. Singly Curved Panels

Next to a flat plate, the simplest type rectangular panel is one that is singly curved and has a constant radius of curvature in the curved dimension. Such panels are sections of the surface of a right circular cylinder, the flat dimension being an element of the cylinder. In this analysis it is assumed that the flat dimension, w, of all panels is the same and that the chordal length, h, of the curved dimension of all panels is the same. The geometry involved is shown in Fig. 3.

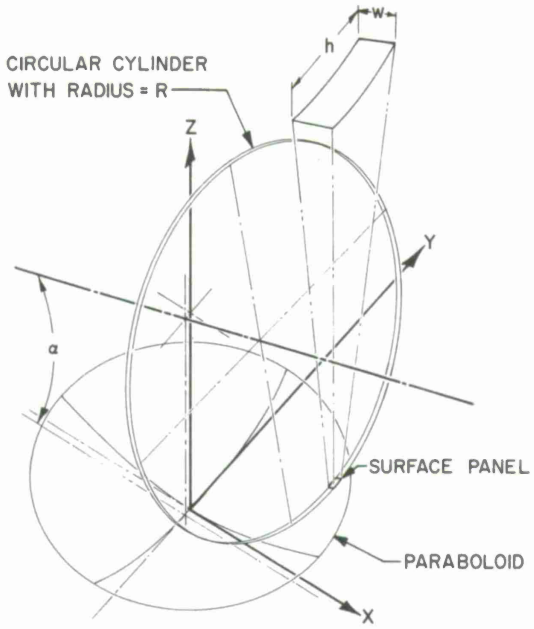

Figure 3. Geometry for singly curved surface panel.

For the purpose of fitting the singly curved panels to the paraboloid, it is assumed that the axis of the circular cylinder is rotated about the y axis through the angle α and displaced parallel to the xz plane. As shown in Fig. 4, the intersection of the cylinder with the yz plane is the ellipse

$$a^2(y - y_0)^2 + b^2(z - z_0)^2 = a^2 b^2 \tag{6}$$

where

y_0, z_0 are the coordinates of the center of the ellipse

a = semimajor axis of the ellipse

b = semiminor axis of the ellipse .

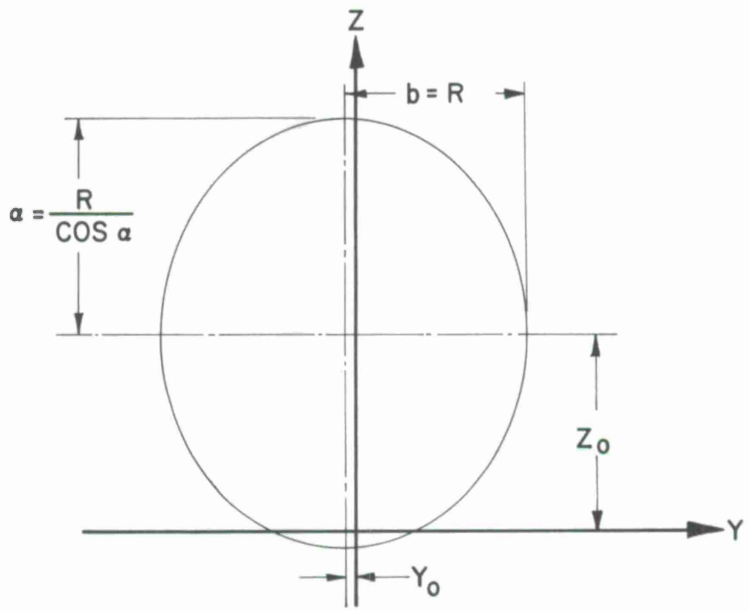

Figure 4. Intersection of cylinder with yz plane.

Since the axis of the cylinder is rotated only about the y axis, the equations for any element of the cylindrical surface are

$$y = u \tag{7}$$

$$z = mx + v \quad , \tag{8}$$

where m is the slope of the projection of an element on the xz plane, or

$$m = \tan \alpha \quad . \tag{9}$$

Letting x = 0 in (7) and (8) gives the coordinates of the point at which any element of the cylindrical surface pierces the yz plane. All these points lie on the ellipse and therefore substituting in (6)

$$a^2(u - y_0)^2 + b^2(v - z_0)^2 = a^2 b^2 \quad . \tag{10}$$

Solving (7) and (8) for u and v and substituting in (10) one obtains

$$a^2(y - y_0) + b^2 (z - mx - z_0)^2 = a^2 b^2 \quad . \tag{11}$$

Noting that

$$a = R/\cos \alpha$$

$$b = R$$

where R is the radius of the cylinder, one has as the equation of the cylindrical surface

$$(y - y_0)^2 + \cos^2 \alpha (z - x \tan \alpha - z_0)^2 = R^2 \quad . \tag{12}$$

For determining the constants in (12) for a given panel and therefore fitting it to the surface of the paraboloid, the flat dimension edges of length, w, constitute elements of the cylinder. The sequence for fitting them is the same as that outlined for the flat-plate panel above. From this fitting a value for m and, therefore, α is obtained. The geometry for fitting the curved dimension is similar. The ends of the chordal length, h, for one edge of the panel are made to coincide with points on a paraboloid determined by a constant value of x. Calling these two points x_1, y_1, z_1 and x_1, y_2, z_2, one has for y_0 and z_0

$$(y_1 - y_0)^2 + \cos^2 \alpha (z_1 - x_1 \tan \alpha - z_0)^2 = R^2 \tag{13}$$

$$(y_2 - y_0)^2 + \cos^2 \alpha (z_2 - x_1 \tan \alpha - z_0)^2 = R^2 \quad . \tag{14}$$

The radius of curvature, R, nominally is taken as the mean value of the radius of curvature of the parabola over the interval x_1, y_1, z_1 to x_1, y_2, z_2. The radius of curvature of the parabola at any point is given by

$$R = \frac{2}{f^{1/2}} (z + f)^{3/2} \quad . \tag{15}$$

In (13) and (14) let

$$A_1 = z_1 - x_1 \tan \alpha$$

$$A_2 = z_2 - x_1 \tan \alpha$$

$$K_1 = \cos^2 \alpha$$

$$K_2 = R^2 \quad .$$

Then one has for y_0 and z_0

$$(y_1 - y_0)^2 + K_1 (A_1 - z_0)^2 = K_2 \tag{16}$$

$$(y_2 - y_0)^2 + K_1 (A_2 - z_0)^2 = K_2 \quad . \tag{17}$$

Solving (15) for z_0 and substituting in (17) one obtains for y_0

$$\left\{4(y_1 - y_2)^2 + 4K_1 (A_2 - A_1)^2 \right\} y_0^2$$

$$+\left\{4(y_1 - y_2)\left[y_2^2 - y_1^2 + K_1 (A_2 - A_1)^2\right] - 8K_1 y_1 (A_2 - A_1)^2 \right\} y_0$$

$$+\left\{ \left[y_2^2 - y_1^2 + K_1 (A_2 - A_1)^2\right]^2 - 4K_1 (A_2 - A_1)^2 \left(K_2 - y_1^2\right) \right\} = 0 \quad . \tag{18}$$

Substituting the value of y_0 from (18) in either (16) or (17) gives z_0 and therefore the remaining constant for (12).

The deviations of the singly curved panel from the paraboloid can be obtained by taking the difference between the z obtained from (12) and the z for the paraboloid given by (5). As in the case of the flat-plate panel, the minimum R. M. S. error or

best fit for the singly curved panel is obtained by a translation of the panel parallel to the z axis such that the mean of the average deviation in z is zero. Again, averages of the deviations over the range of 0.25 - 1.0 square foot of the panel are adequate.

To demonstrate the feasibility of utilizing singly curved panels for the Hammerhead antenna reflector, values of w and h were selected and an estimate of the reflector geometrical R.M.S. error obtained from calculations of the R.M.S. errors for a limited number of panels. The values selected were based on sample calculations of deviations and were w = 4 feet and h = 13 feet. A value of 4 feet for the flat dimension of the panel gives R.M.S. panel errors of approximately 0.021 inch in the central portion of the reflector. For the 13-foot chordal dimension of curved panel, it was found that the same radius of curvature could be used for two adjoining rows in the y direction without introducing a significant additional error. The controlling error resulting from the h dimension is that due to increasing values of the angle α. This error, which becomes significant for x greater than 100 feet, produces an R.M.S. panel error of approximately 0.043 inch for x = 200 feet. It does, however, decrease with increasing y for a given x, being approximately 35 percent less for maximum y at the edge of the reflector.

One additional deviation exists in a surface composed of singly curved panels. This deviation is due to the fact that the curved dimension of adjacent panels will only abut at the ends of the panels. The separation at the midpoint of the curved dimension will be a maximum in the central portion of the reflector where the radius of curvature is a minimum and the rate of change of the angle α is a maximum. For h = 13 feet the maximum separation is 0.010 inch, which is considered negligible for the CAMROC application.

Based on the calculation of R.M.S. errors for representative panels, it has been concluded that the geometrical R.M.S. surface-error requirement of 0.025 inch can be met utilizing singly curved panels with dimensions of 4 feet by 13 feet. Without attempting to tailor reflector rim panels to form a circle, 2944 panels of nine different types are required for the Hammerhead antenna concept. The different types correspond to different constant radii of curvature for the 13-foot

dimension. Based on the area of the panels, the effective diameter of the resulting reflector is approximately 420 feet. Since this simplest type of singly curved panel was found to meet the geometrical R. M. S. surface-error requirement, no other types were investigated.

III. RECOMMENDATIONS

Based on the results outlined above, it is recommended that consideration be given to the use of singly curved rectangular surface panels for the Hammerhead or any similar antenna concept that may be proposed for CAMROC. Such consideration should include an examination of the maximum value that can be allotted to the geometrical surface error since any increase above the value assumed here will permit the use of larger panels and, hence, a smaller number. If further consideration is given to rectangular panels, it is also recommended that a program be written for the 360/67 computer to calculate panel positions, panel R. M. S. errors, and the R. M. S. surface error for the complete reflector.

ANNEX 13

REPORT TO THE CAMBRIDGE RADIO OBSERVATORY COMMITTEE

CAMROC WORKING MEMORANDUM

Prepared by

Panel for Antenna Surface Accuracy Measurement

Smithsonian Astrophysical Observatory
Harvard College Observatory
Massachusetts Institute of Technology
MIT Lincoln Laboratory

ABSTRACT

The Panel for Antenna Surface Accuracy Measurement (PASAM), a working group of the Cambridge Radio Observatory Committee (CAMROC) in Cambridge, Mass., has investigated the problems associated with determining the surface geometry of a steerable, radome-enclosed 400-foot diameter antenna system. The most difficult problem has been established as being the determination of the primary reflector-surface geometry by the measurement of several thousand target points on that surface.

It was found desirable to aim for a 15-minute time for the complete measurement cycle to prevent thermal changes from seriously affecting the reflector before the measurement cycle is completed. The planned operation of the antenna system up to 6 GHz requires a reflector-surface accuracy of 0.10-inch rms. Hence, location of target points on the reflector within 0.05 inch is desirable, an angular resolution better than 3.5 arc sec.

Several general techniques feasible for the measurement, such as photogrammetry, electromagnetic ranging, and automated civil engineering, have been thoroughly investigated, and measurement schemes used in the past are illustrated and discussed.

The Panel's investigation revealed that photogrammetry, in its present state of development, could not meet the accuracy requirements and that electromagnetic ranging techniques still require considerable engineering development with attendant high costs and high risk. Automated civil-engineering techniques, on the other hand, were found to be capable of meeting the accuracy and speed requirements. These techniques also appear to involve a minimum of developmental aspects and offer promise of low cost and risk.

Consequently, a conceptual design of an automated theodolite system meeting all the CAMROC telescope requirements was evolved. Recommended as a proposed system, it is presented here. The total cost of this measurement system is estimated at approximately $300,000. Supporting calculations covering speed of operation, illumination, electronics, and optics requirements developed by the Panel are presented.

I. INTRODUCTION

The Cambridge Radio Observatory Committee (CAMROC), as part of its overall program to investigate the feasibility of establishing a large radio-astronomy facility in the Northeastern United States, has assigned the study of particular aspects of this major project to several separate smaller groups. One such group, the Panel for Antenna Surface Accuracy Measurement (PASAM), was originated in April 1966. It consists of staff members from Lincoln Laboratories, Massachusetts Institute of Technology, and Smithsonian Astrophysical Observatory. (See note on page iii for a list of members and their affiliations.)

The overall purpose of PASAM is to provide CAMROC with information relative to the measurement of the accuracy of a large antenna. After meetings and individual contributions during the past 6 months, PASAM submits this first interim report. (An abstract report was submitted on September 1, 1966, to the CAMROC Project Office to provide information required for proposal preparation.)

This report presents as much of the background information collected by PASAM as is relative to CAMROC. This presentation discusses various techniques, proposes a system that appears to satisfy the immediate requirements of CAMROC, and recommends future considerations pertinent to antenna-accuracy determination.

II. THE MEASUREMENT PROBLEM AND THE REQUIRED MEASURING-SYSTEM CHARACTERISTICS

A. Introduction

We will first define the characteristics of the required large antenna. PASAM has assumed that the CAMROC antenna will be a paraboloidal main reflector, approximately 400 ft in diameter, combined with a smaller subreflector in a Cassegrain or Gregorian configuration. In addition, we have assumed that this antenna will be fully steerable on an elevation-over-azimuth mount and will be completely enclosed within a space-frame radome. We are aware that antenna configurations and arrangements not within the above definition have been and are being considered by CAMROC, but for the purposes of our study, we have chosen to apply the above definition. Should any other antenna configuration be selected by CAMROC, the majority of the PASAM effort will still be directly applicable.

B. Discussion

1. Antenna measurements as related to antenna characteristics

Many theoretical approaches to the determination of antenna electrical characteristics have been published.[1] From these has evolved a basic technique of determining these characteristics by performing some form of geometric measurement on the antenna.

The electrical characteristics of the antenna are uniquely defined by a knowledge of the spatial current distribution induced in the main reflector and the subreflector. Since these currents are confined to the surfaces of the reflectors, a knowledge of the spatial surface geometry determines the spatial current distribution and hence the antenna electrical characteristics.

Determination of the antenna electrical characteristics from the actual spatial surface geometry of an actual antenna system, especially a large

antenna, is difficult. However, an adequate approximation of the antenna electrical characteristics can be obtained if we represent the actual reflector surfaces by "best-fit" geometrically simple theoretical surfaces – a paraboloid for the main reflector and a hyperboloid or ellipsoid for the subreflector – and if we have knowledge of the spatial geometric relationship between the main reflector and the subreflector. From such a simplified representation it is only a matter of machine computation to arrive at a reasonable approximation of the antenna-system characteristics.

The geometric relationship between the main reflector and the subreflector can be implied or measured readily and adequately by direct, state-of-the-art methods. The subreflector, relatively small and hence relatively rigid, can be fabricated to reasonably close tolerances, measured with sufficient accuracy, and maintained in such a manner that the theoretical hyperboloidal or ellipsoidal representation of its surface is readily determined.

On the other hand, determining the best-fit paraboloidal representation of the main reflector is a difficult task and represents the greatest source of error in the whole determination of the antenna electrical characteristics. Because the main reflector is very large compared to the other pertinent components and, for economy and other reasons, must be lightly constructed, rigidity is limited. Gravity forces, which will change relative to the main reflector with variations of elevation angle, will affect the main reflector. In addition, differential thermal expansion forces due to nonisothermal and nonstatic thermal environments, as well as manufacturing and assembly tolerances, lead to serious deviations of the surface from the intended true paraboloidal shape. Inertial forces will be negligibly small because of the modest tracking rates anticipated in the CAMROC operation, and wind-load deflections will be completely eliminated by the enclosing radome.

The most practical approach developed to determine the best-fit paraboloidal representation of the main reflector is to locate accurately in three-dimensional space, relative to a reference, a number of points on the

surface of the reflector. Then, using these points mathematically determines a theoretical smooth paraboloidal best-fit surface. The latter step is readily accomplished by machine computation. The location of points on the surface of the reflector, however, represents the real crux of the measurement problem and hence has become the main topic of consideration for PASAM.

Measurement of other parameters of the reflector surface, such as slope or curvature at a number of known locations, could be considered as pertinent information from which to derive the best-fit true paraboloidal surface. These quantities, however, are more difficult to measure in practice, and experience has shown that measurement of the location of a large number of surface points is sufficient.

The measured points on the reflector surface must be close enough together so that the actual surface can be faithfully represented. Inherent in this statement are the assumptions that the actual antenna surface is relatively smooth and that it has no significant discontinuities.

The accuracy required in the determination of the main-reflector geometry (hence the accuracy needed in the location of the measured points) is dictated by the minimum wavelength for which the antenna will be used. This accuracy should be a small fraction, $\sim 1/20$, of this shortest wavelength to ensure that the best-fit paraboloidal representation of the actual reflector can be obtained to within the wavelength tolerance. For the CAMROC antenna, which may operate up to 6 GHz, the shortest wavelength will be on the order of 5 cm; an antenna with an rms surface error of approximately 0.1 inch is required. A measuring system capable of locating the reflector surface points to within 0.05-inch or 1.25-mm peak error has been selected as a design goal.

The number and distribution of reflector-surface points to be measured to achieve the overall accuracy required will be determined largely by the type of reflector-surface construction, the rigidity of the surface support structure, the means of its attachment in the actual antenna fabrication, and

the time and the money available for measuring. These details are unknown at this time for the CAMROC antenna, but past experience indicates that between 500 and 4000 points must be measured to describe the large reflector surface accurately.

2. Thermal changes and the need for automation

We anticipate that significant thermal changes in the antenna may occur over a time period as short as several hours. In order to measure all the points before the antenna surface is affected by thermal changes, the measurement time should be much shorter — about 15 min. Automation of the measuring system may be necessary if 500 to 4000 target points are to be measured in 15 min.

3. Mechanical considerations

It would be advantageous, but not mandatory, if the system could allow measurement of the antenna at any and all elevation angles and could be compatible with the RF system operation to the extent that both could be utilized simultaneously or with only a short time delay in the switchover of one to the other.

C. Summary of the Desired Measuring-System Characteristics

General characteristics and specifications have been determined by the Panel for a realistic CAMROC measuring system. The major ones are as follows:

1. The system must have an overall accuracy capability of defining the antenna primary reflecting surface to within 0.10-inch rms from observations of between 500 and 4000 target points. The locations of target points should be measured to within 0.05-inch peak.

a high state of development, and a reasonably practical system promises to have an equally reasonable cost.

2. Ranging techniques, employing electromagnetic or sound waves, to measure linear distances are used separately or with precision angle measurements. These techniques, just now emerging from development laboratories, have not yet been used on antennas. A practical laser system may prove to be costly because an acceptable level of background and experience has not yet accumulated. However, ranging techniques offer great promise for fast-reaction and fully automated operation.

3. Photogrammetry and other methods deriving angle or distance information by photographic means have been used on many antennas and even more extensively in many other measurement applications. Their use for measuring radome-enclosed antennas has not been developed and may involve substantial costs. It has not yet been established whether the required accuracy can be obtained.

The following sections discuss these three catagories of measurement techniques.

B. Discussion of Individual Measurement Techniques

1. Civil-engineering techniques

The civil-engineering techniques refer to methods in which a point in space can be located by triangulation, using a theodolite and tape. For CAMROC, the measurement of angle is the important consideration, since the target locations, once measured, can be considered to stay fixed in radial distance from the measuring point at the vertex without serious error. Gravity forces on the antenna will change mainly the angular location of the targets with respect to the vertex.

2. The system should be able to perform a complete measurement in 15 min. or less, to minimize the influence of thermal environmental effects on the antenna during the measurement.

3. The system-output data collection during the measurement must be compatible with automatic data-processing techniques.

4. The system should be capable of measuring the antenna surface at all elevation angles.

III. SURVEY OF TECHNIQUES

A. Background

A review (see Appendix A) of the many methods that have been used or proposed in the measurement of reflectors shows that the precision of almost all of them depends upon calibrations against a precision theodolite. Other systems that employ angle measurement are not self-calibrating. The non-theodolite, nonangle measuring systems are either large and cumbersome or are unsuitable for other reasons.

None of the nontheodolite angle systems to date has resulted in any significant improvement over the theodolite with respect to speed of operation. Costs can be expected to exceed $100,000 for the nontheodolite instrument alone. These instruments do not have any history of use or any backlog of experience.

We have classified measuring techniques into those of civil engineering, ranging, and photogrammetry. From a detailed study of these catagories, certain pertinent characteristics have become apparent.

1. Civil-engineering techniques employing precision angle measurements and implied or directly measured linear distances have been used and are being used to a great extent by others and thus have a large background of experience to draw from. The specific types of equipment required have generally reached

An angular movement (or error) of 3.5 sec produces an 0.05-inch deflection at the antenna rim 209 ft from the vertex. Since the CAMROC measuring system must know the target position to within 0.05 inch, the angular accuracy of the theodolite needed for target-position determination must then be on the order of 1 sec. With much of the available theodolite field equipment, accuracies of 1-sec peak error are obtainable.

The time required to level, boresight the target, and read the angle circles on a theodolite is about 30 sec a target, or 2000 targets in 16 hours — a time much too great for the CAMROC measurement. The accuracy of the theodolite suggests its use as a "primary standard," to which any operational measuring system can be spot checked.

The time required to measure the angular position of a target with a theodolite is largely spent in reading the angle circles of the theodolite and in boresighting on the target. Hence, a scheme that uses shaft encoders to give electrical readout of angular information and that determines automatically the target position in relation to the boresight of the theodolite significantly reduces the angular measurement time. The use of encoders to give angular information results in the theodolite device becoming more of a telescope with electrical readout of angular position.

The automatic feature, which relates target position to the boresight, can be accomplished by an electrical measurement of the displacement of the target from the boresight of a telescope-television camera. No servo control is needed to "point" the telescope-television camera at the target, since displacement of the target from boresight is measured for each target. The location of boresight is obtained from the shaft encoders.

This measurement system has appeal because of its possible automation capability and its fast measurement time. Consequently, PASAM has recommended it for CAMROC, and such a system has been designed. The telescope-television-camera measurement system is detailed in section IV.

2. Ranging techniques (electromagnetic radar)

The term ranging techniques characterizes measurements where distance is obtained as a direct output.

Obviously, if it were mechanically practical to make such a large reflector with a surface of optical quality throughout, then a direct laser method based on interference fringe counting would give measurement information of superb quality.

The interferometric technique is particularly precise, but it appears to have two practical limitations. The first is the degradation of the fringe pattern that comes from air turbulence. Since good fringes have been observed at distances of 390[2] and 580 ft[3] and since the vibrations of a large overhead crane have been demonstrated in the presence of sunlight,[4] this problem does not appear to be a serious one for CAMROC measurements. The second limitation is the speed at which automatic fringe counting instruments can operate. The brightness of the laser has already made counting rates up to 1 ft/sec possible with a 1-mc counter.[5] This rate, although rapid, requires 3 1/2 min for the measurement of a single point at the antenna's rim. More speed will be needed for CAMROC.

A CW modulated laser could be used to radiate a narrow optical beam illuminating a small moving spot on the surface of the dish. The practical limitations of the CW modulated light beam are the difficulties in producing a modulation of small enough wavelength and in measuring its phase changes with sufficient precision. Microwave modulation is feasible, but difficult. The same problem in measuring small phase angles exists as in the direct use of microwaves. Shorter wavelengths can be produced directly rather than by modulating light beams. An additional difficulty is the size of the optical beam. While an uncollimated CW laser beam at a distance of 100 m would probably have a diameter of several centimeters, it is conceivable that the spot could be made quite small with the aid of appropriate optics, and possibly could have dimensions of a few millimeters. However, use of the

large-diameter optical beams is possible since the receiving optics could have a high resolution and a small field of view; thus, at the cost of some loss in the received power, only a portion of the illuminated spot would have to be observed for range determinations.

The CW laser, in order to be used for the CAMROC measurement, would need to resolve 0.05 inch, representing a modulating wavelength not commercially available. While laboratory CW lasers do exist that will resolve the 0.05 inch, the phase detector must operate with a very high signal-to-noise ratio. This suggests that, for a laser to be used for CAMROC, corner reflectors would be necessary at target points to give a large returned signal.

Measurement with wavelengths nearer those for which the reflector is intended will give a more useful and less redundant survey than interferometric or CW laser methods. Techniques of generating, controlling, and measuring the most desirable wavelengths already exist and can be applied as an engineering problem.

For example, an appropriate radar system using 3-cm wavelengths could be devised. A pulsed system of transmission is probably desirable to give a signature for the location of the surface to the first rough approximation. The final accuracy could then be obtained by phase measurements made possible by accurately controlled frequency standards that regulate the pulse generator as a microwave amplifier.

This method avoids the problem of making a pulse of sufficiently sharp rise time to give the required accuracy (± 2 mm) from the pulse itself. In fact, this accuracy will require phase comparisons of a few degrees of phase angle (360° corresponds to 3 cm, and 24° corresponds to 2 mm). Fortunately, such phase measurements are quite practical by means of micrometer-driven trombone transmission lines because of the possible elimination of reflection effects by means of unidirectional coaxial or wave guide transmission elements. Experience has shown that such phase comparisons are stable, repeatable, and

meaningful either by a null method or by fringe counting systems. Thus, it seems possible to measure the reflector contour from a mechanical stable platform near the reflector's self-focusing point. The deviation of the reflector from a spherical surface centered on the survey radiation source can be determined. The nearness and excellence of the reflecting surface should permit the use of sufficiently low-level pulses so that bridge-type duplexing methods can be sufficiently well balanced to allow the use of a single antenna for both receiving and transmitting. The problem of directing the survey radiation with sufficient angular accuracy still remains.

The diameter of the Airy disk of a radiator is given in ideal terms for a circular aperture and converging waves by

$$d = \frac{1.22\,\lambda R}{D} \quad ,$$

where d is the focal-spot diameter for the central-radiation lobe to the first minimum, D is the effective diameter of the radiator aperture, R is the one-way range to the target, and λ is the wavelength. The diameter should be about one or two wavelengths for the shortest wavelength for which the reflector is to be used. As a trial, consider λ = 3 cm, d = 21 cm, and R = 12,000 cm or 120 m; then the required aperture for the survey instrument is D = 20.9 m. This scheme thus is impractical unless much smaller wavelengths can be used.

The use of smaller wavelengths requires a compromise, since the reflector surface must be reasonably smooth at the survey wavelength to make meaningful phase measurements possible, and the wavelength required may be in a region where generation and reception equipment is extremely difficult to build. A present limit in this direction, which may be compatible with a reasonable mechanical finish on the main reflector surface, is about 3 mm. This is a factor of 10 shorter wavelength and requires only a 2-m aperture for the survey radiation. This size might be feasible but is in itself an engineering job of considerable magnitude since its accuracy must be about ± 6/1000 inch.

A similar system using sound waves may be considered. This is fundamentally possible because the main reflector will be used for radiation of random polarization, and a scalar wave surface should therefore be adequate. The same problems of surface accuracy and size for the survey radiator occur here. Sound, however, would have no advantage, since it has the same principal difficulty as the use of microwave electromagnetic radiation as a survey probe. In addition, the velocity of sound depends on the temperature of the air and is disturbed by air velocity. The required temperature stability is far beyond any reasonable expectation and thus rules out sound ranging in air. The velocity of sound in air c is proportional to $\sqrt{T}$; then

$$\frac{\Delta c}{c} = \frac{\Delta T}{2T} \quad .$$

For T = 300°K and $\Delta c/c = 1/120,000$, the required accuracy is

$$\frac{\Delta T}{2T} = \frac{\Delta T}{600} \quad , \qquad \text{or} \qquad \Delta T = \frac{1}{200} \text{ degrees.}$$

The use of an electromagnetic radar system and lasers seems an engineering possibility and in some ways an ideal solution. However, the cost in time, money, and engineering effort is difficult to justify in comparison with civil-engineering methods that are already backed by experience and existing equipment.

3. Photogrammetry

a. The basic principle of photogrammetric measurements

The following discussion is based on Hallert.[6] Let us photograph a target stereoscopically from the points O_1 and O_2, with the camera axes parallel and perpendicular to the base b. The camera constant is c (see Fig. 1).

In the diagram the corresponding image points are denoted by P'_1, P'_2, P''_1, and P''_2. We can see that the distance between the related points in the images must be dependent on the distances of the target points from the cameras because of the central projection. The distances P'_1 P''_2 and P'_2 P''_2 would become equal only if the two points P_1 and P_2 were located at the same distance from the base. In the case illustrated in Fig. 1 it is evident that the first-named distance must be the larger one.

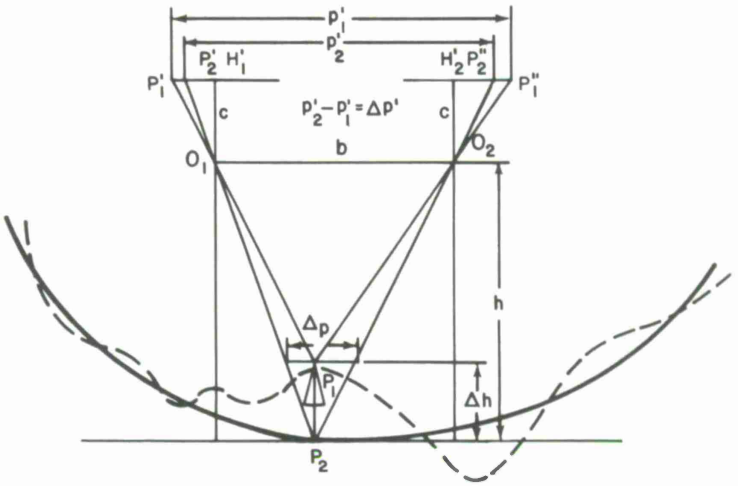

Fig. 1. Diagram of the fundamental procedure of stereoscopic photogrammetry to determine the distance differences from the differences in the horizontal parallaxes.

From similarity it is clear that a simple relation exists between $\Delta p'$ in the images and Δp in the photographed reflector (Fig. 1), namely,

$$\Delta p = \frac{\Delta p' (h - \Delta h)}{c} \quad . \tag{1}$$

As is directly evident from the diagram, it is important to note to which plane the photography distance h is referred. From similar triangles

$$\frac{\Delta h}{\Delta p} = \frac{h}{b} \quad ; \tag{2}$$

or, after substitution of the expression for Δp,

$$\Delta h = \frac{\Delta p' (h - \Delta h)h}{bc} \quad .$$

After some rearrangement of this expression, we have

$$\Delta h = \frac{\Delta p' h^2}{bc} \left(1 - \frac{\Delta h}{h}\right) \quad . \tag{3}$$

In this expression, however, the second term in the parentheses is of importance only in cases of a larger Δh and can, therefore, often be ignored. In such a case the expression simplifies to

$$dh = \frac{dp' h^2}{bc} \quad . \tag{4}$$

The notations dh and dp′ mean a certain approximation. If the base can be measured in the images as b′, we have $b = b' h/c$, and Δh becomes

$$\Delta h = \frac{\Delta p' h}{b'} \left(1 - \frac{\Delta h}{h}\right) \quad . \tag{5}$$

If Δh is too large for $\Delta h/h$ to be ignored, it can first be corrected, with an approximation allowed for practical purposes, by means of the expression $-\Delta h^2/h$, after the value of Δh has been computed by the preceding equation.

b. Application to the CAMROC dish

The general dimensions of the CAMROC dish are depicted in Fig. 2. For the quantities in formula (4) the following values have been assumed:

$h = 40$ m,
$b = 25$ m,
$c = 0.30$ m,
$dh = 1.27 \times 10^{-3}$ m (PASAM accuracy goal of 0.05 inch).

We therefore obtain for dp′

$$dp' = \frac{1.27 \times 10^{-3} \times 25 \times 0.3}{16 \times 10^{2}} \cong 6\,\mu \quad .$$

Because an error of about 1 to 2 μ must be expected from the lens systems of the two photogrammetric cameras, we must be capable of reading dp′ in each picture with an accuracy of 5 μ. With photographic-plate resolution of 20 line pairs/mm, we can reach the required accuracy by a gain of a factor of 10 over picture resolution by virtue of cross correlation between the two stereoscopic pictures. Such a gain is about 50% above the present state of the art.

With a slide size of 90 mm × 90 mm, each picture covers (with overlapping) about 10 m × 10 m of the dish surface. Approximately 150 pictures must be taken to cover the entire surface.

If we assume that 2000 targets will be used on the CAMROC antenna surface, 15 will appear in each photogram. If 3 sec are needed for camera steering, picture taking, and film unrolling, then about 7 1/2 min are needed to record the overall surface.

The films could then be converted into digital tapes for computer processing and contour plotting.

The research and development activity of SAO in Project Celescope[7] suggests that a fully electronic photogrammetric system could also be conceived, along the lines of a digital TV-camera approach. With an image orthicon having a 5-cm × 5-cm target, and with the same optical parameters indicated above, each exposure could cover (with overlapping) 40 m^2 of the surface; 350 exposures could complete the surface survey. With a resolution of 50 TV lines/mm (50% in excess of the present state of the art), we could have about 6 million picture elements per frame. Using a target image with 100 picture elements, and 6 targets per frame, we would have only 600 picture elements in each frame.

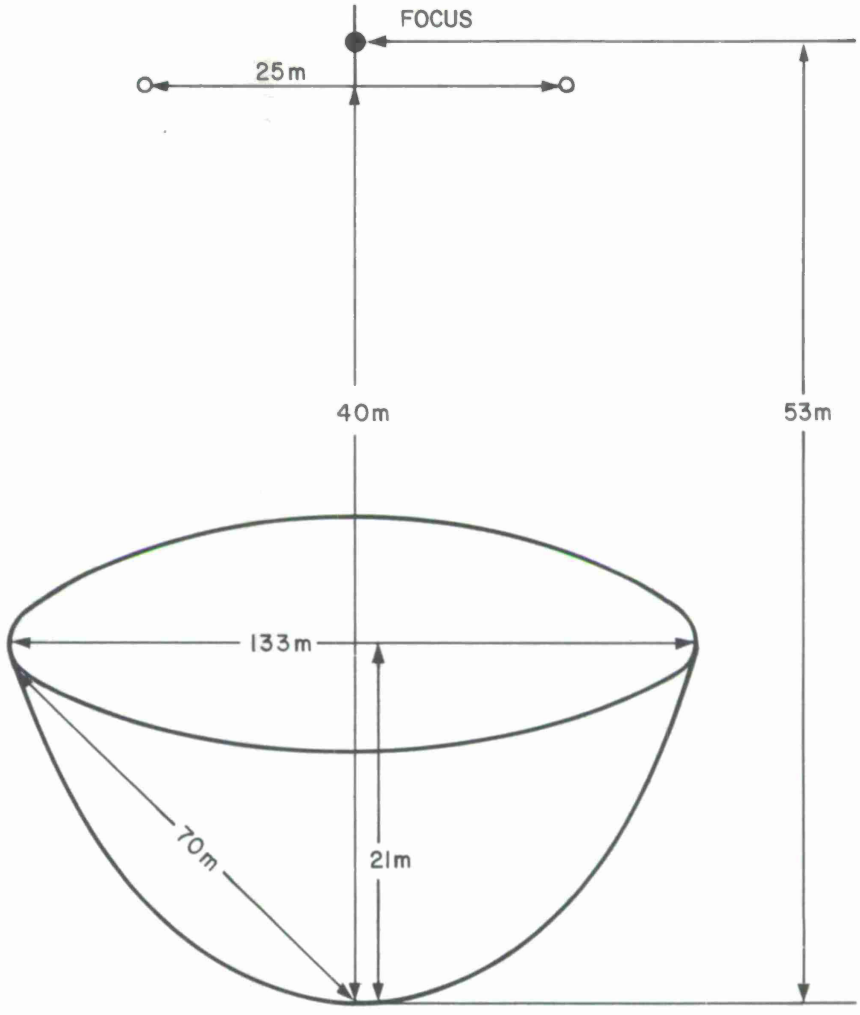

Fig. 2

By use of Celescope's digital approach, only the picture elements occupied by an image would be encoded and a 31-bit word (10 bits for x, 10 for y, 8 for z, 3 for parity check) would describe each of the 600 picture elements active in each frame (18,600 bits/frame). The description of the overall dish requires approximately 6.5 megabits, and with a write-in speed of 1.2 megabits/sec (state of the art), less than 0.1 sec is needed to record 1 frame. If we assume that 1 sec is necessary for TV-camera steering and picture taking (no time to be alloted to film unrolling), we need a total of about 6 1/2 min to record the overall reflector.

With a tape density of 20,000 bits/inch, 50 ft of tape are needed to record an entire reflector sampling. As far as measurement accuracy is concerned, we have a resolution of

$$\frac{50}{2500} \times 10^3 \mu = 20 \mu$$

with the TV raster above indicated, and therefore, as in the photographic case, cross correlation gain must be called upon to make up the difference to the 5-μ goal. This gain can be realistically expected, as the following analysis indicates.

Let us assume that the "image" of each target is a three-dimensional Gaussian figure with $\sigma = 2$ picture elements (Fig. 3). We postulated that the intensity Z can be read within 1 part in 256 (signal-to-noise ratio of approximately 48.5 db) in each Gaussian shape (we have one per camera corresponding to a given target on the dish surface). By cross correlation of the two images (the two figures are supposed to be identical), the minimum detectable variation in cross-correlation value is

$$\frac{1}{256} + \frac{1}{256} = \frac{1}{128}$$

of its value for $\tau = 0$.

Figure 4 indicates that we can detect positional differences as small as 0.13 σ = 0.26 picture element, and therefore the resolution of 20 μ can provide approximately the desired positional accuracy of 5 μ.

c. Conclusions

From the previous sections, it is clear that photogrammetry today could not meet PASAM accuracy requirements, although the method is not too far from the required goals. However, because of the speed of data gathering it offers and because the CAMROC project schedule will undoubtedly cut into the 1970's, the photogrammetry technique should be kept in mind.

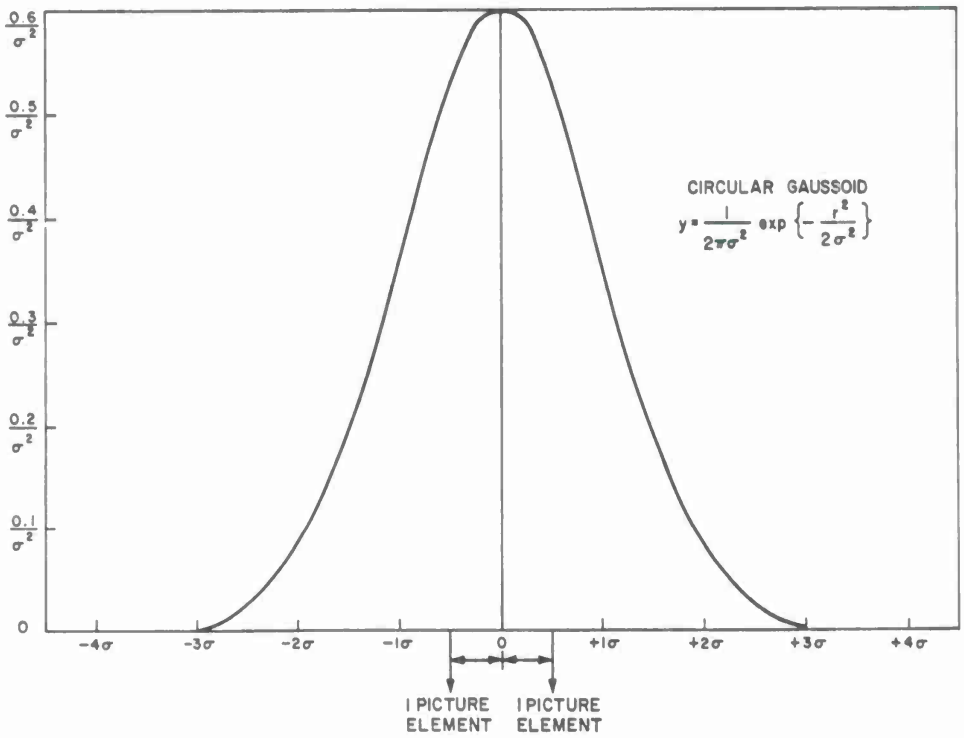

Figure 3.

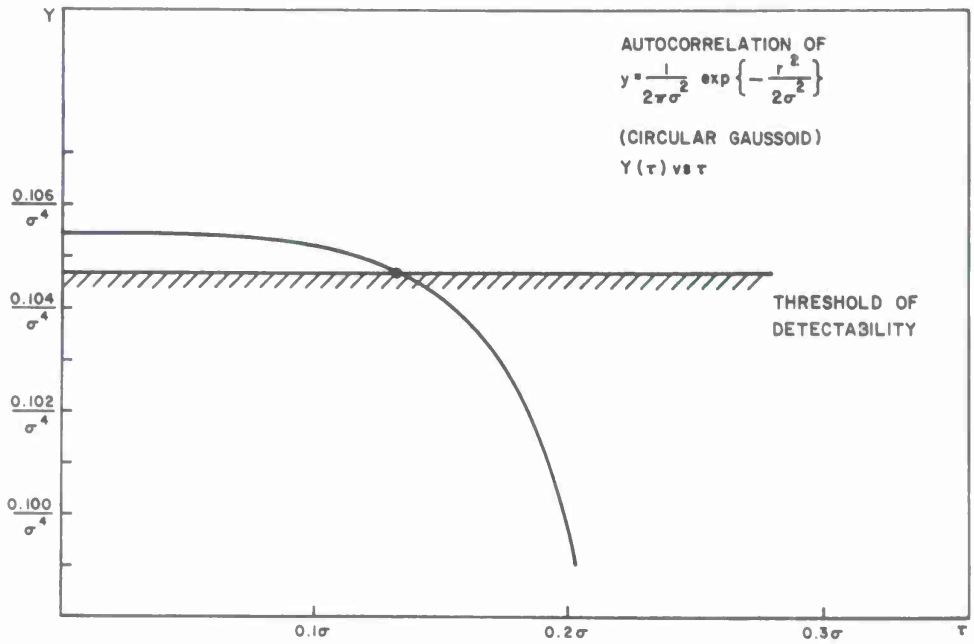

Figure 4.

C. Conclusion of Survey

The Panel has concluded that, while the approaches of photogrammetry and ranging offer some desirable features, automated civil-engineering techniques should receive the initial detailed study. A practical workable system can be now built, and the amount of development effort required would be acceptably low. We believe the system costs for this approach would be the lowest of the several alternatives. Further investigation of ranging and photogrammetry techniques would be desirable and should be undertaken.

Consequently, we present next a system design for CAMROC utilizing automated civil-engineering techniques that meet the required specifications and characteristics.

IV. PROPOSED MEASUREMENT SYSTEM FOR CAMROC

A. System Operation

Figure 5 is a conceptual sketch of the proposed measuring system, consisting of an automated telescope mounted near the vertex of the antenna and of ancillary equipment to measure antenna target elevation and azimuth angles. This equipment should be of sufficient accuracy so that when it is combined with an implied radial distance, a 400-ft-diameter antenna surface will be defined to within 0.10 inch rms.

The automated telescope will incorporate two 20-bit angular shaft encoders, resulting in 1.24-arcsec resolution elevation and azimuth information. A television system, strobe lights, and appropriate optics will be incorporated with the telescope to allow remote readout of target positions, and electronic data-processing equipment will be used to process the information. The telescope will be equipped for manual use by an operator when the antenna is pointing at the zenith, as well as for fully automatic remote operation for all antenna elevation positions.

With the antenna pointing at zenith, an operator will be able to sight the telescope on the target and actuate a switch that transmits into a computer both the elevation and azimuth angles of the target. The computer will be programmed for the approximate location of each target, so that each set of incoming elevation and azimuth information will be identified with the proper target. The operator will be comfortably seated in a chair mechanically isolated from the telescope but revolving in azimuth with the telescope. An operator should be able to locate and read a target every 12 sec, or 300 targets in 60 min, under these conditions.

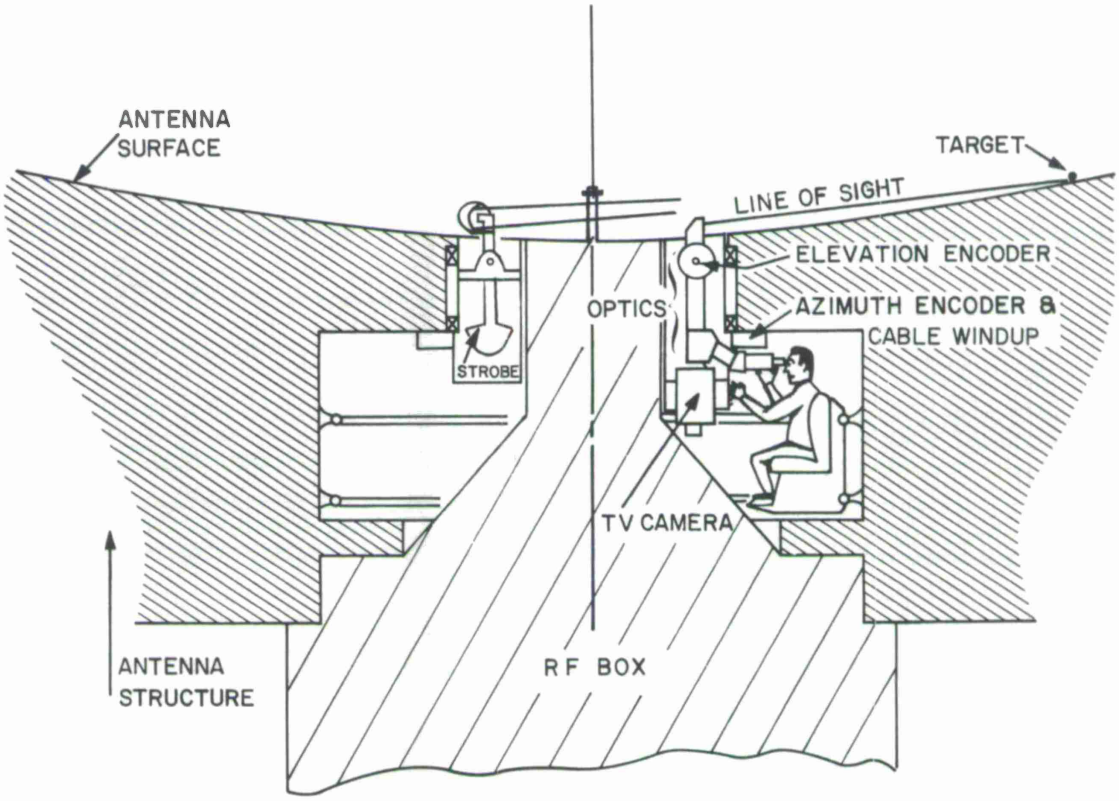

Figure 5.

For a remote automatic operation, a television camera rather than an operator views the target through the telescope. The target location is electronically measured with reference to the boresight of the television camera-telescope unit.

The sequence for remote automatic operation begins by indexing the television camera-telescope unit to sight at a preprogrammed fixed elevation angle where a circle of targets is located. A drive motor turns the television camera-telescope unit at approximately 4 rpm in azimuth, sweeping all targets at that elevation angle. As each target comes into the television camera's field of view, it is illuminated by a 2-μsec strobe light triggered by an azimuth encoder monitor, thus exposing a television frame. The targets consist of a low reflective background several feet in diameter with a highly reflective center approximately 1/16 inch in diameter. Because of its high reflectivity, the center will produce a large voltage in the video output.

The target's position relative to the boresight of the television-camera-telescope unit is obtained by an electronic determination of the line number in which the target appears and by a measurement of the time delay from the beginning of the framesweep to the target's appearance. The first is accomplished by amplitude detection of the video wave form from the television camera. The boresight angles of the telescope unit are known at the instant of the strobe flash from the azimuth and elevation angular shaft-encoder information, and therefore, the actual target location can be determined by combining the target-from-boresight displacement and the boresight angles. After sweeping all targets plus an overlap of at least one at the fixed elevation angle, the television camera-telescope unit sights at the next preprogrammed elevation angle, sweeping another circle of targets. This procedure is repeated until all targets have been scanned. It appears that 4000 targets can thus be located in approximately 15 min.

The actual location of the telescope, television camera, strobe light, shaft encoders, drive motors, and other components must be the result of an extensive design study; however, preliminary findings indicate that it may be

feasible to incorporate the whole measuring system, similar to the conceptual sketch in Fig. 5, as a permanent installation on the antenna so that it will not interfere with the RF receiver or its auxiliary equipment. This arrangement would minimize any antenna downtime for the purpose of antenna-accuracy measurement and may allow simultaneous operation of the two systems.

B. System Details

1. Supporting calculations and details

a. Telescope

Figure 6 shows a sketch of the antenna configuration assumed for CAMROC. The antenna surface areas is 1.37×10^5 ft^2. If 4000 targets are to be uniformly spaced, their density will be one per 34 ft^2; consequently, the field of the measuring telescope must cover less than this surface area no matter in what direction the telescope is pointed. The telescope field is determined by the resolution required and the area of the vidicon used. The optimum resolution turns out to be 0°. 8, which can take in at most 15 ft^2 of the antenna surface; consequently, more than one target point will never appear at one time in the telescope.

The telescope must be capable of measuring a target displacement of 0. 05 inch at a point on the antenna's rim, 209 ft from its vertex. The corresponding resolution is 3. 5 arc sec. An 800-line vidicon may be expected to resolve a square 0. 00125 inch on a side. If a distance of 0. 00125 inch at the image is to correspond to 3. 5 arc sec, the telescope's focal length must be 6 ft, although a Barlow lens could be used to obtain this focal length in a smaller physical length.

b. TV camera

The TV-camera requirements for the measuring system can be defined by sensitivity, resolution, and stability.

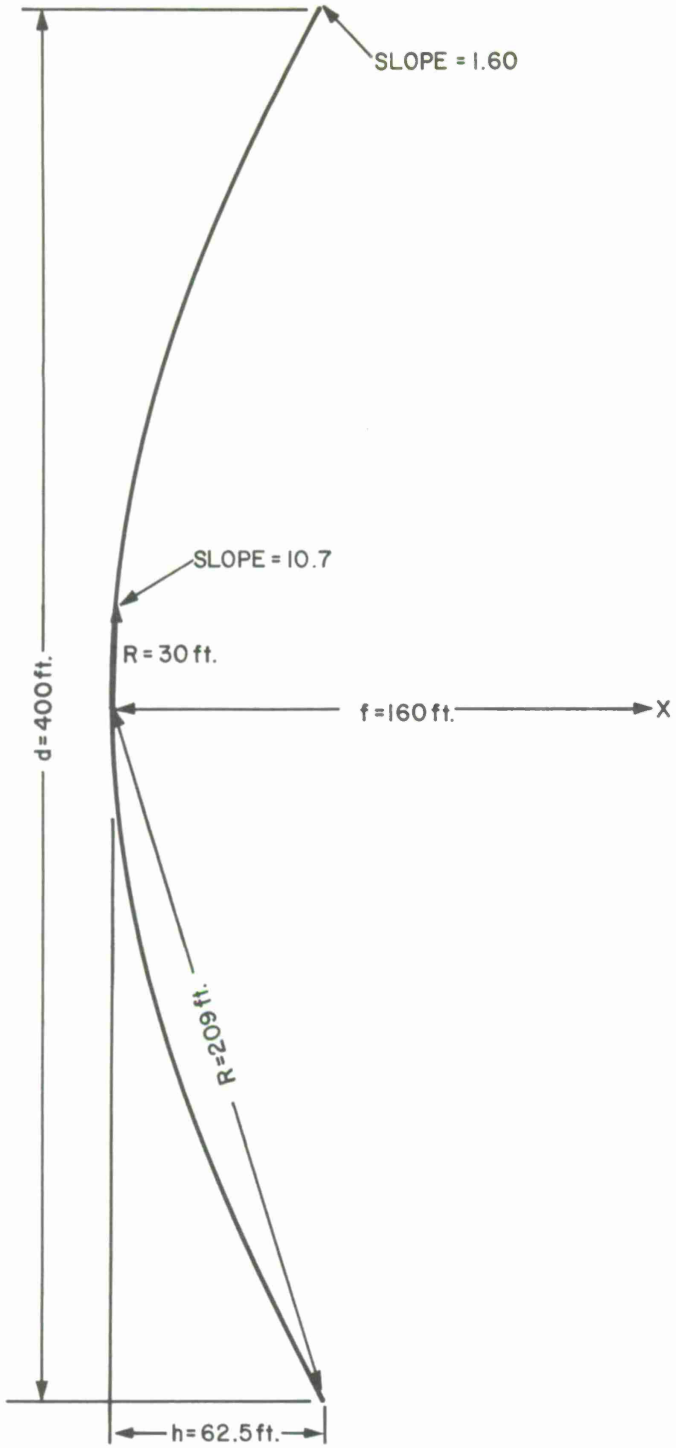

Figure 6. Assumed figure of the CAMROC antenna

The sensitivity of the TV camera is determined ultimately by the strobe-light intensity, since the amount of light returned from the 1/16-inch-diameter reflective material of the target center must be sufficient to produce a a large output indication in the video output. The strobe-light intensity should be 10 times the background light on the antenna to eliminate background noise. Then if the reflection from the target center is 10 times more than that of the low-reflective surrounding area, a large signal-to-noise ratio will exist in the camera video output, enabling reliable detection of the target center. Available TV cameras have sensitivities from 10^{-4} footcandle for image orthicon tubes to 10^{-1} footcandle for vidicon tubes. As shown in the next section on strobe-light illumination calculations, choosing a vidicon camera with 0.2-footcandle sensitivity results in a strobe-light/TV-camera sensitivity relationship that is workable and easily obtained.

The resolution of the TV camera is dictated by the field of view chosen for the telescope. A telescope focal length of 6 ft implies an 800-line vidicon. Vidicons are available up to 1000 lines of resolution.

The stability of the TV camera must be such that the relationship between the mechanical mounting of the camera boresight and the electrical lines on the vidicon is held to within one line width during the antenna measurements. The primary contribution to drift in the vidicon line is in the drift of the deflection coil's power supply. SAO's experience in Project Celescope indicates that with the best possible power-supply drift compensation, a stability of less than 10 lines is not feasible. For the electrical scan lines to the mechanical boresight to be stabilized, a beam-splitting technique could be used in the vidicon. The beam splitter impresses on the vidicon a set of reference targets that are fixed in relationship to the mechanical boresight of the TV camera. The reference targets can thus correct for drift in the line position on the vidicon.

c. Target illumination requirements

As the telescope scans the surface of the antenna, a flashing strobe light illuminates each target when the target nears the center of the telescope field. The maximum duration of the flash necessary to stop the motion can be obtained from the speed of the telescope's angular motion in azimuth. This speed can be calculated by assuming that the 4000 targets are equally spaced on 63 circles evenly separated in elevation. If the telescope is to complete its 63 revolutions in azimuth in 15 min, its speed must be 4.3 rpm. At this speed, the strobe flash must be less than 11 μsec if the telescope is not to move more than 1 arc sec while the target is illuminated. The strobe must produce these flashes at a rate of about 5 per sec.

The intensity of the flash must be sufficient to register an image on the vidicon and to mask out a reasonable amount of background light. If the primary lens of the telescope is 5 inches in diameter, then its f number is 12. This value and the rated sensivity of 0.2 footcandle for the vidicon give a required brightness of 37 lumens/ft^2 sr. For a highly reflecting target center, the brightness at the target must have the same value; consequently, the intensity at the target surface (assuming the reflective material has unity reflectivity and Lambertian) must be $37\pi = 115$ footcandles. This value is 10 times above the illumination of an indoor office[8] and so probably at least 10 times above the ambient light level of a radome-enclosed antenna. Since the flash is only 11 μsec in duration, and a vidicon integrates over a 1/30-sec interval, a peak intensity of 3.6×10^5 footcandles must be provided by the flashlamp. A light beam of 1° will fully illuminate the telescope's field of view. The antenna surface area covered by such a beam is about 35 ft^2. Consequently, the peak beam candle-power required is about 10^6 candles.

A modified General Radio Strobotac appears to be a suitable source of illumination. Since its maximum flash duration is 3 μsec rather than 11 μsec, 3×10^6 candles are needed. The unit provides 10^7 candles at a rate of 2 to 11 flashes/sec. The beam angle of the manufactured reflector is 10°,

so a reflector 10 times larger would be needed for a beam of 1°. Such a reflector would be a few feet in diameter — probably not an excessive dimension for the present application.

2. Data collection and reduction

In the proposed measurement scheme, two 20-bit words, representing altitude and azimuth, will be recorded on magnetic tape for each target during a particular scan. The data-writing device should be capable of recording the binary information in suitable record lengths and in such a manner that it can be read by a standard tape-reading device such as any 800-bpi, IBM-compatible, 7-track tape reader. For more than one data scan on a tape, the insertion of data block separators and the writing of end-of-file marks, signifying the end of data, should be provided for.

If one uses an incremental tape recorder and records at high density (800 bpi) the azimuths and elevations of about 100 targets can be recorded in 1 inch of tape with an accuracy of 24 (or fewer) bits each. If an incremental recorder is not used, then an "end-of-record gap" is left after each target. Since this gap amounts to about 3/4 inch, essentially all the tape will be occupied by end-of-record gaps.

Translated into numbers, this means that with an incremental recorder, one tape will accommodate over 2 1/2 million targets. Utilizing a non-incremental recorder, one tape will accommodate about 30,000 targets.

The data gathered by the measurement scheme can be used to determine a best-fit 3-dimensional paraboloid. A computer program can be available to designate the proper adjustments in order to minimize the resultant residuals with respect to the previously determined best-fit paraboloid.

The equation of the paraboloid and the resultant residuals can be printed. In addition, computer programs are available that will enable an x-y plotter to draw contour lines representing the deviation of the antenna surface from a paraboloid.

It is estimated that for 4000 target points, all calculations can be accomplished in less than 1 hour of machine time. If only 500 points are used, the maximum amount of machine time needed should be reduced to less than 20 min.

V. ADDITIONAL CONCLUSIONS AND RECOMMENDATIONS

There are other important factors to consider in the selection of an appropriate optical and mechanical instrument for the measurement of a reflector surface. The problem of a suitable thermal environment cannot easily be dismissed. When there is a lack of sufficiently stable temperature conditions, the data from an otherwise precise instrument are reduced to a meaningless tangle of conflicting information. A measurement position must be included as a part of the reflector design to provide the ultimate in stability at the measurement position. The mechanical layout of the measurement system must be considered in the initial CAMROC design.

Since it will probably be almost impossible, in a structure the size proposed, to hold for any great period of time the thermal-time gradients to levels consistent with the best measurement performance, it should be one goal of the reflector design to keep the thermal-time constants of the various elements of the reflector structure equal in order to produce a reflector relatively insensitive to thermal-time gradients.

We have investigated the availability, state of development, cost, and size of the major critical elements and components of the proposed system. All required items are currently available or in active developmental programs sponsored by such agencies as the U.S. Army. It would thus appear that no further major component development is required. The greatest expenses for the procurement of a surface-accuracy measurement system for the CAMROC antenna, to be working in approximately 5 years, will be for system design, actual component purchase, installation, and system checkout.

Our initial cost estimate of the proposed remote automated system is between $250,000 and $350,000. This complete estimate includes costs for certain associated investigative programs, such as target-optimization studies.

VI. REFERENCES

1. H. Bruckerman 1963. Antenna pattern measurements by satellite. Trans. IEEE on Antennas and Propagation, vol. AP-11, pp. 143-147.

   E. V. Jull 1962. An investigation of near field radiation patterns measured with large antennas. Trans. IEEE on Antennas and Propagation, vol. AP-10, pp. 363-369.

   J. D. Kraus 1950. Antennas. McGraw-Hill Book Co., New York, Chapter 15.

   S. Silver 1949. Microwave Antenna Theory and Design. McGraw-Hill Book Co., New York, Chapters 5, 6, and 15.

   P. G. Smith 1966. Measurement of the complete far-field pattern of large antenna by radio-star source. Trans. IEEE on Antennas and Propagation, vol. AP-14, pp. 6-16.

2. F. T. Arecchi and A. Sona 1966. Long distance interferometry with a He-Ne-laser. ZAMP, pp. 128-129.

3. R. Bruce Herrick and Jurgen R. Meyer-Arendt 1966. Interferometry through the turbulent atmosphere at an optical path difference of 354 m. Appl. Optics, vol. 5, pp. 981-983.

4. J. M. Burch 1965. Laser applications in the field of physics and optics. Proc. Int. Symp. on Laser-Physics and Applications. ZAMP, vol. 16, pp. 111-119.

5. W. R. C. Rowley 1965. A fringe-counting interferometer system employing a laser for precision length measurements. Lasers and Their Applications, IEEE, pp. 4-1 – 4-3.

6. B. Hallert 1960. Photogrammetry. McGraw-Hill Book Co., New York.

7. R. J. Davis 1962. Project Celescope: an astrophysical reconnaissance satellite. Smithsonian Astrophys. Obs. Spec. Rep. No. 110, 105 pp.

8. G. H. Shortley and D. E. Williams 1961. Elements of Physics. Prentice-Hall, Inc., Englewood Cliffs, New Jersey.

Additional references for the PASAM Report. These references are not mentioned in the Report.

9. A. V. Robinson 1966. An instrument for the measurement of aerial profile accuracy. Design and Construction of Large Steerable Aerials (for Satellite Communication , Radio Astronomy, and Radar), IEE Conference Publication No. 21, London, England, pp. 75-79.

C. Kühne 1966. Techniques for measuring paraboloidal antennas. Design and Construction of Large Steerable Aerials (for Satellite Communication, Radio Astronomy, and Radar), IEE Conference Publication No. 21, London, England, pp. 187-198.

R. Justice and T. Charlton 1966. Laser surface measuring system. Design and Construction of Large Steerable Aerials (for Satellite Communication, Radio Astronomy, and Radar), IEE Conference Publication No. 21, London, England, pp. 177-181.

H. E. Pearson, J. C. North, and C. N. Kington 1966. Measurements of the reflector profile of the modified Goonhilly no. 1 aerial. Design and Construction of Large Steerable Aerials (for Satellite Communication, Radio Astronomy, and Radar), IEE Conference Publication No. 21, London, England, pp. 277-282.

10. M. J. Puttock and H. C. Minnett 1966. Instrument for rapid measurement of surface deformity of a 210 foot radio telescope. Proc. IEE vol. 113, no. 11, pp. 1723-1730.

11. J. Ruze 1966. Antenna tolerance theory-A review. Proc. IEE, vol. 54, no. 4, April.

APPENDIX A

A review of various methods for reflector measurement, some of which have actually been used and some of which have only been proposed, is presented. A discussion of relative merits and shortcomings, where they can be known or deduced from practical experience, accompanies each presentation.

ELEVATION ANGLE AND RADIAL DISTANCE

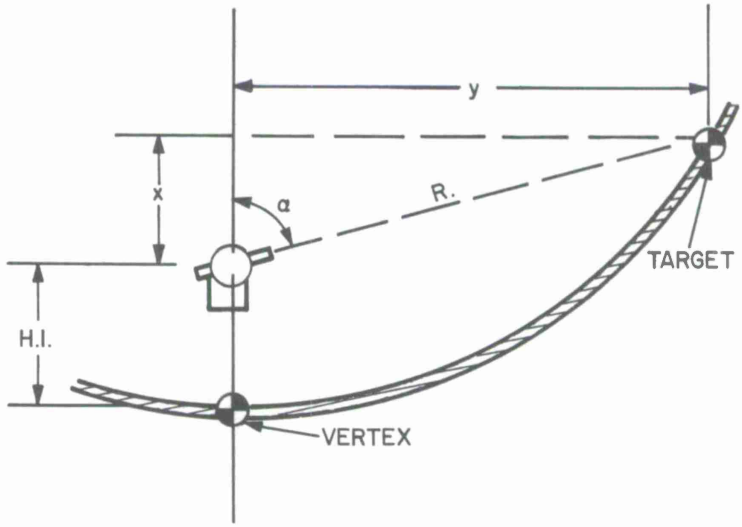

This very common approach is used successfully in many installations. The choice of optical instrument, depending somewhat upon the required accuracy, has generally been a precision theodolite. Various tapes, such as civil-engineering chain tapes or optical tooling tapes, have been used for the radial measurement.

The theodolite is usually mounted on a firm post or stanchion a sufficient distance above the vertex to guarantee good intersections of the line of site of the instrument with the observed targets. Usually a fixture holds one end of the radial tape at the exact measurement center of the optical instrument. The elements of the target location, x and y, are calculated from the vertical

angle and the measured radius. The height of the instrument, shown as H. I., may be either directly measured from some known point, or deduced later from an analysis of the calculations for all the targets.

Variations of this method have been used where the elevation angles were set to fixed values by the use of pentaprisms, or pentamirrors, and the deviations from the fixed values were measured by an optical micrometer.

The angle and distance method is slow and tedious, and generally requires a great amount of calculation. Stable mounts and environments are a prerequisite.

THEODOLITE AND GAUGE RODS

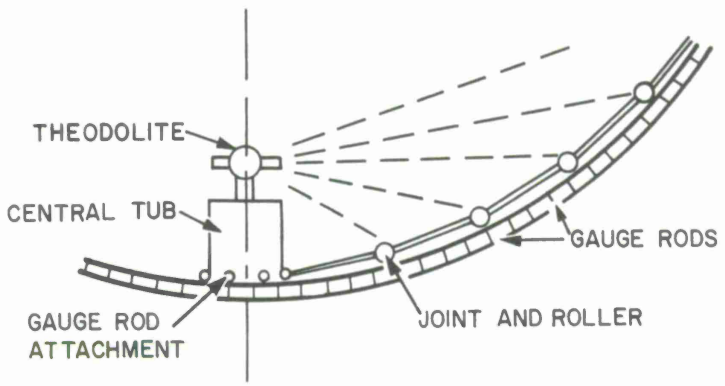

This is a variation of the angle-and-distance approach. Raytheon used it with satisfactory results to check out the surface of the 60-ft AMRAD reflector at White Sands, New Mexico.

In this particular application the precisely dimensioned gauge rods are made from Fiberglas. The line of site of the theodolite is set tangent to the rollers and the angles recorded. The rollers are spring-loaded against the reflector by a T-headed rod inserted in the channel formed by the edges of adjacent panels. This allows angles to be read at other than zenith attitude of the reflector.

The setting of the line of site tangent to the rollers causes complicated calculations to determine the exact point of contact with the reflector. Judging the point of tangency introduces errors and is not the best optical practice for highly precise work.

Not shown in the illustration is a work platform around the central tub, which is used to isolate the instrument operator from the instrument and reflector. More precise results could probably be obtained if a few refinements to this measurement method are made.

PENTAMIRROR OR PENTAPRISM PROBE

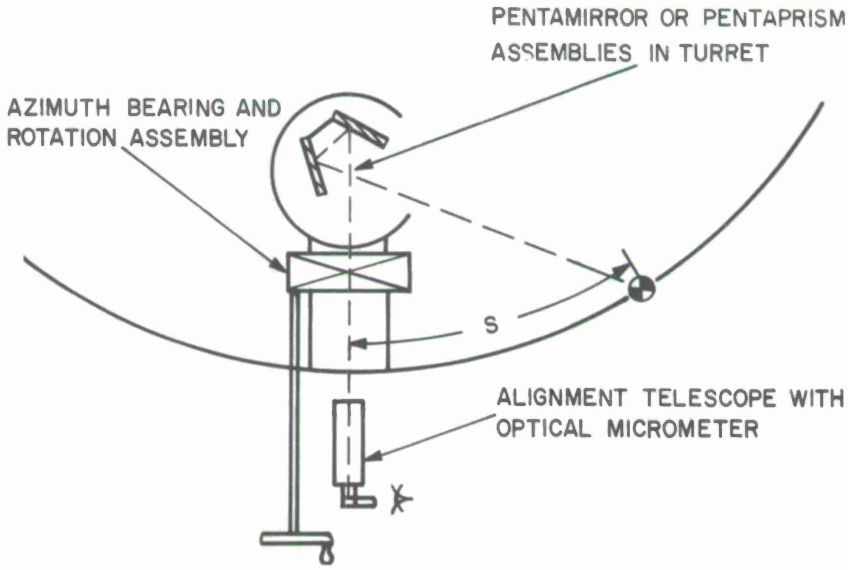

Another variation of the angle-distance method is the pentaprism or pentamirror probe, used by North American Aviation in the assembly and rigging of the Haystack reflector. The probe assembly, manufactured by Keuffel and Esser, contains eight pentamirror assemblies. The optical targets were placed on the reflector panels in tooling jigs during manufacture of the panels.

This system is slightly faster than the equivalent system with a theodolite; however, it is most difficult to calibrate in the field during use and is quite expensive compared with the theodolite. The device offers more comfort

for the operator since he generally occupies a fixed relation to the instrument and is not required to adjust his position with varying elevation angles. Considerable setup time is involved for each use of the probe. Stability of the pentamirror assemblies is a problem. The probe assembly lacks the versatility of the comparable theodolite system, and depends upon a theodolite calibration for its authority. Lateral and vertical shifts of the mirror assemblies introduce errors, and mirror locations must be monitored.

RANGE-FINDER APPROACH

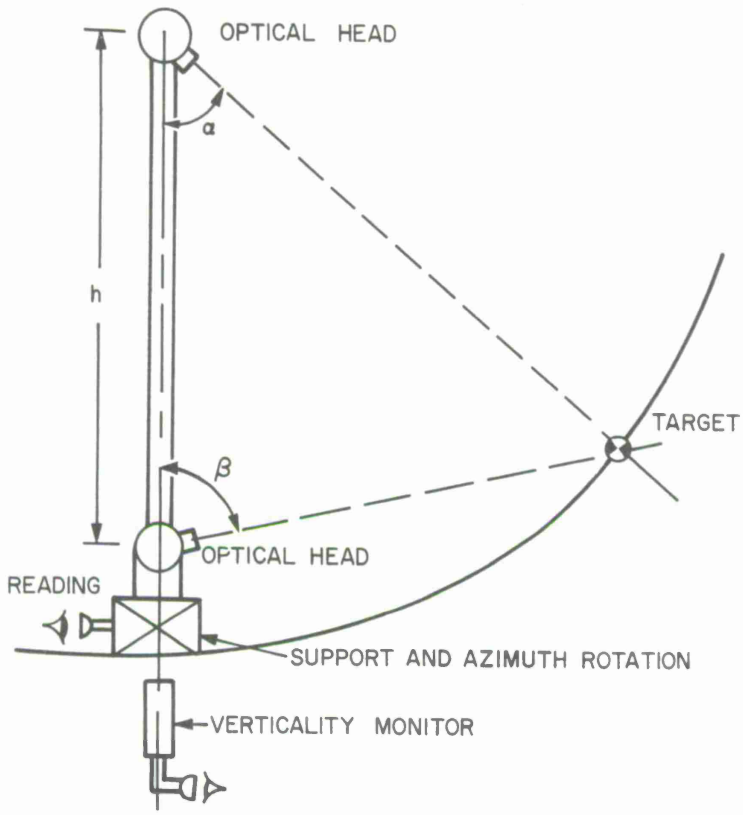

Many different types of range finders have been proposed. Most of them employ the vertical base line for use in reflectors, owing to the relatively large size required to gain the necessary precision.

The variously proposed range-finder approaches have used an assortment of optical heads to make the angle measurements. For precise work

all the proposed heads have been quite large and very heavy, and they all require monitoring the verticality to ensure precision. Although this type of device does offer the possibility of exact solutions without other measurements to the targets, its great bulk and weight make its use impractical for large reflectors.

PROJECTED-IMAGE RANGE FINDERS

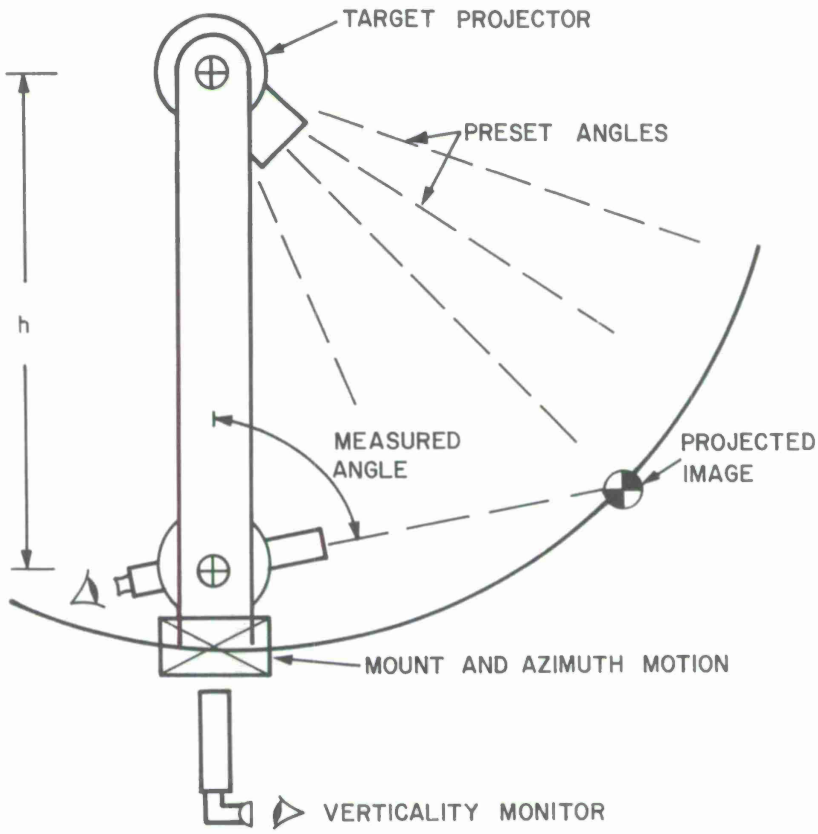

Several variants of this approach have been proposed. For large reflectors the device must be large, bulky, and heavy. For precise work either the verticality of the instrument must be monitored at each reading, or an additional operator must carry out the monitoring function. It does, however, offer an exact solution and does not require any targets or access to the reflector surface.

PHOTOGRAPHIC RANGE FINDERS

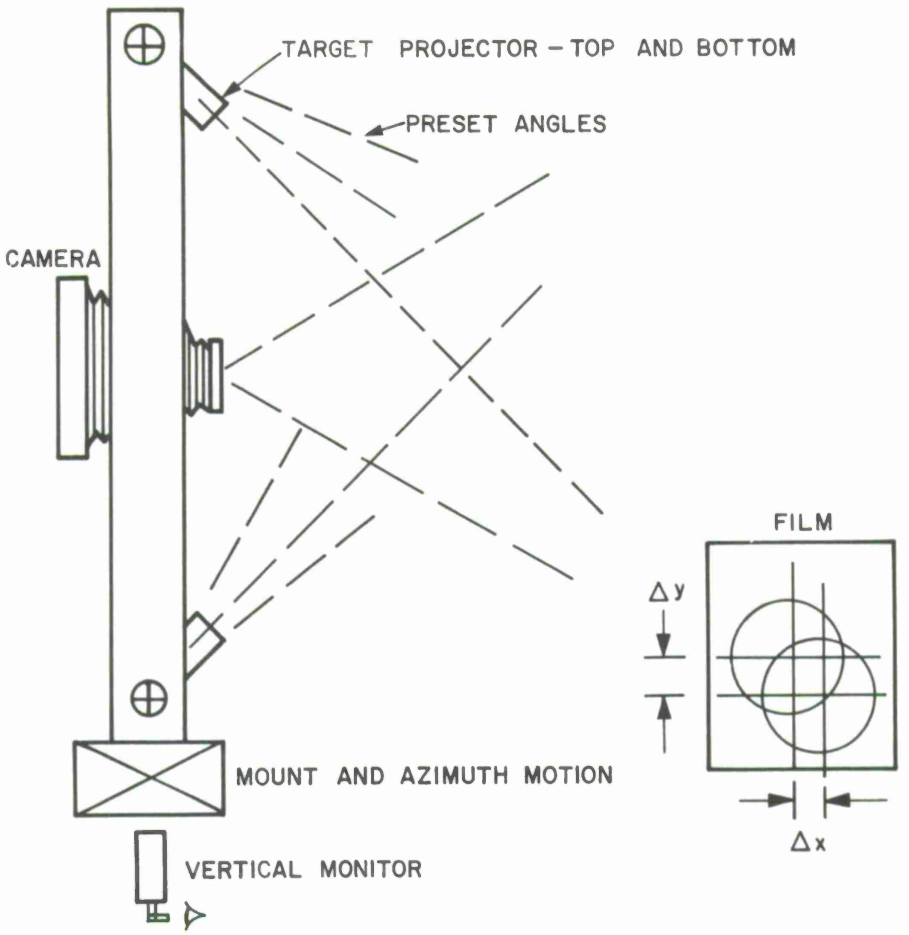

This family of range finders introduces the further problem of servicing the camera equipment. A time delay is involved during the processing of the films or plates, and additional equipment is required for the reading of the resulting films. The system suffers from all the problems of range finders in general, plus the complexities of the camera operation. This seems to be a very impractical approach for reflector measurement.

This approach has been used with some success on reflectors of a low order of surface tolerance. The method requires considerable traffic on the reflector surface. The feed or secondary reflector support structure is assumed stable within an amount consistent with the results desired. For very large reflectors, with many measurement points, the method is slow and tedious. It is, however, quite inexpensive.

THREE TAPED DISTANCES

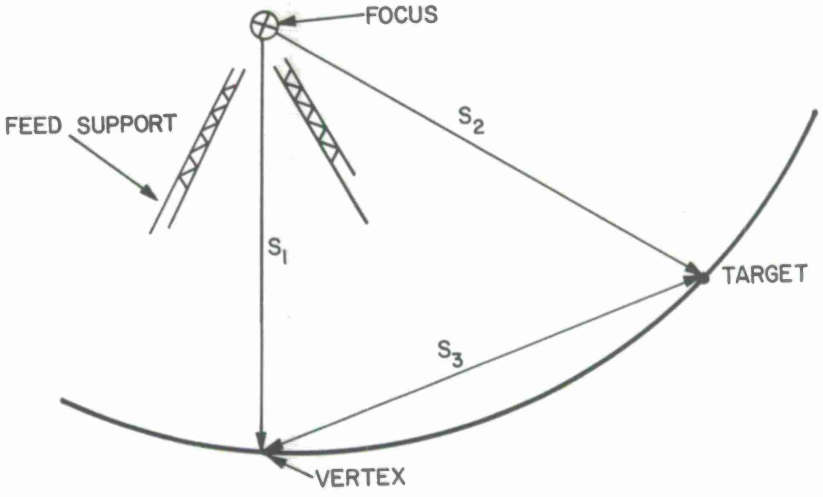

This approach should be reserved for very low surface-tolerance reflectors and probably can best be used in field-checking a dubious reflector when more sophisticated equipment is not available.

LEVEL AND DISTANCE VARIATION OF TOOLING APPROACH

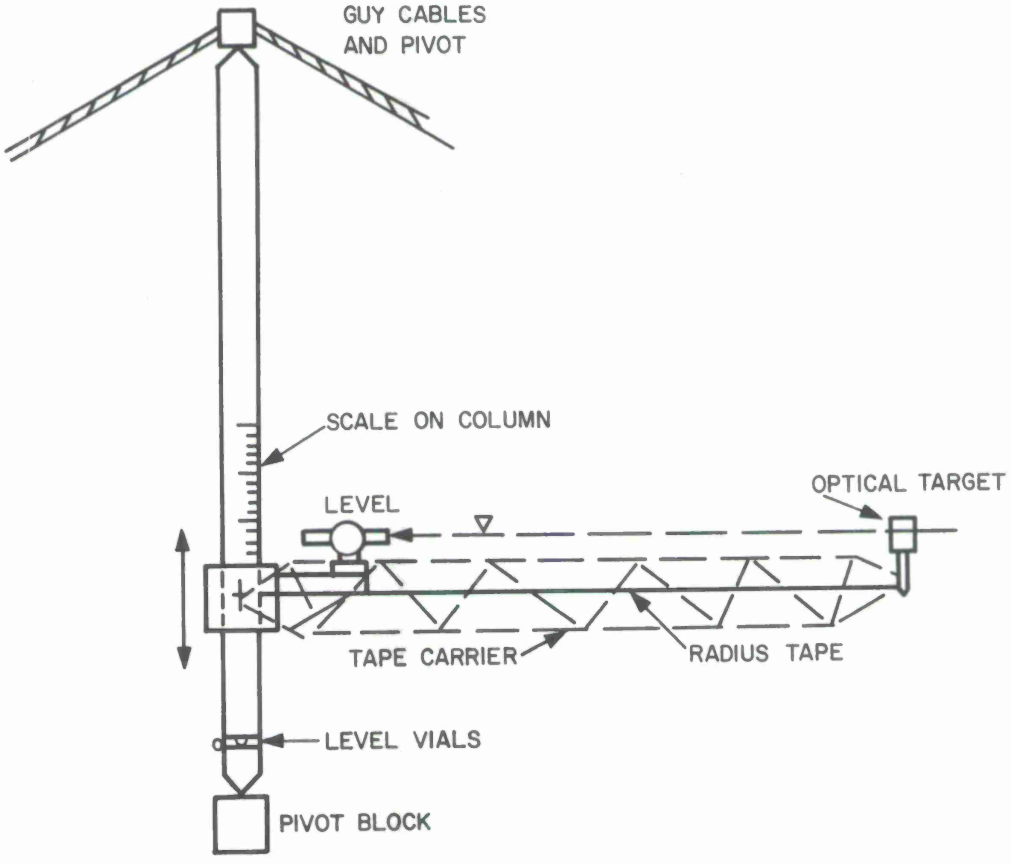

This approach was successfully used by the D. S. Kennedy Co. in the measurement of the present Millstone Hill reflector. During the initial assembly of the reflector, the measurement was made with the reflector set up on the ground on specially prepared concrete piers. The reflector was then checked aloft by this same operation. This method uses quite ungainly equipment in the large reflectors and probably would be much too cumbersome for use in reflectors over 85 ft in diameter.

PERISCOPE VARIATION OF OPTICAL TOOLING APPROACH

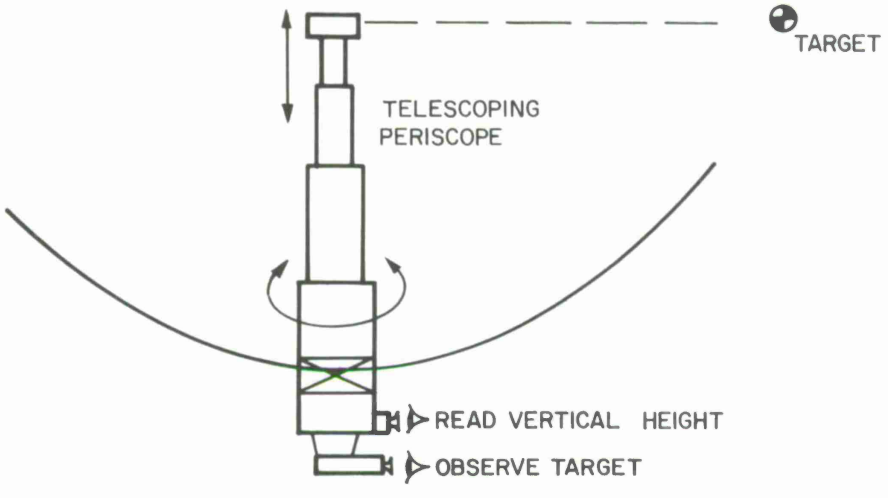

Only one such device is known to have been used. Called the Parabolascope, it is believed to be proprietary. The locations of the targets must either be measured or be assumed as one element of the solution. For a reflector on the order of 400 ft in diameter, this would necessarily have to be a very large device, and would probably thus be quite expensive for precise work. It is not clear that there would be any significant advantage to this approach for a large reflector.

DIRECT OPTICAL TOOLING APPROACH

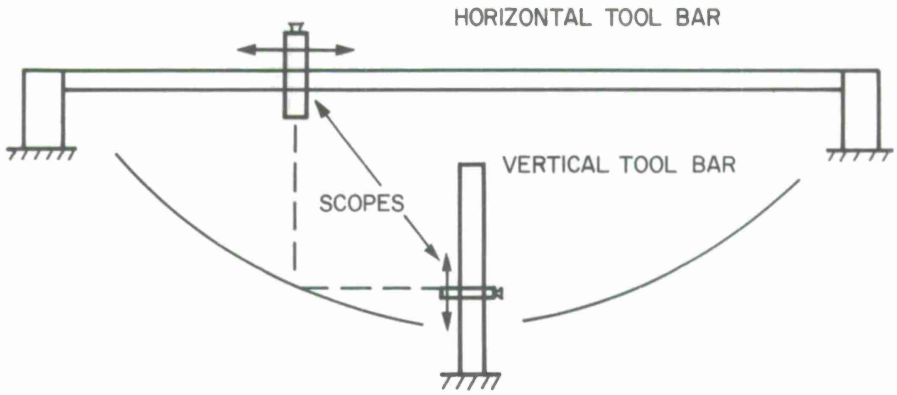

A system similar to the illustration has been proposed by Boeing. The approach is a straightforward application of optical tooling principles. The actual construction of a tooling dock the size required for the CAMROC reflector would be a major task in itself. The system requires either that the rotatable horizontal tool bar can travel around the periphery of the reflector, or that another horizontal bar be added perpendicular to the one shown in the illustration.

It is obvious that the scope and expense of such an approach render it highly impractical for reflectors the size of CAMROC's.

ANGLE DISTANCE EMPLOYED IN CISRO REFLECTOR

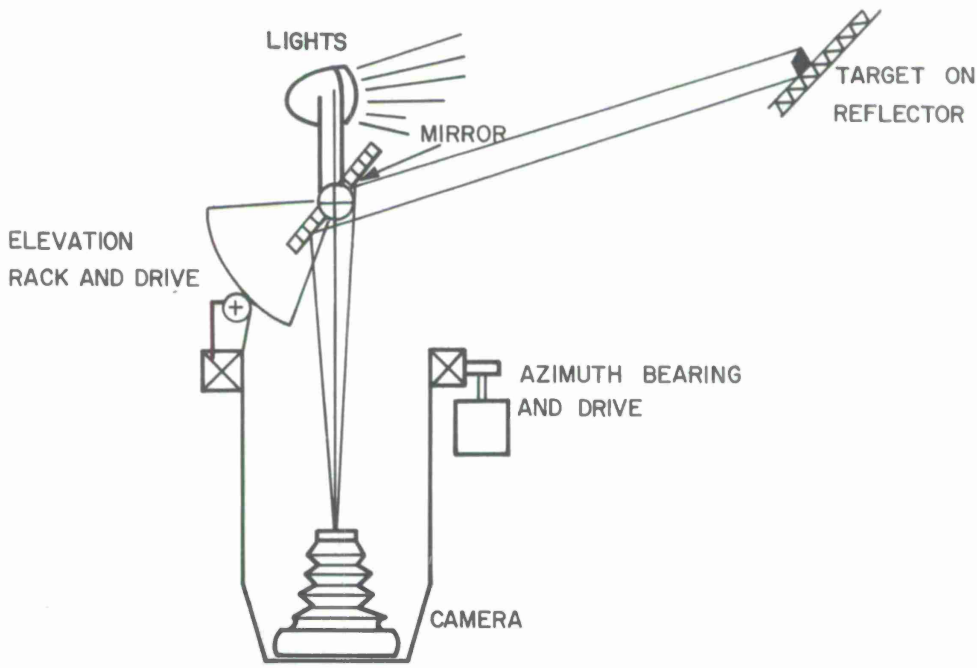

This photographic device was employed by CISRO to enable rapid data collection. A variant of the angle-distance method, it does not constitute a measurement system. The approach requires a previous accurate calibration of many targets to be used in making comparisons in the resulting films. Consequently, the time required in the field to collect a set of measurement data is reduced. A similar system is being developed by M. I. T. Lincoln Laboratory for use in the Haystack reflector. In both cases the basic authority for the validity of the results depends upon theodolite measurements made in conjunction with this rapid data collection.

ADAPTATION OF SPHEROMETER

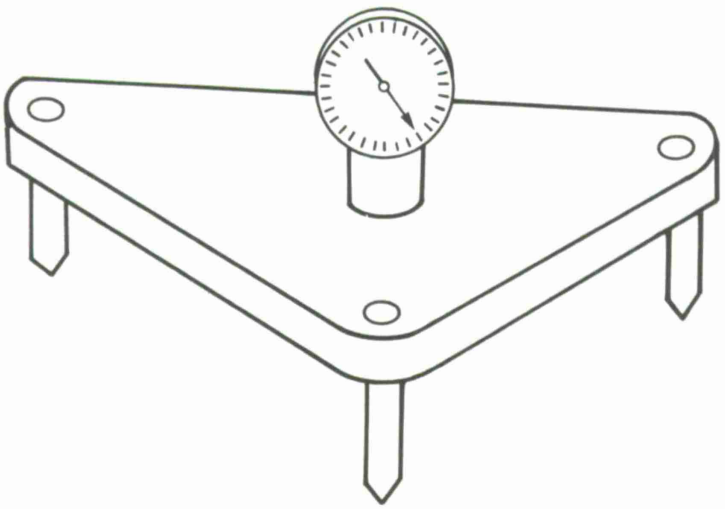

This adaptation of a spherometer depends upon the measurement of surface curvature at many places on the reflector surface. Considerable traffic is generated in the reflector. The method is slow and tiresome; also, large amounts of involved calculations are necessary to analyze the results of the measurements. Absolute measurements of the surface cannot be obtained by this method without some other control measurements.

SLOPE MEASUREMENTS

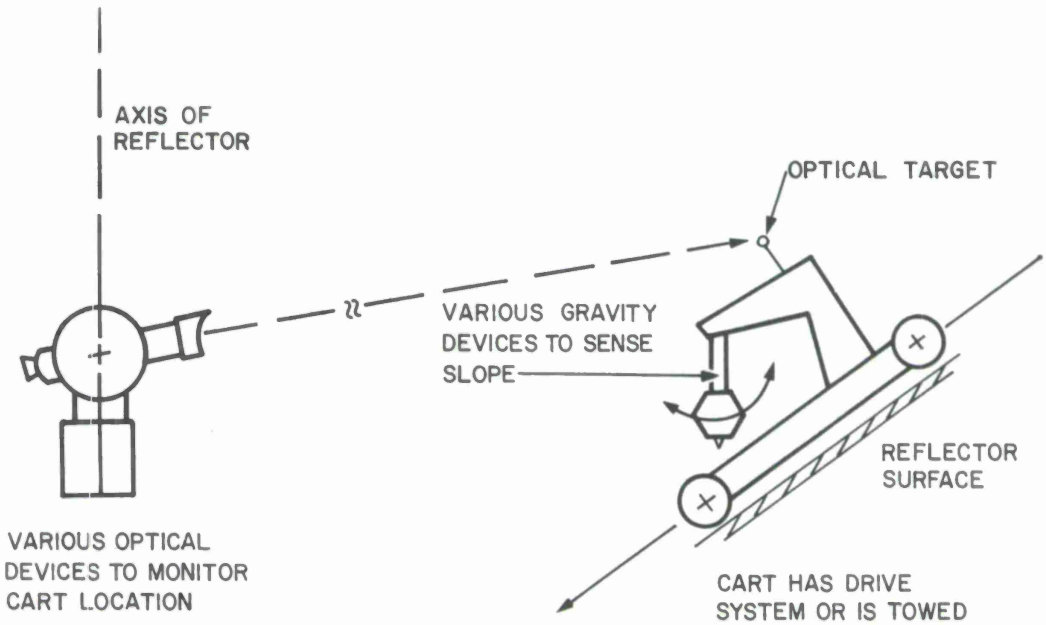

The illustration is representative of many suggestions for slope-detection devices. In general, they depend on a gravity reference of some sort and on a method of mobility, e.g., a sled or cart, about the reflector. A means of monitoring the location of the slope-measurement unit must also be provided. It is unlikely that any reasonable construction of the cart can be found that would ensure its being able to "crawl" up the slopes of most reflectors. Towing the cart calls for large complications of wires and pulleys. We doubt that any meaningful results can be obtained by this method.

SWEEP-ARM DEVICES

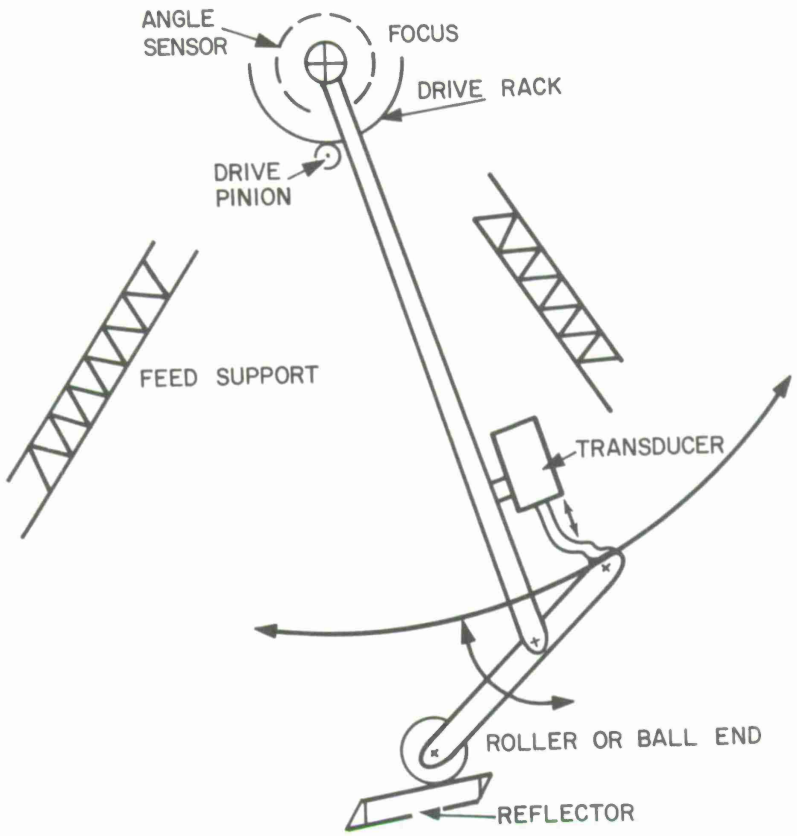

This illustration is representative of many proposals for mechanical-electrical sweep-arm gadgets. The difficulties of construction, support, and operation of such devices make them unsuitable for reflectors of any great size. Transducers with both the range and precision required are not readily available.

OTHER DEVICES

Sweep Template

The sweep template has been of much use in the measurement of reflector surfaces. It is direct and straightforward, and very useful in the smaller sizes. Reasonably high precision can be obtained with carefully made and controlled templates. Their use is best confined to reflectors below 50 ft in diameter. Templates for reflectors of about 50 to 60 ft begin to be difficult to manufacture and operate with high precision.

Shadow Graphs

Observations of distortions caused in various styles of shadow patterns created by projecting these patterns upon the reflector surface have been suggested as a method for evaluating surface quality. Since the actual distortions of a precision reflector are quite small, the resulting distortions in such shadow patterns are almost impossible to detect.

SUPPLEMENT

LARGE-DIAMETER RIGID RADOMES

This Supplement comprises Sections 1, 2, 3, and 6 of the Ammann & Whitney report of same title, dated April 1965, plus all of a Supplementary Report prepared for CAMROC by the same company in May 1966.

AMMANN & WHITNEY

NEW YORK

TABLE OF CONTENTS

April 1965 Report		Page
1	INTRODUCTION	S-1
2	SUMMARY AND CONCLUSION	S-2
3	STRUCTURAL CONSIDERATIONS	S-4
6	FABRICATION, ERECTION, AND COST	S-34
	REFERENCES	S-48

May 1966 Report		
1	INTRODUCTION	S-49
2	CONCLUSIONS AND RECOMMENDATIONS	S-49
3	SOME NEW CONCEPTS	S-50
4	FURTHER STUDIES ON SNAP-THROUGH BUCKLING	S-60
Appendix 1	FIBERGLAS TENSION MEMBERS – SUMMARY OF DATA	S-65

LARGE-DIAMETER RIGID RADOMES

1. INTRODUCTION

There is a need for larger diameter steerable antennas for space communication, satellite tracking, and scientific research. In the mechanical design of such a facility, the loads caused by wind, snow, and ice play a dominant role. These loads not only raise the overall cost of the instrument to a prohibitive point but also affect its precision. A large-diameter rigid radome enclosing the antenna will protect it against the elements of environment.

One may ask the following questions regarding radomes:

(1) Is it feasible to design and build a large-diameter radome in the range of 550 ft to 1100 ft in diameter?

(2) How much will such a radome cost? Is the cost of radome justified taking into account the savings in the antenna structure?

(3) Is the loss due to aperture blocking and induced current of the radome tolerable?

One objective of this report is to provide information on these questions. It is also hoped that this report will serve as a guide to planners of communication, radar, and radio-astronomy installations in their study of large antenna systems.

2. SUMMARY AND CONCLUSION

Among the configurations for large-diameter radomes considered, the spherical, space-frame-type construction is the most efficient structure. The space-frame members are covered by 1/32-inch-thick filament wound Fiberglas panels.

Space-frame-type radomes to 1100-ft diameter and larger are structurally feasible.

Computer techniques make it possible to analyze the structure quite accurately. Modern fabrication and welding techniques and the availability of high-strength steels and Fiberglas-reinforced plastics make it possible to fabricate the structure economically. Experience gained in erecting tall buildings and high towers can be successfully applied to the erection. As a matter of fact, not one but several erection methods are possible.

The estimated cost for 550-ft-diameter, 7/8 radome is $ 7-3/4 million. The corresponding costs for an 800-ft and an 1100-ft radome are $ 18 million and $ 46 million, respectively (see Fig. 1). These radomes cost only 8 cents/ft^3.

Anticipated savings in the antenna design due to radome protection are believed to be much more than the cost of the radome.

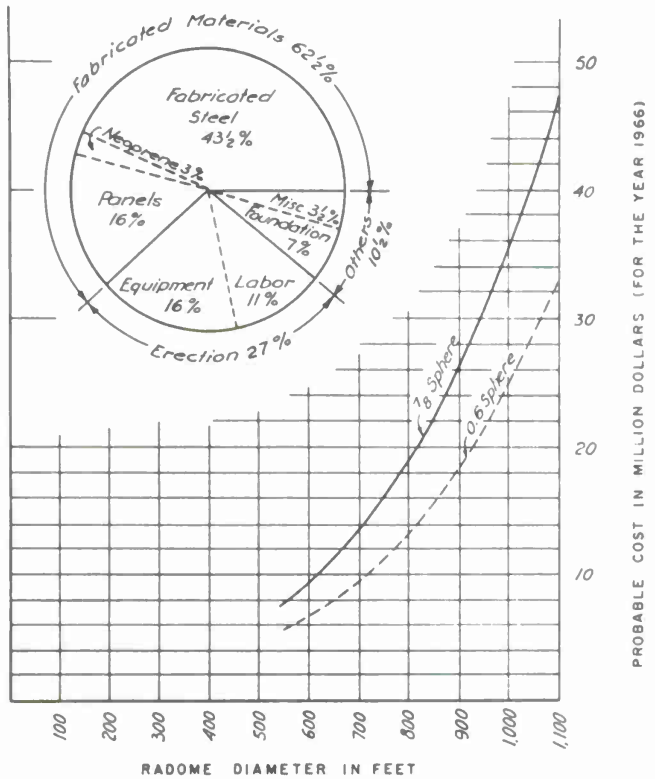

Figure 1. Cost curve.

As the radome size increases, the aperture blocking tends to increase because wind-velocity escalation, bending of members due to lateral loads, and Tsien buckling all necessitate the use of deeper and wider members. However, by use of special connection details that invoke full restraint, relatively narrow members have been proven feasible (see Fig. 2).

Effective aperture blocking, including the effect of obliquity toward the edges of the dish, is about 9-1/2%. If the obliquity effect is neglected, aperture blocking will be about 5-1/2% (see Fig. 3).

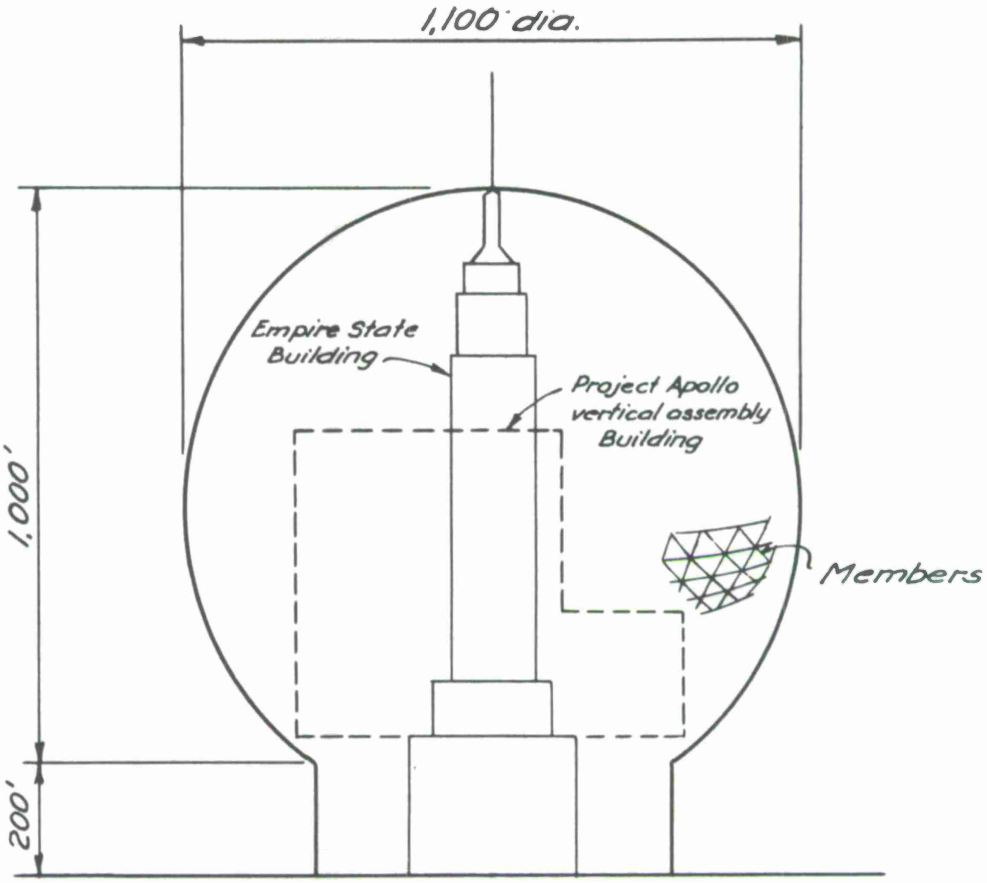

1100-FOOT-DIAMETER RADOME – COMPARATIVE SIZES

TYPICAL MEMBERS			
Radome dia.	550'	800'	1,100'
Member section	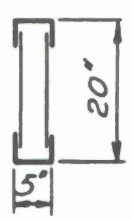	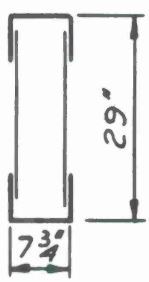	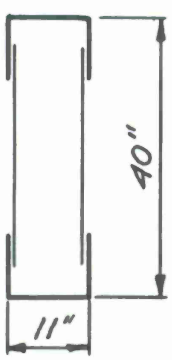
Member length	30' ±	45' ±	65' ±

Figure 2. 1100-ft-diameter radome – typical members.

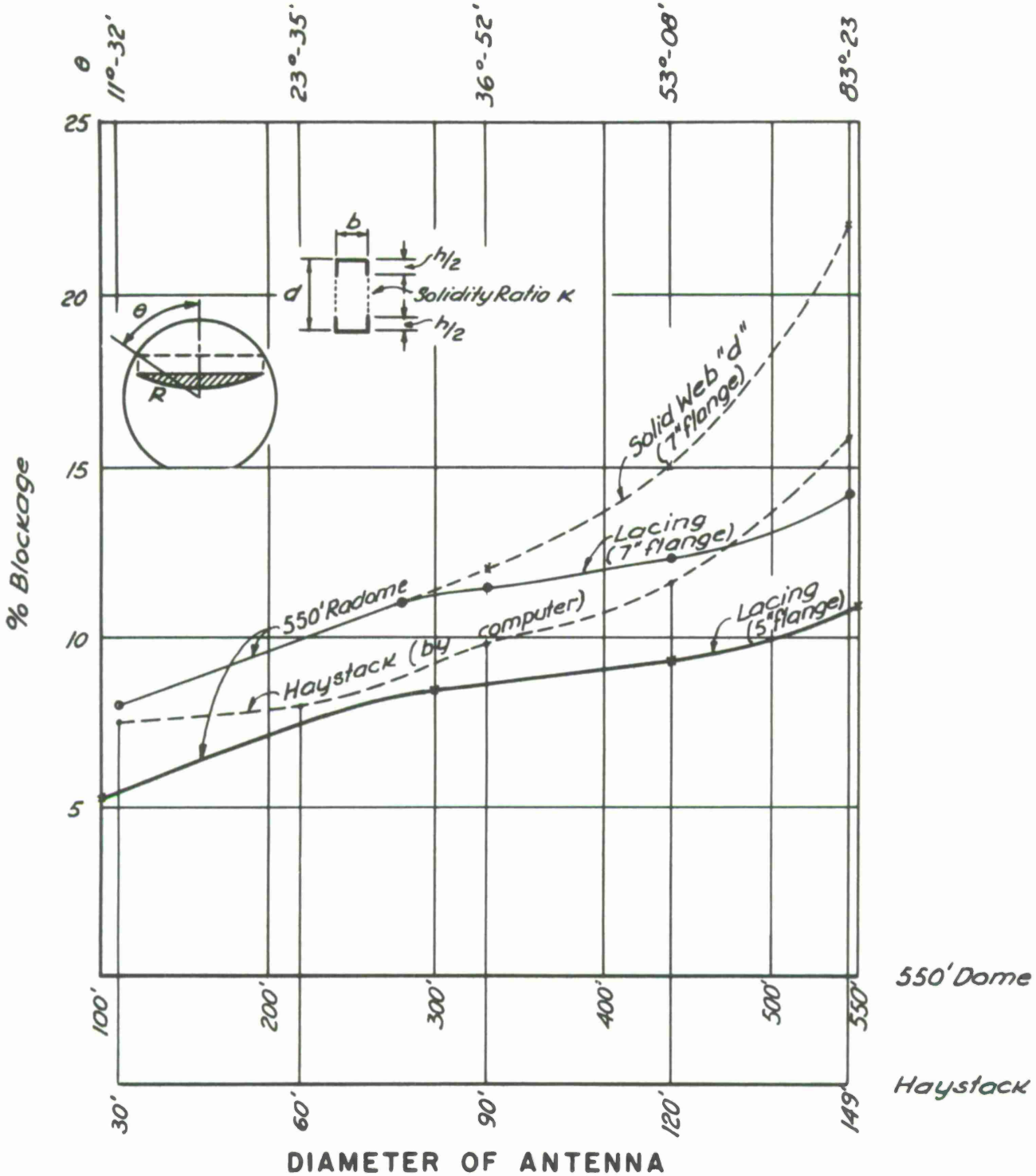

Figure 3. Aperture-blocking curve.

3. STRUCTURAL CONSIDERATIONS

3.1 Criteria

3.1.1 Service life

The service life of the structure is assumed to be 20 years.

3.1.2 Aerodynamic loads

Wind load is the most important load applied to the radome during its service life. The pressure distribution as well as the magnitude of wind load are of prime importance in the structural design of any radome. The basic wind velocity used in the design of the final structure (not during erection), the wind pressure and its distribution, the effects of gust and height escalation, and the actual design wind velocities at various height zones are summarized as follows:

3.1.2.1 Basic wind velocity

The fastest mile velocity for a 50-year recurrence interval at a height of 30 ft above the ground at the expected site is about 100 mph. The corresponding velocity for a 100-year recurrence is 105 mph (see pages 1132 and 1133 of reference (1)). Although a basic velocity pressure with a 50-year recurrence interval is recommended, since the structure is very sensitive to wind. The basic wind velocity is 105 mph, which will be further modified for gust and height effects, as described in Section 3.1.2.5. The recommended wind velocities and modifications are for normal exposure where surface friction is relatively uniform for a fetch of about 25 miles. If the exposure is elevated, subject to channeling or other special conditions, further adjustments must be made.

3.1.2.2 Pressure distribution

The wind-pressure distribution may be approximated by the following equation:

$$\frac{p - p_o}{q} = A + B \cos \mu + C \cos 2\mu \quad , \tag{1}$$

where

p = wind pressure at any point on the outside surface of the radome,

p_o = atmospheric pressure inside the radome,

q = velocity pressure at 60° F at sea level

$= 0.002558\ V^2$, where V is the wind velocity in mph.

Coordinates ϕ, μ, λ are shown in Figure 4.

Parameters A, B, and C depend on the height-to-diameter ratio of the radome, the height and shape (cylindrical or prismatical) of the supporting tower, adjacent buildings, and type of terrain at the site.

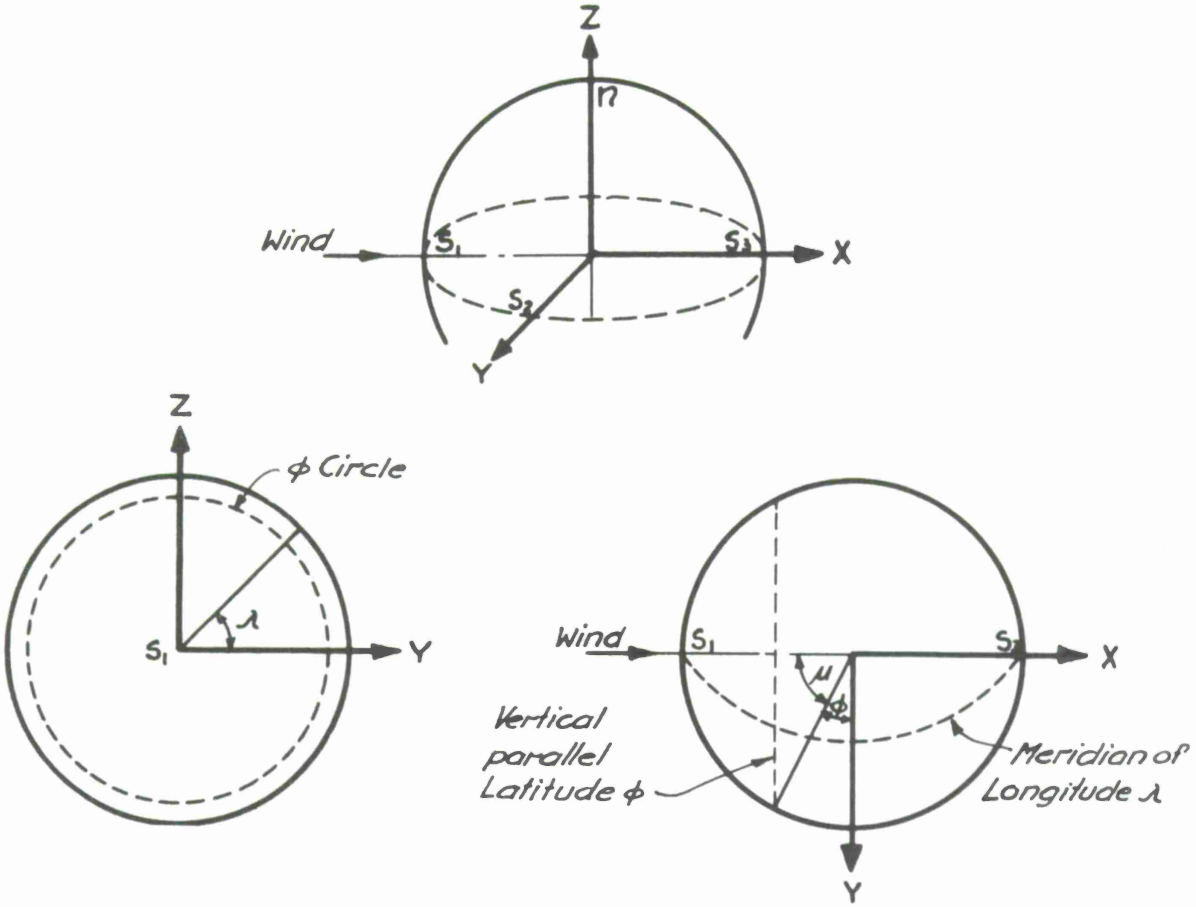

Figure 4. $\phi(\mu)$ - λ system of coordinates.

The parameters used for the Haystack Radome design were used. They are based largely on the wind-tunnel tests conducted by MIT Lincoln Laboratory and Goodyear Aircraft Company, primarily on 7/8 spheres with prismatical supporting towers. The effect of adjacent buildings was taken into account.[2]

The parameters A, B, and C used are

$A = -0.65457$,

$B = +0.43228$,

$C = +1.22229$.

The pressure-distribution coefficients c_p, which equal $(A + B \cos \mu + C \cos 2\mu)$ along any great circle passing through the stagnation axis $S_1 S_3$, are shown in Figure 5.

The accuracy of Figure 5 may be questioned, especially at point S_3 on the leeward side of the radome where inward pressure rather than outward suction is given. Undoubtedly, a more accurate pressure distribution can be obtained by measurement over the surface in a model under wind load, and more accurate representation by use of a Fourier series of more than three terms. However, the parameters used are derived from the best available sources and are considered adequate for this study. Some refinement may be warranted in a final design.

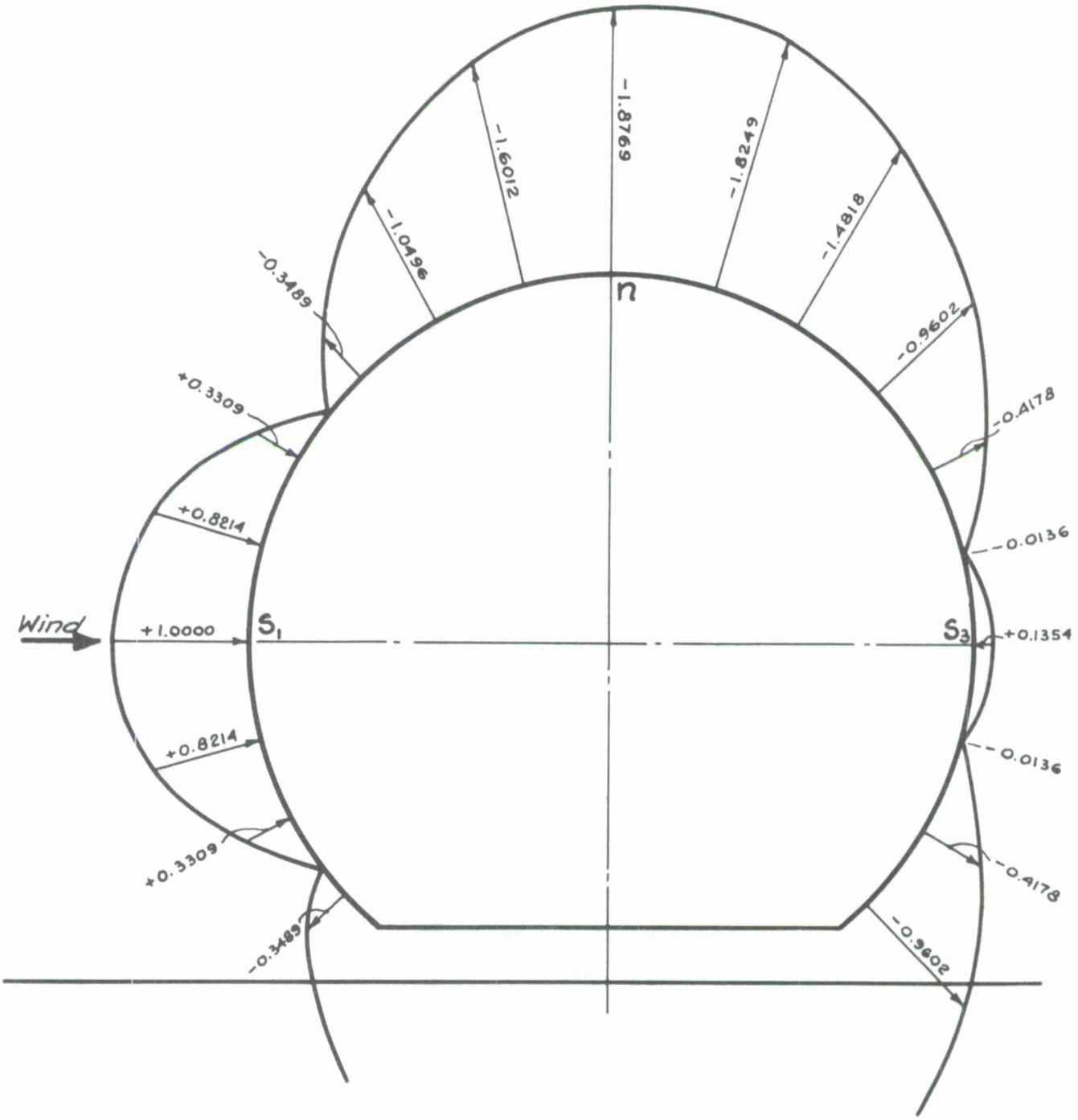

Figure 5. Pressure-distribution curve — sphere with ground.

The overall drag and lift forces for $\psi B = 142° 59'$ acting on the spherical portion, using θ, ψ system of coordinates (see Figure 6), are

$$\text{drag} = 2qR^2 \int_0^{\pi} \int_0^{\psi B} Cp \sin^2 \psi \cos \theta \, d\psi \, d\theta \quad ,$$

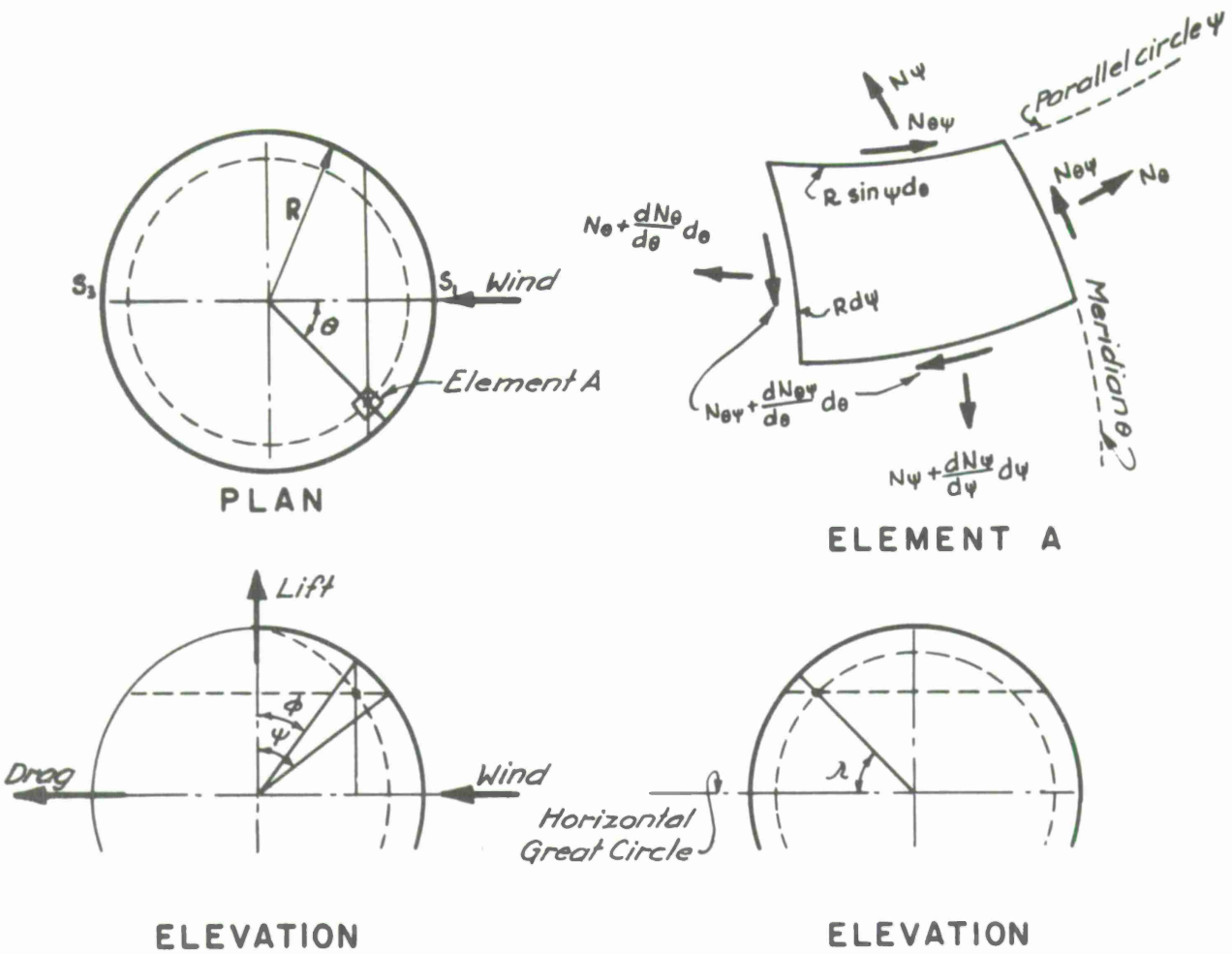

Figure 6. θ, ψ system of coordinates.

$$\text{lift} = 2qR^2 \int_0^{\pi} \int_0^{\psi B} Cp \sin\psi \cos\psi \, d\psi \, d\theta \quad ,$$

and the corresponding drag and lift coefficients are

$$C_D = \frac{\text{drag}}{Aq} = 0.64 \quad ,$$

$$C_L = \frac{\text{lift}}{Aq} = 0.68 \quad .$$

Actually, the coefficients C_D and C_L are obtained from wind-tunnel tests, and the parameters A, B, and C are derived from these coefficients. It should be noted that the wind-drag coefficient, 0.64, is substantially larger than that for a sphere without a ground plane, which is 0.20.[3] (The pressure distribution for a sphere without a ground plane is shown in Figure 7 for comparison.) The increase is due to the effect of the supporting tower as well as to the ground plane.

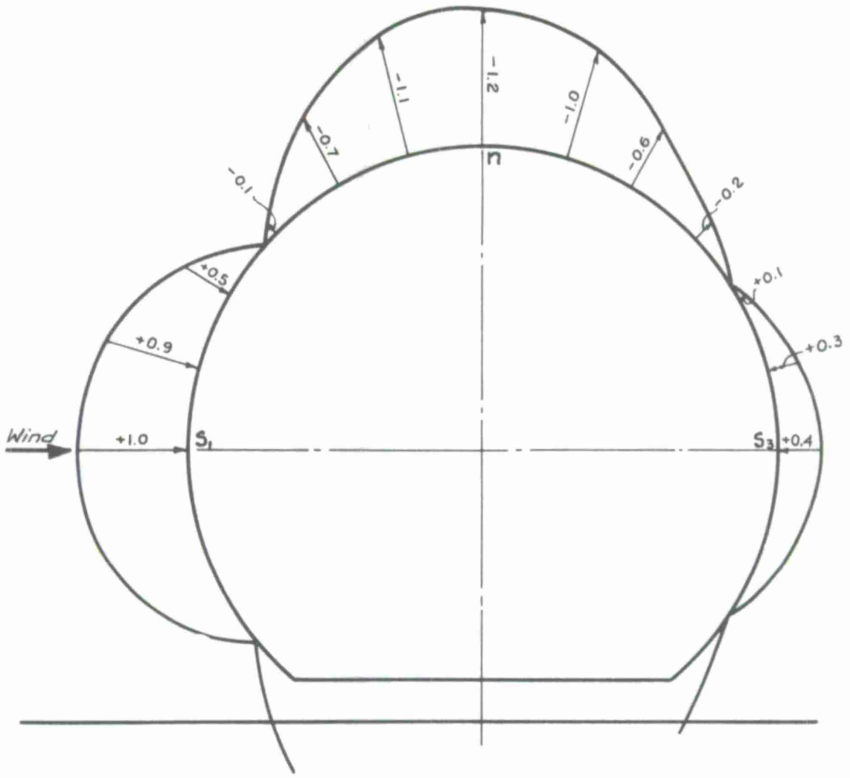

Figure 7. Pressure-distribution curve — sphere without ground.

It also should be noted that the drag coefficient for a streamlined object shows a large increase at the critical Reynolds number of about 0.5×10^6. For example, at Reynolds number = 0.5×10^6, the drag coefficient for a sphere is 0.20. This coefficient will increase to 2.0 at Reynolds number = 50. For radomes in the range of 200 ft to 1100 ft in diameter, and wind in the range of 33 mph to 105 mph, the minimum Reynolds number for standard air is about 6.2×10^7. (Wind velocities under 33 mph need not be considered since any increase in drag coefficient will be offset by the decrease in dynamic pressure.) Therefore, for the ranges of radome sizes and wind velocities under consideration, the wind load is in the supercritical Reynolds number range, and there is no danger of any increase in drag coefficient.

3.1.2.3 Gust

To allow for the effect of gust, a constant gust pressure should be added to the velocity pressure in all height zones. The additional pressures (not velocities) are 20% for the overall structure, and 30% and 40% of the velocity pressure over areas 100 ft × 100 ft and 20 ft × 20 ft, respectively.

3. 1. 2. 4 Height escalation

The free-field wind velocity increases with height in accordance with the formula

$$V_Z = V_{30}\left[\frac{Z}{30}\right]^{1/7} , \qquad (2)$$

where Z = height of point being considered in feet, V_Z and V_{30} are the wind velocities at heights Z and 30 ft, respectively. Because the relatively streamlined radome should not interfere with the distribution appreciably, the velocity of the wind impinging on the structure should be increased accordingly. However, the value of the exponent should be reevaluated after the site for the radome is selected.

The pressure-escalation curve is shown in Figure 8. From the curve, it can be seen that the pressure at elevation 420 ft is twice that at elevation 30 ft. The pressure-variation curve based on a stepped approximation recommended by the ASCE for inland areas is also shown in Figure 8.

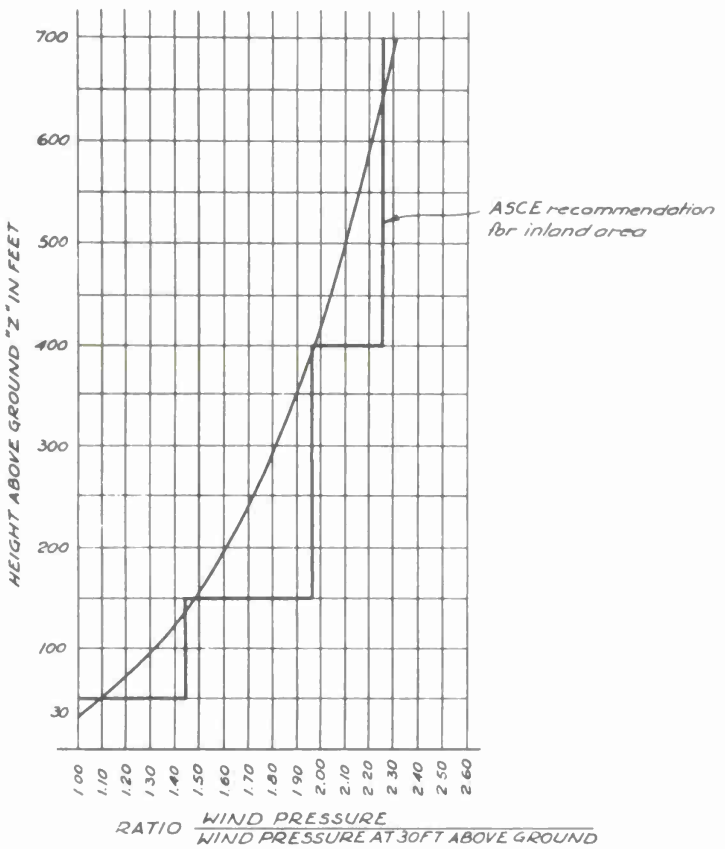

Figure 8. Pressure versus height.

3. 1. 2. 5 Design wind velocity

Although the basic wind velocity used is 105 mph, the actual design wind velocity is much higher on account of gust, height variation, and local conditions.

For overall structural design, the following velocities were used for this report. The lower values represented by the smooth curve in Figure 8 are recommended for final design.

Height zone (ft)	Design wind velocity (mph)
0 to 50	115
50 to 150	134
150 to 400	154
400 to 700	164

For very local conditions, such as the panels at the top of radome, the design wind velocity is as high as 170 mph.

3. 1. 3 Other loads

The snow load is assumed to be 30 psi of horizontal projection. A combination of one-half snow weight and one-half wind pressure is also considered. To allow for rigging for antenna and radome repair, a 4000-lb vertical load per hub on three adjacent hubs and a concentrated 500-lb load on any member have been selected. In estimating the dead load, liberal allowance is made for a heating and ventilation duct system.

3. 1. 4 Factor of safety

A factor of safety of 1. 20 for wind load or for one-half snow plus one-half wind is used. A factor of safety of 1. 65 is used for snow load. A factor of safety against Tsien or classical buckling of at least 2 for any loading is used.

3. 2 General Configuration

3. 2. 1 Concepts

The following structural concepts have been considered in this study:

1) Thick-walled polystyrene or polyurethane dome. – Rejected after correspondence with manufacturer showed it to be unfeasible.

2) Air-inflated dome. – Felt to be of doubtful reliability because of the great size. The system was not studied in detail.

3) Cylindrical wall with cable-supported and domed roofs. – Preliminary design study showed lowered erection cost but very high material cost due to loss of membrane behavior. Heavy ring required at junction of roof and wall is undesirable electrically.

4) Intersecting bars or pipes in space-frame pattern. – Very efficient in fabrication and material costs. Has been used successfully for several smaller domes. However, the buckling capacity proved too small to permit use in the large diameters studied.

5) Moveable wind screen. – No satisfactory concept could be developed.

6) Space frame dome. – Recommended concept, described further below.

The following coverings over the space-frame elements have been investigated:

1) Sandwich panels. – These consist of polystyrene or polyurethane foam protected by mylar or mylar-tedlar on each surface. Because the panels are rigid, they cannot take advantage of membrane behavior. The great thickness required makes them uneconomical.

2) Mylar-dacron-tedlar laminate. – This laminate has excellent electrical properties. However, it has a low tensile strength (7000 psi). Its low modulus (250,000 psi) leads to very large deflections. It is flammable and its maximum size between splices (7-1/2 ft) makes it unsatisfactory for large-diameter domes of this study.

3) Filament wound Fiberglas-reinforced plastic. – This is recommended and is described further in this report.

3.2.2 Space-frame construction

Typical space-frame concepts are shown in Figures 9 through 13. The basic parameter, after the decision to use triangular framing is made, is the length of the frame member.

The length, which determines the width of the triangular space between members, is governed by the strength and manufactured width of the panels. Structural-steel shipping and manufacturing limitations are not so severe.

The width of the frame member for a given length is influenced by lateral load capacity, by lateral buckling capacity, and by the minimum size available for panel-connection details.

The depth is essentially governed by Tsien-type buckling, although local buckling and bending are factors.

A member approximately 30 ft in length and 20 inches in depth is most suitable for the 550-ft-diameter radome. If the length of the member is reduced, the increased number of hub joints and the minimum structural depth requirement for buckling will increase the optical blockage. On the other hand, if the length of the member is increased, say to 60 ft, the bending of the member becomes so great that a very deep member is required. The use of deeper members beyond the buckling requirement will unnecessarily increase the optical blockage and reduce the inside clearance of the radome.

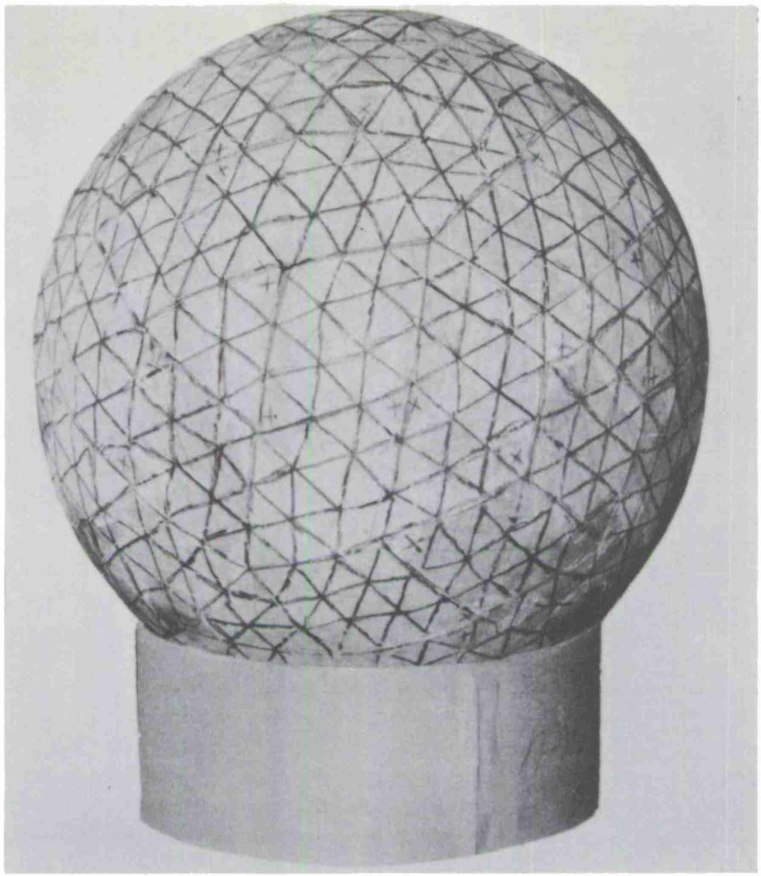

Figure 9. TTR uniform geometry.

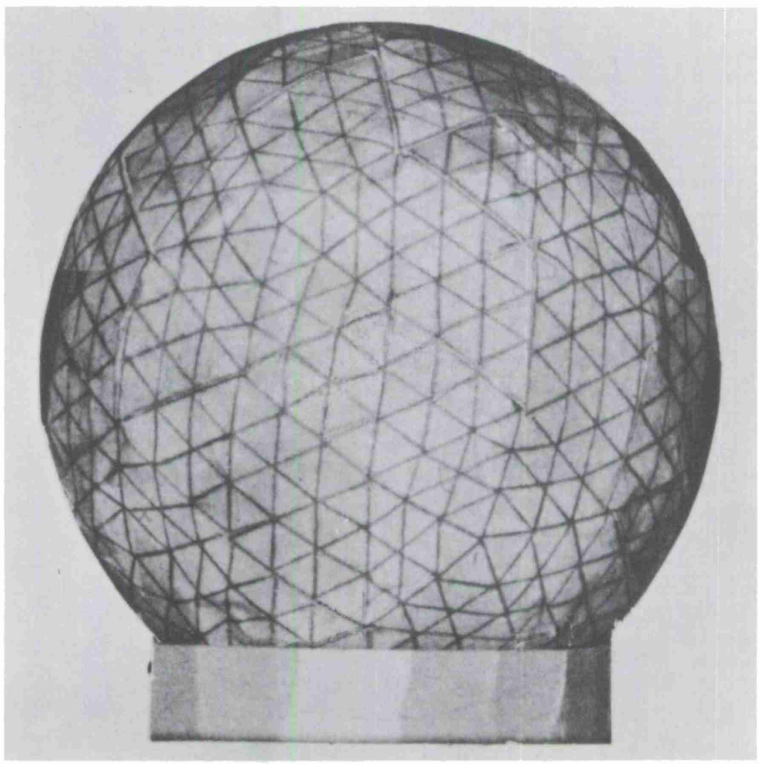

Figure 10. Uniform geometry.

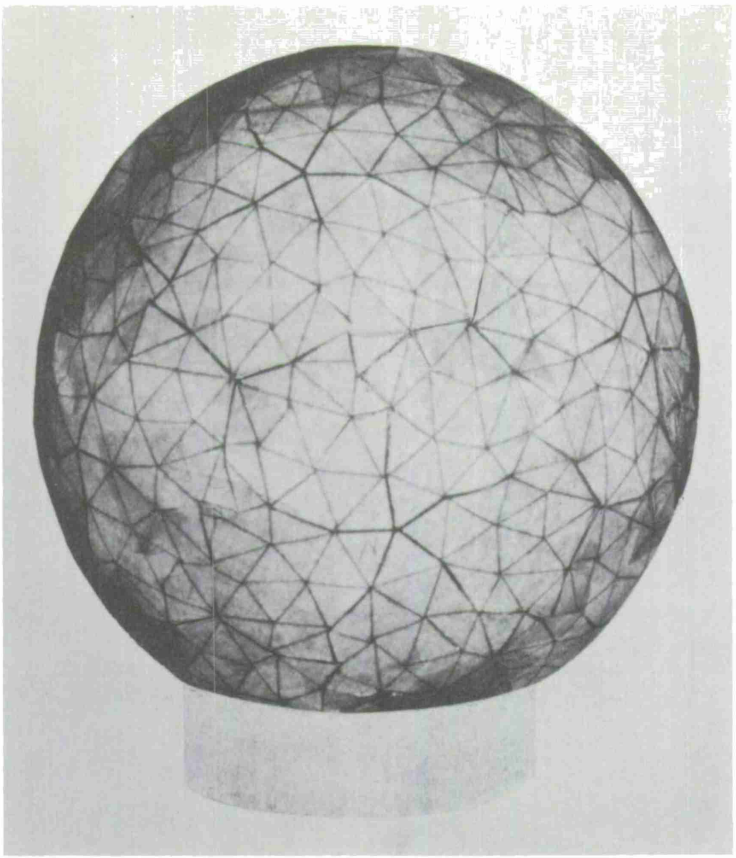

Figure 11. Haystack geometry.

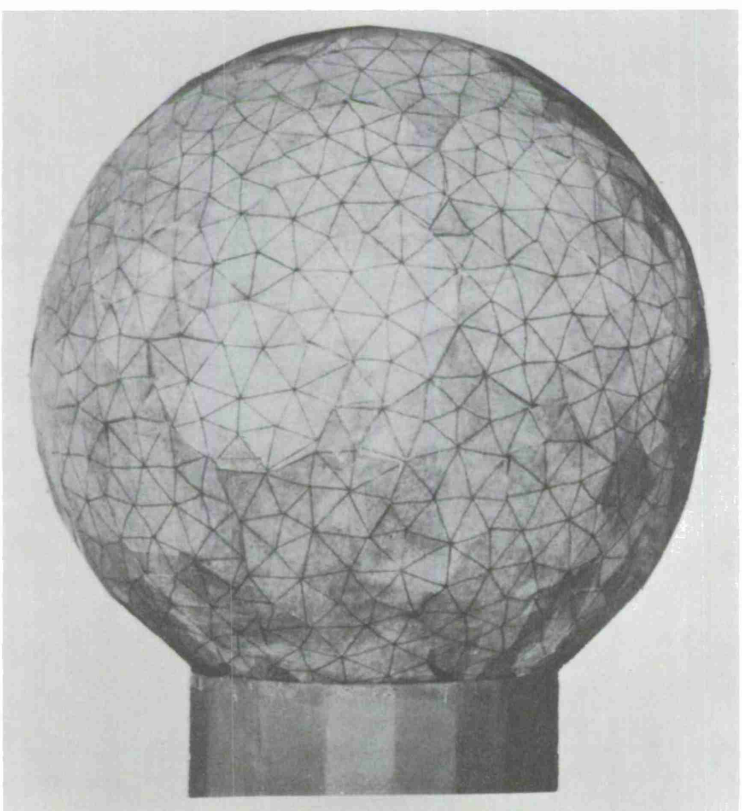

Figure 12. TTR random geometry.

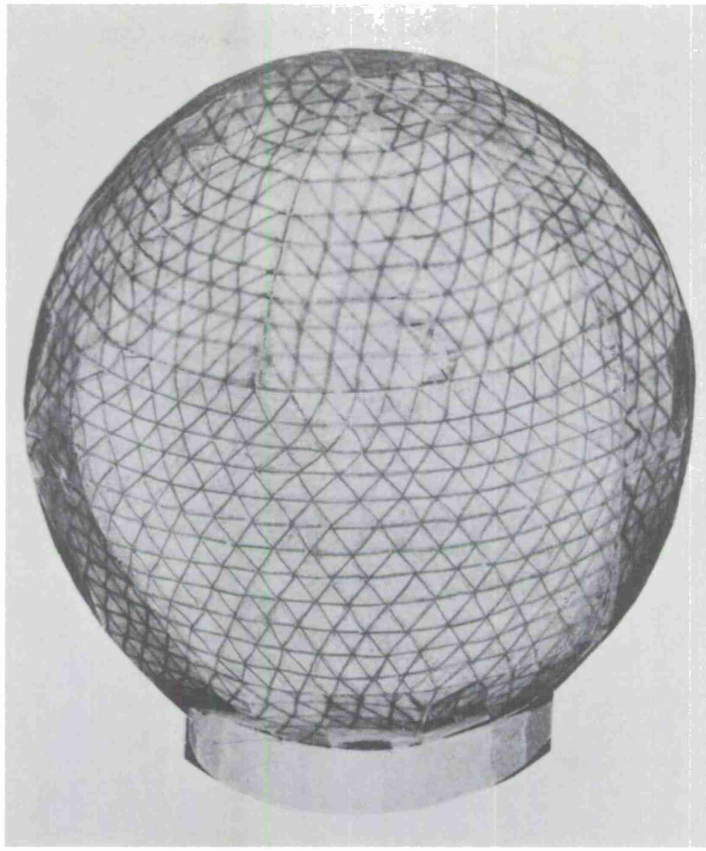

Figure 13. Horizontal ring geometry.

The member lengths for 800-ft diameter and 1100-ft diameter radomes have been set at 45 ft and 65 ft, respectively. Special tooling is required for manufacturing Fiberglas panels for these domes.

3.2.3 Frame geometries

Several space-frame geometries have been considered. They are listed as follows:

TTR uniform geometry, see Figure 9
Uniform geometry, see Figure 10
Haystack geometry, see Figure 11
TTR random geometry, see Figure 12
Horizontal ring geometry, see Figure 13
Nontriangular geometry, see Figure 14.

The first four geometries are based on drawings furnished by MIT Lincoln Laboratory (LL Dwg No C-199981, 1 of 4 to 4 of 4 inclusive). The basic geometry of these four schemes consists of 60 congruent spherical quadrilaterals. Each of these quadrilaterals can be divided into two spherical triangles. One is the reflection of the other. These triangles are also called Schwarz triangles.

In TTR uniform and uniform geometries each spherical quadrilateral is subdivided into 18 spherical triangles. Haystack and TTR radome geometries use 17 and 28-1/3 triangles, respectively, in the quadrilateral.

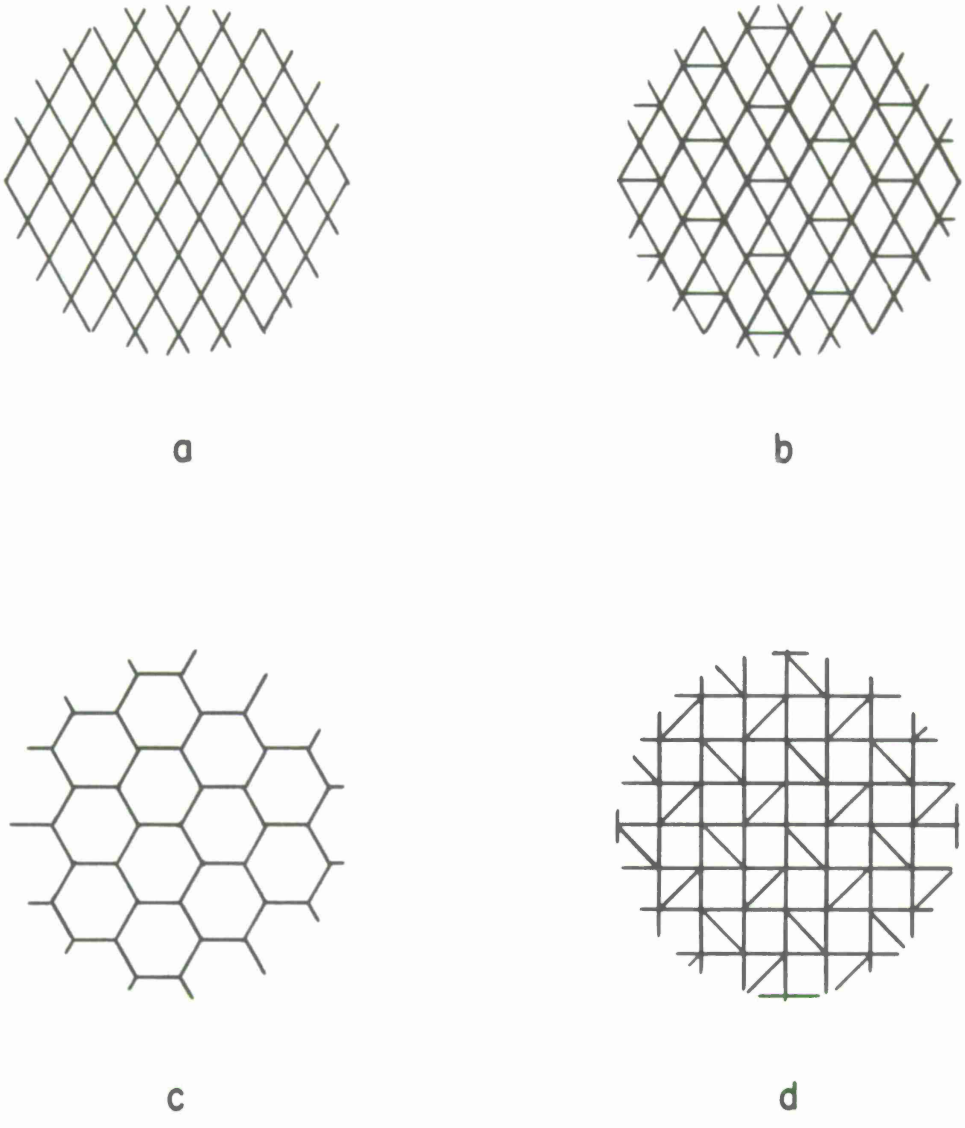

Figure 14. Nontriangular geometry

In the horizontal ring geometry, the surface of the radome is divided into horizontal rings with diagonals between the rings. The lengths of various members are given in Figure 15.

The nontriangular geometry is based upon the triangular geometries, but many members have been eliminated to decrease optical blockage.

The characteristics and merits of various geometries are listed in Table 1.

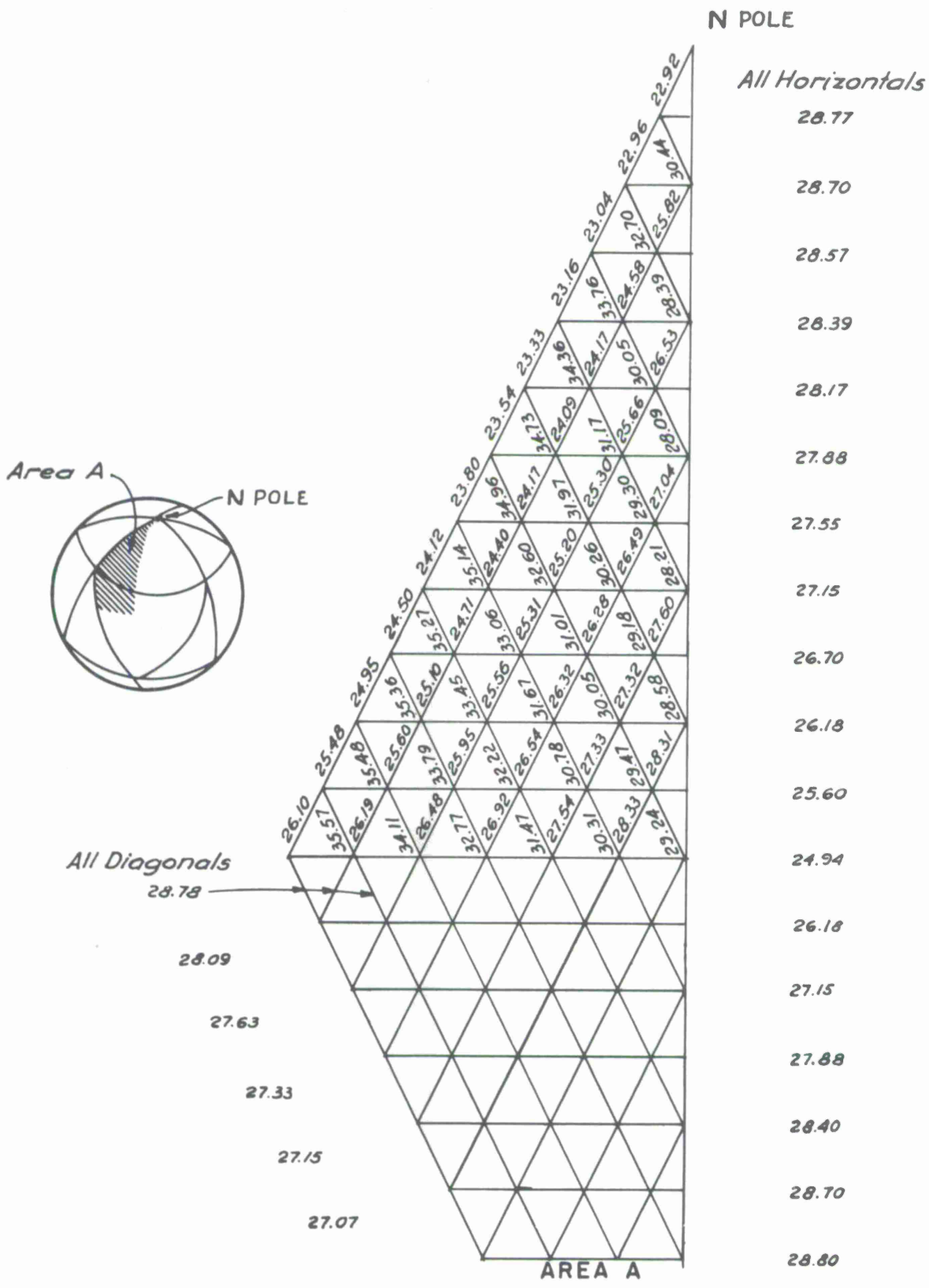

Figure 15. Member length.

Table 1.

Geometry	Number of different sizes of panels	Number of different lengths of members	Ratio $\frac{\text{Longest}}{\text{Shortest}}$	Order of merit				Remarks
				Structure	Erection	Optical blockage	Random scattered energy	
TTR uniform	6	8	1.22	1	2	1	2	
Uniform	7	11	1.22	1	2	1	2	
Haystack	11	12	1.68	2	2	2	1	
TTR random	12	11	1.82	2	2	2	1	
Horizontal ring	59	73	1.10*	1	1	2	2	*For governing members in structural design only
Nontriangular	--	--	--	2	2	-	-	

TTR uniform and horizontal ring geometries are structurally favorable because all members are of about the same length. For constant-member cross section, the uniformity in member length will yield a most efficient design. However, in the large-size domes studied, member sections will not be held constant. It should be noted that there are long members near the top of the radome for the horizontal ring scheme. Because these members are governed by tension, the length will not affect its strength. It should also be noted that there are more sizes of panels and more different lengths of members in this geometry. However, there is so much repetition for both panels and members, that fabrication cost will not be appreciably affected.

The nontriangular geometry requires primary bending in the member. Furthermore, the stress in the panels increases rapidly since they have to span greater distances. Panels four times as thick as in the triangular scheme are required. The nontriangular framing is therefore not recommended.

As for erection, the horizontal ring geometry is most advantageous, especially for jacking construction and geometry control during erection, although the advantages are small.

From the electrical performance point of view, TTR uniform and uniform geometries are better than other schemes since they will yield a minimum optical blockage.[4] However, Haystack and TTR random offer a distribution of the scattered energy.[5] It is believed that the adoption of any of the first five geometries listed in Table 1 will not affect substantially the overall cost of the structure, although the uniform geometries are slightly favorable. The use of nontriangular scheme will result in an increase in overall cost.

3. 3 Stress Analysis

3. 3. 1 Membrane stresses

To find the stresses in all members due to various loadings, a computer analysis such as FRAN or STAIR should be used.

An approximate method using membrane theory has been developed to determine the stress in an individual member. This method showed poor correlation when applied to the Haystack radome and compared to the stresses from the STAIR analysis.[6] However, the analysis[7], [8], [9] is considered satisfactory for computing average member sizes in different zones of the space frame for the purpose of determining weights.

Stresses at various points in the radome due to dead load, wind, truncation, etc., have been evaluated by using membrane theory. The results of the computer program for the Haystack radome[6] have been used as a guide in selecting the points to make certain that the highly stressed areas are included.

The summary of stresses for a 550-ft diameter radome is given in Table 2. See Figure 6 for coordinate system, "+" in Table 2 denotes tension; "-", compression. The locations of the points and stress distribution along certain horizontal circles are shown in Figures 16, 17, 18, and 19. From stresses $N\psi$, $N\theta$, and $N\theta\psi$ (Figure 6) the principal stresses at various locations have been found.

Since the wind can blow in any direction, the maximum tensile and compressive stresses along any horizontal circle can occur at any point on the circle. Figure 20 is an envelope of the maximum principal stresses at all the points along any longitudinal. Stresses at point N have been adjusted to take into account the wind-velocity escalation with height.

3. 3. 2 Elastic stability

In the winter of 1963, a large metal space-frame dome in Bucharest, Rumania, collapsed after a 3-ft snowfall.[10] This structure of 307-ft span and 62. 7-ft rise was made of a lattice of steel tubes up to 4 inches in diameter by 0. 236 inch in wall thickness. Its failure was attributed to buckling. This reinforces the belief that buckling is the most critical aspect of any large-diameter random design.

In the buckling study, classical theory (linear, small-deflection)[11] Tsien's buckling (snap-through),[12] and member buckling have been considered. For the types of loadings and configuration of the radome, there is no exact theoretical solution available for the first two types of buckling. However, available approximate buckling criteria[9] are considered adequate. Member buckling will be discussed in Section 3. 4.

The critical uniform radial pressure for a spherical space radome can be derived from the general buckling equation for spherical shells:

$$P_{crit.} = K E \left(\frac{t}{r}\right)^2 , \qquad (3)$$

where E = Young's modulus, t = shell thickness, r = radius of the shell, K = buckling coefficient. By using an idealized isotropic plate with simultaneously equivalent bending stiffness and axial stiffness for the steel space frame, the following equation can be obtained:

$$P_{crit.} = \frac{12,600,000\ tw\ V}{R^2} , \qquad (4)$$

where P crit. = critical pressure in psf, tw = thickness of weight (equivalent plate in inches), V = radius of gyration of members in inches, and R = radius of the radome in feet.

Equation (4) shows that for a given diameter of radome, the critical buckling pressure varies directly with tw and V. Since tw is determined by membrane-stress requirement, the depth of member is established from the "V" requirement. For the 550-ft

Table 2. Stress summary in k/ft

ψ	Load	θ = 0°			θ = 45°			θ = 90°		
		Nψ	Nθ	Nθψ	Nψ	Nθ	Nθψ	Nψ	Nθ	Nθψ
0°	Wind	+ 5,490	+25,965	0						
	Truncation	-	-	-						
	D. L.	- 1,790	- 1,790	0						
	Total	+ 3,700	+24,175	0						
30°	Wind	+ 2,066	+15,540	0	+13,851	+ 9,943	+ 8,175	+25,994	+ 5,490	- 994
	Truncation	-	-	-	-	-	-	-	-	-
	D. L.	- 1,916	- 1,180	0	- 1,916	- 1,180	0	- 1,916	- 1,180	0
	Total	+ 150	+14,360	0	+11,935	+ 8,763	+ 8,175	+24,078	+ 4,310	- 994
90°	Wind	- 4,762	-12,014	0	+10,615	- 4,763	- 3,417	+25,994	+ 5,490	- 4,834
	Truncation	-	-	-	-	-	-	-	-	-
	D. L.	- 3,575	+ 3,575	0	- 3,575	+ 3,575	0	- 3,575	+ 3,575	0
	Total	- 8,337	- 8,439	0	+ 7,040	- 1,188	- 3,417	+22,419	+ 9,065	- 4,834
112°	Wind	+ 165	-10,658	0	+13,802	- 4,694	-10,426	+25,994	+ 5,490	- 9,310
	Truncation	+ 542	- 542	0	0	0	- 542	- 542	+ 542	0
	D. L.	- 5,716	+ 7,055	0	- 5,716	+ 7,055	0	- 5,761	+ 7,055	0
	Total	- 5,009	- 4,145	0	+ 8,086	+ 2,361	-10,968	+19,736	+13,087	- 9,310
138°	Wind	+24,904	-16,189	0	+30,400	-11,295	-30,236	+25,994	+ 5,490	-31,893
	Truncation	+ 3,377	- 3,377	0	0	0	- 3,377	- 3,377	+ 3,377	0
	D. L.	-14,273	+16,953	0	-14,273	+16,953	0	-14,273	+16,953	0
	Total	+14,008	- 2,613	0	+16,127	+ 5,658	-33,613	+ 8,344	+25,820	-31,893

Table 2 (contd).

ψ	Load	θ = 135°			θ = 180°		
		Nψ	Nθ	Nθψ	Nψ	Nθ	Nθψ
30°	Wind	+15,069	+13,851	- 9,581	+ 3,788	+21,066	0
	Truncation	-	-	-	-	-	-
	D. L.	- 1,916	- 1,180	0	- 1,916	- 1,180	0
	Total	+13,153	+12,671	- 9,581	+ 1,872	+19,886	0
90°	Wind	+10,615	+ 5,493	- 3,417	- 4,762	+ 2,490	0
	Truncation	-	-	-	-	-	-
	D. L.	- 3,575	+ 3,575	0	- 3,575	+ 3,575	0
	Total	+ 7,040	+ 9,068	- 3,417	- 8,337	+ 6,065	0
112°	Wind	+ 8,868	+ 9,748	- 2,746	- 6,811	+ 9,766	0
	Truncation	0	0	+ 542	+ 542	- 542	0
	D. L.	- 5,716	+ 7,055	0	- 5,716	+ 7,055	0
	Total	+ 3,152	+16,803	- 2,204	-11,985	+16,279	0
138°	Wind	- 3,408	+29,301	-14,868	-22,907	+41,221	0
	Truncation	0	0	+ 3,377	+ 3,377	- 3,377	0
	D. L.	-14,273	+16,953	0	-14,273	+16,953	0
	Total	-17,681	+46,254	-11,491	-33,803	+54,797	0

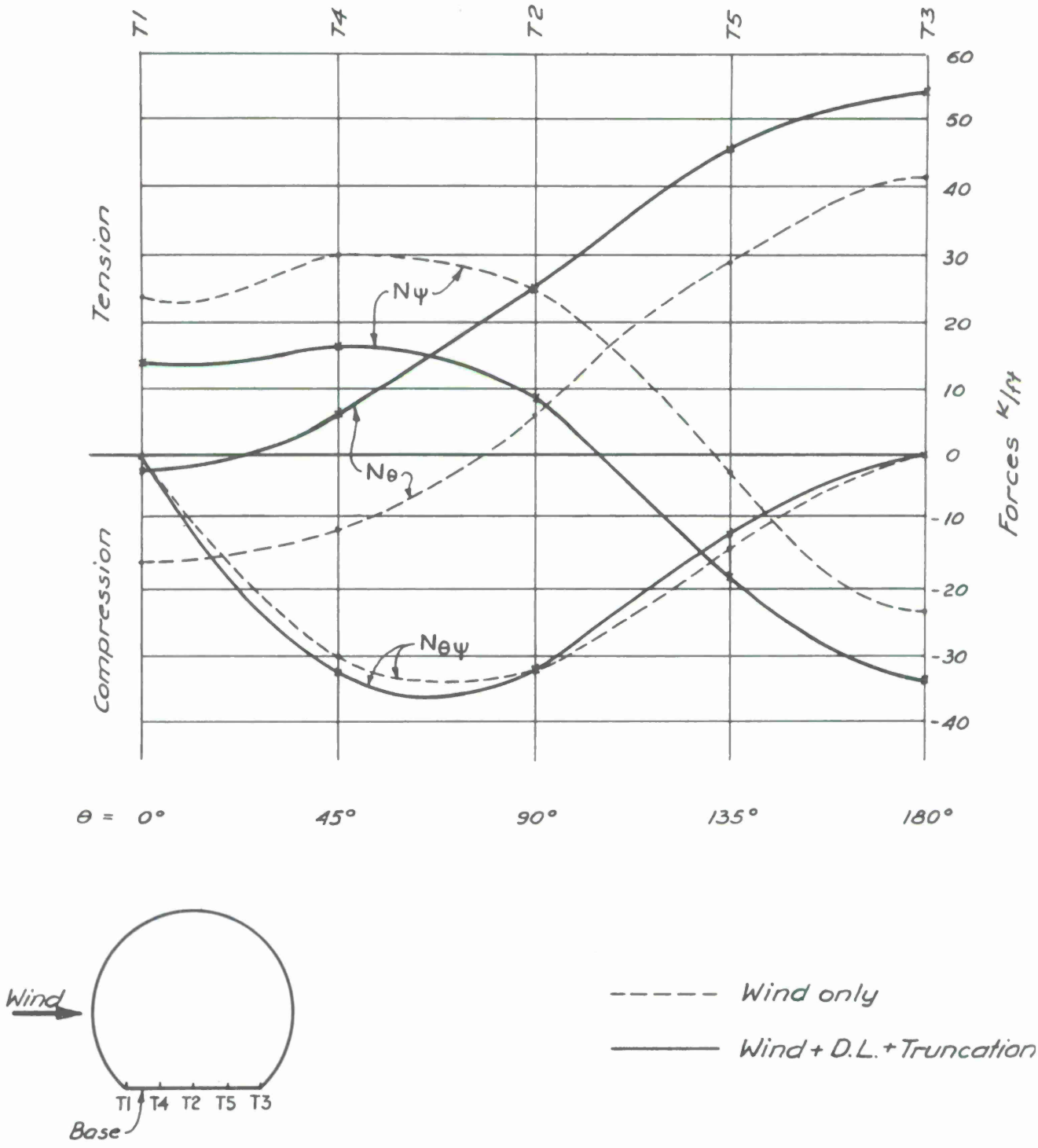

Figure 16. Stress curve at base.

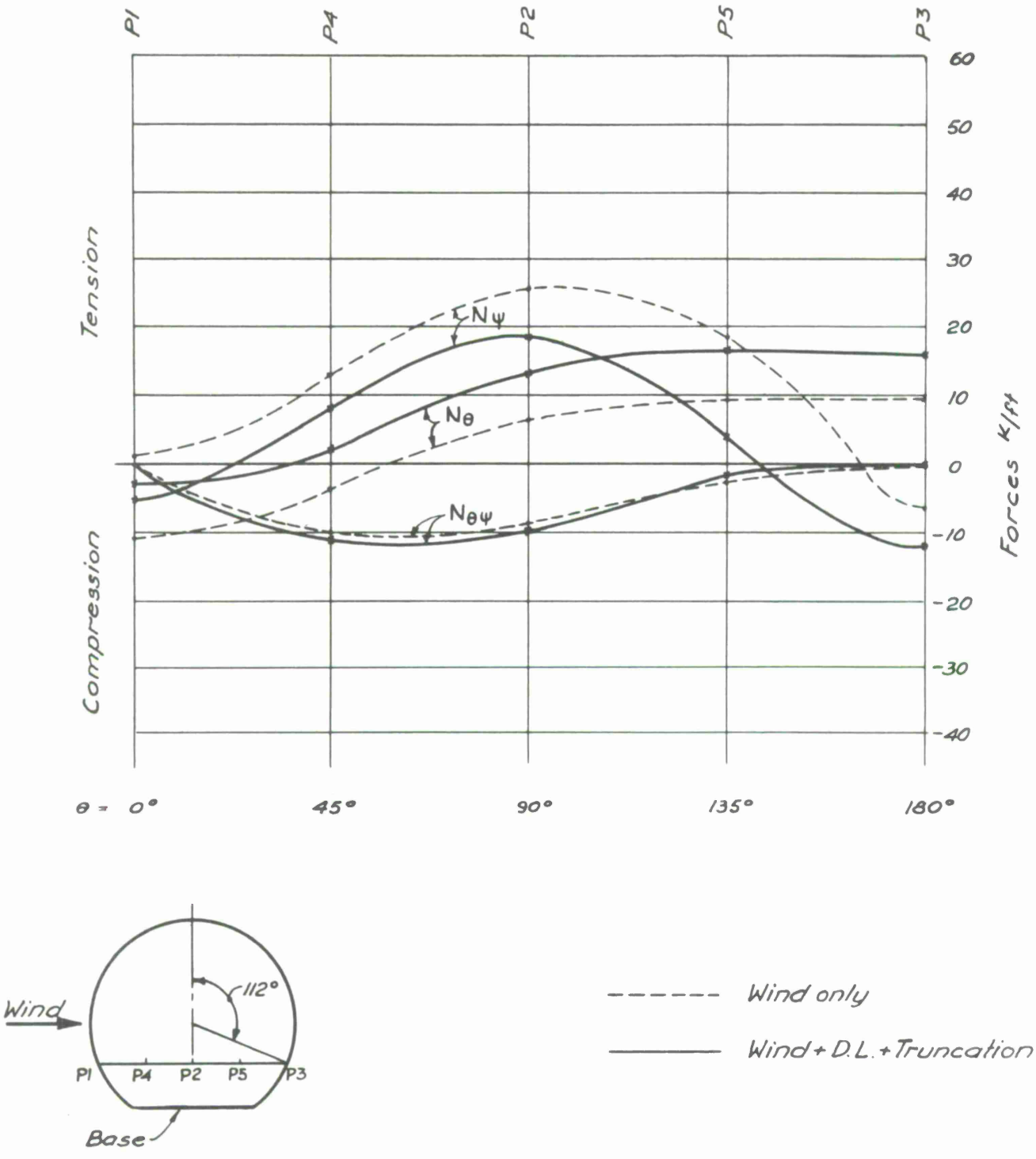

Figure 17. Stress curve at line P.

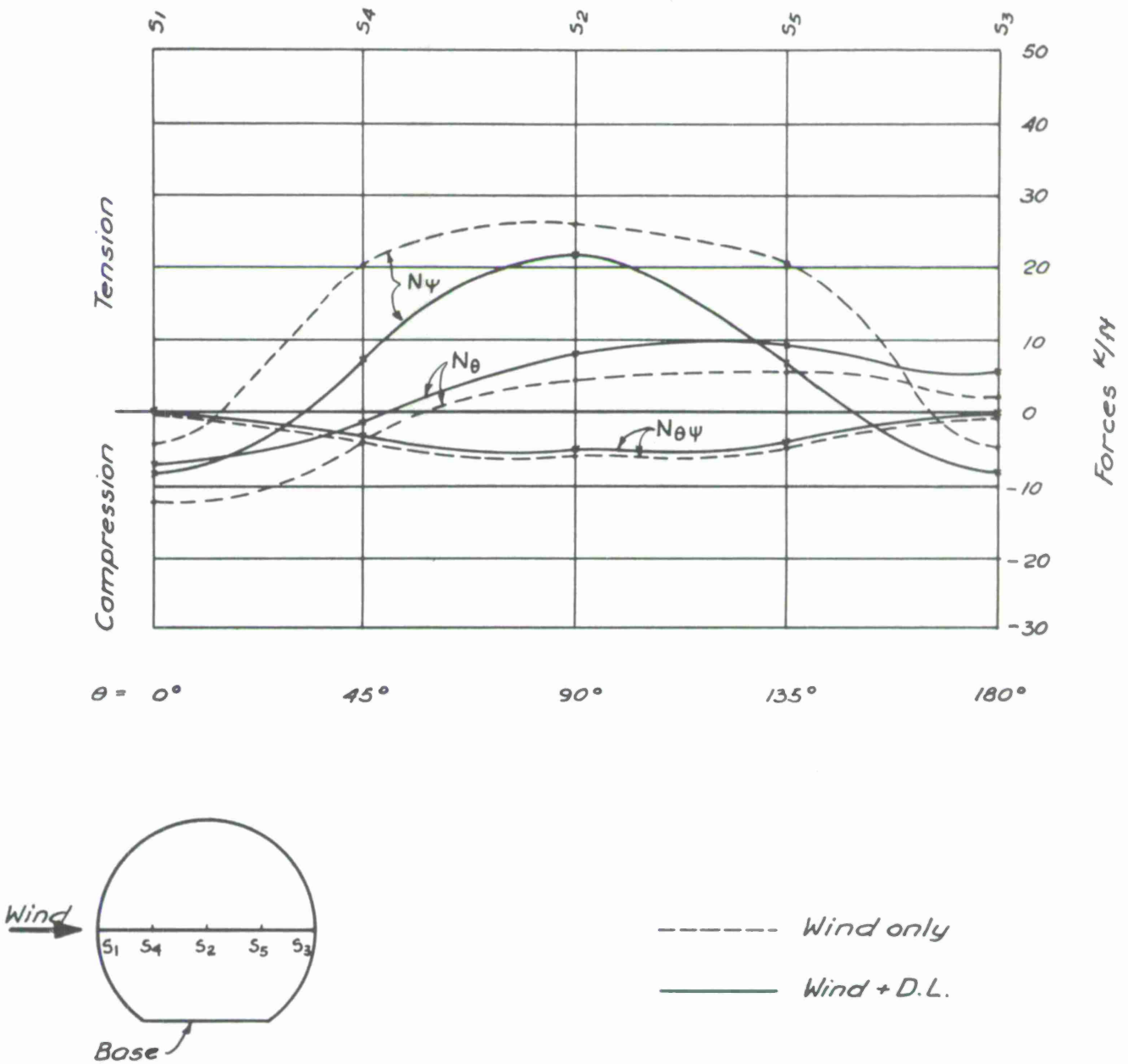

Figure 18. Stress curve at line S.

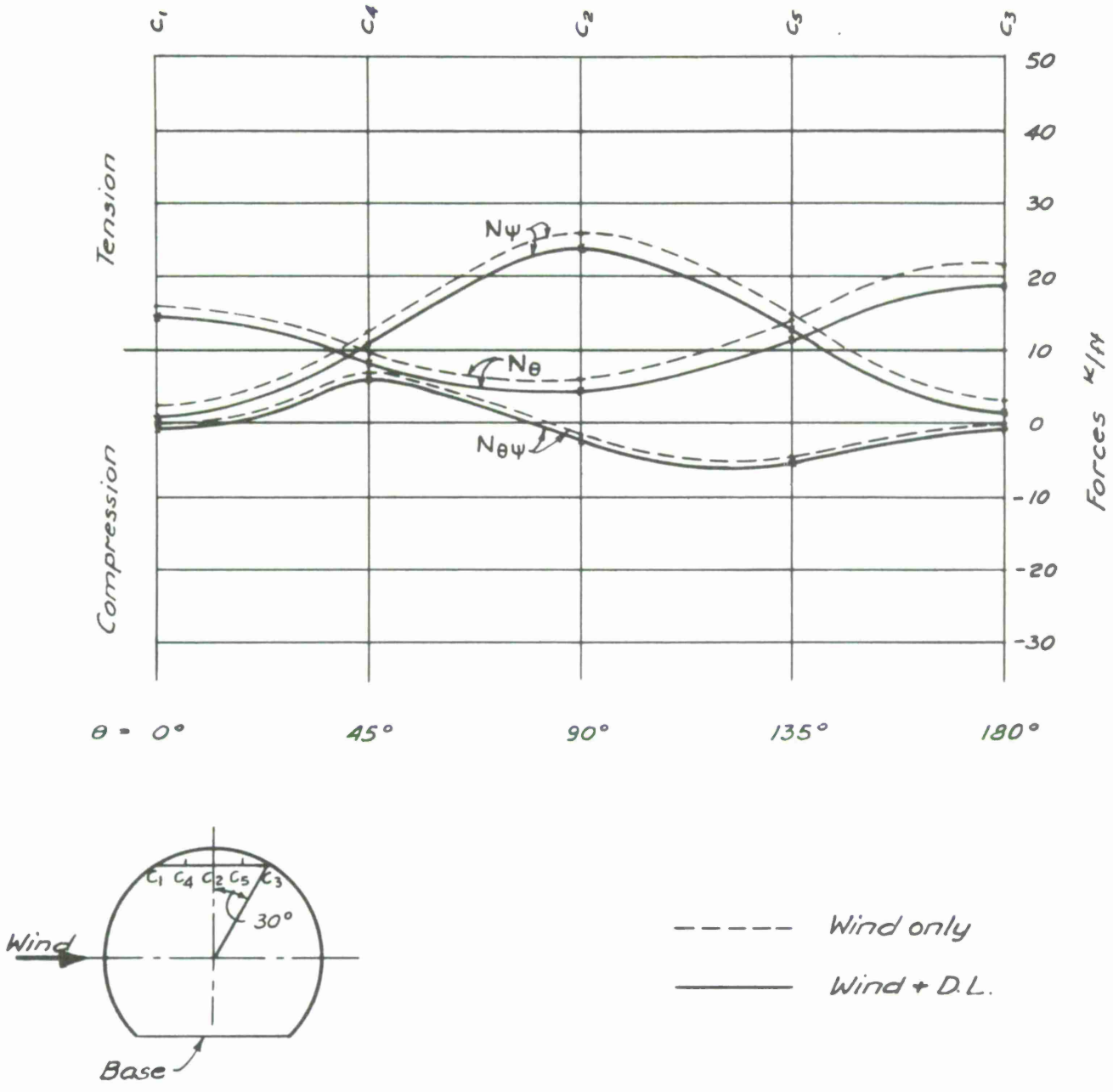

Figure 19. Stress curve at line C.

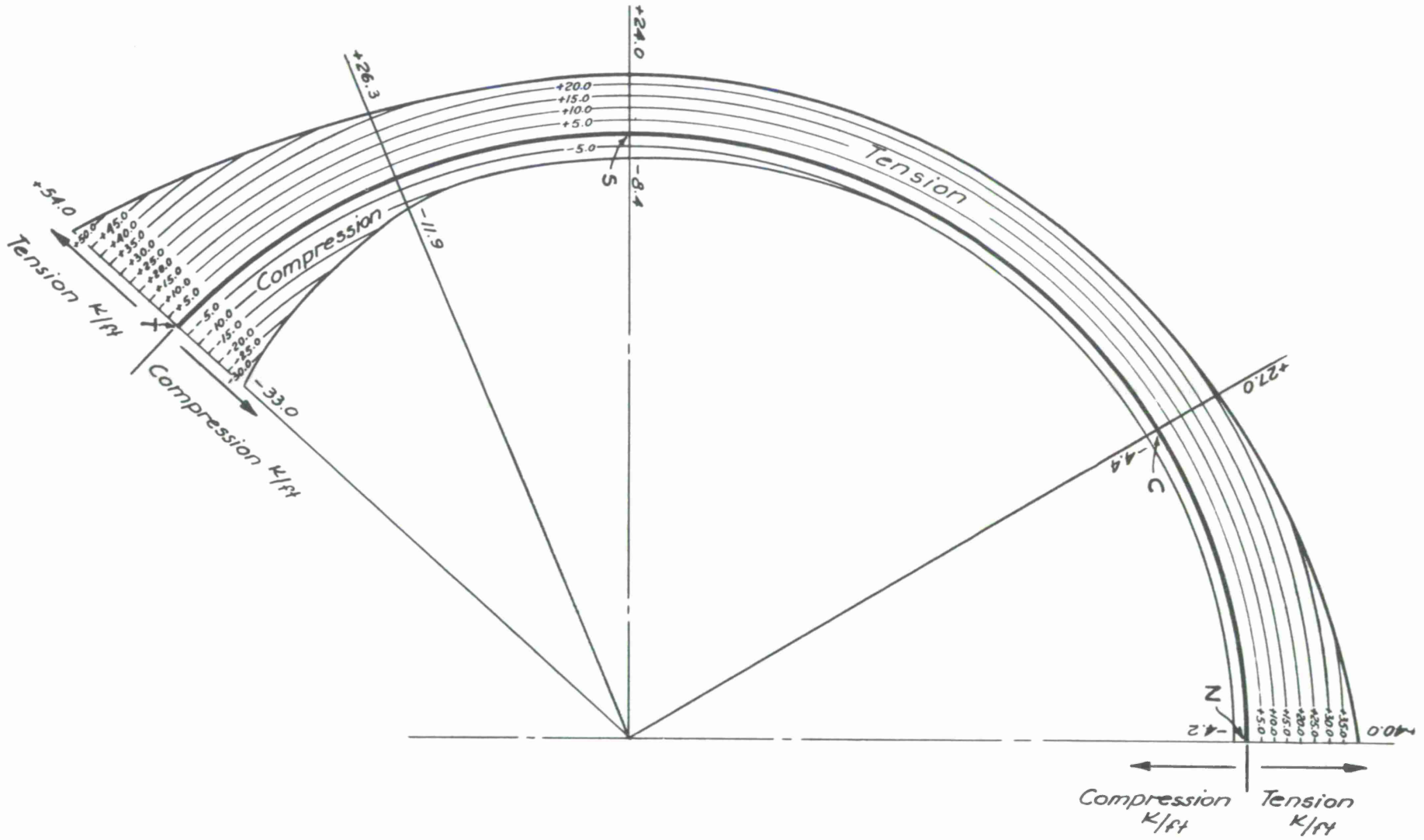

Figure 20. Principal stress.

diameter radome, 20-inch-deep members are used for this reason. Members 29 and 40 inches deep are used for the 800-ft-diameter and 1100-ft-diameter radomes, respectively. A factor of safety of slightly less than 3 against buckling has been provided in all cases. If the buckling requirement is disregarded in the design, a solid steel plate 0.16 inch thick will be satisfactory for stress requirement for the 550-ft-diameter dome. The dome would probably buckle under 2 inches of snow. The maximum design wind pressure is more than 60 times that for the 2 inches of snow.

3.4 Component Design

3.4.1 Members

The axial loads in members were found from membrane stresses by using approximate methods. Each member is also under lateral wind pressure. Since the axial load and lateral load act simultaneously, the majority of the members act as beam-columns. The design of most members near the top of the radome is governed by tension and bending. It should be noted that the axial loads as well as the bending loads in compression members are increased by approximately 30%, due to the facts that the panels transmit the lateral load through membrane stress and that the panels deflect appreciably under lateral load. For tension members, these effects reduce the axial loads as well as the bending loads.

The member design contemplates the use of Bethlehem V60 steel, which has the highest strength-to-price ratio. Although this is a proprietary grade of steel, most major steelmakers manufacture an equivalent grade. It is expected that it will come under an ASTM specification before any final design work is done on the structure.

Figure 21B, Section C-C, shows an average member for the 550-ft-diameter radome. This specially rolled (or possibly automatically welded) channel provides a minimum width for lateral buckling and has good torsional rigidity.

Although heavier members are required near the truncation line of the radome, the added weight is offset by lighter members near top of the radome. The weight of tension members can be further reduced by using higher strength steel such as USS TI or nickel-copper-columbium steel. For the L/r range of these members, little is gained by using higher strength steel for compression members. The higher strength steels have not been used in this estimate and are not recommended at present. They may prove economical in the future.

Lacing at both faces of the member is used rather than lacing at the center of member only. The torsional stiffness of the former is more than 12 times that of the latter. This not only improves the torsional buckling capacity of the member, but also provides restraint to other members meeting at the same joint. By using special connection details that invoke 3 dimensional restraint, relatively narrow members have proven feasible. The narrowest members feasible for 550-ft, 800-ft, and 1100-ft radomes are shown in Figure 2.

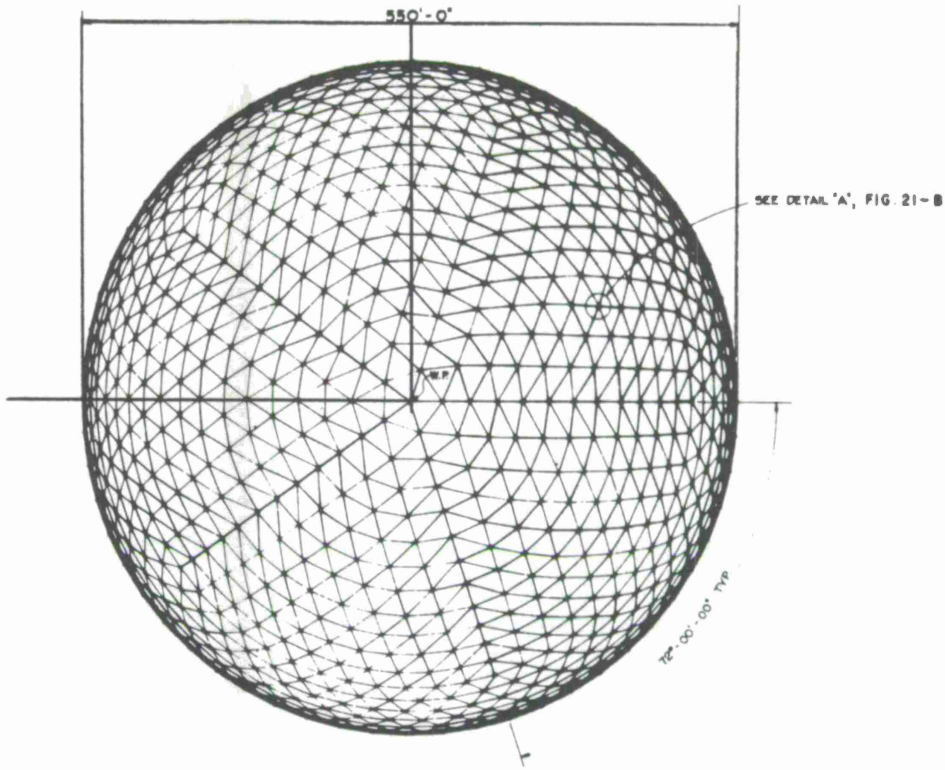

PLAN

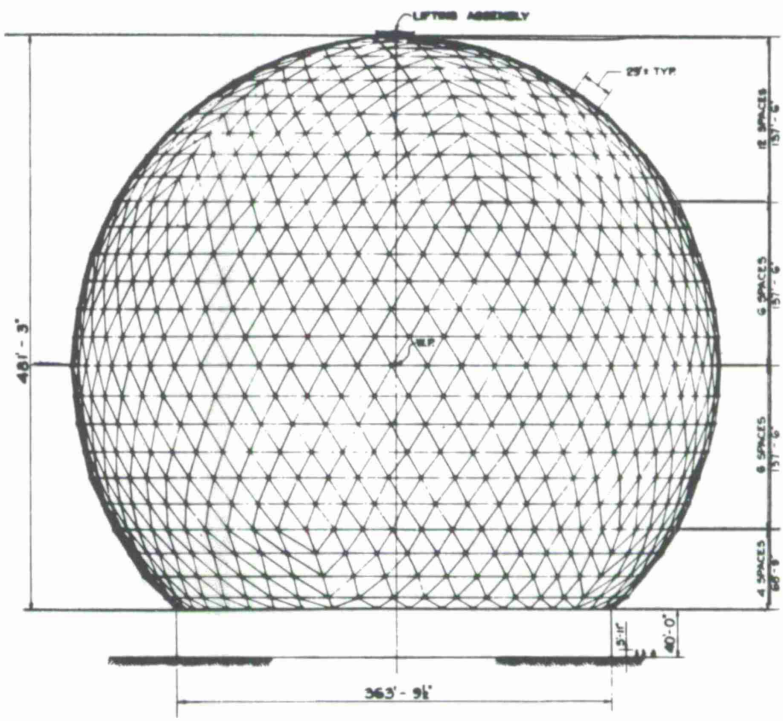

ELEVATION

Figure 21A. 550-ft-diameter radome — plan and elevation.

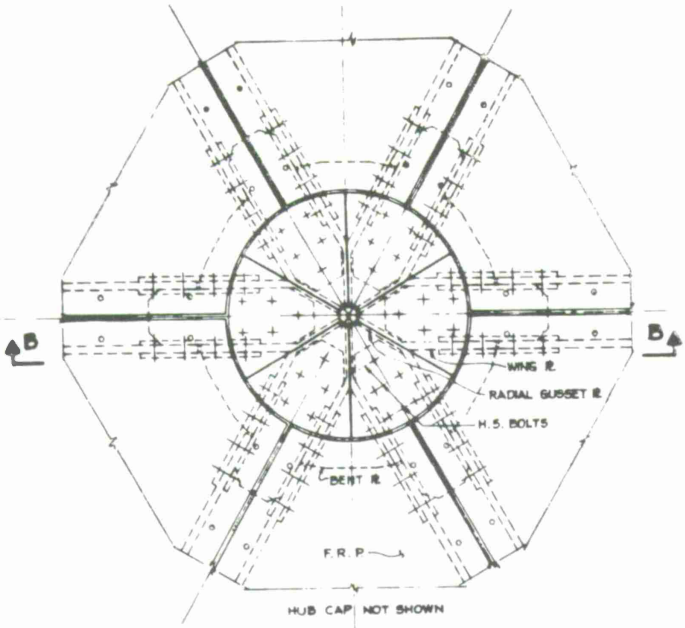

DETAIL 'A' (SEE FIG. 21-A FOR LOCATION)
HUB

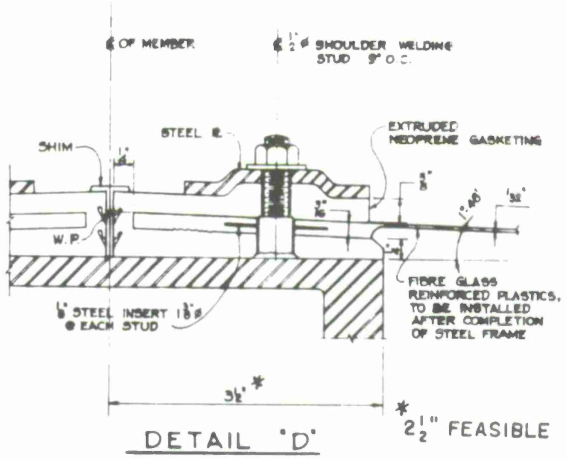

DETAIL 'D'

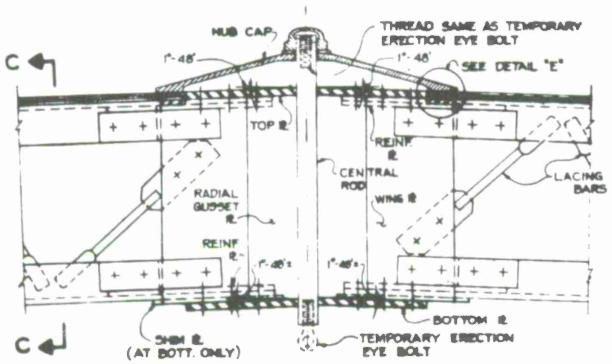

SECTION B-B

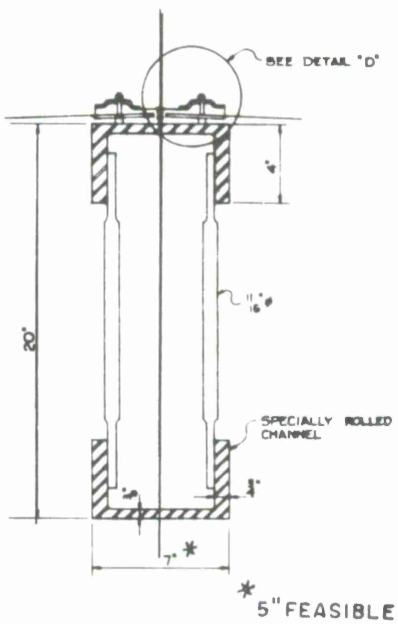

SECTION C-C

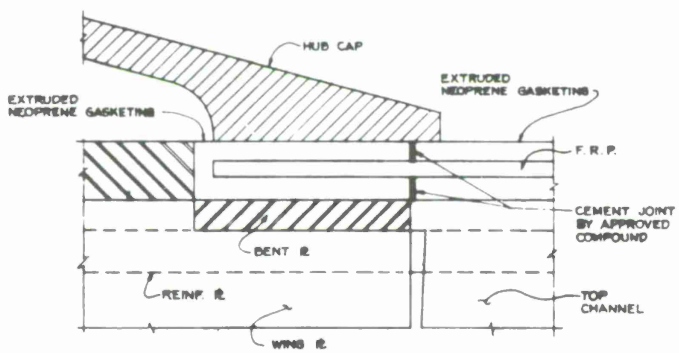

DETAIL 'E'

Figure 21B. 550-ft-diameter radome — details.

3. 4. 2 Hub

In order to make the member narrow to improve the electrical performance of the radome, end restraints in both directions of the members are required. The hub design as shown in Figure 21B is based on this criterion. One-inch-diameter high strength bolts are to be used. Among the types of steel considered are USS TI steel, Bethlehem V steel (normalized), nickel-copper-columbium steel, maraging steel, etc. Bethlehem V steel was used for cost estimates.

The hub basically consists of a central rod with radial gusset plates butt-welded to it Two wing plates, parallel to the vertical surfaces of two adjacent members, are butt-welded to each radial gusset plate. Top and bottom plates consist of several segments parallel to the top and bottom surfaces of the respective members. The joints between two segments are butt-welded, using radial gusset plates as backup material. Although estimated as a weldment, the use of a casting or cast-weld combination may prove more economical.

Each member is connected to the hub in all four faces, using two wing plates and top and bottom plates. Tap holes are required at both ends of the central rod to receive the hub cap and temporary erection bolts. Hub caps are used to press on the circular neoprene gaskets for water tightness.

3. 4. 3 Panels

In selecting the proper material for the panels of the radome, both structural and electrical performance requirements have to be considered. Products by various manufacturers have been studied for possible use as panel material. The following companies have been contacted:

E. I. duPont de Nemours Corp., Wilmington, Del.
Owens Corning, N. Y.
Filon Corp., Calif.
American Cyanamid, N. Y.
Lunn Laminate, N. Y.
Hooper Chemical, N. Y.
Rohm & Hass, N. Y.
U. S. Rubber, N. Y.
Air Tech. Industries, N. Y.
Lamtex Industries, N. Y.
Johns Manville, N. Y.
Napco Chemical, N. Y.
Dow Chemical, Mich.
G. T. Schjeldahl, Minn.

Two types of material are electrically suitable: Filament-wound Fiberglas-reinforced plastic and mylar-dacron-tedlar laminate. Fiberglas is recommended.

Filament-wound Fiberglas-reinforced plastic with polyester resin manufactured by Lamtex Industries of Koppers Company has the following properties:

Tensile strength	90,000 psi (50,000 psi required)
Tensile modulus	3,000,000 psi
Dielectric constant	3.5
15- to 20-year life.	

The maximum width available is about 40 ft. The maximum available width of other Fiberglas-reinforced plastic is only 6 ft except for handmade material. A steel plate can be inserted at the edges of the panel to reinforce bolt-hole openings. The coefficient of expansion of the material is the same as for steel, a very desirable quality since stresses in both skeleton and skin caused by differential contraction can be appreciable.

The stress in the panels can be approximated by solving for the stress in a circular panel with an equal area.[7] However, laboratory tests[13] indicated that the actual stress developed in triangular panels is only 80% of the stress computed by this method. For the 550-ft-diameter radome, the required panel thickness is 1/32 inch. The factor of safety against tearing is about 5. The maximum deflection of panels under wind load is about 9 inches.

Details for attaching the panels to the steel frame by using 1/2-inch-diameter studs are shown in Figure 21B. The details of the extruded neoprene gasketing for sealing the edges of the panels are also shown. The gasketing should be fitted to the panels on the ground before installation.

The panels should be held taut to minimize "oil canning" of the panels, which may ultimately cause fatigue cracking. An internal pressure in the order of 5 psf will prevent most panel buckling. Whatever system is adopted to tighten the panels need not be foolproof, since occasional loss of panel tension will not lead to failure. For this reason, the following methods have been investigated.

1) Application of small internal pressure inside the radome.

2) The using of springs between oversized bolt holes on the panels and the studs.

3) Warming the panels just before installation.

Method 1) is considered to be most effective. It is discussed in detail in Section 6.

The panel material should be tested for ultimate strength in three directions, for tensile modulus of elasticity, yield stress at 1% offset elastic range, percent elongation, inflammability, water absorption, thermal coefficient of expansion, dielectric constant, weathering resistance, resistance to chemicals, impact strength, hardness, etc.

3.4.4 Base fitting and foundation

Details for the base fittings and foundation for the 550-ft-diameter 7/8 sphere are shown in Figure 22. The foundation consists of a ring girder, A-frames, a shear wall, and footings. The foundation design assumes favorable soil conditions but not rock.

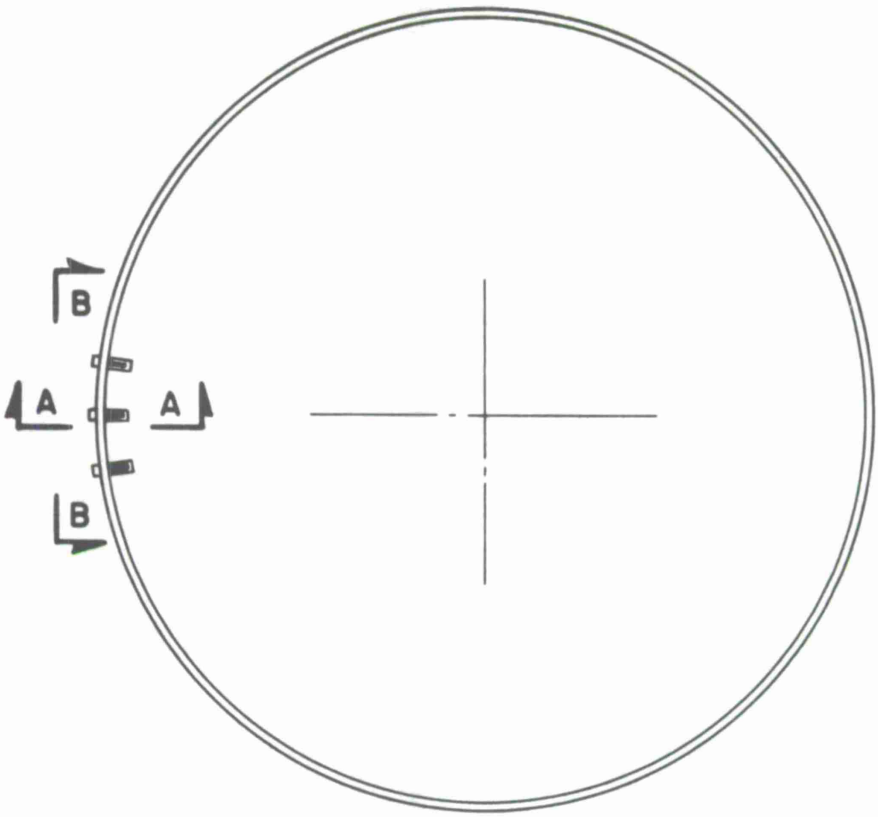

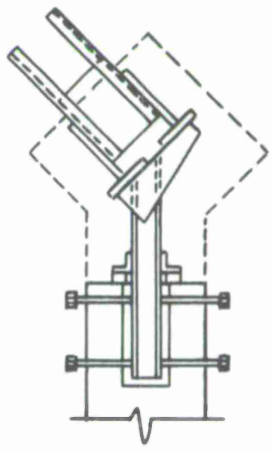

DETAIL A

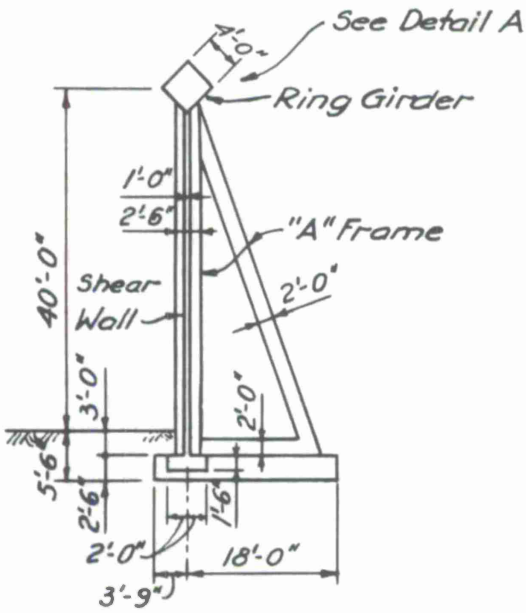

SECTION A-A

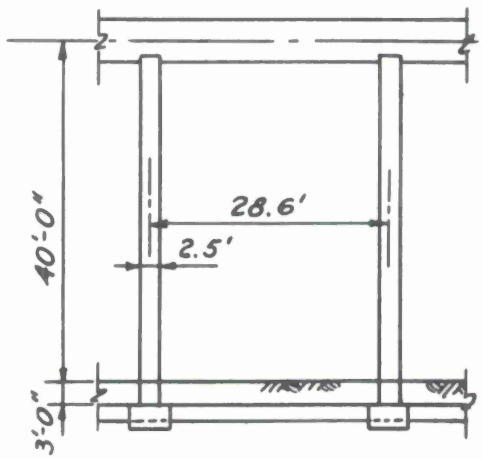

ELEVATION B-B

Figure 22. Foundation and base fitting.

The weight of the concrete foundation plays an important role in stabilizing the structure. The foundation is 50% heavier than the superstructure. By assuming a drag coefficient of 0.64 and lift coefficient 0.68, the overall structure has the following factors of safety at the 100-year storm:

Against sliding	1.7
Against uplift	2.6
Against overturning	1.8.

6. FABRICATION, ERECTION, AND COST

6.1 Fabrication

There is no difficulty in manufacturing the specially rolled channel section as shown on Figure 21B. The mill charge for this special rolling will be about $28,000.00 to $38,000.00. This extra charge has been included in the unit price for fabrication. The lacing is fabricated from a continuous bar bent on a jig. The bent part of the bar is then flattened to facilitate welding.

All steel members and hubs should be fabricated in the shop except the steel studs, which may be welded on the member in the field to facilitate shipping. All hubs should be stress-relieved after welding. Steel and welding should be carefully tested during fabrication stage. It is also advisable to preassemble adjoining components in the shop to ensure proper fit in the field.

Structural and electrical tests should be made on samples of Fiberglas-reinforced plastic for conformance with specified requirements before production begins. The panels are to be shipped by truck or rail in rolled-up form. Samples of neoprene gaskets should also be tested.

It is important to specify all required tests on all components in the procurement documents.

6.2 Erection

6.2.1 Erection schemes

Several erection schemes have been studied. They are: 1) 4 erection towers, 2) one traveling tower, 3) jacking construction, 4) tilt-up, 5) rotating scaffold, 6) complete scaffold, and 7) Potain crane. It is also possible to use a combination of the above-mentioned schemes.

Erection methods were discussed with the following contractors:

Bethlehem Steel Company, Pa.
Merritt-Chapman & Scott, N. Y.
A. J. McNulty Co., N. Y.
Manitowoc Engineering Co., Wisc. (Potain crane)
Beasley Construction Co., Texas (traveling tower)
American Hoist & Derrick Co., Minn. (cranes and towers)
Patent Scaffold, N. Y. (complete scaffold)
Richard Dudgeon, Inc., N. Y. (jacks).

The erection procedures, advantages, and disadvantages of each scheme for a 550-ft-diameter radome are summarized as follows:

1) Four erection towers. – The radome is to be erected in four stages, see Figure 28.

Stage 1. Erect the dome to elevation 345 ft ± by using four American Hoist #999C high-lift cranes outside the dome. Erect four towers inside the dome.

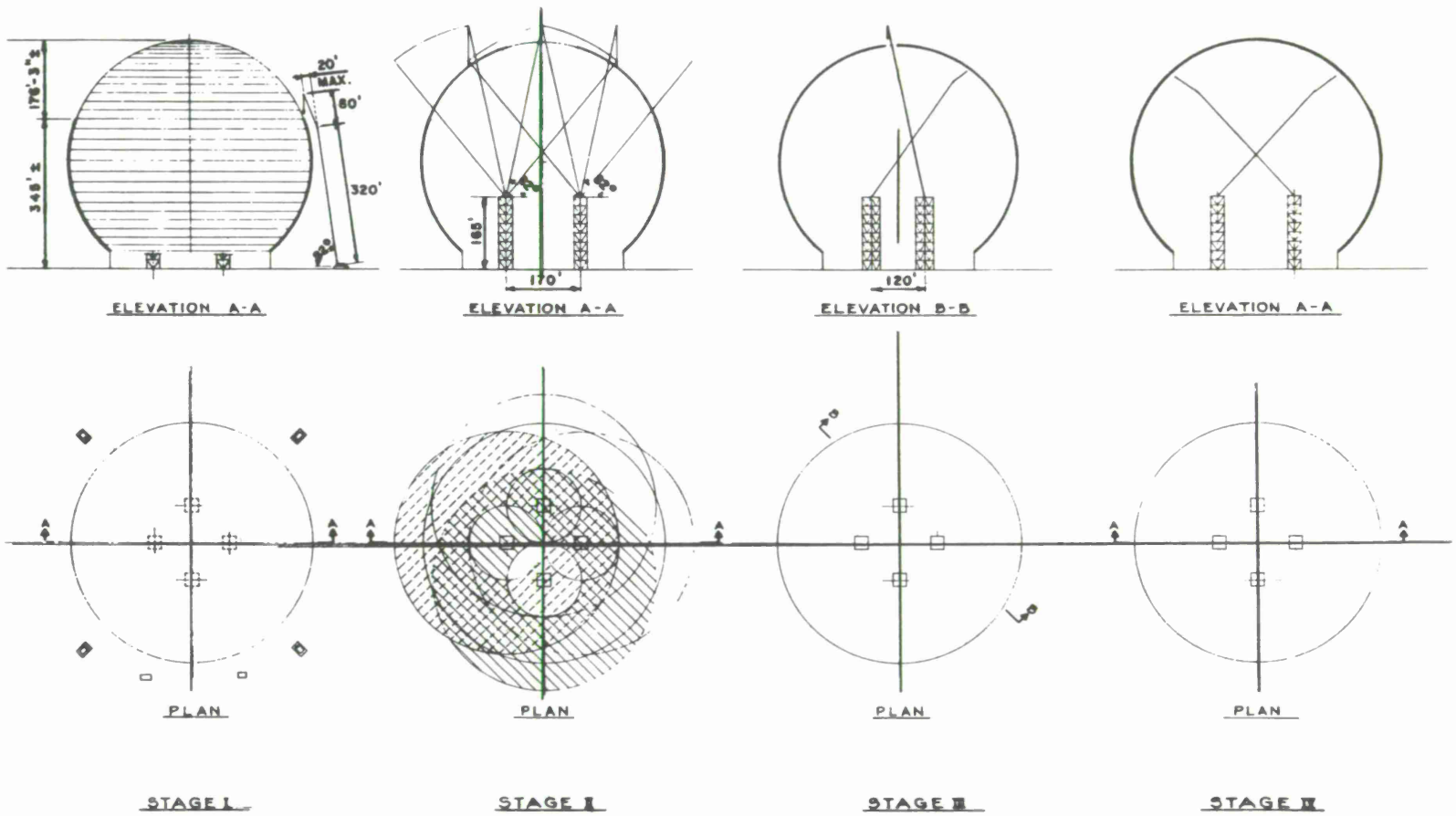

Figure 28. Erection scheme — erection towers.

Stage 2. Lift the #999C crane upperworks to top of towers by using one #9299 crane and one smaller crane. Erect upper part of dome.

Stage 3. Retract three cranes inside the dome. The fourth crane erects top portion.

Stage 4. Retract the fourth crane. Erect panels. Dismantle #999C cranes and towers.

This method is fast and economical. It can be modified to erecting domes of larger diameter. Type of geometry used is not important for this scheme.

The disadvantage of this method is the high-erection stress of the partially completed dome under wind.

2) One traveling tower. – This method is proposed by John F. Beasley Construction Company, see Figure 29. The erection procedure is as follows:

Stage 1. Set rails for tower on existing foundation adapted to carry tower loading.

Stage 2. Erect tower as high as possible with 9299 crawler crane. Set 100-ton-capacity guy derrick on tower.

Stage 3. Erect remainder of tower and stiffleg derrick by jumping guy derrick up as required.

Stage 4. Begin erection of dome with tower derrick and crawler crane erecting a complete tier at time-varying closure points as dome progresses in height.

Stage 5. Complete erection with tower derrick.

Stage 6. Dismantle derrick and tower with guy derrick and crawler crane.

The advantages and disadvantages of this scheme are the same as method 1).

The Contractor has indicated that they could erect a dome 700 ft in diameter with a minimum expenditure for special equipment, and, with just a modest expenditure for special equipment, they could erect a dome 1000 ft in diameter or possibly a little larger, depending on the structural details of the dome itself.

3) Jacking construction. – There are essentially two stages in this method (see Figures 30A and 30B).

Stage 1. Erect top of dome on false work.

Stage 2. Jack the dome up in 23 lifts. Average jacking height each time is 21 ft. Erect members while jacking.

Twenty-three jacks with 400-ton capacity, 13-inch stroke, and 80-ton shear capacity are required. Richard Dudgeon, Inc., indicated that they could furnish all the jacks without any problem.

The 23 jacks will be arranged in six groups of four each, each group having its own pump and a lift-increment signaling device. Each jack will have its own directional control valve to allow the jacks to be set for lift or retract stroke; and each pump will

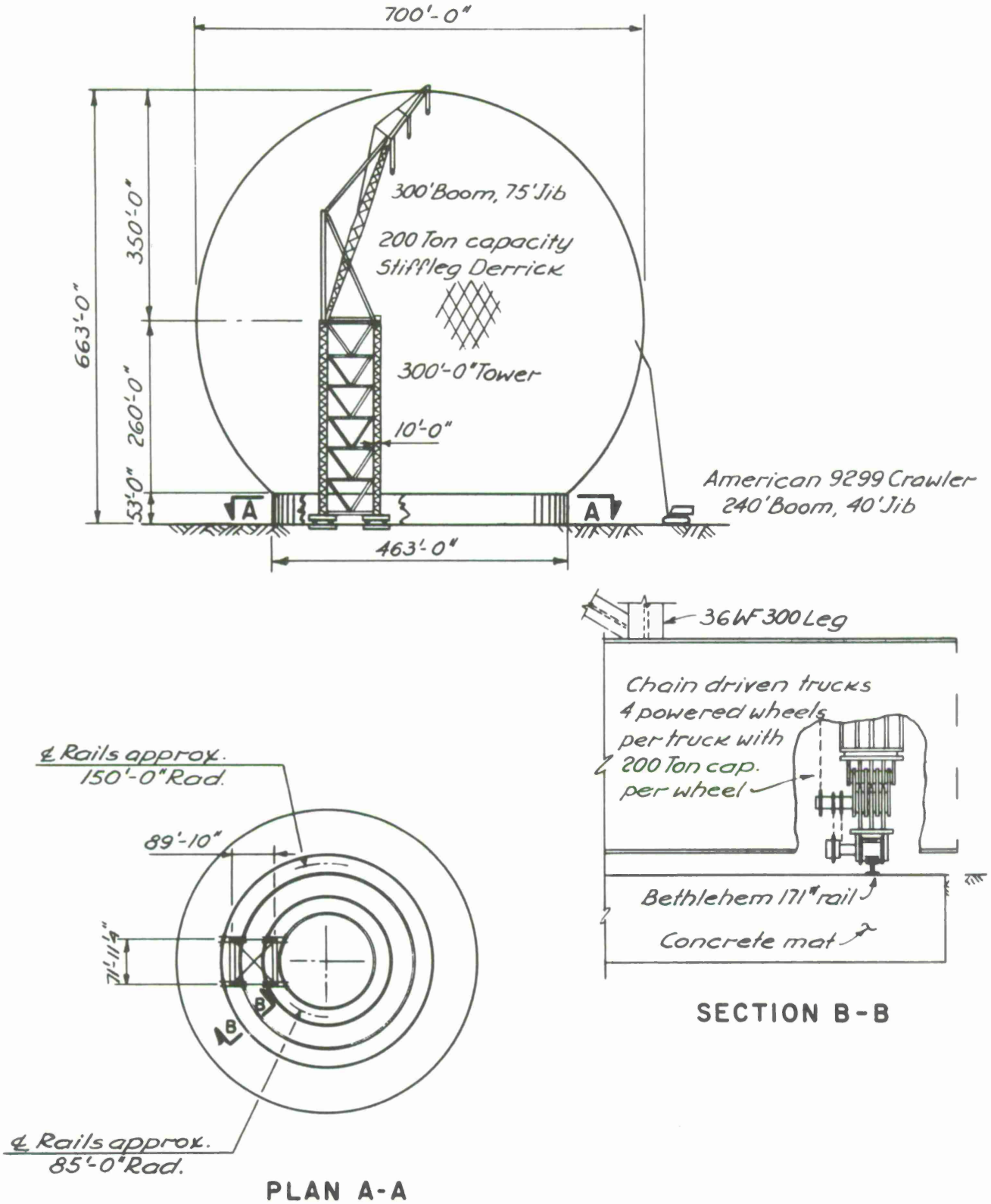

Figure 29. Erection scheme — traveling tower.

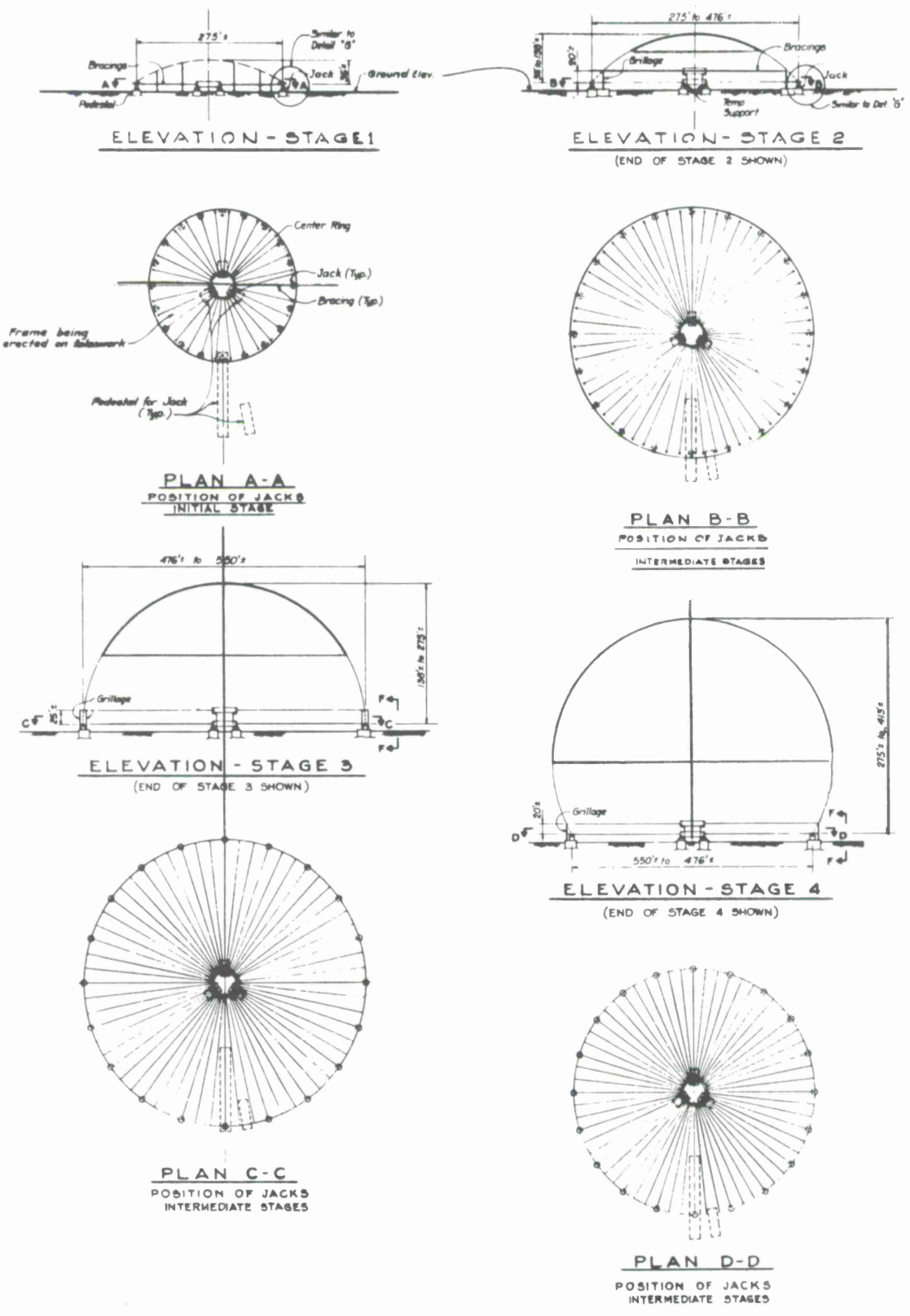

Figure 30A. Erection scheme — jacking.

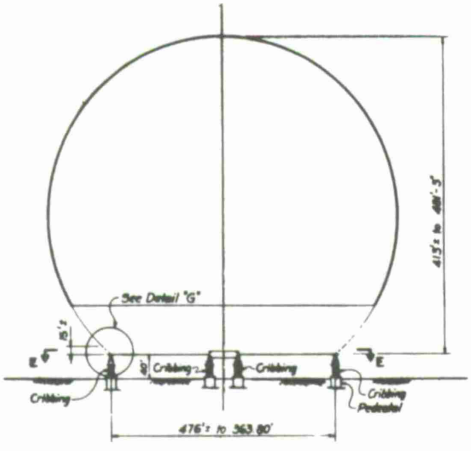

ELEVATION - STAGE 5
(END OF STAGE 5 SHOWN)

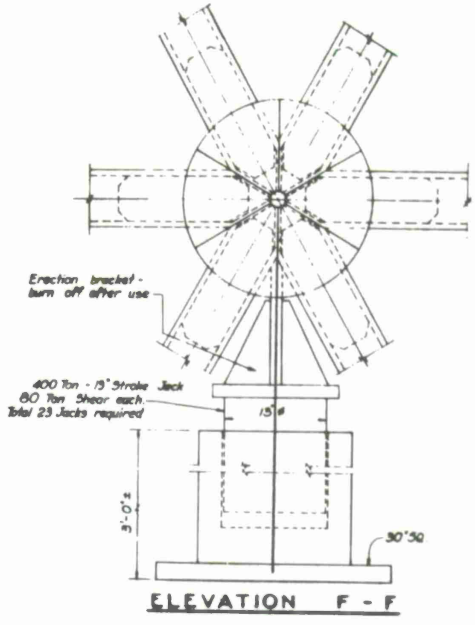

ELEVATION F - F

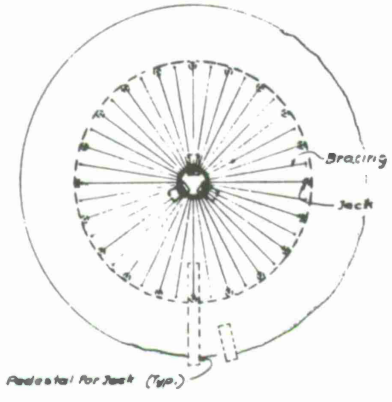

PLAN E-E
POSITION OF JACKS
FINAL STAGE

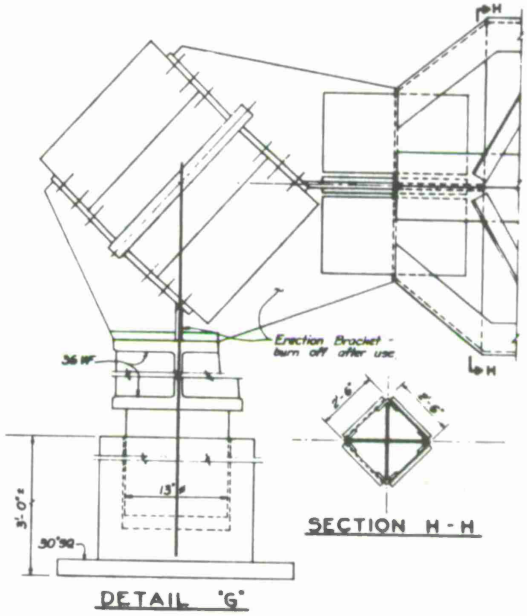

DETAIL "G"

SECTION H-H

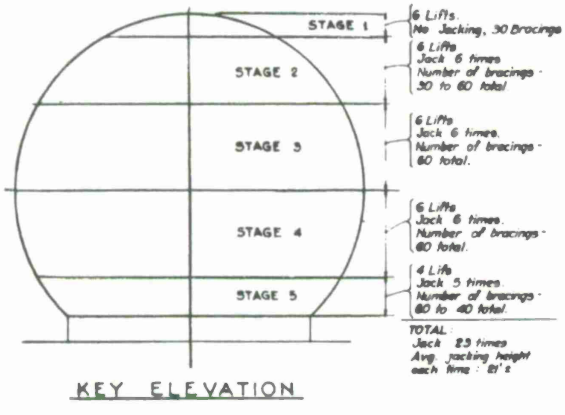

KEY ELEVATION

Figure 30B. Erection scheme jacking (contd).

have its own starter and push-button station so that each jack and each group of jacks can be operated separately (see Figure 31).

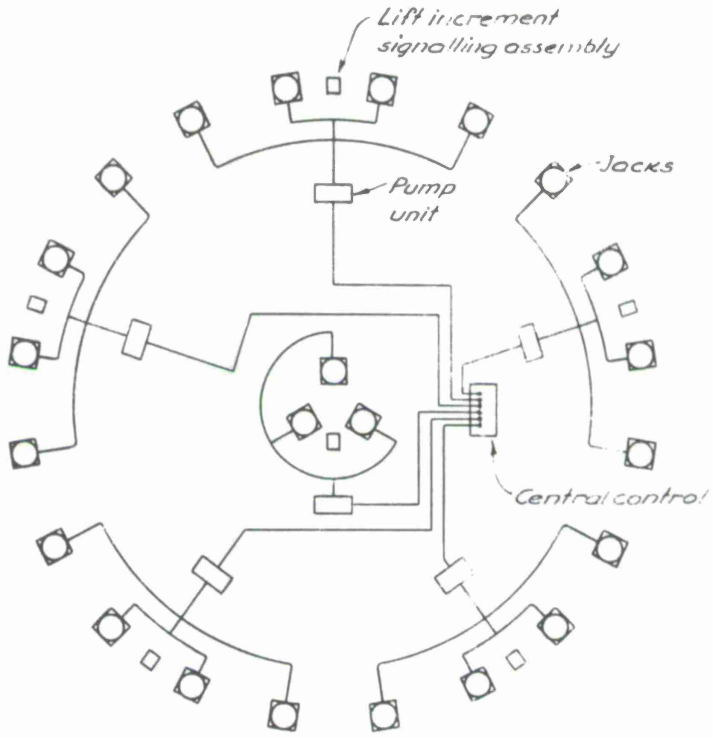

Figure 31. Erection scheme – jack arrangement.

There will also be a central control station, which will have hydraulic gauges to indicate the load on each jack group, magnetic counters to indicate each half-inch of lift increment, and remote push-button stations to start, stop or "inch" each of the pump motors.

When the central station is advised by each of the groups that cribbing and the jack-control valves are set for a lift, central control would start each of the pump motors to close daylight and show approximately 10% of the calculated pressure required for the lift. This would be done for the six groups of jacks in turn.

Then the lift-increment signaling devices would be set and the magnetic counters set to zero. At this time, the four pump motors would be started simultaneously.

As the lift progresses, the counters should click over together. If any jack group gets ahead of the others, its pump motor can be stopped momentarily. Since the usable stroke of the jacks will be 12 inches, and the maximum stroke 13 inches, 24 counts of lift will indicate a 12-inch lift.

During the lift the safety locknut on the threaded ram is to be kept up into position. This will be a manual operation.

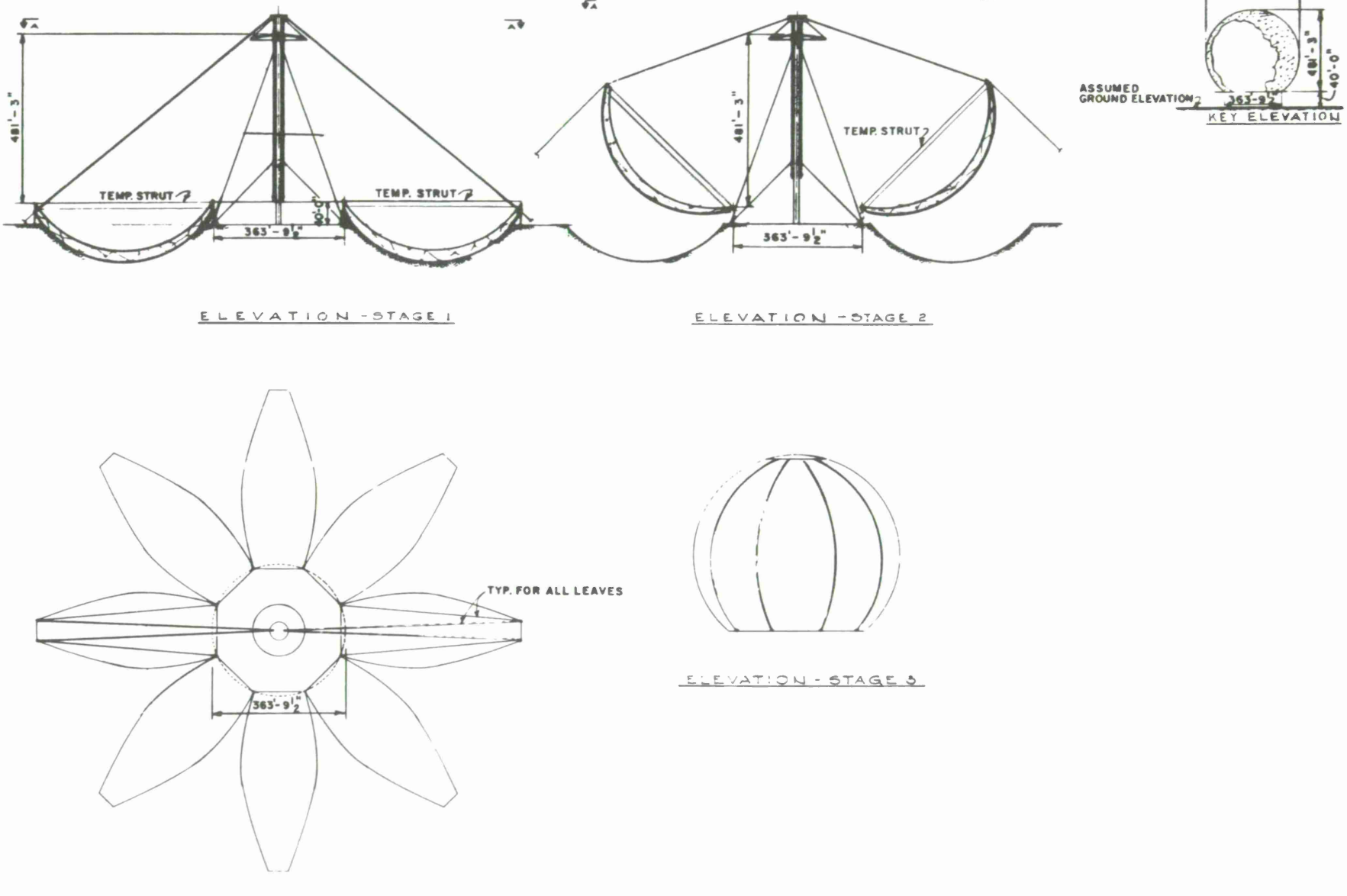

Figure 32. Erection scheme — tilt-up.

At the completion of a lift, and after cribbing is set, each jack will be released individually, either independently or upon a telephoned instruction to all 23 jacks to transfer the load from all jacks to all cribbing simultaneously.

Retraction of the rams for placing of temporary cribbing for the next lift again can be done either individually or after everything is set by central control.

The advantage of this scheme is that all the erection work is done on ground or near ground. Erection stresses in the partially completed dome are small. The structure is stable under wind. It is possible to build very large-diameter domes by this method.

This method costs a little more because heavy temporary bracings are required at bottom of the 7/8 sphere. However, for H/D = 0.60 sphere, the bracing requirements are nominal. For this erection scheme, the "horizontal ring" frame geometry is preferred.

4) Tilt-up construction. – No contractor has expressed any interest in this scheme (see Figure 32). They felt that the extensive equipment and supports required have very little resale value. They also felt that joining the adjacent edges of the eight leaves will be difficult.

5) Rotating scaffold. – (See Figure 33). Unless the turntable for the antenna is suitable and available for use, this method is not practical. It was not considered in detail.

6) Complete scaffold. – This method is safe, but it is the most expensive method.

7) Potain cranes. – (See Figure 34). The maximum available height of a horizontally guyed Potain crane is about 450 ft at the present. The use of inclined guys is not recommended, since they will induce substantial vertical load on the mast. This limits the scheme to domes of about 200 ft in diameter.

6.2.2 Erection stresses

The erection stresses in a partially completed dome are appreciable.

Since the erection of the dome can be completed in less than a year, and the life expectancy of the structure is 15 to 20 years, the design wind velocity during erection should be less than that used in the final structure. A 100-year recurrence velocity is used in the final structure with a 14% probability of exceeding this velocity in its life span. A 7-year recurrence velocity in the order of 85 mph will give the same probability in 1-year period.

From preliminary computation, the members of the partially completed dome are overstressed under this wind velocity. Temporary erection guys at several levels should be provided to tie down the structure in the case of a strong wind storm during erection (see Figure 35). These guy wires can also be used for geometry control. Since the erection stresses are critical, it is advisable to check them with the available FRAN computer program.

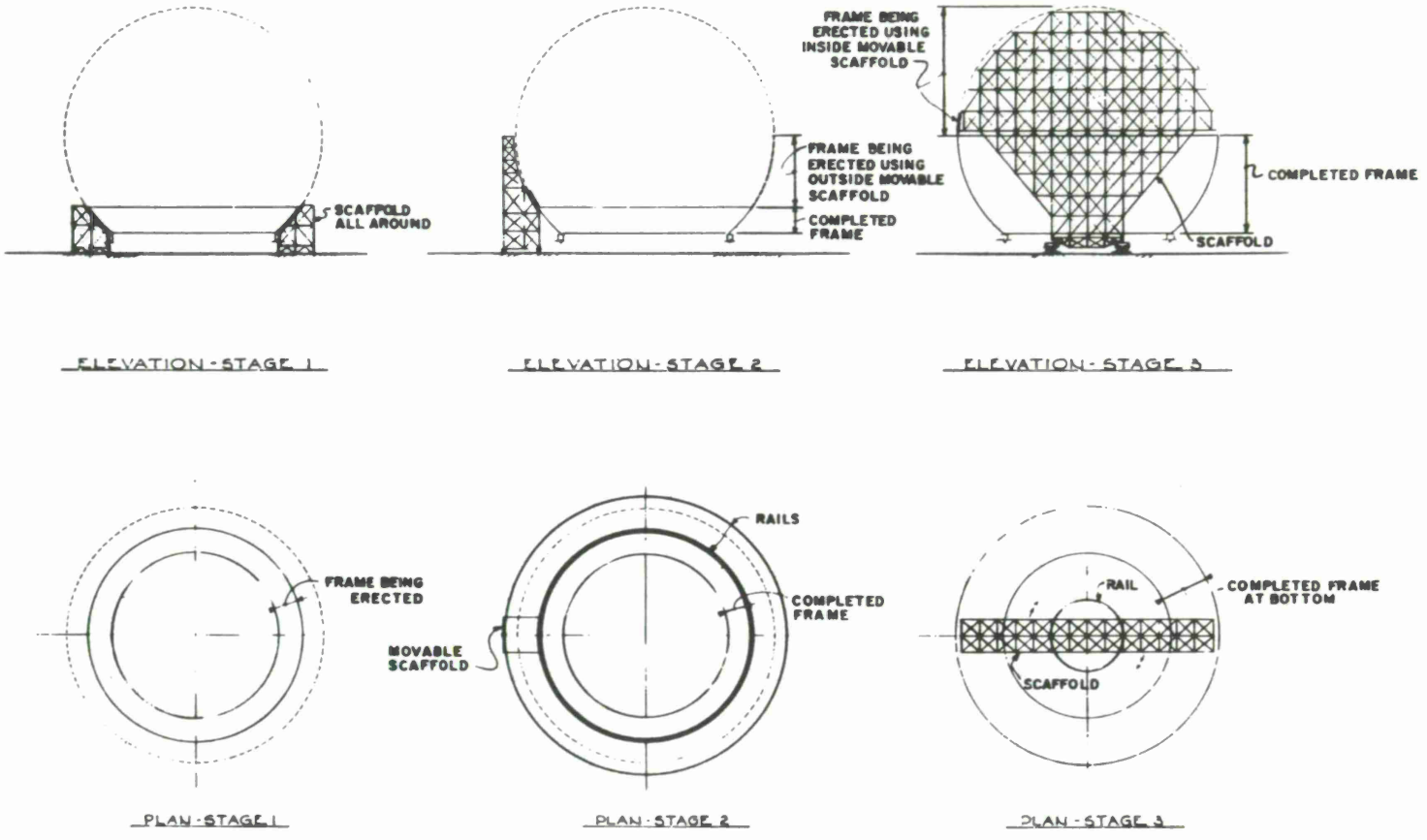

Figure 33. Erection scheme – scaffold.

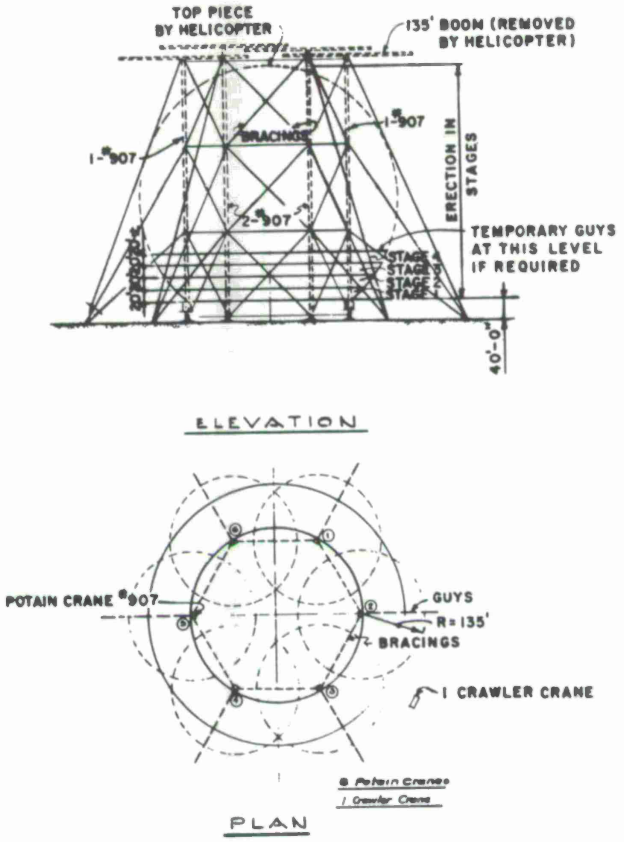

Figure 34. Erection scheme — Potain crane.

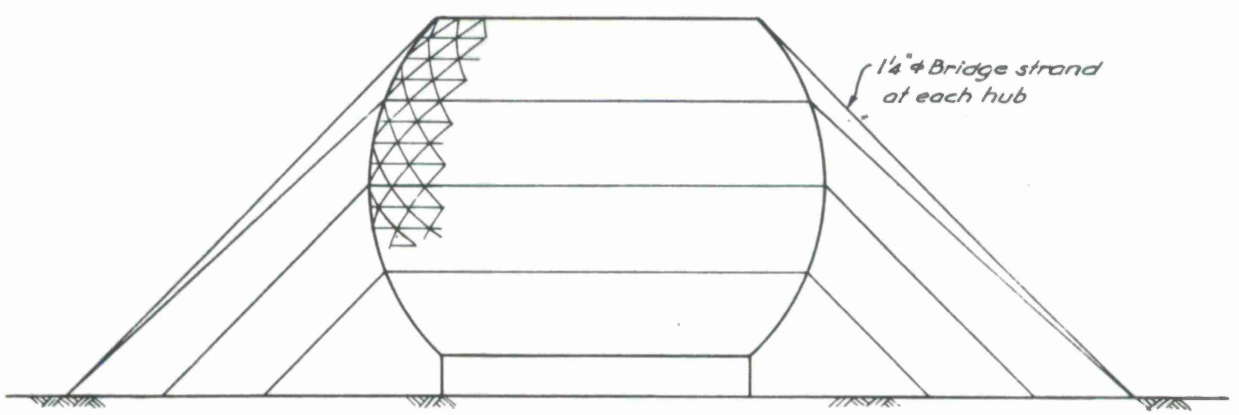

Figure 35. Erection — geometry control.

6.2.3 Geometry control and tolerances

Anchors and guy wires of precut lengths can be used as geometry control. The correct alignment of base fittings in the ring girder is essential for correct geometry.

Tolerance during erection should be specified.

6.2.4 Time required for erection

It is estimated that 9 months to 1 year is required for erecting the 550-ft-diameter radome. This does not include the foundation work and fabricated items.

6.3 Cost

6.3.1 550-ft-diameter 7/8 sphere

The cost for the 550-ft-diameter-7/8 sphere radome is estimated as follows:

a.	Fabricated steel (3,860 members) (1,301 hubs)	10,300,000 lbs at $0.30 =	$3,090,000.00
b.	Steel stud	270,000 pcs at $0.15 =	41,000.00
c.	Neoprene	228,000 LF at $0.85 =	194,000.00
d.	FRP panels	2,560 panels	1,102,000.00
e.	Erection		1,900,000.00
f.	Foundation		500,000.00
g.	Painting		236,000.00
			7,063,000.00
		10% Contingencies	706,000.00
		Total Cost	$7,769,000.00

Mechanical and electrical cost associated with lighting, temperature control, and snow removal, and the cost of engineering, testing, and administration are not included.

Explanations for the items are listed below:

Item a. Fabricated steel: Price is based upon the quotation from Bethlehem Steel Company. The price includes one shop coat of paint. The price is also based on using 3-inch-diameter central rod of A441 steel, 1-1/8-inch V50 radial gusset plates, 7/8-inch V50 wing plates, and 3/4-inch V60 top and bottom plates.

Item b. Steel stud: Price is based upon the quotation from KSM Products, Inc. N. J.

Item c. Neoprene: Price is based upon the quotation from Pawling Rubber Corporation, N. Y.

Item d. FRP panels: Price is based upon the use of polyester resin and regular glass. Other glass and resin combination will cost more.

Lamtex Industries, N. Y., has quoted:

Hollow glass-epoxy	—	$8.00 psf
Hollow glass-polyester	—	7.80 psf
Regular glass-epoxy	—	1.35 psf
Regular glass-polyester	—	1.25 psf

Tooling $50,000.00 to $60,000.00

Hollow glass is very expensive because this material is not made as yet in production quantity. Hollow glass itself costs about $10.00/lb.

Item e. Erection: For estimating the erection cost, the "four erection towers" scheme is used. The rates for equipment and labor are as follows:

	Rental (8-hr shift)	Freight, 1 way
#9299 crane	$7,000.00/month	$7,500.00 - $8,500.00
#999 crane	6,000.00/month	7,500.00 - 8,500.00
#7250 crane	3,500.00/month	3,000.00

The four 165-ft-high towers (stationary) are not for rent. They can be purchased at $60,000.00 each.

The labor costs are based on 1966 Boston area rates.

The breakdown for erection:

Rental of equipment and freight	$397,000.00
Purchasing 4 towers and freight	268,000.00
Labor cost	539,000.00
Guys, platforms, safety devices	174,000.00
	1,378,000.00
Overhead profit, etc. 25%	344,500.00
	1,722,500.00
Contingencies	172,250.00
	1,894,750.00

Say: $1,900,000.00

The erector's estimate for the traveling tower is $1,500,000.00. However, several hundred thousand dollars has to be added to cover the cost of temporary guys and geometry control.

The estimated erection cost for jacking construction is $2,135,000.00.

If complete scaffold is used, the erection cost alone will be $5,000,000.00 to $6,000,000.00.

Item f. Foundation: Foundation design assumes favorable soil conditions but no rock. If the soil is unfavorable, the foundation cost may increase. Site work is not included in the cost.

Item g. Painting: The costs of painting for panels and steel are as follows:

Panels		
Paint (Radalon)	$ 20,888.00	
Primer	12,138.00	
Labor	57,500.00	
	90,526.00	
25% Overhead and profit	22,631.00	
	113,157.00	
10% Contingencies	11,315.00	$124,472.00
Steel: (2 field coats)		
Paint	12,400.00	
Labor	69,000.00	
	81,400.00	
25% Overhead and profit	20,350.00	
	101,750.00	
10% Contingencies	10,175.00	111,925.00
Total	—	$236,397.00

Say: $236,000.00

6.2.2 800-ft-diameter and 1100-ft-diameter radomes

The cost breakdown for the 800-ft-diameter and 1100-ft-diameter radomes are estimated as follows: The sizes and lengths of typical members are shown in Figure 2.

800-ft diameter		
Fabricated steel		$ 8,976,000.00
Neoprene		270,000.00
FRP panels		2,660,000.00
Erection		5,800,000.00
Foundation		615,000.00
Painting		500,000.00
	Total	$18,821,000.00
1100-ft diameter		
Fabricated steel		$22,000,000.00
Neoprene		500,000.00
FRP panels		7,200,000.00
Erection		14,000,000.00
Foundation		1,700,000.00
Painting		1,000,000.00
	Total	$46,400,000.00

REFERENCES

(1) ASCE: "Wind Forces on Structures," Transaction, Vol. 125, 1961.

(2) MULDOON, R. A.: "Determination of Force Coefficients and Pressure Distribution Parameters," MIT Lincoln Lab. Report, December 1962.

(3) "Normen fur die, Belastungsannahem, die Inbetriebnahme und die uberwachung der Bauten," Swiss Code.

(4) MULDOON, R. A.: "Optical Blockage of Haystack Space Frame Radome Geometry," MIT Lincoln Lab. Report, December 1964.

(5) COHEN, A., DARIS, P., and ORABONA, J. F.: "U. S. Patent No. 2978704" as signed to U. S. Government, 1959.

(6) FANNY, W. R.: "Computer Analysis of Haystack Radome," MIT Lincoln Lab. Report, November 1962.

(7) TIMOSHENKO, S.: "Theory of Plate and Shells," McGraw-Hill, 1940.

(8) FLUGGE, W.: "Stresses in Shells," Springer-Verlag, 1962.

(9) FOERESTER, A. F.: "Stress Distribution and Stability Criteria of Spherical Ground Radomes," WADC TR 58-272, Vol. 1.

(10) WRIGHT, D. T.: "Membrane Forces and Buckling in Reticulated Shells," ASCE Proceedings, February 1965.

(11) TIMOSHENKO, S.: "Theory of Elastic Stability," McGraw-Hill, 1936.

(12) TSIEN, H. S.: "Theory of the Buckling of Thin Shells," J. of Aeronautical Science, August 1942.

(13) HANSEN, R. A.: "Microwave Scanning Antennas," Academic Press, 1964.

(14) WEISS, H. G.: "The Haystack Microwave Research Facility," IEEE Spectrum, February 1965.

LARGE-DIAMETER RIGID RADOMES
SUPPLEMENTARY REPORT

1. INTRODUCTION

In the report entitled "Large-Diameter Rigid Radomes," dated April 1965, prepared for MIT Lincoln Laboratory, the structural systems, environmental control, methods of fabrication and erection, electrical performance, and cost estimates pertaining to radomes from 550 ft to 1100 ft in diameter were presented. Although the recommended radome configuration was satisfactory, it was felt that other types of construction should be explored further from the standpoint of minimum aperture blockage and temperature stratification.

The new types suggested for study included: 1) the use of steel wire or dielectric cable bracing to reduce member size, 2) the use of nontriangular space-frame configuration, 3) the use of a rigid panel permitting wider member spacing or narrow members, 4) the use of Fiberglas pipe for space-frame members, 5) the use of double-layer construction, and 6) the removal of panels at the top of the dome to minimize temperature stratification.

The findings of these additional studies are summarized in this supplementary report.

2. CONCLUSIONS AND RECOMMENDATIONS

Of all the concepts studied, the use of steel wire or dielectric cable to reduce blockage appears the most promising. The use of Fiberglas tension member bracing is recommended as a desirable alternate to the framing in the original report.

The increased cost of the tension members is offset by simpler connection costs of the main members, making the cost curves in the original report still valid.

The electrical blockage has been recomputed based upon suggestions made by Dr. Ruze of MIT Lincoln Laboratory subsequent to the issuance of the original report. For a 400-ft antenna in a 550-ft radome, at 1 Gc/sec, the blockage using unbraced members is approximately 11-1/2%, while members braced by Fiberglas tension members reduce the blockage to about 8-1/2%.

Nontriangular framing consisting of hexagons spaced throughout the basic triangle field can reduce the blockage caused by the space frame by about 10%. However, the skin panels spanning the hexagonal openings are not available, and any splicing system would dissipate the 10% gain. Nontriangular framing is therefore not recommended.

Although rigid panels may permit some width reduction, the cost is so great as to preclude their use.

Fiberglas pipe compression members in the sizes needed do not offer appreciable improvements in the electrical performance of the radome. They are therefore not recommended.

The use of double-layer construction contributes somewhat to the reduction of temperature stratification and assists in snow removal and condensation control. However, the costs are excessive, considering the relatively minor nature of the problem, and the system is not recommended.

The omission of top panels was originally suggested for the purpose of minimizing temperature stratification in the radome. The effectiveness of this scheme is questionable. The redistribution of wind pressure due to the opening at the top of the dome is unfavorable. Furthermore, rain and snow will enter the dome from the top. Therefore, this system is not recommended.

3. SOME NEW CONCEPTS

3.1 Narrow Members with Wire Bracing

The width of members can be substantially reduced if steel wires are used to brace the members at one-third points. This scheme reduces the unsupported length of members by a factor of 3. Corrosion-resisting aircraft strand in the order of 1/4 inch in diameter is adequate for the bracing. The widths of members can be reduced to about 2-1/2 inches and the lengths of members increased to 40 ft (the maximum available size of Fiberglas panels) for the 550-ft diameter radome.

Details that have been developed sufficiently to prove feasibility and economy are shown in Figures 1 to 4. The hub, half lengths of the members, and the bracing can be fabricated as a unit in the shop or on ground. During erection, the complete prefabricated units can be lifted by a stiffleg derrick one at a time as shown in Figure 5. The only field connections in the steel frame are the simple member splices shown in Figure 2, one for each member.

Since the hub-to-member connections are shop welded, rather than field bolted, hub sizes can be reduced from 30-inch diameter in the original design to about 18 inches, permitting appreciable blockage reduction. The bracing is located and pretensioned in such a manner that the dead load stresses in the members are reduced.

It is also feasible to use Fiberglas tension members with 240,000 to 270,000 psi tensile strength as bracing. Since Fiberglas has a low dielectric constant, its use will further improve the electrical performance.

A potential difficulty with Fiberglas tension-member bracing is due to its low Young's modulus (5.2×10^6 psi). The stiffness furnished at the third points of the members may not be enough to reduce the unsupported lengths of the member in the weak direction.

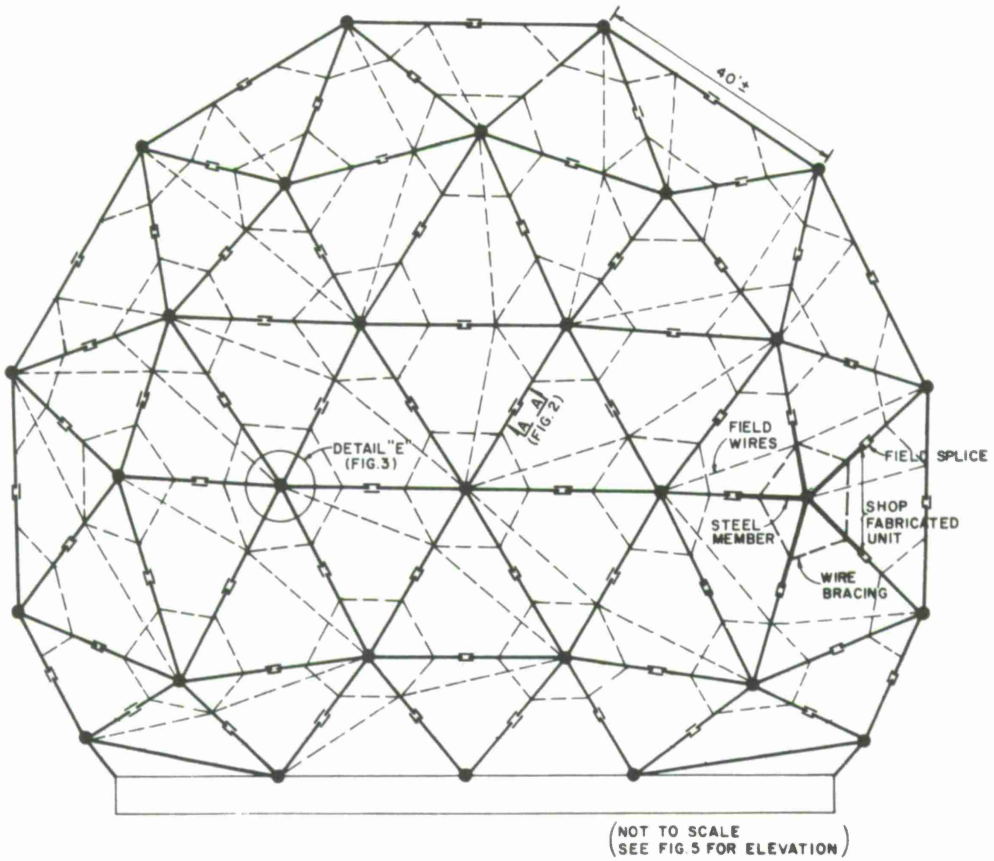

Figure 1. Narrow members braced by wires – schematic sketch.

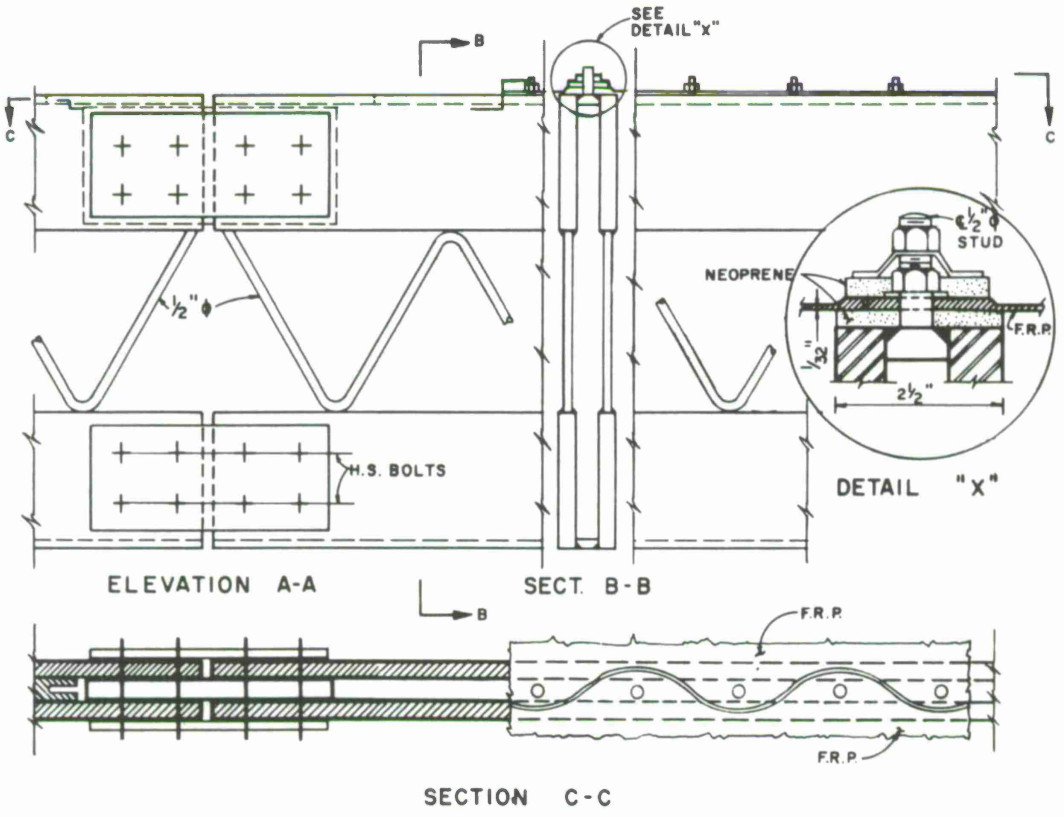

Figure 2. Member and splice details.

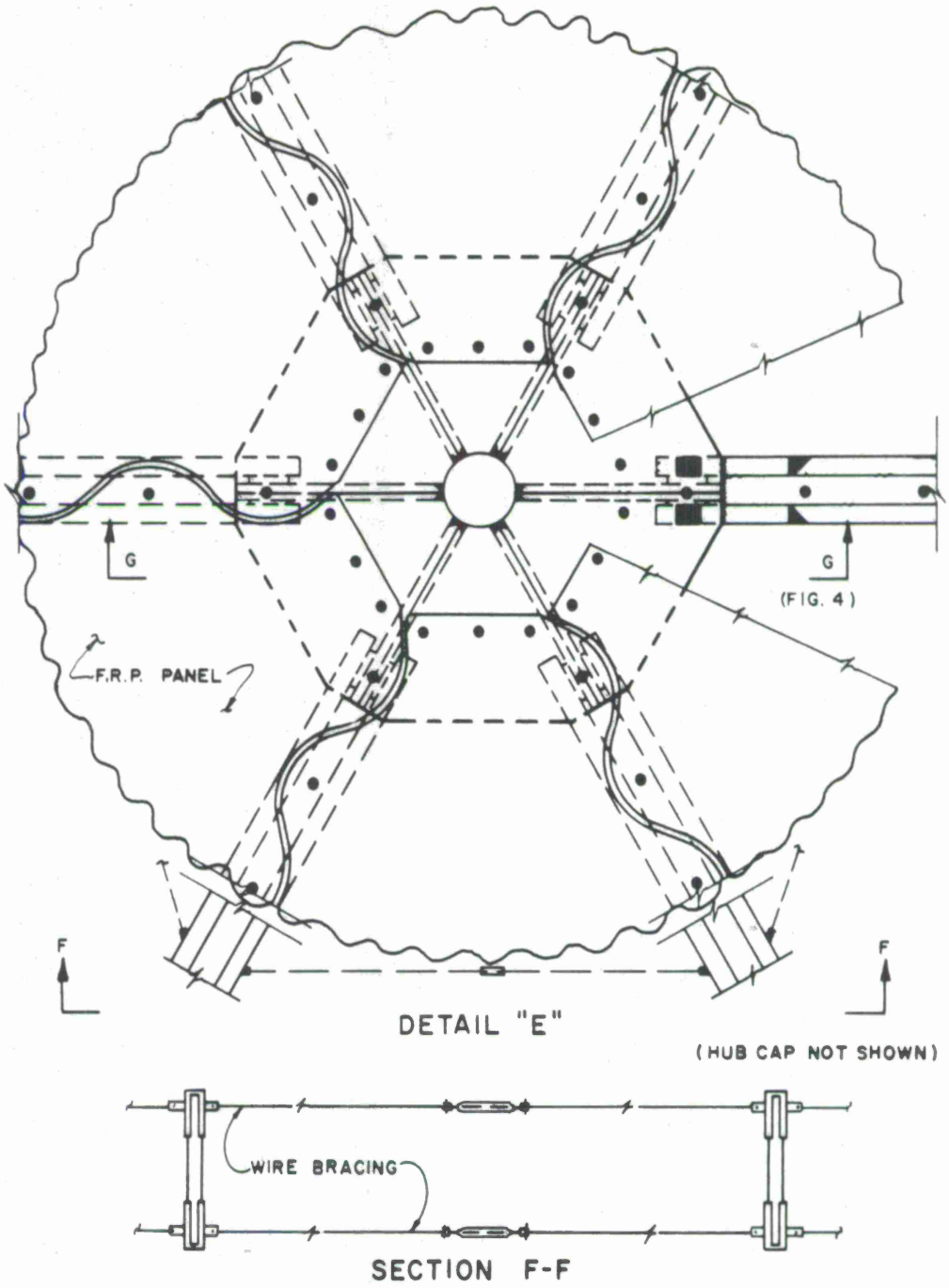

Figure 3. Hub and bracing details.

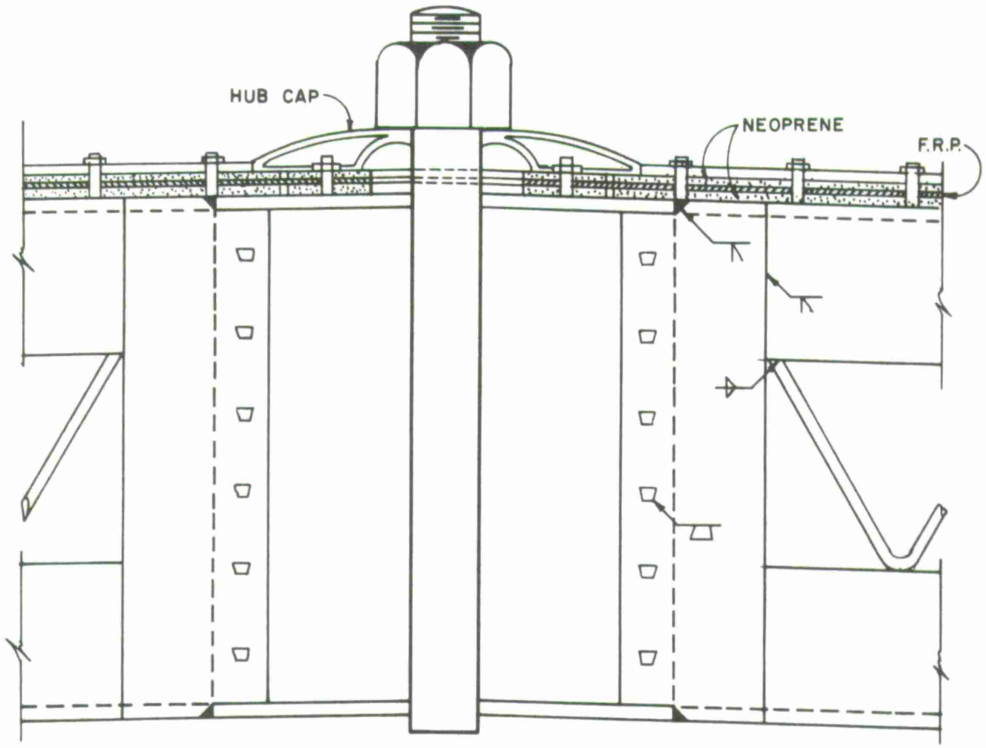

SECTION G-G

Figure 4. Hub details.

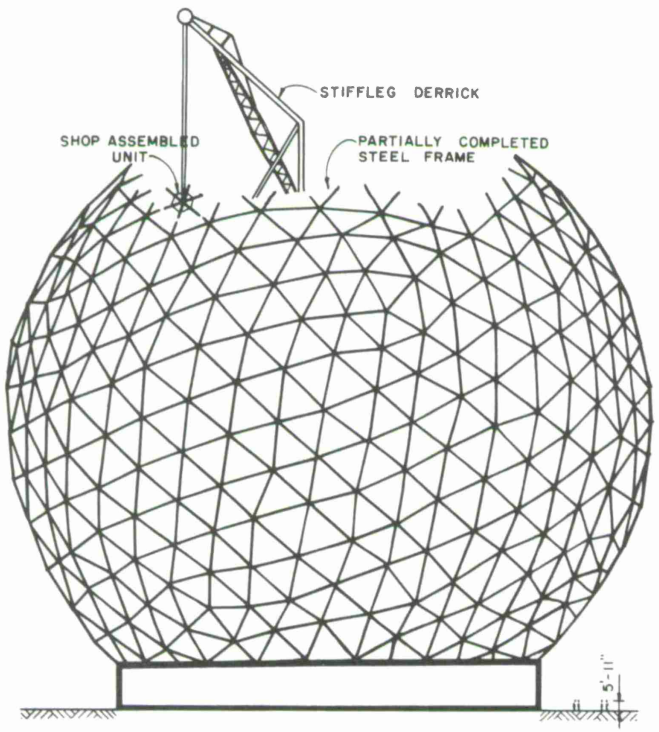

ELEVATION

Figure 5. Erection scheme — traveling tower.

However, if the Fiberglas tension members are pretensioned, braces at both sides of the member will be effective in resisting the buckling, thus providing the required stiffness. Properties and test results for Fiberglas tension members are given in Appendix 1.

Two layers of bracing are shown in Figure 3 because members are under bending due to lateral wind pressure as well as to axial compression due to shell action. The double-layer system is required to prevent the lateral torsional buckling as well as torsional buckling.

The connections (terminals) of the Fiberglas tension members with 95% efficiency have been developed by the Owens-Corning Corporation.

In order to prevent all the members meeting at a hub from rotating in the same direction, field wires connecting each loop of bracing to the hubs are required, as shown in Figure 1. Steel wire bracing requires 1 field wire per triangle (see Figure 6). Fiberglas tension members require 2 per triangle (see Figure 7). The exact size and spacing of all the bracing wires may be determined in the final structure by an eigenvalue analysis.

The deep, narrow members braced by wires or Fiberglas tension members will substantially reduce the blockage ratio. The reduction is due both to the narrow width of the members and to the compact hub details made possible by shop-welded fabrication.

The hub contribution to blockage is reduced from 10% of member blockage for conventional radomes to about 1%. The ratios do not consider the suggested increase of the hub diameter by one-half wavelength to account for the microwave energy that does not pass freely near the junction of five or six members. Recent experiments at ESSCO Corporation indicated that such an increase in hub diameter is a pessimistic assumption. (See Dr. John Ruze's memo of January 4, 1966, to CAMROC file, Subject: Correlation of Theoretical and Experimental MSF Radome Transmission Loss.)

However, the induced current ratio for the deep members cannot be neglected. Dr. Ruze, in his memo of January 3, 1966, to CAMROC file (Subject: Evaluation of Ammann & Whitney Radome Proposal) stated that "the basic difficulty in using extremely deep members is that (1) on the beam axis the average induced current ratio is high (2.0 at 1,000 Mc) and (2) beyond about one-half the antenna radius the projected optical blockage is increased by a factor of about three. This is three-quarters of the antenna area."

Although shallower and wider members are desirable from an electrical standpoint, the depth of the members is determined by the requirements of snap-through buckling and transverse bending and can hardly be changed. From the extrapolations of curves given by Dr. Ruze in his January 3 memo for the frequencies and member sizes considered, it was found that for a given depth, narrower members will reduce the blockage, even taking the induced current ratio into account.

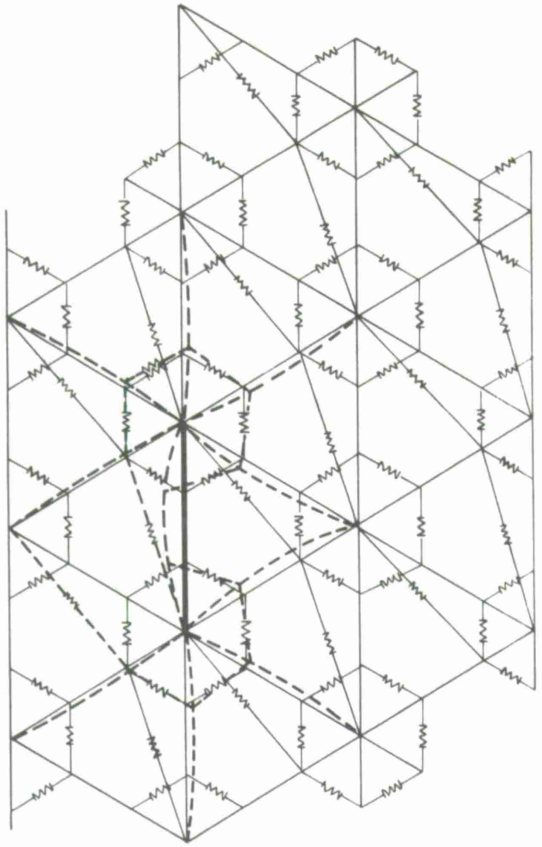

Figure 6. Buckling of members – one field wire per triangle.

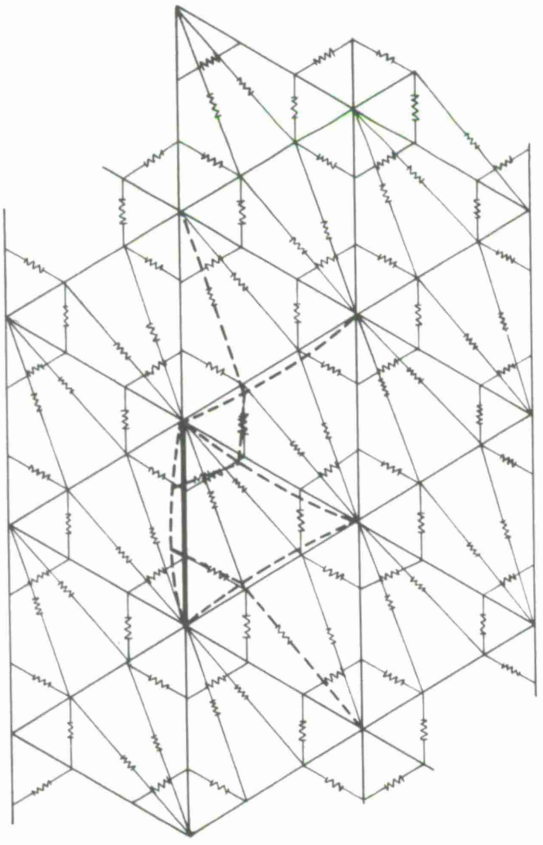

Figure 7. Buckling of members – two field wires per triangle.

Because the total effect of the induced current ratio and the web solidity can only be determined by testing, the upper and lower limits for blockage for representative frequencies and antenna radome configurations are given in Table 1. The table assumes that the Fiberglas tension members are used. The blockage will be greater if steel wires are used.

Table 1. Aperture blockings of radomes on a 400-ft-diameter antenna

	500-ft-diameter radome		550-ft-diameter radome	
Frequency	Pessimistic: solid web I.C.R.	Optimistic: open web No. I.C.R.	Pessimistic: solid web I.C.R.	Optimistic: open web No. I.C.R.
300 Mc	10.2*	6.9†	9.8†	5.9†
1000 Mc	8.9*	6.9†	8.5†	5.9†

NOTE: Members are assumed to be 2-1/2 inches wide, 20 inches deep, and 35 to 40 ft long braced by Fiberglas wires.

*Derived from Dr. Ruze's figures with optical, flat, and hub adjustments.

†Derived by using blockage formulas in the original report.

Pessimistic assumptions include full blockage by the beam lacing and the full effect of the induced current ratio in accordance with Ruze's memorandum. Optimistic assumptions include some transparency for the lacing and ignore the induced current ratio of the deep beams.

It is possible to use less deep members at the top portion of the dome to improve its electrical performance. This is possible because the compression at the top of the dome is much smaller than that at the stagnation point, the potential location for snap-through buckling. This scheme is most efficient electrically when the antenna dish is facing the zenith.

Narrow Members Applied to Smaller Diameter Radomes

At the request of Lincoln Laboratory, the feasibility of such a framing system applied to radomes of the Haystack range was investigated.

For small-diameter radomes, say in the order of 150 ft in diameter, if low alloy steel is used and the members are braced at one-third points, the member length can be increased to 30 ft from the present 9- to 15-ft range. The widths of the members can be reduced from 3 inches to 2-1/2 inches. The depth of the members required is 5 inches. Since the aperture blockage ratio is directly proportional to the length of the members, the blockage can be cut at least in half. For an antenna operating at X band frequencies, the induced current ratio of the deep members becomes negligible.

However, the sharp reduction in the number of members may be objectionable. The antenna may see discrete elements rather than a multiplicity that appears to be a uniform loss of gain.

Although such a blockage reduction is highly desirable, it might be most appropriate to design such a dome as a scale model of the proposed CAMROC radome in order to test the electrical efficiency. This will produce more blockage than the optimum design.

3.1 Nontriangular Geometry

Because the dome, if considered pin connected, is somewhat statically indeterminate, some members can be removed from the pattern shown on Figure 21A of the original report without causing primary bending stresses in the structure. However, the number is quite limited. In the case of Figure 21A, 77 members, or about 2% of the total of 3860, can be removed. Such removal would create nonrandom decreases in blockage and might prove undesirable.

If more than 77 members are removed, the dome members will be subject to primary bending. That is, member participation in the overall space-frame behavior will cause bending, whereas the system shown in Figure 21A is subject to bending due to local loads and secondary deformation only. Unless the removal is done judiciously, the primary bending stresses can build up to very large values. In effect, the structure becomes the reticulated analog of a plate rather than of a shell.

Figure 8 shows a possible method in which hexagonal openings are created by the removal of members. In this case it was found that if the openings are spaced three triangles apart, the perturbation damps out before the next hexagon is reached. Therefore, the overall three-dimensional shell behavior is preserved.

Nonetheless, those members around the edge of the opening will be under high axial and bending loads. They must be built of high-strength steel reinforced with thick plates.

This concept permits the removal of approximately 10% of the members with a corresponding reduction in blockage. The construction cost was not investigated, but it should not be much different than the basic cost, since the added material will be offset by reduced fabrication and erection.

The primary disadvantage is the size of the Fiberglas-reinforced plastic panels required at the hexagonal openings. Although the necessary thickness of these panels is still less than 0.10 inch, their length and width are far beyond the available sizes. If the material is spliced, the splice material will be electrically equivalent at least to the omitted members.

If nontriangular geometry is adapted to the availability of the skin material, only rectangles about 40 ft on a side appear reasonable. Such rectangles reinforced with diagonal Fiberglas X bracing were considered, but the reduction in snap-through buckling capacity in these schemes is excessive.

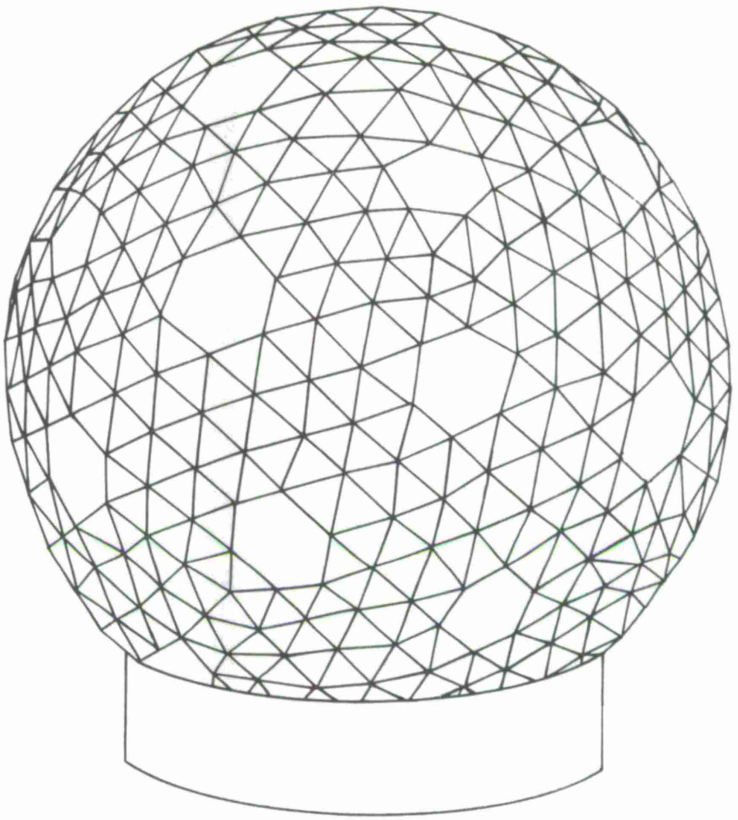

ELEVATION

Figure 8. Triangular geometry with hexagonal openings.

3.3 Rigid Panels

Several rigid-panel materials including Plexiglas and sandwiches of polyurethane and Fiberglas-reinforced plastics, mylar, or tedlar were explored further without much success.

The required thicknesses of these planes are so large that either they are uneconomical or electrically unacceptable.

Concepts using domed or pyramidal facets in lieu of Fiberglas panels were also considered, since certain facet configurations could reinforce the space frame below, eliminating some of the frame members. All these concepts increased the wind drag excessively and would have produced a structure that trapped snow or rain for long periods of time.

3.4 Fiberglas Space-Frame Members

The wall thickness of pipe required for structural strength and stability will be at least 1/8 inch. The total thickness penetrated will be 1/4 inch or more. In these thicknesses, the Fiberglas is practically as bad as a metal member in its blockage contribution.

The cost of joining is high, as are the bare material costs. There is therefore no electrical or structural merit in the concept.

3.5 Double-Layer Construction

Figure 9 shows a form of double-layer construction using 3-inch polyurethane insulation for the inner layer. This construction offers the following advantages:

1) Sharply reduced solar heat gain and attendant thermal stratification.

2) A cavity through which warm air can be pumped for snow removal and for condensation control.

3) FRP skin that can be protected from oilcanning by a slight pressure (or vacuum) within the cavity.

4) Three-inch-thick polyurethane panels that can provide lateral stability to the steel members except during erection and repair.

The disadvantages are:

1) The construction cost is high. It would add at least $1,000,000 to the cost of a 550-ft-diameter dome.

2) The downtime of the antenna due to snow on the radome is expected to be too small to justify the added expense. Observations over the last few years showed that snow rarely accumulated on top of the Pittsburgh Auditorium in Pittsburgh, Pa., and the TWA Terminal in J. F. Kennedy International Airport in New York. This phenomenon can be attributed to the higher wind at the top of the dome and to the heat provided inside the dome.

3) The reasoning applies as well to temperature stratification. Double-layer construction will minimize the problem, but will not solve it entirely. Since the surface error of the antenna is largely due to erection and fabrication, the added cost to reduce the temperature stratification contribution to the error cannot be justified.

3.6 Removal of Members at the Top of the Dome

A large-enough hole at the top of the dome will function somewhat as a chimney, permitting the air heated by solar radiation to escape from the dome. This should reduce stratification and thermal gradients.

Experience with Haystack indicates that the error due to stratification is manageable and major expense to control it is not justified. In this case, because the cost of removable panels is moderate, a certain amount of experimentation on existing smaller radomes is justified.

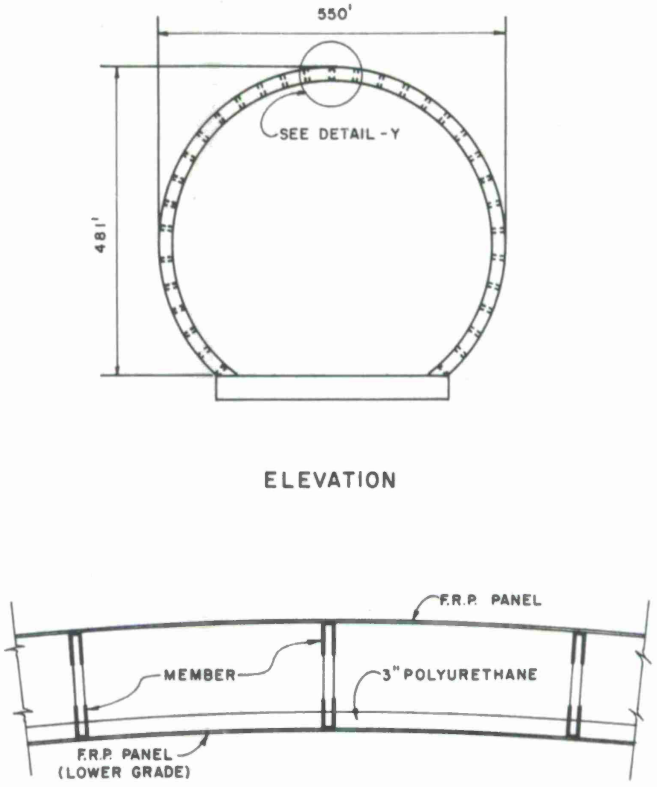

Figure 9. Double-layer construction.

It should be kept in mind, however, that the removal of these panels destroys the streamlining of the sphere and increases the wind drag on the structure. The panels should always be replaced if the instrument is left unattended or if heavy winds are predicted.

For this reason, removal of panels is considered to be practical only in improving an already satisfactory condition. It should not be relied upon to convert a marginal or submarginal error.

4. FURTHER STUDIES ON SNAP-THROUGH BUCKLING

The elements of the snap-through buckling problem had been discussed in the original report. On page 32 of the report, we stated:

> In the buckling study, classical theory (linear, small-deflection), Tsien's buckling (snap-through) and member buckling have been considered. For the types of loadings and configuration of the radome, there is no exact theoretical solution available for the first two types of buckling. However, available approximate buckling criteria are considered adequate.

Since snap-through buckling criteria govern the overall depths of the members, which in turn affect the electrical performance of the radome, it would be well to amplify the assumptions made for this and the original report and to explain the approximate procedure that was contemplated for final design.

4.1 History

The critical external hydrostatic pressure that will cause a uniform spherical shell to buckle is

$$K \cdot E \cdot \left(\frac{T}{R}\right)^2 \quad ,$$

where E is the modulus of elasticity, R is the shell radius, T is the shell thickness, and K is a coefficient.

Using small-deflection theory analogous to that used for an Euler column, Zoelly and Timoshenko obtained a K of 1.21 when Poisson's ratio is 0.3. This is classical buckling.

Because laboratory tests were never able to duplicate this value, von Karman and Tsien investigated the possibility of another mode of buckling associated with large deflections. This mode eventually became known as oilcanning or snap-through buckling.

Their preliminary work showed that K should be reduced from 1.21 to 0.365. Further investigation by Tsien showed that K varied from 0.28 for R/T = 1500 to 0.40 for R/T = 450. Tsien's theory agrees favorably with the experiments.

4.2 Limitations

Tsien's work applies only to surface shells subject to uniform external pressure. Because the radome is reticulated, the theory cannot be applied directly to it. Other factors such as boundary effects, residual stresses, imperfections, joint effects, and plasticity further complicate the problem.

4.3 The Approximations Used in the Preliminary Design

An analogous membrane that has the same extensional stiffness and flexural stiffness as the space frame was obtained. If the lowest of Tsien's coefficients is adopted for conservatism, the critical load in pounds per square foot as derived on page 40 of the original report is

$$P_{crit.} = \frac{12,600,000\ tw\ V}{R^2} \quad ,$$

where tw is the thickness of a weight-equivalent shell in inches, V is the radius of gyration of one of the space-frame members in inches perpendicular to the surface, and

R is the dome radius in feet. The maximum principal stress at the stagnation point of the wind was then computed. This stress included the effects of both wind and dead load. That is, a fictitious hydrostatic pressure causing the same principal stress as the computed maximum was assumed to act on the analogous membrane. It was this conservative value of the pressure that was compared with the critical pressure to determine the safety factor against oilcanning.

Because deep members are required to reduce bending stresses due to transverse wind loads, a safety factor on the order of 3 is provided for all domes investigated by this manner.

This was believed conservative for preliminary design for the following reasons:

1) The highest principal stress at the stagnation zone was assumed to act in all other directions.

2) The lowest value of Tsien's coefficient was used.

3) In the very large domes studied we expect several joints to be within a buckled area. Because these joints are rigid joints, the actual structure and the idealized shell should behave similarly.

4) A large safety factor was provided since the required depth proved efficient in resisting transverse bending.

4.4 Approximations Proposed for the Final Design

Although these procedures covered in Section 4.3 were judged adequate for the preliminary design of the many radomes investigated to establish cost curves, a more rigorous method was contemplated for final design. Briefly, the method can be described as follows:

For the probable buckling mode A shown in Figure 10a, the mirror image of the part of the dome above the horizontal plane $a_1 a_2$ (shown in dotted line) can be used as the first assumed shape. To this purpose, assume that a node exists at the intersection of members with the symmetry plane. If all members above the plane are assumed to move to their mirror image nodes below the plane, no change in length will take place.

To maintain directional compatibility, assume that the ends of each member remain parallel to their original tangents. Such a condition is shown in Figure 10b. At this stage the end moments are not in equilibrium at the nodes. The forces at the nodes must be relaxed by normal linear theory. This will have the effect of rotating member ends and displacing nodes, smoothing the assumed shape to one that does not require external loads for equilibrium.

All these stages can be performed by conventional computer operations, the non-linear aspects being covered by ignoring the displacements when getting end forces and by creating a new stiffness corresponding to the new geometry.

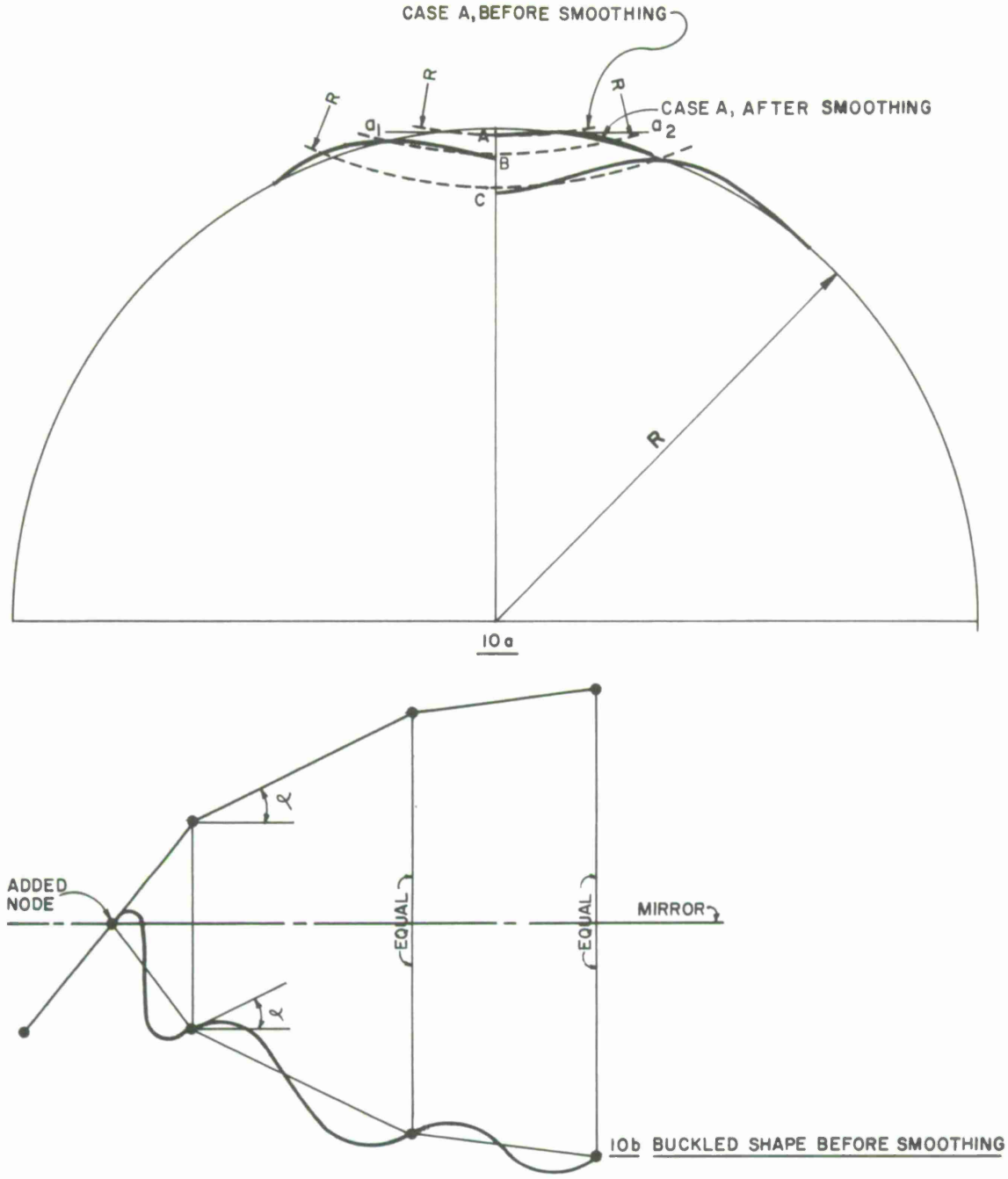

Figure 10. Buckling modes.

The strain energies of bending and stretching of the members as well as the potential energy loss of the external loading for the buckled shape can be computed by conventional computer matrix operations. The ratio of the strain energy to the potential energy loss is the safety factor against buckled mode A.

Similarily, the safety factors against the buckled modes B, C, etc., can be found. The mode with the smallest factor of safety is the critical mode.

It is interesting to note that the use of the above-mentioned approach will reduce the large-deflection problem to a small-deflection problem, and it can be performed by using special input to existing programs such as FRAN, STRESS, or GISMO.

Unlike the preliminary stage, only one dome will be under investigation. A relatively small amount of computer time would be required to repeat the steps for many assumed shapes (say 100) in order to find the smallest safety factor.

The shapes with the lowest safety factors should be studied further for the effects of plasticity. That is, the plastic redistribution effect on smoothing and the loss of strain energy due to yield would be considered.

The procedures are not rigorous, in that the assumed shapes do not indicate improvement that converges to the exact shape. However, it can be brought as close to the theoretical solution as is necessary. In some respects, it is superior to the available shell theory, since in the proposed procedures the external loads do not have to be hydrostatic and the effect of boundaries can be included.

4.5 The Effect of Buckling Criteria on Blockage Ratio and Cost of Construction

In order to measure the effect of buckling on cost and blockage, assume that an otherwise satisfactory concept must be given a larger buckling safety factor.

From the equation in Section 4.3, it can be seen that for a given diameter of radome, the buckling resistance is directly proportional to the product of thickness of weight-equivalent plate and the radius of gyration of the members. Since the increase in thickness of weight-equivalent plate increases the tonnage of the fabricated steel and therefore the overall cost of construction, it is more logical to increase the radius of gyration by use of deeper members. The deeper members will also reduce the bending stresses due to transverse wind load. Such deepening adds to the weight of lacing only and has a small effect on cost.

Although deeper members increase aperture blocking, the increase would not be excessive, since the beam width is more significant in aperture blocking than beam depth. If some transparency due to the lacing of the truss members can be used instead of assuming 100% blockage in laced faces, even this increase will be reduced.

APPENDIX 1

FIBERGLAS TENSION MEMBERS – SUMMARY OF DATA

Fiberglas Tension Members (FTM) as developed by the Owens-Corning Fiberglas Corporation, New York, New York, are strands of different diameters made of approximately 80% S-type glass fibers and 20% epoxy resins. The basic properties of the glass fibers and the finished strands are given in Tables 2 and 3.

Table 2. Properties of S and E glass fibers

Property	S Glass	E Glass
Density, lbs/in^3	0.090	0.092
Tensile modulus, psi	12.4×10^6	10.5×10^6
Virgin filament strength, ksi	665	500
Dielectric constant, 10^{10} cycles, room temp.	5.2	6.13
Loss tangent	0.0068	0.004

Table 3. Properties of Fiberglas tension members

	FTM diameter (inches)			
Property	0.027	0.036	0.065	0.090
Tensile, ksi	250-300	250-300	240-270	240-270
Elongation @ break, %	5-5.5	5.5	4.5-5.5	4.5-5
Young's modulus (10^6 psi)	5.5	5.5	5.2	5.2
Specific gravity	1.6	1.6	1.6	1.6
Weight/1000 ft (lbs)	0.42	0.70	2.40	4.70
Breaking strength (lbs)	160-180	280-300	800-900	1600-1750

Fiberglas cables or ropes made of several strands are also available. The largest cable made at Owens-Corning to date is a cable with 7 strands, each strand 0.14 inch in diameter, with an ultimate breaking strength on the order of 15 tons. There will also be no difficulty in making thin flat ropes.

FTM terminals (end connections) with 95% efficiency are also available. These terminals are made chemically. Expoxy resin and glass are used as potting compound.

Recent test results made at Owens-Corning's Aerospace Research Laboratory on FTM materials are very encouraging. They are summarized as follows:

Creep: The amount of creep at a load 30 to 35% of the ultimate strength is less than 1%. The creep occurs in the first few days.

Static fatigue tests (90% survival): Static fatigue tests were made for various combinations of room temperature (-40°F to 150°F) and relative humidity (low humidity to saturated humidity). It was found that for a load equal to or less than 30% of the ultimate strength, the life span of the FTM materials is almost indefinite.

Dynamic flexural fatigue tests (90% survival): For various combinations of temperature and humidity, it was found that FTM can sustain 10,000,000 cycles of load up to 20% of the ultimate strength.

Dynamic axial fatigue tests: For ambient conditions, the tests indicated that for 22% ultimate strength, the cycles to failure for 90% survival and 50% survival are 600,000 and 4,000,000, respectively. However, these data are preliminary. The grip system is being revised and environmental control added to the tests.

Based on the results of the above-mentioned tests, the Owens-Corning engineers recommend the use of 30% of the ultimate strength as the working load.